# Interactions of Phosphate and Silicate with Iron oxides in Freshwater Environments

by

Md Abdus Sabur

A thesis
presented to the University of Waterloo
in fulfillment of the
thesis requirement for the degree of
Doctor of Philosophy
in
Earth Sciences (Water)

Waterloo, Ontario, Canada, 2019

# Examining Committee Membership

External Examiner

Dr. Grant Ferris
Professor
Department of Earth Sciences
University of Toronto


Supervisor

Dr. Philippe Van Cappellen
Professor, Canada Excellence Research Chair
Department of Earth and Environmental Sciences
University of Waterloo


Co-supervisor

Dr. Christopher T. Parsons
Research Assistant Professor
Department of Earth and Environmental Sciences
University of Waterloo


Internal Member

Dr. Carol J. Ptacek
Professor
Department of Earth and Environmental Sciences
University of Waterloo


Internal-external Member

Dr. Roland I. Hall
Professor
Department of Biology
University of Waterloo


Other Member

Dr. Thai Phan
Assistant Professor
Department of Earth and Environmental Sciences
University of Waterloo

# AUTHOR'S DECLARATION

This thesis consists of material all of which I authored or co-authored: see Statement of Contributions included in the thesis. This is a true copy of the thesis, including any required final revisions, as accepted by my examiners.

I understand that my thesis may be made electronically available to the public.

# Statement of Contributions

This thesis consists of a series of co-authored chapters. As a first author on each chapter, I was primarily responsible to design the study and execution. The contributions of co-authors in each chapter are summarized below:

Chapter 2: Philippe Van Cappellen (PVC) and I defined the scope of the research. I designed the experiment with assistance from PVC and Christopher T. Parsons (CTP). Taylor Maavara (TM) initially provided the computer codes for the surface complexation model. I conducted the laboratory experiments, calibrated the surface complexation model, and analyzed the data. I wrote the chapter with feedback from PVC, CTP and TM.

Chapter 3: PVC and I defined the scope of the study. I designed the experiments, analyzed the data, and wrote the paper with inputs from PVC and CTP.

Chapter 4:  PVC, CTP and I defined the scope of the study. I designed the experiments, after discussions with PVC and CTP, for the synthesis of iron, phosphate and silicate co-precipitates and their dissolution experiments in ascorbate-citrate media. Christina Smeaton and I conducted the reductive dissolution experiments with *Shewanella putrefaciens*. I wrote the chapter with input from CTP and PVC.

Chapter 5: PVC, CTP and I designed the study. I performed the laboratory experiments, analyzed the data, and wrote the chapter with feedback from PVC and CTP.

# Abstract

Internal phosphorus loads, from bottom sediments to surface waters, are often comparable in magnitude to external phosphorus loads, particularly in water bodies with a history of high external phosphorus inputs from point and non-point sources. The benthic release of phosphorus can be influenced by several factors including pH, redox potential, temperature, microbial activity and the concentration of competitive anions at or near the sediment-water interface. Dissolved silicate occurs ubiquitously in natural waters and may act as a competitive ion to phosphate. Nonetheless, prior to the work in this thesis, the effect of silicate on internal phosphorus loading remained poorly understood. This thesis addresses several of the mechanisms through which silicate may influence the mobilization of aqueous phosphate from sediments in aquatic environments. The thesis starts with a thorough literature review of phosphorus biogeochemical cycling in relation to eutrophication, sediment-surface water interactions, mineralogy, competitive anions and microbial activity (Chapter 1).

Next, adsorption/desorption of phosphate on/from goethite, a model ferric (hydr)oxide mineral, is investigated in the absence and presence of dissolved silicate. The influence of dissolved silicate on phosphate adsorption is evaluated through laboratory experiments and application of the CD-MUSIC model (Chapter 2). The results show that increasing concentrations of silicate decrease phosphate adsorption, leaving more phosphate in the aqueous phase. The competitive effect of dissolved silicate is more pronounced under alkaline conditions. Subsequently, phosphate desorption experiments were conducted under dynamic pH conditions in the presence and absence of silicate (Chapter 3). The experimental results show that the gradual transition from acidic to alkaline conditions induces the desorption of phosphate adsorbed to goethite under acidic conditions. The presence of silicate in the phosphate/goethite system does not affect phosphate desorption, because of the stronger surface complexation of phosphate to goethite.

In addition to adsorption and desorption processes, the co-precipitation of phosphate with iron and the potential subsequent dissolution of these co-precipitates as a result of changing physico-chemical conditions may also control the mobility of phosphate in aquatic environments. The effects of dissolved silicate on the co-precipitation of phosphate with iron and the reactivity of the resulting solids are examined (Chapter 4). Ferric (co)-precipitates (i.e.,

Fe-P-Si) with variable Si:Fe ratios, were synthesized either via oxidation of $Fe^{2+}_{(aq)}$ or by increasing the pH of $Fe^{3+}_{(aq)}$ solution. The solids were characterized by a combination of chemical and spectroscopic techniques including attenuated total internal reflectance Fourier transform infrared spectroscopy (ATR-FTIR) and X-ray powder diffraction spectroscopy (XRD). Similar solid phase P:Fe ratios were found in co-precipitates formed from solutions with different dissolved silicate concentrations, regardless of the method of preparation. This suggests that the interactions between phosphate and iron during co-precipitation were not affected by dissolved silicate.

The ferric (co)-precipitates were subsequently reductively dissolved abiotically in buffered ascorbate-citrate solution to determine their reactivity under reducing conditions. The kinetic data show that the co-precipitates with higher Si:Fe ratios were more recalcitrant to dissolution. For co-precipitates synthesized via oxidation of $Fe^{2+}_{(aq)}$, reductive dissolution experiments were also conducted in the presence of the facultative anaerobic iron reducing bacteria *Shewanella putrefaciens.* XRD analyses of the residual solids imply that solids with the higher Si:Fe ratios may be more resistant to microbially mediated reductive dissolution. The relative reactivities of the co-precipitates obtained by the two synthesis methods are also addressed in Chapter 4.

In Chapter 5, the effect of silicate on the mobility of phosphate in a natural sediment was evaluated via flow-through experiments. The results show that dissolved silicate enhances the mobility of phosphate at the sediment-water interface. Ferric (co)-precipitates were formed at the oxic surface of sediment columns via the oxidation of ferrous iron supplied with upflowing solutions containing variable silicate concentrations. The subsequent dissolution of these co-precipitates under imposed anoxic conditions at the sediment-water interface indicates that the co-precipitates formed at higher dissolved silicate concentrations were more reactive towards reductive dissolution. These results are therefore in apparent contradiction to those observed in Chapter 4.

The ferric (co)-precipitates (i.e., Fe-P-Si) evaluated in Chapter 4 were prepared from solutions containing high concentrations of iron, phosphate and silicate, by imposing either rapid aeration or pH increase. These conditions were selected to maximize the yield from the syntheses. The synthesis methods in Chapter 4 are therefore most representative of aquatic environments where co-precipitation occurs rapidly (e.g., groundwater springs) and the

concentrations of these dissolved constituents are fairly high. However, in many other aquatic environments, the diffusion-controlled release of $Fe^{2+}_{(aq)}$ from the deeper sediments results in the gradual oxidation of $Fe^{2+}$ at the sediment-water interface under oxic conditions. This process is typical in lake sediments with minimal advective exchange between surface water and groundwater. This gradual oxidation (at relatively low concentrations of $Fe^{2+}$) results in the slow formation of ferric (co)-precipitates which may be dissimilar to those synthesized herein and discussed in Chapter 4. The ferric (co)-precipitates synthesized with the flow-through column system in Chapter 5 may be better analogues of slow forming co-precipitates in diffusion dominated or moderately advection influenced aquatic sediments than those synthesized in Chapter 4.

Finally, to elucidate the likely importance of the various influences of dissolved silicate on phosphate mobility investigated in this thesis, concentrations of dissolved phosphate and silicate as well as pH data are extracted from the US National Water Information System (NWIS) network (data shown in Chapter 1 and Chapter 2). The NWIS data along with combined experimental and modeling results suggest that silicate-mediated phosphate mobilization is likely a commonly occurring process at the sediment-water interface of lakes and reservoirs. This thesis also demonstrates the multiple roles of silicate on the mobilization of phosphate in aquatic environments, and improves our fundamental knowledge of iron, phosphorus and silicon cycling in freshwater environments.

# Acknowledgments

First and foremost, I would like to express my sincere appreciation and thanks to my supervisor, Philippe Van Cappellen, for providing me with the opportunity to work with him in complete independence. I am grateful to you, Philippe, for patiently listening to my research ideas and hypothesis, even that those were not concise, particularly at the beginning of my project. You never dismissed nor discouraged any of my raw research thoughts, but instead guided me to stay focused in the right direction, whenever perhaps I needed. Working with you was a great pleasure and experience that will remain with me. I thank you again, Philippe.

Next, I want to express my gratitude to my co-supervisor, Christopher T. Parsons, for his valuable suggestions, comments, and feedbacks throughout this work. Coming from a purely chemistry background, I learned a lot from him on my way towards environmental research involving a biogeochemical complexity. Chris, your critical questions and suggestions always helped me to improve the design and organization of my experiments as well as study findings. Without your support and guidance, this work would not have come to this stage.

I also would like to thank my examination committee members, Grant Ferris, Roland I. Hall, Carol J. Ptacek, and Thai Phan for their constructive questions and comments on my thesis, which eventually helped me in improving this dissertation. Since the start of my PhD, Hind A. Al-Abadleh and David O'Connell had been in my committee, but they were away during my thesis defense. I wish to thank them as well for their time and great comments I received on my research.

The Ecohydrology Research Group at Waterloo consists of a genuine group of hardworking kind people. I enjoyed my time with them while working in the laboratory as well as outside of work. Particularly, I am thankful to Marianne Vandergriendt, senior laboratory technician, for keeping her patience with me, a student probably not very organized in the laboratory. Moreover, I thank Christina Smeaton, a research scientist of our research group, for sharing her expertise in completing an experiment with bacteria. A special thanks to Jenna Paik, co-op student, for all her hard work and co-operation in completing the experiment with the flow-through reactor system. Thanks goes to Taylor, Lu, Christine, Linden, Shuhuan, Bijen, Healther, Shannon, Erin, and Tatjana. They helped me in laboratory analysis and by checking my writings, and so, I am grateful to them for the cooperation in my project.

During my last few years in waterloo, I had the opportunity to make many good friends and spend a lovely time with them. Including their names here would be a long list. Here, I can not mention their names, but I surely believe they know who they are.

The last person I want to express my gratefulness to is, my wife, Sharmin Jahan. Without her unconditional support, I would not be able to complete this challenging journey. Sharmin, you maintained and managed all the family affairs; took care of our son, Raahil, single-handedly. Of course, you happily did everything and did not make me feel the family pressure. I simply want to say that you are a great part of this achievement at Waterloo.

# Dedication

This thesis is dedicated to my son, Raahil Nayyir Rahman, whose arrival has made my every moment pleasant

# Table of Contents

# List of Figures

# List of Tables

# List of Abbreviations

| | |
|---|---|
| ATR-FTIR | Attenuated total internal reflectance Fourier transform infrared |
| Ca | Calcium |
| CD-MUSIC | Charge distribution multisite surface complexation |
| DIP | Dissolved inorganic phosphorus ($H_2PO_4^-$/$HPO_4^{2-}$) |
| DO | Dissolved oxygen |
| DOC | Dissolved organic carbon |
| DOP | Dissolved organic phosphorus |
| DP | Dissolved phosphorus |
| EDS | Energy-dispersive (X-ray) spectroscopy |
| Fe | Iron ($Fe^{2+}$ + $Fe^{3+}$) |
| IC | Ion chromatography |
| ICP-OES | Inductively coupled plasma-optical emission spectrometry |
| Mg | Magnesium |
| Mn | Manganese |
| OP | Organic phosphorus |
| P | Refers to both organic and inorganic phosphorus |
| PIP | Particulate inorganic phosphorus |
| POP | Particulate organic phosphorus |
| PZC | Point of zero change |
| PZNPC | Point of zero net proton charge |
| SEM | Scanning electron microscope |
| XRD | X-ray diffraction |

# Chapter 1
## General Introduction

### 1.1 Environmental importance of phosphorus

Phosphorus (P) has been an essential element for all biological systems since the emergence of life on early earth (Pasek, 2008; Series and Mar, 2007). It has few allotropes, among them white and red P are the more abundant (Ashley et al., 2011). The element P is, however, very reactive and therefore usually found in the environment as compounds and ions. Phosphorus has historically been used for different purposes; from human welfare to destructive war weapons since its discovery in the 17th century (Figure 1.1). Even though P is a compulsory nutrient for plant growth, over the last few decades, it has received global attention as a contributor to the increasing problem of harmful and nuisance algal blooms, the decay of which results in the degradation of surface water quality.
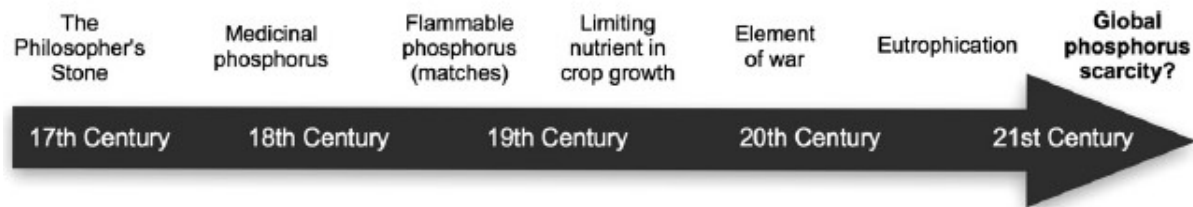


**Figure 1.1.** Historical uses of P and the associated concerns. Reproduced from Ashley et al. (2011).

The systematic application of P fertilizer in agriculture started in the early-20th century to meet the growing needs of world's increasing population. Its extensive and increasing use as a fertilizer combined with pesticides, herbicides and detergents started after the 2nd World War (Ashley et al., 2011; Filippelli, 2008). In agricultural lands, large amounts of P are removed with each food harvest. Therefore, if P is not replaced with fertilizer, the amount of P in the soil will decrease over time, which results in the decrease of agricultural yields. To ensure good agricultural yield, an excess amount of P fertilizer is often added because farmers do not want to risk a loss of yield due to limiting P, and P fertilizers are cheap compared to the value of the crop. This unconsumed P builds up in the soil and eventually finds its way into

aquatic systems, e.g., aquifers, rivers, lakes and coastal environments. The environmental and ecological consequences of elevated levels of P in surface waters are generally known as eutrophication (Carolina, 2002; Heisler et al., 2008; Paytan and Mclaughlin, 2007; Ruttenberg, 2003; Smith and Schindler, 2009; Tilman et al., 2001). The major physical and biogeochemical processes of P cycling on land and in aquatic environments are discussed in the following sections.

## 1.2 Inland phosphorus cycling

Phosphorus is present in very small amounts in most bedrocks, soils and sediments. It contributes to only about ~0.1% of the weight of the earth's crust, moreover only a very small fraction of P is readily available for biological uptake (Filippelli, 2008; Paytan and Mclaughlin, 2007). In typical sedimentary rocks, P is usually associated with authigenic carbonate-fluorapatite, and the concentration of P in most sedimentary rocks is similar to that of the crustal average (Filippelli, 2008; Filippelli and Street, 2002; Ruttenberg, 2003). However, the concentration of P in the earth's crust is highly variable and some individual rocks and minerals may contain P at concentrations of approximately 100 times the crustal average (Paytan and Mclaughlin, 2007). There are approximately 300 known P bearing minerals (Paytan and Mclaughlin, 2007), of which fluorapatite in igneous rocks exhibits the highest P content (Filippelli and Street, 2002; Ruttenberg, 2003).

Weathering of P-minerals results in the release of soluble orthophosphate, which is readily accessible by plants and microorganisms in soil, sediment, and water (Filippelli, 2008; Filippelli and Street, 2002; Ruttenberg, 2003). The application of P fertilizer on agricultural lands also increases soluble phosphate (aqueous speciation shown in section 1.5.3.2.2) in soil which (i) can be attenuated by the soil reactive components, or (ii) may enter into the primary producers, e.g., plants, for supporting photosynthesis, and later to the higher animals through the food chain (Filippelli, 2008). The abiotic immobilization of phosphate in soil generally takes place by adsorption, precipitation, and co-precipitation, with the majority of the immobilization associated with particulate inorganic phosphorus (PIP) fractions (Filippelli, 2008; Ruttenberg, 2003). The PIP in soil includes P sorbed and co-precipitated to metal (hydr)oxides, carbonate minerals, and clay minerals. Generally, soluble phosphate is the most bioavailable, although low molecular weight organic-P compounds can also support primary

production in phosphate-limited conditions (Orihel et al., 2017; Paytan and Mclaughlin, 2007). The uptake of phosphate by phytoplankton can be represented by the general chemical equation (Paytan and Mclaughlin, 2007):

$$106\ CO_2 + 16\ HNO_3 + H_3PO_4 + 122\ H_2O + trace\ elements\ and\ vitamins$$
$$\rightarrow C_{106}H_{263}O_{110}N_{16}P + 138\ O_2$$
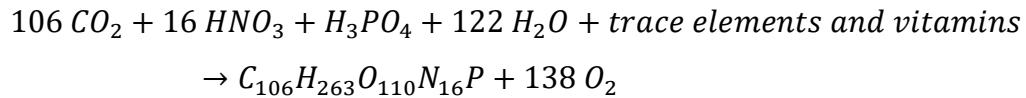
Major building blocks in plants and animals, e.g., DNA, RNA, ATP, phosphoproteins, and phospholipids contain P in their structures (Paytan and Mclaughlin, 2007; Ruttenberg, 2003). When plants and animals die, the dead biomass can release phosphate due to enzymatic hydrolysis (Filippelli, 2008; Filippelli and Street, 2002; Ruttenberg, 2003). The unaltered biomass gradually builds up in soil as particulate organic-P (POP) (Filippelli, 2008). In higher animals, P is also present in teeth and bones which are relatively stable and insoluble under normal conditions (Filippelli, 2008).

The particulate forms of P, inorganic and organic, are usually less bioavailable compared to soluble phosphate, although PIP in soil can further release phosphate usually due to microbial activity or by the influence of organic acids released by plant roots (Filippelli, 2008; Filippelli and Street, 2002; Ruttenberg, 2003). In the upper soil, the uptake by plants and attenuation by soil components limit P leaching into the groundwater. Soil P may also be introduced into nearby streams and rivers, as a result of physical, chemical and biological weathering, and eventually enters into the receiving water bodies, e.g., lakes and the ocean (Domagalski and Johnson, 2012; Filippelli and Street, 2002; Paytan and Mclaughlin, 2007; Ruttenberg, 2003).

## 1.3 Eutrophication: a surface water problem

Phosphorus is an essential nutrient for the growth of phytoplankton and is often limiting in freshwater systems (Filippelli and Street, 2002; Schindler et al., 2008). Therefore, additions of P to the aquatic environment can result in an accelerated algal growth in surface waters, such as rivers and lakes. The degradation of algal biomass often depletes water quality in multiple different ways. For example, degradation of dead algae consumes dissolved oxygen (DO) and often causes water column hypoxia and anoxia. The depleted DO level results in unsuitable living conditions for many aquatic life forms. Furthermore, some algae (commonly cyanobacteria) also produce toxins in freshwater environments which are harmful and

poisonous to living organisms (Landsberg, 2002). In addition, the presence of algal cells generally increases turbidity in water; this prevents sunlight penetration and ultimately affects benthic photosynthesis (Smith et al., 1998). These environmental and ecological problems associated with algal blooms are generally known as eutrophication.

Depending on the degree of biological production, surface waters are generally classified as oligotrophic, mesotrophic, eutrophic, or hypereutrophic. The oligotrophic, mesotrophic, and eutrophic systems have low, intermediate, and high levels of biological productivity, respectively. The hypereutrophic systems, on the other hand, experience extremely high levels of biological productions and are generally less common. Surface waters are also classified based on various water quality parameters, e.g., the concentrations of P, N, chlorophyll-a, turbidity etc. For example, average concentrations of total P <10, 10-30, 30-100, and >100 mg/L are often used to distinguish oligotrophic, mesotrophic, eutrophic, and hypertrophic lakes, respectively (Smith et al., 1998). Figure 1.2 shows an algal bloom in the west pond of Cootes Paradise in Hamilton Harbor, ON. Cootes Paradise has a history of receiving high P loads from the combination of a nearby wastewater treatment plant's effluent as well as urban runoff (Parsons et al., 2017).
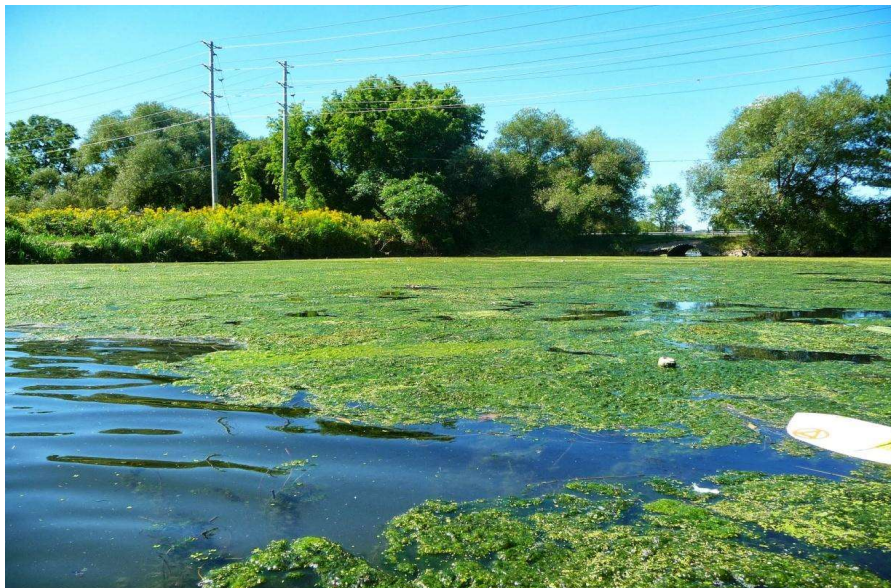


**Figure 1.2.** Cootes Paradise, a eutrophic water body connected to Hamilton Harbor, Hamilton, ON. Picture courtesy of Chris Parsons.

The depleted water quality as a result of eutrophication causes millions to billions dollar of economic losses annually in many countries (Eitzmann et al., 2009; Hudnell, 2010; IISD, 2017; Mason et al., 2003). For example, because of severe eutrophication in Lake Erie (Canada-USA), the drinking water supply for the residents of Toledo in Ohio (USA) had to shut down for a week in 2014 (Fitzsimmons, 2003). The degraded water as a result of eutrophication is not suitable even for recreational purposes (Chislock et al., 2013). Therefore, understanding the biogeochemical cycling of P in aquatic environments (discussed in section 1.4 to 1.5) is important to identify the potential causes of eutrophication and to develop management strategies.

## 1.4 Phosphorus cycling in the water column

Both dissolved and particulate forms of P are transported by streams and rivers into lakes where they undergo a number of biogeochemical transformations (Orihel et al., 2017; Zhang et al., 2016) (Figure 1.3).Dissolved forms of P generally include inorganic ortho- and poly-phosphate and low molecular weight organic-P compounds. The particulate forms of P in surface waters are also characterized as both inorganic and organic. Inorganic forms of particulate P (PIP) can be associated with metal (hydr)oxides (where the metal is most commonly Fe or Al) as well as with calcium, for example in bio-minerals which form teeth and bone. Organic forms of particulate P (POP) generally includes living or dead biomass. The degradation of biomass and the mineralization of particulate and dissolved organic-P generate phosphate in water which can either be removed by further phytoplankton uptake or as PIP through adsorption, precipitation or co-precipitation. Both dissolved and particulate P may be relocated from surface waters with the outflow or removed from the water column by sedimentation and downward diffusion into the underlying bottom sediments followed by adsorption and secondary mineralization below the water-sediment interface.
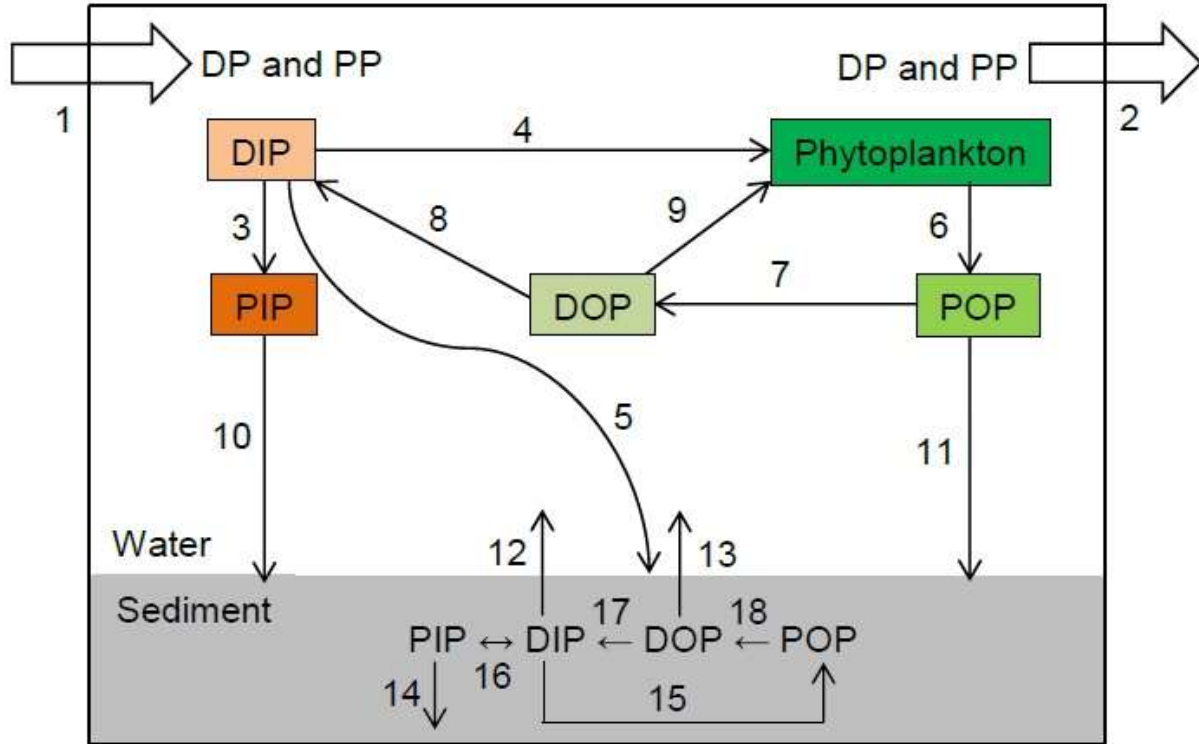
**Figure 1.3**. Schematic illustrating the P cycling in water bodies including lakes. DP and PP represent dissolved and particulate phosphate, respectively and can be organic and inorganic. DIP and PIP represent dissolved ($H_2PO_4^-$/$HPO_4^{2-}$ or polyphosphate) and particulate inorganic phosphate. DOP and POP represent dissolved and particulate organic-P forms, respectively. The chemical, biological and physical processes involved in P cycling shown by the arrows are listed in Table 1.1.

**Table 1.1.** Chemical, biological and physical processes shown in Figure 1.3 for cycling of P in surface waters.

| Processes | Description | Increase (+) and decrease (-) of phosphate ($H_2PO_4^-$/$HPO_4^{2-}$) in overlying water |
|---|---|---|
| 1 | External input | + |
| 2 | Removal with outflow | - |
| 3 | Adsorption or co-precipitation | - |
| 4 | Uptake for photosynthesis | - |
| 5 | Adsorption or downward diffusion | - |
| 6, 7, 8 | Decay or degradation, and mineralization | + |
| 9 | Uptake for photosynthesis | - |
| 10, 11 | Sedimentation | - |
| 12, 13 | Benthic efflux | + |
| 14 | Burial into deeper sediment | - |
| 15 | Bacterial uptake | - |
| 16 | Interconversion between PIP and DIP | +/- |
| 17, 18 | Similar processes as shown for 6, 7, 8 | + |

## 1.5 Phosphorus cycling in aquatic sediments

## 1.5.1 Phosphorus pools

Phosphorus can accumulate in sediments in any aquatic environment with a history of external P loadings (Matisoff et al., 2016; Orihel et al., 2017; Scavia et al., 2014). In the sediment, P can be associated with PIP and POP where both can be buried into the deeper sediment or may re-release phosphate into the sediment pore-water. The efflux of phosphate from sediment to the overlying water is known as internal phosphate loading.

### 1.5.1.1 Particulate organic phosphorus

Particulate organic phosphorus (POP) in sediments is generally associated with living biomass or with necromass, primarily originating via sedimentation from primary production or higher organisms, though it can also be supplied from the catchment area (Reitzel et al., 2007). The sediment biota is also included in the POP pool because they consume dissolved phosphate from sediment pore-water (Orihel et al., 2017). There are several classes of organic-P compounds that are commonly found in aquatic environments including nucleic acids, phospholipids, phosphoproteins, inositol phosphate, and phosphonates etc. (Baldwin, 2013). Some low molecular weight organic-P compounds can also sorb to the surfaces or form structural parts of metal (hydr)oxides or carbonate minerals (Lü et al., 2017; Ruttenberg and Sulak, 2011; Wang et al., 2016). The organic-P in sediments represents on average about 40% (by weight) of total sediment-P (Giles et al., 2015; Zhu et al., 2013).

### 1.5.1.2 Particulate inorganic phosphorus

Particulate inorganic phosphorus (PIP) in sediments can be associated with the surfaces of metal (hydr)oxides, clay and carbonate minerals, incorporated in the structures of these minerals, or precipitated with metal cations such as Ca, Fe, Mn, and Al (Christophoridis and Fytianos, 2006; Orihel et al., 2017; Oxmann and Schwendenmann, 2015; Søndergaard et al., 2003). The anion adsorption capacities of different sediment minerals vary depending on factors such as surface charge, surface area, surface site densities, temperature, concentrations and speciation of anions, etc. Therefore, phosphate released from one mineral can be redistributed to other mineral surfaces in sediments with many different types of minerals. The surface binding groups of metal (hydr)oxides and silicates are generally dominated by

hydroxyl groups which undergo acid-base reactions, forming $S-OH_2^+$, $S-OH$, and $SO^-$ depending on pH, where S generally denotes Fe, Al, Mn, or Si (Langmuir, 1997a). The distribution of surface groups ($S-OH_2^+$, $S-OH$, and $SO^-$) depends on pH, and the point of zero net proton charge (PZNPC) of the solid (Langmuir, 1997a). The term PZNPC represents a pH at which the net charge on a surface is zero. However, other cations or anions together with $H^+$ and $OH^-$ can contribute to the mineral surface charge and therefore, the pH referring to the zero surface charge is represented as the point of zero charge (PZC). Table 1.2 shows the PZNPC, surface area and site densities of some minerals commonly found in sediments. The potential pools of PIP in sediments are discussed below separately.

**Table 1.2.** Surface area (SA), point of zero net proton charge (PZNPC) and site densities of some common minerals. All the data were taken from Langmuir (1997a) except when mentioned with a superscript which were taken from Kosmulski (2006).

| Minerals | PZNPC | SA ($m^2/g$) | Site density (sites/$nm^2$) |
|---|---|---|---|
| Goethite | 4.2 to 6.9, 7.7 to 9.3[a] | 45 to 169 | 2.6 to 18 |
| Hematite | 5.9 to 6.7, 5.5 to 10[a] | 47 | 5 to 22 |
| Ferrihydrite | 8.5 to 8.8 | 250 to 600 | 20 |
| Gibbsite | 10, 6.4 to 9.5[a] | 120 | 2 to 12 |
| $Al(OH)_3$ (amorphous) | 7 to 11.5[a] | 175 | - |
| $MnO_x$ (general) | 1.5 to 7.3 | 180-290 | 18 |
| Kaolinite | 2 to 4.6 | 10 to 38 | 1.3 to 3.4 |
| Illite | | 65 to 100 | 0.4 to 5.6 |
| Silica (amorphous) | 1 to 3, 2.1 to 3.34[a] | 53 to 292 | 4.5 to 12 |
| Quartz | | 0.14 | 4.2 to 11.4 |
| Calcite | 8.5, 8.10 | 0.22[b] | 0.6 to 4 |

**Ferric oxides and hydroxides:** Ferric iron (hydr)oxides have long been implicated as a controlling factor in the mobilization of phosphate in many aquatic sediments (Kosmulski, 2006). The role of ferric (hydr)oxides in phosphate mobilization at the sediment-water interface is important for several reasons: (i) these minerals have high natural abundances and very high surface areas (Jambor and Dutrizac, 1998; Liu et al., 2014), (ii) they are redox sensitive (Christophoridis and Fytianos, 2006; Melton et al., 2014; Søndergaard et al., 2003; Weber et al., 2006), (iii) the surface charge of ferric (hydr)oxides is most responsive at near neutral pH, (iv) phosphate adsorption on these minerals is highly pH dependent (Geelhoed et al., 1997; Mayer and Jarrell, 2000; Nowack and Stone, 1999), and (v) ferric (hydr)oxides can transport P in colloidal form (Baken et al., 2016a, 2016b; Hartland et al., 2015).

**Aluminum oxides/hydroxides:** Aluminum (Al) is the most abundant element in the earth's crust (~8%, by weight) after silicon and oxygen. Al-(hydr)oxides in sediments are generally stable under dynamic redox conditions across the range of pH (pH 5 to 9) found most commonly in natural waters. The adsorption of phosphate on Al-(hydr)oxides generally takes place with the exchange of surface –OH or -$OH_2^+$ group (Gächter and Müller, 2003; Gérard, 2016). The phosphate adsorption capacities of Al-(hydr)oxides are often comparable to those of Fe-(hydr)oxides because of their similarities in PZC and surface areas (Borggaard et al., 2005; Danen-louwerse et al., 1993; Gérard, 2016).

**Carbonate minerals:** In carbonate minerals, e.g., calcite, the surface sites are assumed to derive from >Ca-OH and >$CO_3$H (Van Cappellen et al., 1993). The adsorption site densities on the surface of carbonate minerals are comparable to ferric (hydr)oxides (Antelo et al., 2010, 2005; Atouei et al., 2016; Geelhoed et al., 1997; Van Cappellen et al., 1993), although the specific surface areas of pure carbonate minerals are typically much lower, 0.6 to 4 $m^2$/ g (Pokrovsky et al., 1998; Wang and Tzou, 1995), compared to metal (hydr)oxides (Table 1.2). Therefore, the maximum phosphate adsorption capacity of carbonate minerals is significantly lower, about a hundred to a thousand times smaller than pure ferric (hydr)oxides (Hamad et al., 1992; Van Cappellen et al., 1993).

**Calcium phosphates:** In sediments, Ca-phosphate phases commonly occur as carbonate fluorapatite (CFA) impurities within $CaCO_3$ rather than as individual minerals (Orihel et al., 2017). In carbonate minerals, the conversion of adsorbed phosphate or its direct precipitation with $Ca^{2+}$ promotes the formation of various Ca-phosphate phases (Oxmann and Schwendenmann, 2015). For example, adsorbed phosphate on calcite results in the initial formation of dicalcium-phosphate (DCP) which slowly converts to octacalcium-phosphate (OCP) (Freeman and Rowell, 1981). The adsorbed or precipitated phosphate on/in carbonate minerals may partially diffuse into the interior structure (Avnimelech, 1983). The formation and dissolution of individual Ca-phosphate phases, or P in association with calcium carbonate minerals are sensitive to pH (Orihel et al., 2017). Alkaline pH generally favors the formation of Ca-phosphate phases whereas acidic conditions (below ~4) promote their dissolution (Oxmann and Schwendenmann, 2015; Van Cappellen et al., 1993). Generally Ca-phosphate

phases with lower solid phase Ca:P ratios are more water soluble than those with higher Ca:P ratios (Dorozhkin, 2016). For example, the solubility constant ($logK_{sp}$) of DCP with a Ca:P ratio of 1.0 is much higher than that of OCP with a Ca:P ratio of 1.3, with $logK_{sp}$ values of -6.5 and -96.6 at 25 °C, respectively (Dorozhkin, 2016). The burial of apatite phases, which progressively achieve a more stable structure over time, represents the endpoint of early diagenesis for phosphate and calcium in a similar manner to phosphate and Fe in vivianite.

**Clay minerals:** Clay minerals are also important as a potential pool of phosphate (Gérard, 2016; Norton and Amirbahman, 2005). The phosphate adsorption capacities of clay minerals have been found to vary largely depending on the mineral type (Gérard, 2016). The presence of Fe and Al in clay minerals can significantly increase phosphate adsorption, even higher than typical Fe/Al-(hydr)oxides (Gérard, 2016). Clay minerals, in general, have relatively lower PZC compared to other minerals, e.g., metal (hydr)oxides in soil/sediment (Table 1.2). The maximum phosphate adsorption on clay minerals generally takes place between pH 4 to 7 which is overall controlled by the binding sites provided by Fe and Al (Gérard, 2016), mostly along the clay edges (Pissarides et al., 1968). Yet, the phosphate binding capacity of clay minerals may be decreased significantly under neutral to slightly alkaline conditions (Gérard, 2016).

## 1.5.2 Geochemistry of phosphorus in aquatic sediments

The cycling of P in sediments and the diffusion of P from sediment to the overlying water largely depends on the depth of oxygen penetration into the sediment. The downward diffusion of oxygen from oxic bottom water in combination with photosynthetic activities by autotrophic benthic diatoms and other algae primarily control DO levels at the sediment-water interface (SWI) (Santschi et al., 1990). Oxygen influx into the sediment generally takes place by simple molecular diffusion or by physical activities such as tidal/wave action or bioturbation (Precht et al., 2004; Santschi et al., 1990). Sediment texture and grain size are also important in determining sediment hydraulic properties and hence, the depth of DO penetration (Silburn et al., 2017). The aerobic respiration of labile organic matter further controls DO penetration in sediment (Silburn et al., 2017), although the DO in sediment is also consumed in the oxidation of reduced species, e.g., $NH_3$, $Mn^{2+}$, $Fe^{2+}$, $H_2S$, and $CH_4$, via biotic and abiotic processes

(Santschi et al., 1990). Therefore, the depth of oxygen penetration in sediments is usually limited to a few millimeters, or even less in mesotrophic and eutrophic conditions (Holmer and Storkholm, 2001; Silburn et al., 2017). In sediments, redox potential also decreases along the downward oxic to anoxic gradient. The pore-water pH, on the other hand, changes with complex oscillation pattern in different biogeochemical redox zones (Figure 1.4).
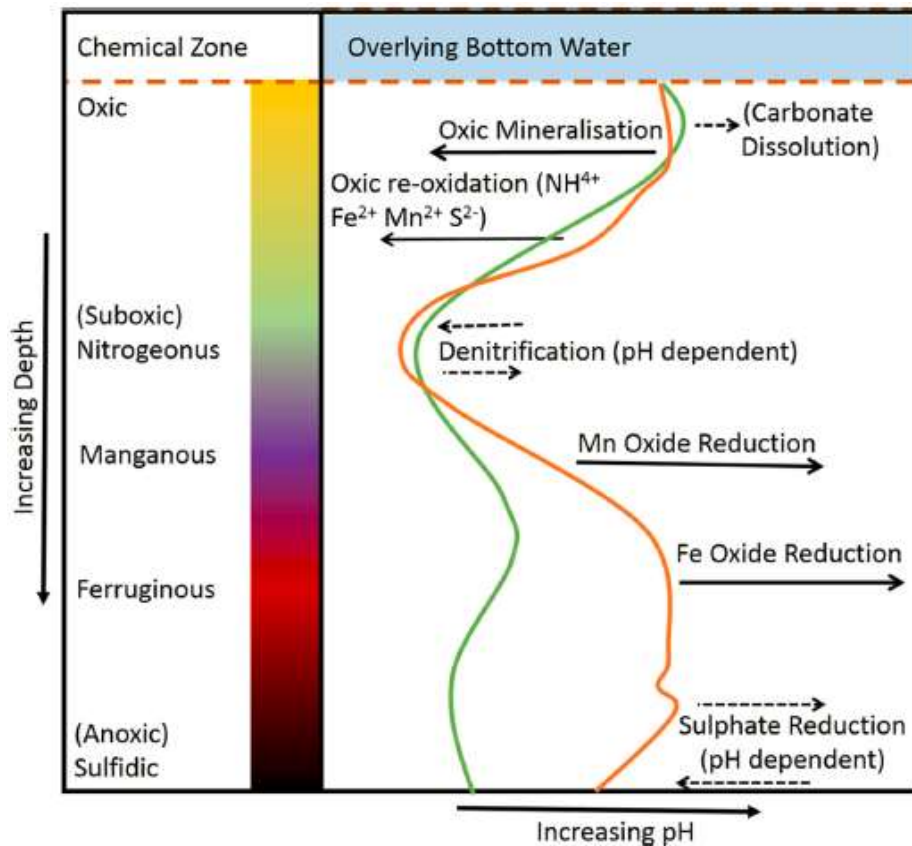


**Figure 1.4.** The change of pH and associated biogeochemical processes along the sediment. The green and orange lines represent pH depth profiles measured from two locations of the Central North Sea. The arrows show the influence of major biogeochemical processes on pore-water pH. Reproduced from Silburn et al. (2017).

In sediments, oxidative degradation of organic matter generates carbon dioxide ($CO_2$) which may form bicarbonate or carbonate depending on the pH. The generated soluble $CO_2$ can produce acidity if not buffered by sediment pore-water. In addition, the oxidation of some reduced species, e.g., $Mn^{2+}$ and $Fe^{2+}$, during their upward diffusion from the deeper sediment, lowers pH near the oxygen penetration depth (Silburn et al., 2017). The degradation of organic matter in sediment is also enhanced with the increased activity of phenoloxidase enzymes or

by Fenton's reaction in the presence of $Fe^{2+}$ ions (Hall and Silver, 2013; Van Bodegom et al., 2005). The re-oxidation of $Mn^{2+}$ and $Fe^{2+}$ near the oxic-anoxic boundary (i) by molecular oxygen, or (ii) by $NO_3^-$ or chlorate ($ClO_4^-$) catalyzed by microorganisms can result in the further formation of Fe/Mn-(hydr)oxides (Weber et al., 2006). The formation of Fe/Mn-(hydr)oxides in sediment result in immobilization of phosphate through adsorption and co-precipitation.

In going deeper in the sediment profile, the release of phosphate can take place by concurrent mineral dissolution of and desorption from metal (hydr)oxides (Christophoridis and Fytianos, 2006; Gächter and Müller, 2003; Orihel et al., 2017; Søndergaard et al., 2003). Nitrate ($NO_3^-$) when present at high concentrations, can delay, or prevent the reductive dissolution of Fe/Mn-(hydr)oxides in sediment because $NO_3^-$ is reduced before $Fe^{3+}$ and $Mn^{4+}$ (Orihel et al., 2017; Parsons et al., 2017; Smolders et al., 2006). The reductively dissolved phosphate from Fe/Mn-(hydr)oxides can be redistributed onto the Al-(hydr)oxides and carbonate minerals or as precipitates of reduced iron, e.g., vivianite ($Fe_3(PO_4)_2 \cdot 8H_2O$) (Connell et al., 2015; Gächter and Müller, 2003; Orihel et al., 2017; Rothe et al., 2014). Authigenic precipitation of phosphate as reddingite ($Mn_3(PO_4)_2 \cdot 3H_2O$) is also thermodynamically possible under anoxic conditions, with slightly lower solubility than vivianite (Connell et al., 2015). However, reddingite has received less attention most likely due to lower natural abundance of Mn relative to Fe, and insufficient evidence necessary for its phase identification in freshwater sediments (Orihel et al., 2017).

In sulfidic sediment, $H_2S$ produced from $SO_4^{2-}$ reduction precipitates with $Fe^{2+}$ as FeS that may convert to $FeS_2$ during further diagenesis. This is the terminal sink of Fe in sulfidic sediment making dissolved phosphate more available (Gächter and Müller, 2003; Orihel et al., 2017). MnS, however, is not commonly the terminal sink for $Mn^{2+}$ as the adsorption of $Mn^{2+}$ on the surface of FeS is more favorable than the precipitation of MnS (Arakaki and Morse, 1993). Increased concentrations of $H_2S$ can also enhance vivianite dissolution, forming FeS and releasing phosphate to the pore-water (Gächter and Müller, 2003). Therefore, permanent burial of phosphate can be decreased or prevented in sulfidic sediment and depends on the relative concentrations of $Fe^{2+}$, $S^{2-}$ and phosphate.

In addition, aqueous $Fe^{2+}$ and $Mn^{2+}$, produced by reductive dissolution, can be immobilized as siderite ($FeCO_3$) (Gächter and Müller, 2003) and rhodochrosite ($MnCO_3$)

(Parkhurst and Appelo, 2013), respectively, with comparable formation and solubility constants (Böttcher, 1998). The solubility of siderite is higher than that of vivianite with $logK$ values -10.9 and -36.0, respectively (Gächter and Müller, 2003; Parkhurst and Appelo, 2013). Therefore, the preferential dissolution of $FeCO_3$ supplies $Fe^{2+}$ for FeS formation buffering phosphate release from vivianite dissolution (Gächter and Müller, 2003). The permanent burial of phosphate in anoxic sediment is generally associated with vivianite and Ca-phosphate phases (Nriagu and Dell, 1974).

The role of aqueous silicate in the stability of phosphate minerals in anoxic sediment is not well documented. Under anoxic conditions, with high concentrations of silicate, the formation of $Fe_2SiO_4$ is theoretically possible but may be unimportant in the environment because its formation would require extremely low sulphide, and $HCO_3^-$ or $CO_3^{2-}$ concentrations (Curtis and Spears, 1968). The presence of aqueous silicate during the precipitation of $Fe(OH)_3(s)$ can result in the formation of silica-ferrihydrite type materials (Cismasu et al., 2014; Dyer et al., 2010; Karim, 1984; O'Melia and Stumm, 1967; Senn et al., 2015). Laboratory experiments have shown that increased silicate concentrations inhibit the re-solubilization and recrystallization of initially formed phases such as Ca-Fe-P during the oxidative precipitation of $Fe^{2+}$ in the presence of phosphate and $Ca^{2+}$ ions (Senn et al., 2015). The authors using data obtained from X-ray absorption spectroscopy and transmission electron microscopy, proposed that the surface of Ca-Fe-P precipitates is stabilized by a thin layer of silica-ferrihydrite. The influence of aqueous silicate on a) the removal of phosphate from solution by co-precipitation with metal (hydr)oxides, and b) phosphate release by mineral dissolution is still not well understood. These effects are discussed in more detail in sections 1.5.3.2 and 1.5.3.3.

## 1.5.3 Re-mobilization of phosphate from sediment

The remobilization of phosphate from sediments generally can take place by (i) degradation and mineralization of organic-P compounds, (ii) the desorption of sorbed phosphate from mineral surfaces, and (iii) the dissolution of phosphate containing Fe/Mn-(hydr)oxides. The phosphate released into the aqueous phase within sediment can enter into the overlying surface water by upward diffusion plus bio-irrigation. The efflux of aqueous phosphate from bottom sediments is known as internal phosphate loading (Orihel et al., 2017). Internal phosphate

loadings are often comparable to external loads in aquatic environments with a history of high P inputs from point and non-point sources (Matisoff et al., 2017, 2016; Nürnberg and Lazerte, 2016; Orihel et al., 2017; Paytan et al., 2017). The internal phosphate loads when combined with external loads may trigger algal blooms in surface waters (Matisoff et al., 2016; Parsons et al., 2017). The sections below discuss the mechanism for the release of phosphate at the sediment-water interface.

### 1.5.3.1 Phosphate release from particulate organic compounds

In addition to phosphate mobilization from mineral sources, degradation and mineralization of POP compounds release phosphate from many lake sediments (Giles et al., 2015; Joshi et al., 2015; Shinohara et al., 2017). Particulate organic-P (POP) or its degradation product (e.g., DOP) mineralize to dissolved phosphate by enzymatic hydrolysis or photolysis (Baldwin, 2013; Liu et al., 2017; Orihel et al., 2017; Wang et al., 2016). Extracellular alkaline phosphatase or phytase enzymes are usually responsible for enzymatic hydrolysis reactions (Baldwin, 2013; Orihel et al., 2017; Ruttenberg and Dyhrman, 2012; Wang et al., 2016). The phosphatase enzyme can hydrolyze nucleic acids, e.g., DNA, RNA, and nucleotides, e.g., ATP. The phytase enzyme is more sensitive to inositol phosphates but it can hydrolyze other organic-P compounds (Baldwin, 2013). The enzymatic hydrolysis of organic-P compounds may occur directly (Baldwin, 2013; Orihel et al., 2017; Ruttenberg and Dyhrman, 2012), or can be surface catalyzed (Baldwin, 2013; Orihel et al., 2017). Similar to enzymatic hydrolysis, photolytic mineralization of organic compounds may occur with or without mineral surface catalysis (Baldwin, 2013). Furthermore, organic-P can also be mineralized during the heterotrophic respiration in some organisms. The oxidation of P containing reduced organic compounds during the reduction of Fe/Mn-(hydr)oxides may also result in the release of phosphate to water.

### 1.5.3.2 Desorption of phosphate
### 1.5.3.2.1 Mechanism

The adsorption of phosphate on a metal (hydr)oxide is controlled by multiple mechanisms: electrostatic attraction and repulsion, ligand exchange and Lewis acid-base reaction (Li et al., 2016). At pH values below the PZC of an adsorbent, e.g., ferric (hydr)oxides, strong

electrostatic attraction between deprotonated phosphate ($H_2PO_4^-$/$HPO_4^{2-}$) and the positively charged surface results in phosphate adsorption via the exchange of surface hydroxyl groups (e.g., –OH or –$OH_2^+$) with the aqueous phosphate (e.g., ligand exchange process) (Figure 1.5). However, at pH values above the PZC, the increasingly negative surface charge results in unfavorable conditions for the adsorption of deprotonated and negatively charged phosphate, e.g., $HPO_4^{2-}$ or $PO_4^{3-}$. Phosphate adsorption under these latter conditions generally occurs with the formation of a covalent bond directly to the metal ion (i.e., via the Lewis acid-base reaction), leading to the formation of a mono-dentate surface complex, particularly on ferric (hydr)oxides. This mono-dentate surface complex may also convert to a bi-dentate complex with the exchange of a surface hydroxyl group (i.e., ligand exchange process) (Li et al., 2016). The activity of other anions (sulphate, bicarbonate, silicate, hydroxyl ions) in the aqueous phase may decrease the phosphate adsorption, but this effect is highly pH dependent.
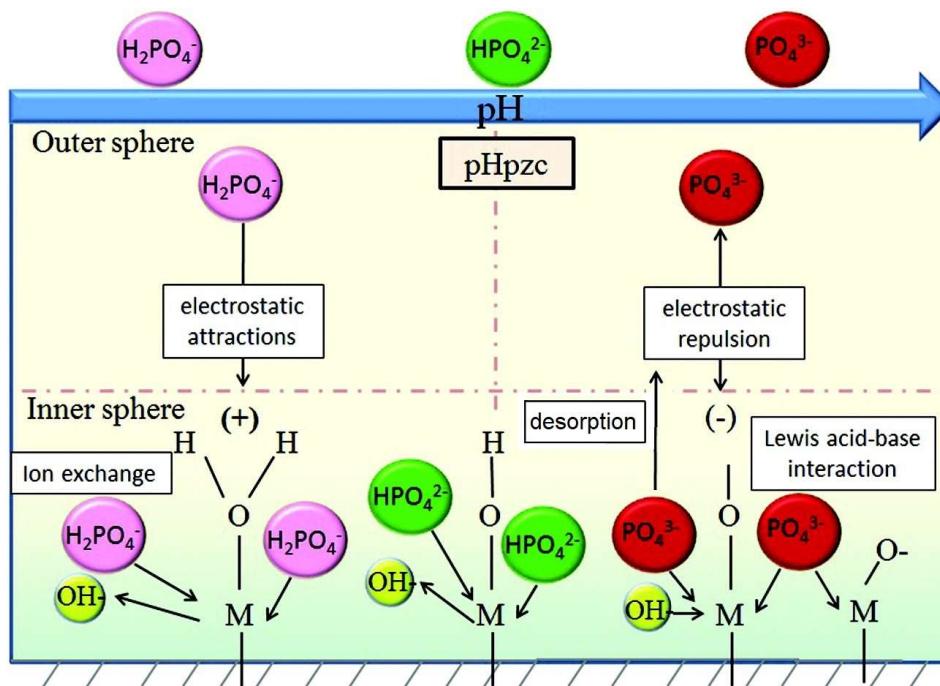


**Figure 1.5.** Schematic illustration showing the effects of pH on the adsorption and desorption mechanisms of phosphate (e.g., $H_2PO_4^-$/$H_2PO_4^{2-}$/$PO_4^{3-}$) on/from ferric (hydr)oxides. Reproduced from Li et al. (2016) with slight modification to highlight the role of $OH^-$ ions in phosphate desorption.

Similar to phosphate adsorption, desorption of phosphate from a mineral surface also depends on phosphate aqueous speciation, the mineral's PZC and the activity of anions

competing for surface adsorption sites. Generally, desorption of phosphate from metal (hydr)oxides is favored at pH values higher than the PZC of the adsorbents. Under alkaline conditions, the hydroxyl ions ($OH^-$) are likely to induce phosphate desorption by displacing the adsorbed phosphate from the metal (hydr)oxide surface (Figure 1.5).

The PZC is an intrinsic property of a solid and is different from one mineral to another, even between the different ferric (hydr)oxides (Table 1.2). Within the most common pH range in sediment (5-9), phosphate released from one mineral may persist in the aqueous phase or be attached onto other surfaces (Oxmann and Schwendenmann, 2015; Parsons et al., 2017). The presence and activity of some cationic and anionic species also influence the degree of phosphate adsorption/desorption. For example, $Ca^{2+}$, $Mg^{2+}$, and $Fe^{2+}$ can increase the phosphate binding with ferric (hydr)oxides minerals by co-adsorption (Atouei et al., 2016; Hinkle et al., 2015; Ler and Stanforth, 2003; Rietra et al., 2001). Common anionic species, such as arsenate, bicarbonate, sulfate, and silicate on the other hand can compete with phosphate for surface binding sites and therefore enhance P release.

To better understand the competitive interactions between phosphate and other anions for the surface binding sites on minerals, the adsorption pH envelopes for the individual anions provide useful information. The approximate shapes for adsorption envelopes for phosphate, bicarbonate, sulfate, and silicate on ferric (hydr)oxides are shown in Figure 1.6. The possible roles and the importance of some naturally occurring anions as a competitor to phosphate for their adsorption onto the surface of ferric (hydr)oxides are discussed below.
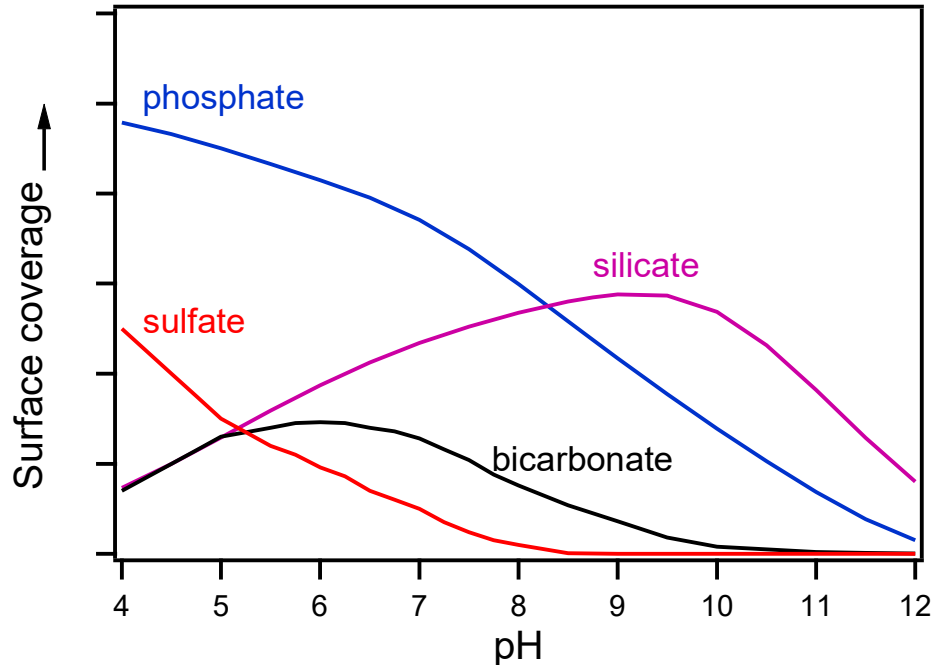
**Figure 1.6.** The adsorption pH envelope shapes (approximate) for phosphate, bicarbonate, sulfate and silicate on ferric (hydr)oxides. The adsorption pH envelope shape for phosphate and sulfate were re-drawn from Geelhoed et al. (1997), and that for bicarbonate and silicate were redrawn from Rahnemaie et al. (2007a) and Hiemstra et al. (2007), respectively.

### 1.5.3.2.2 Roles of naturally occurring anions

Although this thesis deals primarily with reactions occurring between mineral surfaces and pore-water within surficial sediments, a large database of pore-water chemistry within surficial sediments is not available. In lieu of shallow pore-water chemistry data, concentrations of phosphate and other major anions, plus pH were extracted from the National Water Information System (NWIS) database (NWIS, 2017) for surface water i.e., streams, rivers, and standing water bodies including lakes, impoundments, and reservoirs.

The data were extracted for the years between 2010 and 2016 and cover the mainland continental USA, as well as Hawaii and Puerto Rico. These data sets include only analyses on filtered samples, except pH data available for unfiltered water samples. The extracted data were sorted using the Ablebits tool in Microsoft Excel. Figure 1.7 shows the concentrations of major anions in the overlying water of standing water bodies (lakes, impoundments and reservoirs) hence providing an indication of the relative importance of each anion as an adsorptive competitor to phosphate at the sediment water interface.

**Table 1.3.** Average pH and average concentration of dissolved anions in various aquatic environments; groundwater, streams, and standing water bodies, e.g., lakes, impoundments and reservoirs, according to the NWIS database (2010-2016). Except pH, anion concentrations were obtained on filtered samples. The numbers in the 2$^{nd}$ column represent the USGS parameter code used to extract the data. The number in brackets represents the number of data points (N) and the "±" sign denotes standard deviation between the values.

| Parameter | USGS Parameter code | Groundwater mM (N) | Stream mM (N) | Standing water mM (N) |
|---|---|---|---|---|
| pH | 00400, 00403 | 7.3±0.7 (2011) | 7.8±0.6 (11881) | 8.0±0.6 (1530) |
| Phosphate | 00660 | $3.11\times10^{-3}\pm8.85\times10^{-3}$ (2011) | $3.12\times10^{-3}\pm8.85\times10^{-3}$ (11881) | $3.16\times10^{-3}\pm8.5\times10^{-3}$ (1527) |
| Arsenic (total) | 01000 | $9.24\times10^{-5}\pm6.59\times10^{-4}$ (2577) | $5.05\times10^{-5}\pm4.73\times10^{-4}$ (16799) | $9.79\times10^{-4}\pm4.63\times10^{-3}$ (749) |
| Bicarbonate | 00453 | 5.04±7.51 (1700) | 2.69±2.31 (14119) | 2.65±6.52 (1736) |
| Nitrate | 71851 | 0.32±1.15 (12080) | $1.01\times10^{-1}\pm1.83\times10^{-1}$ (40614) | $2.22\times10^{-2}\pm4.43\times10^{-2}$ (3216) |
| Sulfate | 00945 | 1.98±11.27 (5020) | 1.56±4.12 (41001) | 2.15±12.10 (3726) |
| Silicate | 00955 | $3.96\times10^{-1}\pm2.23\times10^{-1}$ (2011) | $1.85\times10^{-1}\pm1.26\times10^{-1}$ (11881) | $1.46\times10^{-1}\pm1.17\times10^{-1}$ (1527) |
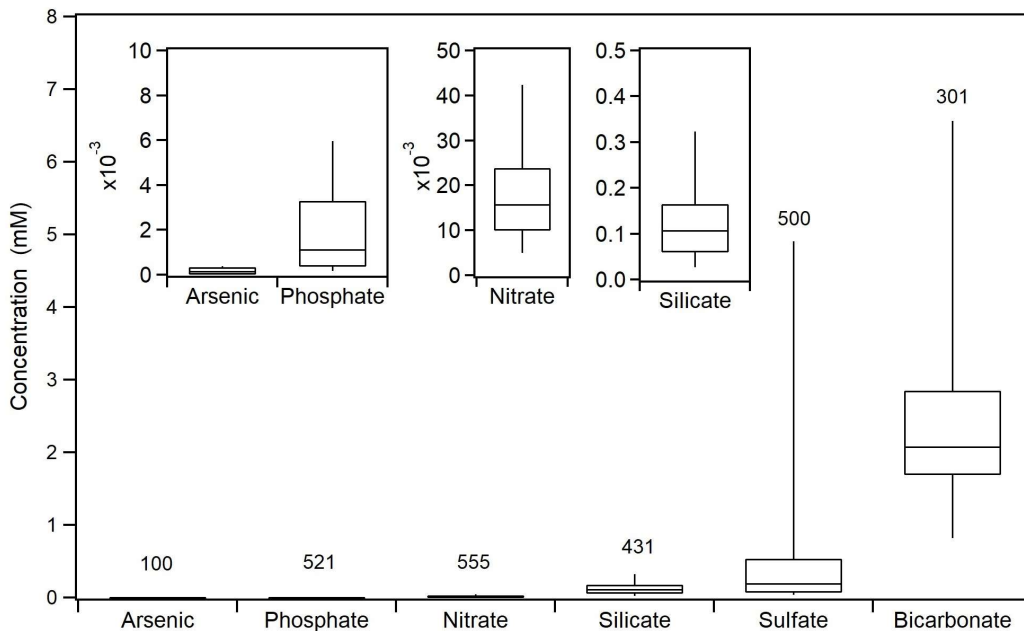


**Figure 1.7.** Concentrations of various dissolved anions in standing water bodies, e.g., lakes and impoundments, and reservoirs according to the NWIS (2015). The number on each box represents the number of data points, which are extracted from all water depths available in the database. The lower and upper boundary of each box represents 25$^{th}$ and 75$^{th}$ percentile, respectively, and the line within the box shows median value. The whiskers are drawn down to the 10$^{th}$ percentile and up to the 90$^{th}$.

**Arsenic:** Among the anionic species, arsenic in the form of arsenate ($H_2AsO_4^-$/$HAsO_4^{2-}$) is structurally similar to phosphate ($H_2PO_4^-$/$HPO_4^{2-}$) and has very similar proton dissociation constants (Gao and Mucci, 2003). There are some laboratory studies where arsenate is shown to desorb phosphate sorbed to ferric (hydr)oxides (Hongshao and Stanforth, 2001; Neupane et al., 2014; Puccia et al., 2009). The reported binding strength of arsenate with ferric (hydr)oxides is comparable to that of phosphate, but this value is slightly higher for arsenate (Neupane et al., 2014). Yet, the concentration of arsenic in majority of surface waters is much lower than phosphate (Table 1.3 and Figure 1.7). Therefore, although arsenate can act as a strong competitive ion to phosphate, except unexceptional cases, it's role may be of minor importance in phosphate mobility due to its relatively low concentrations compared to phosphate.

**Bicarbonate:** In natural waters, bicarbonate ($HCO_3^-$) is the dominant form of inorganic carbon in the natural pH range (pH 5 to 9) (Orihel et al., 2017). In water, $HCO_3^-$ is generally produced due to solubilization of $CO_2$ or dissolution of carbonate minerals such as calcite, aragonite or dolomite (Langmuir, 1997b). The concentration of $HCO_3^-$ in standing water bodies is influenced by the riverine and groundwater inputs. In addition, photosynthesis and respiration control the concentration of $HCO_3^-$ in open water bodies (Verspagen et al., 2014). For example, dissolved $CO_2$ and $HCO_3^-$ are consumed by primary producers during photosynthesis, causing the decrease of $HCO_3^-$ in the photic zone. The dissolved $CO_2$ and $HCO_3^-$ are also generated as the by-products of respiration of organic matter (Verspagen et al., 2014).

Bicarbonate has been reported to form inner-sphere complexes on ferric (hydr)oxides with no, or minor contribution from outer-sphere complexes (Rahnemaie et al., 2007a). The adsorption of $HCO_3^-$ on goethite increases with increasing pH from an acidic to near neutral pH, while further increases of pH cause a decrease in $HCO_3^-$ adsorption (Figure 1.6) (Hiemstra et al., 2007). Though $HCO_3^-$ forms much weaker surface complexes with goethite compared to phosphate, it is typically present in natural waters at higher concentrations than phosphate (Figure 1.7). Furthermore, the concentrations of phosphate and bicarbonate in natural waters generally change in the same direction (Smolders et al., 2006). The latter authors propose that $HCO_3^-$ can increase phosphate concentration in water due to their direct competition for the

mineral binding sites. Alternatively, $HCO_3^-$ can indirectly influence phosphate release by neutralizing acids, which generally inhibit the decay of organic matter and hence, the organic P compounds. In another study, $HCO_3^-$ has been shown to decrease phosphate adsorption on goethite and akaganeite but the effect is limited to acidic conditions (Chitrakar et al., 2006). The NWIS (2010-2016) data also show that higher concentrations of $HCO_3^-$ are generally associated with alkaline pH (Figure 1.8) where the affinity of $HCO_3^-$ to ferric (hydr)oxides is minor (Chitrakar et al., 2006; Hiemstra et al., 2007). Therefore, $HCO_3^-$ is unlikely to exert a large influence on adsorption or desorption of phosphate in most aquatic environments.
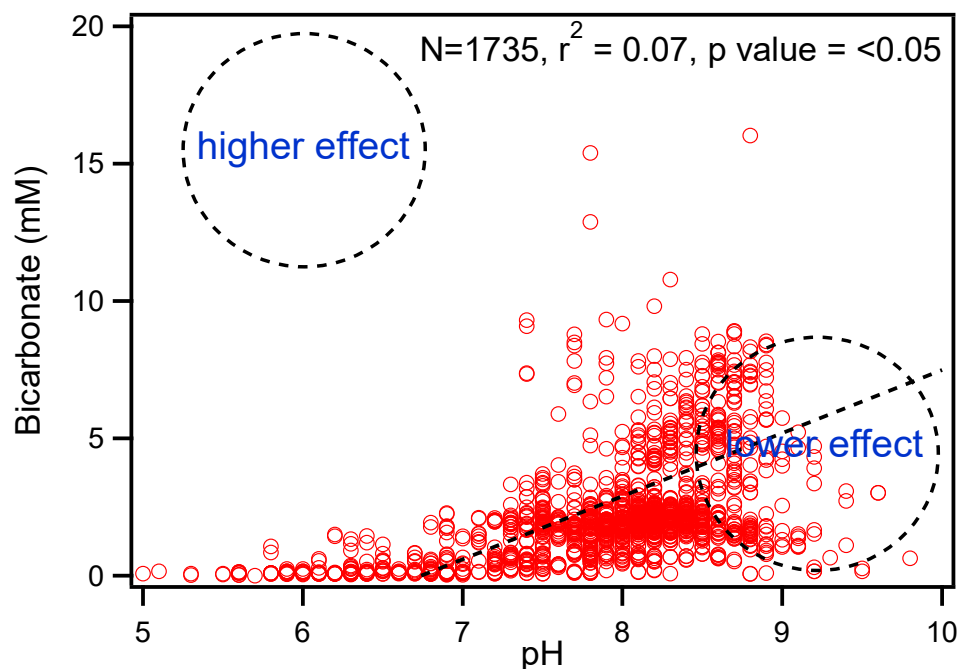


**Figure 1.8.** The relation between bicarbonate concentration and pH in open water bodies, lakes, impoundments and reservoirs, according to the NWIS data (2010-2016, N=1735). The concentrations of bicarbonate and pH were extracted for common sampling stations and dates of sampling from all water depths available in the database. The dashed line represents the linear regression fit between the concentrations of bicarbonate and pH. The dotted circles on the figure show the possible effect of $HCO_3^-$ on the mobility of phosphate from their interactions with ferric (hydr)oxides, according to the bicarbonate adsorption isotherm on ferric (hydr)oxides shown in Figure 1.6.

**Nitrate:** The concentrations of nitrate ($NO_3^-$) in open water bodies are generally not as high as other anions, e.g., $HCO_3^-$, $SO_4^{2-}$ or silicate (Figure 1.7). In addition, $NO_3^-$ as a monovalent anion has a much weaker affinity for ferric (hydr)oxide surfaces compared to phosphate. The

reported affinity constant for $NO_3^-$ for the ferric (hydr)oxides is also weaker than for other anions such as $HCO_3^-$ and $SO_4^{2-}$ (Rahnemaie et al., 2007a). According to the NWIS (2010-2016) data, higher concentrations of phosphate are generally associated with lower concentrations of $NO_3^-$ in standing water bodies, with no significant correlation ($r^2$= <<0.01 and p value = 0.97) (Figure 1.9). Furthermore, the average concentrations of $SO_4^{2-}$ and $HCO_3^-$ in surface waters of lakes are generally much higher than that of $NO_3^-$ (Figure 1.7, Table 1.3). Therefore, $NO_3^-$ likely has a negligible effect on the adsorption or desorption phosphate on/from metal (hydr)oxides in the majority of lakes.
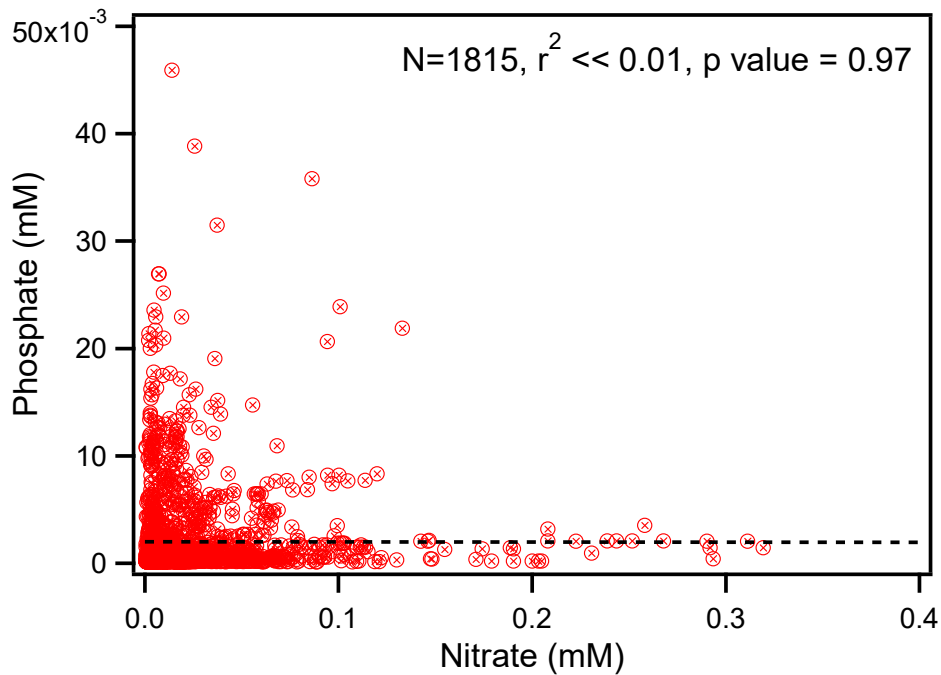


**Figure 1.9.** The relation between the concentration of phosphate and nitrate in standing water bodies, e.g., lakes, impoundments and reservoirs, according to the NWIS database (2010-2016, N=1815). The concentrations of phosphate and nitrate were extracted for common sampling stations and dates of sampling from all water depths available in the database. The dashed line represents the linear regression fit between the concentrations of phosphate and nitrate.

In sediments, $NO_3^-$ is generally reduced before $Mn^{4+}$ or $Fe^{3+}$ reduction starts (Orihel et al., 2017; Parsons et al., 2017; Smolders et al., 2006). Therefore, the role that nitrate plays as an electron acceptor, preventing or delaying the reductive dissolution of iron, is of greater importance compared to its role as a competitive ion for adsorption sites when considering phosphate mobilization from sediment. However, high $NO_3^-$ availability in sediment may also

increase phosphate release by enhancing the mineralization of organic-P (Schauser et al., 2006).

**Sulfate:** The average concentration of $SO_4^{2-}$ (2.15±12.10 mM, N=3726) in standing waters is orders of magnitude higher than phosphate ($3.16×10^{-3}±8.50×10^{-3}$ mM, N=1527) according to NWIS data (2010-2016). Furthermore, the concentrations of phosphate and sulfate in standing waters are positively correlated, although this relationship is not strong ($r^2 = 0.01$ and p value = <0.05) (Figure 1.10). Sulfate is known to form both outer- and inner-sphere complexes with ferric (hydr)oxides, where inner sphere complexes are favored at acidic pH (Peak et al., 1999). The affinity constants for the adsorption of $SO_4^{2-}$ on goethite are lower than those of phosphate. Although $SO_4^{2-}$ has low affinity for ferric (hydr)oxides, it can decrease phosphate adsorption or increase desorption at higher concentrations and under acidic conditions, similar to $HCO_3^-$. At alkaline pH, the influence of $SO_4^{2-}$ becomes minor for phosphate desorption from ferric (hydr)oxides (Geelhoed et al., 1997).
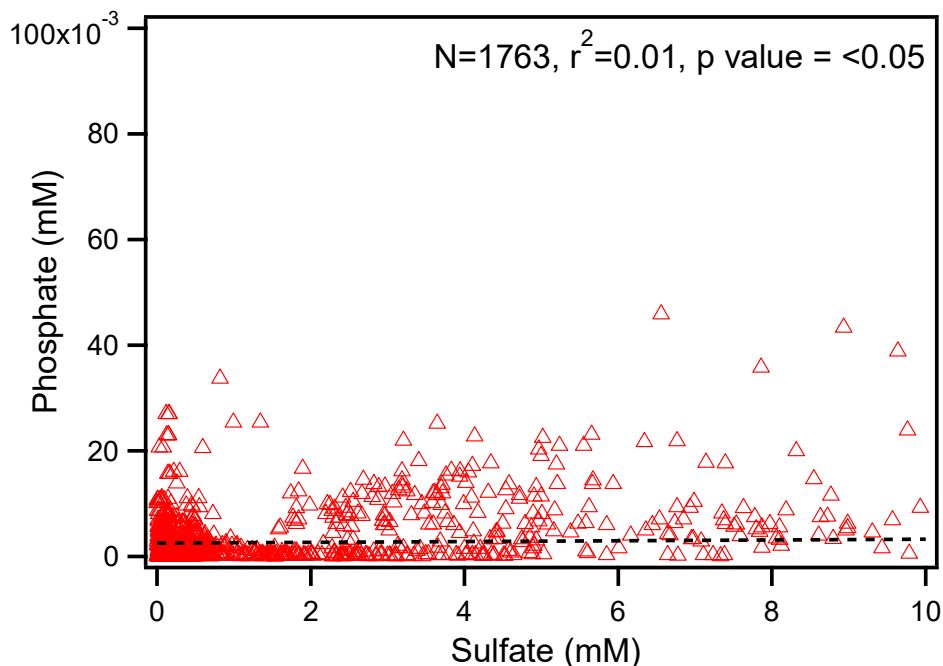


**Figure 1.10.** The relation between the concentrations of phosphate and sulfate in standing water bodies, e.g., lakes, impoundments and reservoirs, according to the NWIS database (2010-2016, N=1763). The concentrations of phosphate and sulfate were extracted for common sampling stations and dates of sampling from all water depths available in the database. The dashed line represents the linear regression fit between the concentrations of phosphate and sulfate.

**Silicate:** Dissolved silicate occurs ubiquitously in natural waters in the form of silicic acid ($H_4SiO_4$), which forms due to dissolution of diatom frustules, plant phytoliths, and detrital silicate minerals (Iler, 1979; Struyf et al., 2009). The average concentration of silicic acid (hereafter, simply silicate) in water decreases in the order: groundwater>streams/rivers>lakes, ponds and reservoirs (Table 1.3). The relatively low silicate concentration in standing water bodies compared to groundwater and river water is indicative of biological uptake by macrophytes and siliceous algae such as diatoms, and subsequent burial into sediment (Maavara et al., 2015).

According to the NWIS (2010-2016) data, the average concentration of silicate in standing water bodies is significantly higher than that of phosphate. In addition, phosphate and silicate concentrations show a positive correlation ($r^2 = 0.17$ and p value = <0.05) (Figure 1.11). Because pH in lakes is often slightly alkaline in general (Table 1.3), high concentrations of aqueous silicate may potentially affect phosphate mobilization under alkaline conditions due to their competitive interactions with mineral surfaces.
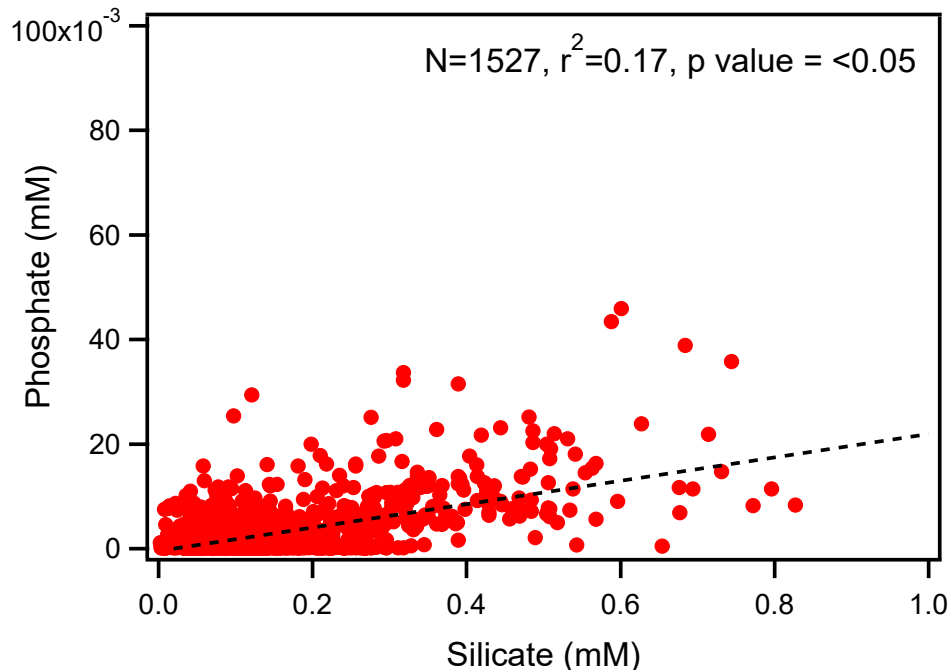


**Figure 1.11.** The relation between the concentrations of phosphate and silicate in standing water bodies, i.e., lakes, impoundments and reservoirs, according to the NWIS database (2010-2016, N=1527). The concentrations of phosphate and silicate were extracted from common sampling stations and dates of sampling from all water depths available in the database. The dashed line represents the linear regression fit between the concentrations of phosphate and silicate.

Silicate forms both monomeric and polymeric surface complexes with ferric (hydr)oxides depending on its concentration and the solution pH (Christl et al., 2012; Kanematsu and Waychunas, 2018; Swedlund et al., 2011, 2010a; Swedlund and Webster, 1999). However, the shape of the silicate adsorption pH envelope on ferric iron (hydr)oxides is different than that of phosphate (Figure 1.6). This difference in adsorption pH envelope results from the aqueous speciation of silicate and phosphate as the adsorbing surface of ferric (hydr)oxides is the same for both.

Silicate in an aqueous solution at pH below 8 remains mostly in the fully protonated form ($H_4SiO_4$) and gets deprotonated as the pH increases (Figure 1.12). Therefore, the adsorption of silicate on ferric (hydr)oxides generally increases with increasing pH, and peaks at around pH 10 depending on the PZC of the solid (Christl et al., 2012; Hiemstra et al., 2007; Jordan et al., 2007). Phosphate with multiple protonation states exists as a deprotonated anion (e.g., $H_2PO_4^-$) even under strongly acidic conditions (e.g., around pH 3). Maximum phosphate adsorption, does therefore, takes place under acidic conditions at around pH ~3 to 4 and decreases continuously with increasing negative charge on the surface, which results from increasing pH (Antelo et al., 2005; Geelhoed et al., 1997).
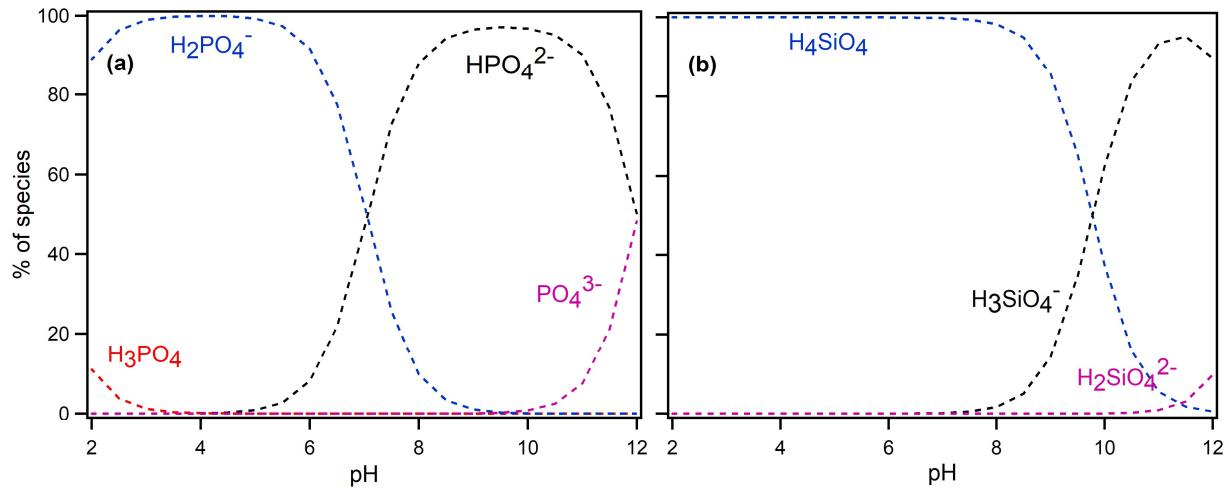


**Figure 1.12.** Speciation of (a) phosphoric acid ($H_3PO_4$) and (b) silicic acid ($H_4SiO_4$) as a function of pH. The speciation diagrams were made for 50 µM solution of phosphate and silicate at 25°C and $I$=10 mM NaCl, using PHREEQC 3 and the phreeqc.dat database (Parkhurst and Appelo, 2013).

The number of published papers on the role of soluble silicate on phosphate mobilization is limited. The majority of published studies have attempted to address the effect of silicate on the release of phosphate from natural sediment (Koski-Vähälä et al., 2001; Koszelnik and Tomaszek, 2008; Tallberg et al., 2008; Tuominen et al., 1998) as well as from soil (Schaller et al., 2019). Experiments with natural sediments and soils more closely resemble natural conditions, but they are also inherently complex. Therefore, an understanding of the molecular mechanisms through which silicate influences phosphate release is lacking.

**1.5.3.3 Dissolution of phosphate bearing minerals**

Dissolution of phosphate containing minerals can generate pore-water phosphate. Phosphate bearing minerals can dissolve according to three different mechanisms: proton promoted dissolution, ligand promoted dissolution and reductive dissolution. The release of phosphate as a result of proton promoted dissolution of carbonate and apatite minerals generally occurs under acidic conditions below pH 4 (Huang et al., 2005; Jin et al., 2006). The proton-promoted dissolution of metal (hydr)oxides, on the other hand, is favored under strongly acidic conditions (pH <3) (Cornell and Schwertmann, 2003), and this mechanism is unimportant for the majority of aquatic environments as the natural pH range is usually between 5 and 9 (Orihel et al., 2017).

Organic chelating agents and high concentrations of anionic species can also promote the dissolution of metal cations, including iron, from (hydr)oxides (Cornell and Schwertmann, 2003; Kraemer, 2004; Reichard et al., 2007) and hence, increase the release of structurally bound phosphate. Figure 1.13 shows the dissimilatory reduction of ferric (hydr)oxides and chemical oxidation of $Fe^{2+}$ in sediments. In bottom sediments, hypoxic or anoxic conditions with decreased redox potential favor microbial reduction of Fe/Mn-(hydr)oxides, where organic carbon generally acts as electron donor (Lovley, 2004). Abiotic reductive dissolution of those minerals is also possible by $H_2S$ under sulfidic condition (Mortimer et al., 2011).
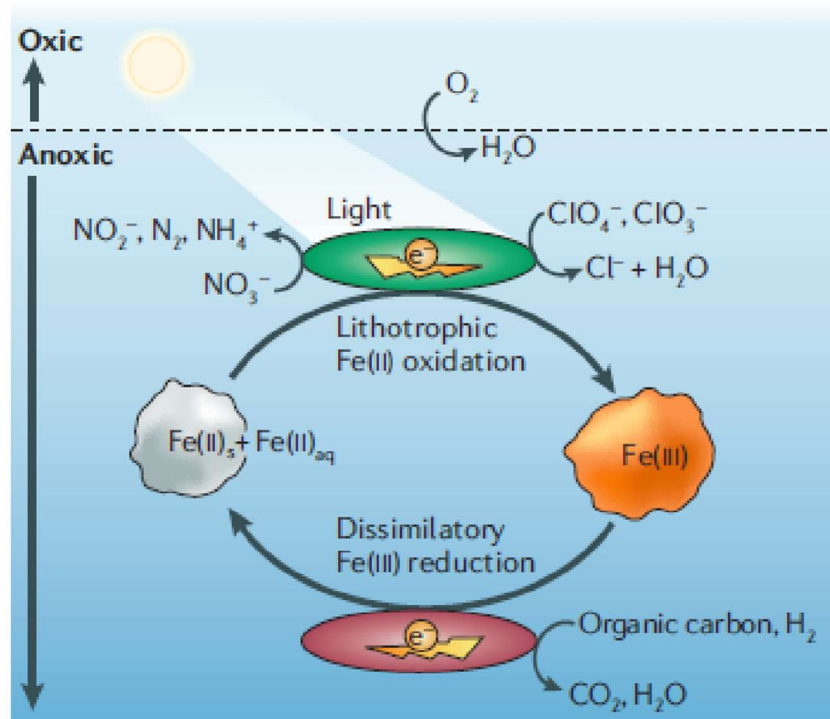
**Figure 1.13.** Biotic reductive dissolution of ferric (hydr)oxide and abiotic re-oxidation of reduced Fe(II) under anoxic conditions. Reproduced from Weber et al. (2006).

In $NO_3^-$ depleted anoxic conditions, the product of $SO_4^{2-}$ reduction, sulfide, can reduce ferric (hydr)oxides and release the associated phosphate (Gächter and Müller, 2003; Katsev et al., 2006). Sulfide ions ($S^{2-}$) preferentially form insoluble complexes with reduced $Fe^{2+}$, forming for example, mackinawite (FeS), over phosphate (also discussed in section 1.5.2). Furthermore, the microbial reduction of $SO_4^{2-}$ to $S^{2-}$ causes a pH increase which also can lead to the desorption of phosphate (Caraco et al., 1989). Therefore, both processes during $SO_4^{2-}$ reduction eventually facilitate phosphate release. However, the sorbed $SO_4^{2-}$, like other oxyanions (e.g., silicate), is known to affect the dissolution kinetics of ferric (hydr)oxides by blocking surface sites (Bondietti et al., 1993). The concentration of $SO_4^{2-}$ is typically higher than phosphate in standing water bodies according to the NWIS (2010-2016) database (Figure 1.7 and Table 1.3). Therefore, $SO_4^{2-}$ may increase phosphate mobility under reducing conditions due to the interactions of $S^{2-}$ with Fe during diagenesis (Gächter and Müller, 2003; Katsev et al., 2006) and under acidic conditions, but not as a competitive ion in alkaline environments.

The removal of phosphate during the precipitation of silica-ferrihydrite (Si-Fh) material, formed by the oxidation of $Fe^{2+}$ in the presence of silicate, has been suggested to exert a potential control on phosphate mobility (Mayer and Jarrell, 2000). Si-Fh materials exhibit a range of physical and chemical properties, with varying solid phase Si:Fe ratios (Cismasu et al., 2014; Karim, 1984). However, existing literature lacks information as to whether newly precipitated phosphate containing Si-Fh results only in temporary retention of phosphate or whether under dynamic redox conditions phosphate may be re-released at the sediment-water interface. Furthermore, due to the ubiquity of both aqueous silicate and phosphate in freshwater sediments, it is unlikely that pure iron-silicate co-precipitates exist without at least some incorporation of phosphate during oxidative precipitation.

## 1.6 Iron oxides in natural environments

### 1.6.1 Formation

Iron minerals are ubiquitous in natural environments, they are introduced to soil and sediments, primarily from the lithosphere. Iron is the fourth most abundant element in the earth's lithosphere (7 to 8% by mass), and primarily exists as $Fe^{2+}$ (ferrous iron) and $Fe^{3+}$ (ferric iron) (Kendall et al., 2012). Iron in the lithosphere is mostly present in igneous rocks, and associated with various minerals including silicate minerals (e.g., olivine, pyroxenes, amphiboles), magnetite, pyrite (e.g., $FeS_2$) and siderite (e.g., carbonates) (Kendall et al., 2012; Schwertmann and Cornell, 2000a). Weathering of these primary minerals and the subsequent hydrolysis of dissolved iron in the presence of oxygen forms various types of secondary minerals such as ferric iron oxides and hydroxides, e.g., ferrihydrite, lepidocrocite, goethite, hematite etc. Formation of other secondary ferrous iron minerals, e.g., vivianite and siderite may also occur (Schwertmann and Cornell, 2000a), and is favoured under anoxic conditions.

The type of iron minerals forming in natural environments depends on various factors such as temperature, pH, redox potential, and the presence of other dissolved constituents (Langmuir, 1997c; Schwertmann and Cornell, 2000b). For example, among the ferric iron oxides and hydroxides, formation of ferrihydrite under oxic conditions is the most kinetically favorable (Schwertmann and Cornell, 2000a). The re-crystallization of ferrihydrite leads to the gradual formation of more thermodynamically stable iron oxides, e.g., goethite and hematite.

The thermodynamic stability of dissolved iron ($Fe^{2+}$ and $Fe^{3+}$), siderite, and ferrihydrite, the initial hydrolyzed product of $Fe^{3+}$, are shown in Figure 1.14.
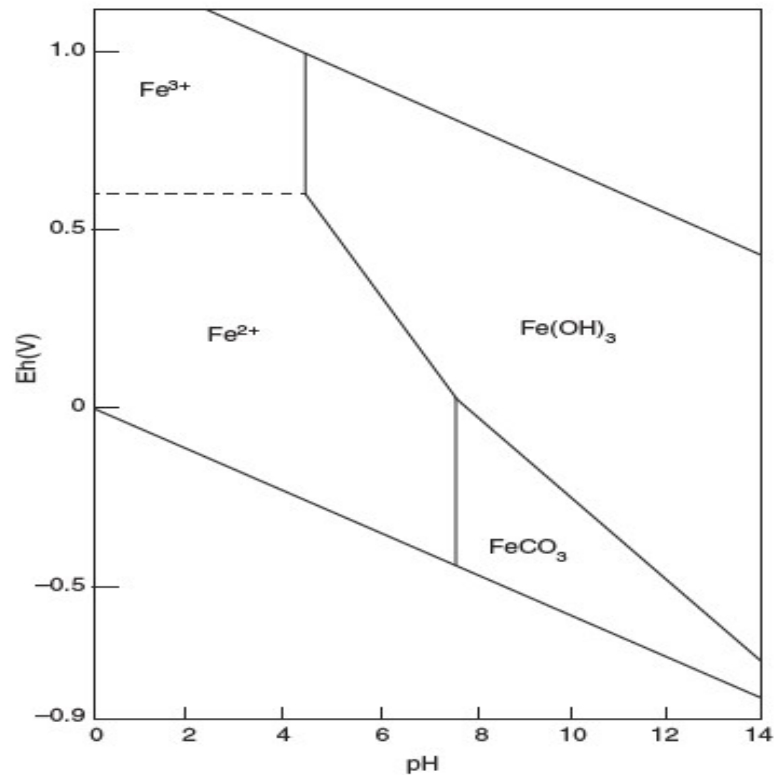


**Figure 1.14.** Eh-pH diagram for iron ($10^{-5}$ mol/kg) $Fe-O_2-H_2O-CO_2$ system at 25 °C. The upper and lower boundary represent the stability field of $H_2O$. Reproduced from (Kendall et al. 2012).

### 1.6.2 Classification

Iron oxides differ from each other depending on their crystalline structures, where iron with variable oxidation states ($Fe^{3+}$ or $Fe^{2+}$) may be surrounded by oxide (-O) and hydroxyl (-OH) ions with an octahedral arrangement (Schwertmann and Cornell, 2000a). These coordinating -O and -OH groups to iron form layers of hexagonal closed packed (hcp) or cubic closed packed (ccp) with tetrahedral interstices. These characteristic hcp or ccp arrangements of the co-ordinating groups around iron atoms are the building blocks of the crystalline structures of different iron oxides (Schwertmann and Cornell, 2000a). Among the iron oxides, ferrihydrite exhibits poorly ordered atomic arrangements whereas the goethite and hematite exhibit well defined crystalline features. In natural iron oxides, the ferric iron atom in the octahedral position may be replaced with other ions with comparable size and charge, e.g., $Al^{3+}$, $Mn^{3+}$, $Cr^{3+}$ (Schwertmann and Cornell, 2000a). Iron oxides may also contain anions including

28

phosphate and silicate on their surfaces or in their structures, and often are referred to as ferric co-precipitates (Cismasu et al., 2014; Kaegi et al., 2010; Senn et al., 2015; Voegelin et al., 2010). The formula of some common iron oxides and hydroxides are listed in Table 1.4. These oxides, hydroxides or oxyhydroxides are commonly referred as iron oxides (Schwertmann and Cornell, 2000a).

**Table 1.4.** Types of iron oxides and hydroxides. Contents reproduced from (Schwertmann and Cornell, 2000a).

| Oxyhydroxides | | Oxides | |
|---|---|---|---|
| Mineral | Formula | Mineral | Formula |
| Goethite | $\alpha$-FeOOH | Ferrihydrite | $Fe_5HO_8 \cdot 4H_2O$ |
| Akageneite | $\beta$-FeOOH | Hematite | $\alpha$-Fe$_2$O$_3$ |
| Lepidocrocite | $\gamma$-FeOOH | Maghemite | $\gamma$-Fe$_2$O$_3$ |
| Feroxyhyte | $\delta'$-FeOOH | Magnetite | $Fe_3O_4$ |

### 1.6.3 Reactivity

Iron oxides in soil and sediment provide active surface groups for the adsorption of various organic and inorganic species including phosphate and silicate. This surface reactivity of iron oxides greatly depends on their crystalline structures, specific surface areas, surface site densities, particle size etc. These factors also influence the reactivity of iron oxides towards their dissolution. The reactivity of iron oxides, in terms of both adsorption and dissolution, generally increases as the crystallinity in the solids decrease (i.e., the reactivity of goethite>hematite>ferrihydrite) (Bonneville et al., 2009, 2004; Gérard, 2016; Roden and Zachara, 1996). Even within each class of iron oxides, such as ferrihydrite or goethite, reactivity may also vary depending on their specific surface areas, site densities, and the presence of other ions on their surface, and in their structural building blocks. These different physico-chemical properties of iron oxides may arise from different precipitation conditions (Langley et al., 2009).

Solubility of iron oxides has been shown to be correlated with their reactivity towards reductive dissolution (Bonneville et al., 2004). These authors have demonstrated that both the solubility of iron oxides and their rate of reductive dissolution decrease from amorphous to well-crystalline iron oxides. In natural environments, particularly under anoxic conditions and around near neutral pH, the reductive dissolution of ferric iron oxides is generally mediated by iron reducing bacteria (discussed in section 1.5.3.3, Figure 1.13). During the microbial

reduction of iron, contact between bacterial cells to the mineral surface typically enhances electron transfer to $Fe^{3+}$ from an electron donor (e.g., reduced organic carbon) (Bonneville et al., 2004). Therefore, the accessible iron centres on a mineral to the bacterial cells is important in determining the dissolution kinetics of iron oxides. Thus, higher surface areas and higher surface site densities of iron oxides increase their reactivity towards their chemical dissolution or the dissolution mediated by iron reducing bacteria (Bonneville et al., 2009, 2004; Roden and Zachara, 1996).

The physico-chemical properties of iron oxides, such as crystalline structure, specific surface area, particle size, and impurities present in the iron oxides, greatly depend on synthesis conditions, and thus their reactivity. For example, iron oxides formed via abiotic oxidation are generally more reactive and exhibit more crystalline forms and larger particle size than those formed via microbial oxidation (Châtellier et al., 2004). Even under both abiotic and biotic oxidation, the presence of other dissolved constituents may influence the rate of oxidation, and the reactivity of mineral products. For example, the presence of dissolved silicate decreases the rate of abiotic oxidation of $Fe^{2+}$ (Kinsela et al., 2016), whereas it increases the rate of oxidation when mediated by $Fe^{2+}$ oxidizing bacteria (Gauger et al., 2016; Konhauser et al., 2007). The dominant mechanisms of iron oxide formation may also depend on the availability of $Fe^{2+}$ oxidizing bacteria, concentrations of $Fe^{2+}$ and other dissolved constituents, pH and redox conditions (Châtellier et al., 2004; James and Ferris, 2004; Konhauser et al., 2007; Phoenix et al., 2003), which may determine the reactivity of iron oxides in natural environments.

## 1.7 Key questions and objectives

The concentrations of silicate and phosphate in standing water bodies, e.g., lakes, are positively correlated ($r^2=0.17$, p value=<0.05) according to the US NWIS data (Figure 1.11). In addition, silicate, like other anions, can have multiple effects on the mobilization of phosphate (discussed in sections 1.5.3.2 and 1.5.3.3). Yet, the influence of silicate on the internal loading of phosphate is often ignored, except for a limited number of studies in the existing literature. These studies have shown that dissolved silicate can increase the phosphate efflux from sediment to the water column (Koski-Vähälä et al., 2001; Koszelnik and Tomaszek, 2008; Tallberg et al., 2008; Tuominen et al., 1998). However, the potential mechanisms by which

dissolved silicate can influence phosphate mobilization are not yet fully understood. Besides the role of dissolved silicate, co-precipitated silicate with iron and phosphate may also control the reductive release of iron and the associated phosphate and hence, the efflux of phosphate across the sediment-water interface. The role of co-precipitated silicate on the mobilization of phosphate has not been assessed in the existing literature. To understand the potential roles of dissolved and co-precipitated silicate on the mobilization of phosphate, this PhD research investigates the interactions between iron, phosphate and silicate that are likely to take place in deposited freshwater sediments. Numerous experiments were completed to address the following key objectives.

- To investigate the effects of dissolved silicate on the adsorption of phosphate onto ferric (hydr)oxides;
- To determine the role of dissolved silicate in the desorption of pre-adsorbed phosphate from ferric (hydr)oxides;
- Dissolved silicate co-precipitates easily with ferric (hydr)oxides, similar to phosphate. Therefore, the role of silicate in the removal of phosphate from aqueous phase was investigated by co-precipitating phosphate with ferric (hydr)oxides at various aqueous Si:Fe ratios;
- To determine the influence of co-precipitated silicate on the dissolution kinetics of iron and phosphate from Fe-P-Si co-precipitates;
- To understand the relative importance of the previously investigated processes, when silicon, phosphorus and iron are present together in natural sediments.

The experimental results contribute to the understanding of potential roles of silicate in natural freshwater systems and their relative importance in the mobilization of phosphate at the sediment-water interface. Additionally, this study improves our fundamental knowledge of the coupled silicon, phosphorus and iron cycling in freshwater environments.

## 1.8 Thesis organization

Based on the potential roles of silicate in the mobilization of phosphate, this PhD thesis is structured with five different chapters, as outlined below.

**Chapter-1:** General introduction

**Contents:** The biogeochemical cycling of P is discussed with focus on the uptake and release mechanisms of phosphate at the sediment-water interface. The concentrations of dissolved anions, e.g., phosphate, silicate and the pH are extracted from the NWIS (2010-2016) database to provide context about their relative importance in phosphate mobilization.

**Chapter-2:** Effects of pH and silicate on the adsorption of phosphate on goethite

**Contents:** Batch adsorption experiments were conducted to (i) quantify the rate of adsorption of phosphate and silicate on goethite at pH 7, and (ii) determine equilibrium adsorption envelopes for phosphate and silicate on goethite, a model ferric (hydr)oxide, over a wide pH range, both independently (P, Si) and simultaneously (P + Si). The experimental results were used to parameterize a charge distribution multisite surface complexation (CD-MUSIC) model. The model was further extended for the adsorption of phosphate and silicate on goethite to a wide range of aqueous phase Si:P ratios. The experimental and modeling results isolate the individual roles played by pH and silicate on the adsorption of phosphate on goethite. The results from laboratory experiments and the CD-MUSIC model are used to interpret data from the NWIS database to better understand the type of aquatic environments where silicate mediated phosphate mobilization may be expected to be significant.

**Chapter-3:** Effect of silicate on phosphate adsorption and desorption under dynamic pH conditions

**Contents:** The adsorption experiments presented in Chapter-2 were conducted using clean goethite surfaces and at static pH. However, in sediment, ferric (hydr)oxides are loaded with sorbates, including phosphate on their surfaces and the pH are dynamic. Therefore, desorption of pre-adsorbed phosphate was conducted by applying a step-wise pH increase in the absence and presence of aqueous silicate. Subsequent adsorption of phosphate was also investigated, by the gradual addition of HCl, after each desorption experiment. The experimental data along with results from the CD-MUSIC model simulating the experiment provide further information

on phosphate desorption/adsorption mechanisms on/from goethite under dynamic pH conditions and the role played by silicate.

**Chapter-4:** Iron-phosphate-silicate co-precipitates: Phosphate mobilization during reductive dissolution

**Contents:** Co-precipitates of iron, phosphate and silicate were synthesized from variable Si:Fe solution ratios. Two sets of co-precipitates were prepared by (i) oxidative $Fe^{2+}$ precipitation, and (ii) $Fe^{3+}$ precipitation via pH increase. The co-precipitates were characterized using multiple physical and chemical techniques, X-ray Diffraction Spectroscopy, Attenuated Total Internal Reflectance Fourier Transform Infrared Spectroscopy (ATR-FTIR), and total elemental analysis. The co-precipitates were reductively dissolved in buffered ascorbate-citrate solution at pH 7.5. The reactivity of the co-precipitates is discussed in terms of kinetic parameters extracted by fitting experimental data to the reactive continuum model. The relative reactivity of the co-precipitates obtained by the two different methods is analyzed. In addition, the results of dissolution kinetic experiments of the co-precipitates in the presence of a facultative anaerobic iron reducing bacteria are presented.

**Chapter-5:** Internal phosphorus loading from marsh sediments: Effect of silicate under variable redox conditions

**Contents:** The experimental results discussed in chapter 2 to 4 consider processes in isolation, under highly controlled conditions. These kinds of experiments are necessary to understand individual mechanisms. However, integrating those findings to understand the overall effect of silicate on phosphate mobilization under natural conditions is challenging because, in natural environments, a plethora of processes occurs simultaneously, and the chemical compositions of solids and aqueous phase are complex. Therefore, experiments with natural sediments were conducted using a flow-through column system under oxic and anoxic conditions. Experimental results are discussed based on the analysis of aqueous outflow and chemical extractions of solid sediments. The relative importance of the individual effect of dissolved and co-precipitated silicate on the mobilization of phosphate at the sediment-water interface is addressed.

# Chapter 2

## Effects of pH and silicate on the adsorption of phosphate on goethite

### 2.1 Summary

Remobilization of sediment-bound phosphorus is one of the potential causes of eutrophication in surface waters. Several physical and biogeochemical factors control the mobilization of phosphate at the sediment-water interface. Among these, dissolved silicate at high concentrations is hypothesized to facilitate the benthic return of dissolved phosphate to the overlying water column. Yet, the potential role of silicate is not fully understood. In this study, batch experiments were conducted to a) quantify the rate of phosphate and silicate adsorption on goethite at pH 7, and b) determine equilibrium adsorption envelopes for phosphate and silicate on goethite over a wide pH range, both independently and simultaneously. The results from the kinetic study suggest that the rate of phosphate adsorption at pH 7 was independent of aqueous silicate whereas that of silicate was strongly influenced by aqueous phosphate. As expected, results from the pH dependent study show that the adsorption of phosphate was higher under acidic pH and decreased with increasing pH from near neutral to alkaline conditions. Maximum silicate adsorption took place around pH 10 with a symmetric adsorption envelope shape. Experimental results from the independent and simultaneous adsorption of phosphate and silicate were used to parameterize the CD-MUSIC model, built on past studies that separately assessed the adsorption of phosphate and silicate on goethite. The optimized model was used to study equilibrium adsorption of phosphate and silicate over a wide pH range at various aqueous phase Si:P ratios and as a function of background electrolyte, $Na^+$ and $Cl^-$, concentrations. The model predicts that increasing silicate concentrations decrease phosphate sorption on goethite. This competitive effect of silicate on phosphate adsorption is very minor under acidic conditions, and more pronounced under alkaline conditions and at higher concentrations of $Na^+$ and $Cl^-$. Water quality monitoring data from the US National Water Information System (NWIS) along with experimental and modeling results suggest that the mobilization of phosphate at the sediment-water interface could be promoted by silicate in lakes and reservoirs, under sufficiently alkaline pH conditions.

## 2.2 Introduction

Phosphorus (P), in the form of phosphate, is an essential nutrient for the growth of plants and phytoplankton (Schindler, 1977). As P often limits primary production in freshwater systems, P additions to aquatic environments can accelerate algal bloom formation causing eutrophication (Smith and Schindler, 2009). Anthropogenic external P input from non-point sources such as fertilizer runoff from agricultural land, and point sources such as wastewater treatment plants, are the important sources of P to surface waters (Carpenter, 2008; Correll, 1998; Scavia et al., 2014). However, internal P loading, from sediment to surface water, has been found to be comparable to external P loading in many aquatic environments, particularly in lakes with a history of significant P accumulation (Matisoff et al., 2017, 2016; Nürnberg and Lazerte, 2016; Orihel et al., 2017; Paytan et al., 2017).

In surface waters, P is present in both soluble and particulate forms which may undergo a number of biogeochemical transformations (Orihel et al., 2017; Zhang et al., 2016). Biological uptake, adsorption and (co-)precipitation are important transformation mechanisms, which convert dissolved-P to particulate-P. Both forms of P in the overlying water may be partially exported to other places or removed by sedimentation. The particulate forms of P, organic and inorganic, are usually less bioavailable and can be deposited at the sediment-water interface. In sediments, P is generally associated with metal (hydr)oxides, carbonates and clay minerals (Christophoridis and Fytianos, 2006; Orihel et al., 2017; Oxmann and Schwendenmann, 2015; Søndergaard et al., 2003) as well as with organic matter, particularly in shallow eutrophic lakes (Zhu et al., 2013).

Remobilization of P from sediment to the water column is the result of mineral dissolution, desorption and the hydrolysis of particulate organic P (Joshi et al., 2015; Orihel et al., 2017; Smolders et al., 2006). In particular, the reductive dissolution of phosphate containing ferric (hydr)oxides (Orihel et al., 2017; Parsons et al., 2017; Smolders et al., 2006; Søndergaard et al., 2003) and the desorption of phosphate from mineral surfaces are generally considered major processes driving internal P loading in lakes (Antelo et al., 2007; Christophoridis and Fytianos, 2006; Geelhoed et al., 1997; Smolders et al., 2006). Anionic species including arsenate, bicarbonate, sulfate, and silicate are known to be competitive ions to phosphate for mineral binding sites (Antelo et al., 2007; Geelhoed et al., 1997; Smolders et al., 2006). Among these, silicate is ubiquitous in aquatic environments and is hypothesized to

affect the mobilization of phosphate from sediment mineral surfaces. Aqueous silicate occurs in natural waters mostly in the form of silicic acid ($H_4SiO_4$) which forms due to dissolution of diatom frustules, plant phytoliths, and detrital silicate minerals (Iler, 1979; Struyf et al., 2009).

Several previous experimental studies have addressed the effect of silicate on the release of phosphate from sediments (Koski-Vähälä et al., 2001; Koszelnik and Tomaszek, 2008; Tallberg et al., 2008; Tuominen et al., 1998). However, these experiments have left some open questions. Specifically, the studies used natural sediments which, although more directly relevant to the natural conditions present at specific sampling sites, are inherently complex with many processes potentially contributing to P mobilization. Recently, Hiemstra (2018) has shown that aqueous silicate decreases phosphate adsorption to ferrihydrite under alkaline conditions. The study, however, does not provide detailed quantitative information, particularly on phosphate adsorption under various Si:P aqueous ratios.

Most previous experiments have also used sodium silicate salts, which increase pH, which in turn cause desorption of phosphate from metal (hydr)oxide surfaces. The role of changes in pH in the presence of dissolved silicate however has not received much attention in previous studies. Additionally, increased pH could promote the hydrolysis of particulate organic-P to inorganic phosphate in natural sediments, which would lead to an overestimation of mineral released phosphate by the influence of silicate, if this is the only mechanism considered (Turner et al., 2005). Diatom frustules have also been used as a source of silicate in some experiments (Tallberg et al., 2008). Frustules themselves may release some phosphate upon dissolution, thus causing an overestimation of silicate induced phosphate release from sediment (Baines et al., 2011). In some cases, the molybdate blue (Mo-blue) method (Hartikainen et al., 1996) was used to determine phosphate concentrations and necessary corrections for the overestimation of phosphate at high Si:P ratio by this method were not documented and may therefore have not been applied. It has been widely demonstrated that the Mo-blue method measures many organic-P species in addition to phosphate (He et al., 2006; He and Honeycutt, 2005; Ivanoff et al., 1998). Therefore, results from previous work do not provide a complete picture on the mechanisms by which silicate affects dynamics in freshwater sediments.

The adsorption of phosphate (Arts et al., 2013; Geelhoed et al., 1997; Kim et al., 2011; Nowack and Stone, 1999; Sabur and Al-Abadleh, 2015; Stachowicz et al., 2008; Swedlund et

al., 2010b; Tofan-Lazar and Al-Abadleh, 2012) and silicate (Hiemstra et al., 2007; Jordan et al., 2009, 2007) on ferric (hydr)oxides has been studied separately through experimental and modeling work. However, the existing literature does not address the competitive effects when both P and Si are present in solution. Therefore, the conditions under which silicate induced phosphate mobilization from mineral surfaces occurs, and the relative importance of this mechanism still require further investigation. In this study, a series of batch adsorption experiments were conducted to a) quantify the rate of adsorption of phosphate and silicate on goethite at pH 7, and b) determine their equilibrium adsorption envelopes, both independently (P or Si) and simultaneously (P+Si). Goethite was chosen as sorbent as it is a stable and abundant iron-mineral with a relatively large surface area (generally varies from 10 to 132 $m^2$/g) in many natural sediments (Liu et al., 2014).

The experimental results from separate and simultaneous adsorption of phosphate and silicate on goethite were used to optimize reaction parameters for the triple layer charge distribution multisite surface complexation model (CD-MUSIC). The model has been previously used in studies on adsorption of phosphate only and silicate only on goethite (Hiemstra et al., 2007; Rahnemaie et al., 2007b). The optimized model developed here is used to quantify the adsorption of phosphate and silicate for a wide range of Si:P solution ratios and at various background electrolyte concentrations to quantitatively determine the influence of silicate on the adsorption of phosphate. The environmental significance of silicate-promoted mobilization of phosphate is addressed using the concentrations of phosphate and silicate in surface water extracted from the US NWIS network.

## 2.3 Materials and methods

### 2.3.1 Chemicals

Goethite (Bayferrox 910 MU) used in the experiments was purified through repetitive washing with 18.2 M$\Omega$cm$^{-1}$ water, followed by centrifugation. The washing procedure was discontinued after 12 washes when the conductivity of the supernatant no longer changed. The purified dried goethite was analyzed for iron, phosphate and silicate by dissolving a small amount of solid in concentrated HCl (Schwertmann and Cornell, 2000b). The goethite purified in this study was found to have iron, phosphorus and silicon contents of 10.22, $6.03\times10^{-3}$ and $1.60\times10^{-2}$ mmol/g, respectively. Specific surface area was determined as 15.0 $m^2$/g by the nitrogen gas adsorption

method using a Gemini VII instrument. The PZC was measured as 10.0 by potentiometric titration as per Vakros et al. (2002).

Solutions of phosphate and silicate were prepared by dissolving sodium phosphate monobasic (Sigma Aldrich, $H_2NaPO_4$, $\geq 99.0\%$) and sodium metasilicate nanohydrate (Aldrich, $Na_2SiO_3.9H_2O$, $\geq 98.0\%$), respectively, in background solutions containing 10 mM NaCl (Fisher Scientific, 99.0%) and 1 mM N-(2-Hydroxyethyl)piperazine-N'-2-ethanesulfonic acid (HEPES) as a pH buffer (Fisher Scientific, $C_8H_{18}N_2O_4S$, $\geq 99\%$). Unless otherwise stated all solutions and reagents were prepared using 18.2 M$\Omega$cm$^{-1}$ water (Millipore). The pH of the solutions was adjusted using NaOH and HCl. The exact amount of goethite used in each experiment was determined by weighing the adsorption vial using an analytical balance. All experiments were performed at least twice to verify reproducibility. To minimize the uncertainties associated with pH drift in adsorption experiments, HEPES (buffering pH range: 6.8 to 8.2) was used, an organic buffer with one -$SO_3H$ group to maintain pH. HEPES has been shown to have no significant effect on the adsorption of arsenate and phosphate (Kanematsu et al., 2011) on ferric (hydr)oxides because of its weak complexing ability with metal ions (Nowack et al., 1996; Nowack and Sigg, 1996). An anaerobic chamber (Coy laboratory products) with a <1 ppmv $O_2$, 97% $N_2$, 3% $H_2$ atmosphere was used for all experiments to avoid interference from bicarbonate in equilibrium with atmospheric $CO_2$.

## 2.3.2 Analytical methods

To avoid the interference from silicate in the determination of phosphate by colorimetry (Hartikainen et al., 1996), inductively coupled plasma optical emission spectroscopy (ICP-OES) was used. Total aqueous concentrations of iron, phosphate, and silicate (as elemental Fe, P, and Si) were measured by ICP-OES (Thermo Scientific iCAP 6300) after acidification with ultra-pure $HNO_3$ (EMD Millipore Corporation) to < pH 2, with a precision of <5% RSD and an accuracy of $\pm$ 10% with respect to NIST validated solutions for all analytes. Three wavelengths per analyte were selected and evaluated to ensure minimal interference from solution components. The method detection limit for Fe, P and Si were 0.89, 1.61, 1.78 μM, respectively. Matrix-matched standards were used for calibrations and all reagents were prepared with analytical grade salts from isoSPEC and 18.2 M$\Omega$cm-1 water (Millipore).

### 2.3.3 Experiments

### 2.3.3.1 Adsorption kinetics

To determine the rates of phosphate and silicate adsorption, 15 polypropylene centrifuge tubes (VWR, 50 mL) each containing 12.5 mg of goethite and 20 mL of the background solution (at pH 7) were agitated on a rotary shaker at 30 rpm at 25°C (Glass-Col, 099A RD4512) to allow equilibration of the goethite surface with the solution. All solutions were degassed thoroughly with $N_{2(g)}$ to remove residual carbon dioxide before the experiments started. The pH was re-measured after equilibration and a change of less than ±0.05 was observed compared to the initial values. Subsequently 5 mL of 0.25 mM phosphate solution (pH 7.00) was added to each of the tubes inside the anaerobic chamber, resulting in a final phosphate concentration of 50 µM. The tubes were removed sacrificially at increasing time intervals (5, 10, 15, 20, 30 min, … to 10 hours) during the adsorption experiment and centrifuged at 1690 RCF for 15 min (Thermo Scientific, Sorvall ST 16R). The supernatant was filtered using 0.45 µm pore size polypropylene (VWR Scientific Inc.) syringe filters and the pH of the filtrate was re-measured using a glass electrode (Thermo Orion 9107BNMD) equipped with a Symphony SP90M5 pH meter. Filtrates were acidified to < pH 2 with ultra-pure nitric acid and were stored at 4°C until analysis by ICP-OES. The same procedure was used for the kinetic studies with silicate only and with equimolar concentrations of phosphate and silicate. To observe the effect of silicate on the adsorption of phosphate on goethite, 50 µM phosphate solution was equilibrated with goethite in the presence of 50 and 100 µM silicate. 5 mL solutions of phosphate or/and silicate were also added to 20 mL of the background solution (without goethite) in a separate vial acidified and stored for ICP-OES analysis. The concentrations of phosphate or/and silicate were used as the background concentrations before adsorption.

### 2.3.3.2 Effect of pH on adsorption

Separate solutions of phosphate and silicate (50 µM each) were prepared and pH was adjusted, using HCl or NaOH solution, between pH 2 to 12 at 1 pH unit intervals. In these experiments, 0.0125 g of goethite (0.5 g/L) was equilibrated for 6 hours with 25 mL of phosphate and/or silicate solutions (50 µM each) at 25°C. The 6 hours equilibration time was determined based on the results from the kinetic studies, as the time required for maximum adsorption under the given experimental conditions (see section 2.4.1). In addition, a set of experiments was

conducted under similar conditions whereby phosphate and silicate (50 µM each) were added simultaneously to study competitive adsorption effects. An experimental control was also prepared whereby background solutions (10 mM NaCl and 1 mM HEPES) without added phosphate or silicate were equilibrated under similar conditions but without goethite present. HEPES was included in the pH dependent studies to maintain consistency with the kinetic studies at pH 7 [Note: HEPES only works as a buffer between pH 6.8 and 8.2]. After pH adjustments, aliquots of each solution were taken before mixing with goethite and were analyzed by ICP-OES after acidification. For each adsorption experiment, equilibrium pH was measured, and the aqueous sample prepared for the analysis with ICP-OES as above.

Similar experiments for the adsorption of phosphate (50 µM) in the presence of higher silicate concentrations (250 to 1000 µM) were also completed at pH around 8, 9, and 10.

### 2.3.3.3 Surface complexation model

Several surface complexation models, e.g., diffuse double layer model (DLM), constant capacitance model (CCM), and triple layer model (TLM), are commonly used to describe the adsorption of cations and anions on ferric (hydr)oxides (Goldberg, 2014; Langmuir, 1997a). These surface complexation models are thermodynamics based, and operationally different from each other depending primarily on how the electrical double layer is defined (Goldberg, 2014; Langmuir, 1997a; Vieira, 2006). To describe the surface complexation of a sorbate on a sorbent, a surface complexation model generally requires various types of model parameters, e.g., the total number of surface sites, speciation of surface groups and the sorbate, and the capacitances in the electrical double later (Goldberg, 2014; Langmuir, 1997a; Vieira, 2006). The number of model parameters for surface complexation models increase in the order: DLM<CCM<TLM. With an increasing number of model parameters models generally provide increasingly better fits to the experimental data.

The DLM, CCM and a simple TLM have been used in past studies to successfully quantify the independent adsorption of various sorbates (e.g., cations and anions) on various solid surfaces including ferric (hydr)oxides (Davis et al., 2002; Gao and Mucci, 2003, 2001; Spiteri et al., 2008). However, none of these models has been shown to better describe experimental data, particularly under competitive conditions (i.e., more than one sorbate in solution) (Gao and Mucci, 2003, 2001).

The CD-MUSIC is a triple layer model, and considers heterogeneity in surface –OH groups, e.g., attached to singly or doubly co-ordinated surface oxygen groups by $Fe^{3+}$ in ferric (hydr)oxides. This additional factor in the CD-MUSIC model allows one to calculate the interfacial charge distribution upon the adsorption of a sorbate. Reasonably, the implementation of the CD-MUSIC model generally requires an additional interfacial charge distribution coefficient for each of the defined surface complexes in the model. The CD-MUSIC model should, therefore, provide better fit to the experimental data in comparison to the other models. This CD-MUSIC model has been shown to describe the competitive adsorption of anions, e.g., phosphate and arsenate, phosphate and selenite as well as phosphate and carbonate (Hiemstra and Van Riemsdijk, 1999; Stachowicz et al., 2008). This study, therefore, considers the optimization of the CD-MUSIC model against the experimental data obtained herein from the independent and competitive adsorption of phosphate and silicate.

The surface complexation reactions for the adsorption of phosphate were taken from Rahnemaie et al. (2007b), and those for silicate from Hiemstra et al. (2007). Here, monoprotonated mono-dentate (($\equiv FeOPO_2OH^{-1.5}$), monoprotonated bi-dentate (($\equiv FeOO)_2POOH^{-}$), and unprotonated bi-dentate (($\equiv FeO)_2PO_2^{-2}$) complexes were considered in the model (reactions 9, 10, and 11, respectively in Table 2.1). For silicate sorption, bi-dentate monomer, tetramer and polymer surface complexes (reaction 12, 13, and 14, respectively in Table 2.1) were included.

The adsorption of ions at a given pH depends on the chemical structure of the crystal-water interface (Hiemstra and van Riemsdijk, 1996). For example, $Fe^{3+}$ at the goethite surface can have singly, doubly and triply co-ordinated groups on the most dominant 110 plane. The CD-MUSIC model considers singly $\equiv FeOH(H)$ and triply $\equiv Fe_3O(H)$ coordinated Fe-O surface groups as the active sites on goethite for surface complexation reactions (Hiemstra and van Riemsdijk, 1996). The doubly coordinated surface $\equiv Fe_2O(H)$ group has been suggested to be inert and remain as $\equiv Fe_2OH^0$ over a wide pH range. Hence, it is not likely to contribute to the PZC of goethite (Hiemstra and van Riemsdijk, 1996). For the singly $\equiv FeOH(H)$ and triply $\equiv Fe_3O(H)$ co-ordinated surface groups, the *logK* values are proposed to be very similar (Hiemstra and Riemsdijk, 2006). Thus, for simplicity, only singly $\equiv FeOH(H)$ co-ordinated surface groups of goethite are assumed to form surface complexes with oxyanions, including phosphate and silicate (Hiemstra and Riemsdijk, 2006). The schematic diagram for phosphate

surface complexes with singly co-ordinated surface ≡FeOH(H) groups on goethite are shown in Figure 2.1.
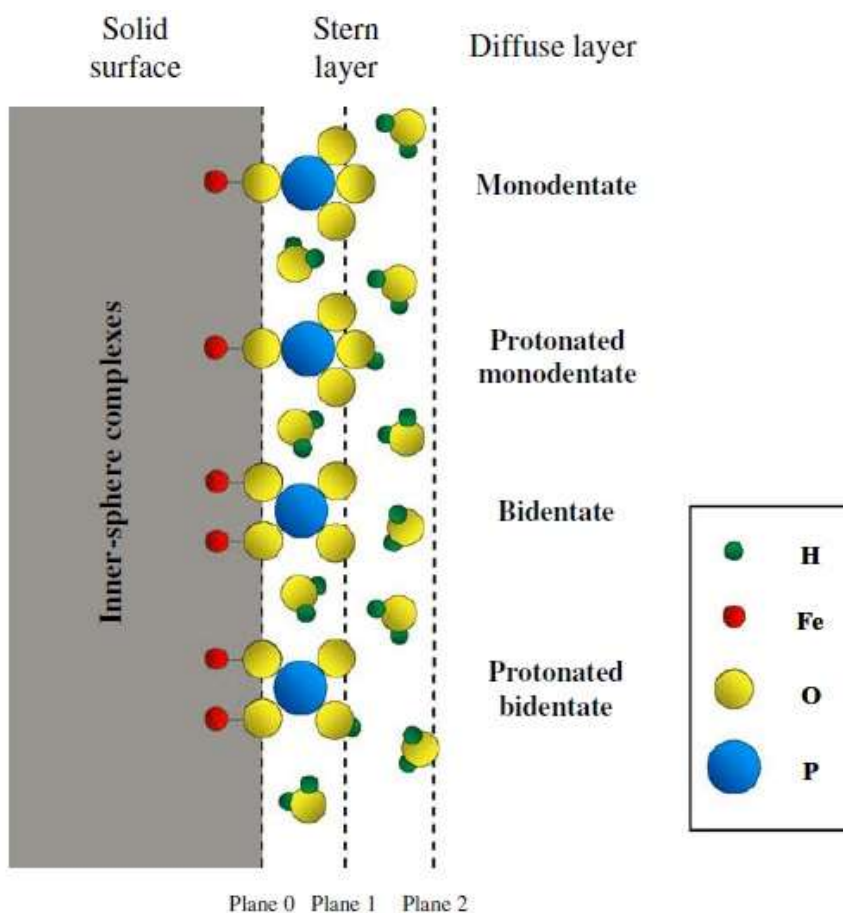


**Figure 2.1.** Schematic diagram showing the inner-sphere phosphate surface complexes formed with singly coordinated surface ≡FeOH(H) group on a metal (hydr)oxide. Electrolyte ions are generally located in the plane 1 of the extended Stern layer (not shown here) where they may form outer-sphere complexes. The figure has been reproduced from Antelo et al. 2010.

The model assumes that the overall double layer capacitance in a metal (hydr)oxide/water system is the combination of inner and outer Stern layer capacitance, due to poorly ordered water molecules (Hiemstra and Riemsdijk, 2006). The type of surface complexes generally used in the CD-MUSIC model are considered mostly on the basis of spectroscopic evidence (Antelo et al., 2010; Hiemstra, 2018; Hiemstra et al., 2007; Rahnemaie et al., 2007b). The specific adsorption of an oxyanion on a metal (hydr)oxide results in the partial neutralization of surface charge as well as the charge on the oxyanion. For example, the adsorption of aqueous $H_4SiO_4$ on a singly coordinated ≡FeOH$^{-0.5}$ surface group of goethite

leads to the change of overall charge $\Delta z_0$ and $\Delta z_1$ in the 0- and 1-plane, respectively (equation 2.1).

$$2 \equiv \text{FeOH}^{-0.5} + \text{H}_4\text{SiO}_4^0 \; = \; \equiv \text{Fe}_2\text{O}_2^{-1+\Delta z_0} \text{Si(OH)}_2^{\Delta z_1} + 2\text{H}_2\text{O} \cdots\cdots\cdots\cdots\cdots (2.1)$$
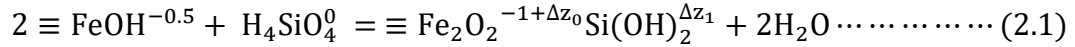
The interfacial charge distribution (CD) values ($\varDelta z$) for a surface complex are obtained by optimizing its geometry with the Brown bond valence approach (Brown and Altermatt, 1985) using molecular orbital calculations by density functional theory (Hiemstra, 2018; Hiemstra et al., 2007; Kersten and Vlasova, 2009; Rahnemaie et al., 2007b). The $\varDelta z$ values can vary depending on the experimental conditions, e.g., ionic strengths, properties of solvents and solids, and the presence of other aqueous ions (Hiemstra, 2018; Hiemstra et al., 2007; Kersten and Vlasova, 2009; Rahnemaie et al., 2007b). The CD-MUSIC model parameters are also dependent on the type and number of surface complexes used to fit the experimental data (Hiemstra, 2018; Hiemstra et al., 2007; Kersten and Vlasova, 2009; Rahnemaie et al., 2007b). The formation constants ($logK$) for the surface complexes are obtained by fitting experimental data against the simulated $\varDelta z$ values (Hiemstra, 2018; Hiemstra et al., 2007).

The previously reported surface site densities and the Stern layer capacitance for synthetic goethite (Table 2.1) were used. The specific surface area and the point of zero charge (PZC) of goethite determined in this study were used in the model. The experimental data obtained from both individual and simultaneous adsorption of phosphate and silicate were fitted to the model separately using different sets of previously reported $\varDelta z$ and $logK$ values (Antelo et al., 2010; Hiemstra, 2018; Hiemstra et al., 2007; Hiemstra and Riemsdijk, 2006; Rahnemaie et al., 2007b). The CD-MUSIC model was implemented in conjunction with PHREEQC 3. The phreeqc.dat database was used for other reaction parameters, e.g., protonation and deprotonation of phosphate and silicate in aqueous phase (Parkhurst and Appelo, 2013). No single set of reported surface complexation reaction parameters used in the model seemed to best describe the experimental data, that is, the data for both independent and simultaneous adsorption of phosphate and silicate. This is not surprising because the experimental conditions in this study were different from the experimental conditions used in previous studies (see Table 2.1), in which the surface complexation reaction parameters were optimized against experimental data. The different experimental conditions used in previous studies also resulted in variable surface complexation reaction parameters. Thus, the $\varDelta z$ and $logK$ values were optimized to achieve the best fit to our entire dataset. This was done by trial

and error, e.g., by manually changing the $\Delta z$ and $logK$ values. Best-fit parameters were identified based on the root mean square error (RMSE) between the experimental data and the model estimation (see supplementary material, section SM-2.1). Refer to Table 2.1 for the surface complexation reactions and the CD-MUSIC model parameters used in this study, as well as previously reported parameters.

**Table 2.1.** Surface complexation reactions and respective CD-MUSIC model parameters for the adsorption of phosphate and silicate on goethite. The value of *logK* represents the equilibrium constant for a given surface complexation reaction and $\Delta z_0$ and $\Delta z_1$ indicate the change of charge upon formation of a complex at the 0- and 1- plane, respectively. The $\Delta z_2$ values in the model were assumed 0 (zero) for all the surface species and, thus, they are not shown here. The model parameters with star mark (*) on the left were used in this study.

| Reaction | logK | $\Delta z_0$ | $\Delta z_1$ |
|---|---|---|---|
| *Goethite (3.45 uni sites/nm², 2.7 tri sites/nm², 15 m²/g, 0.0125g, $C_1=C_2=0.92$ F/m²) (Hiemstra et al., 2007)* | | | |
| (1) $\equiv Fe_3OH^{+0.5} = \equiv Fe_3O^{-0.5} + 0.5H^+$ | 10 | -0.5 | 0 |
| (2) $\equiv Fe_3O^{-0.5} + H^+ = \equiv Fe_3OH^{+0.5}$ | 9.20 | 1 | 0 |
| (3) $\equiv FeOH^{+1.5} = \equiv Fe^{-0.5} + 0.5H^+$ | 10 | -0.5 | 0 |
| (4) $\equiv FeOH^{-0.5} + H^+ = \equiv FeOH_2^{+0.5}$ | 9.20 | 1 | 0 |
| (5) $\equiv FeOH^{-0.5} + Na^+ = \equiv FeOHNa^{+0.5}$ | -0.6[a] | 0[a] | -1[a] |
| (6) $\equiv FeOH^{-0.5} + Na^+ + Cl^- = \equiv FeOH_2Cl^{-0.5}$ | 8.5[a] | 1[a] | -1[a] |
| (7) $\equiv Fe_3O^{-0.5} + Na^+ = \equiv Fe_3ONa^{+0.5}$ | -0.6[a] | 0[a] | 1[a] |
| (8) $\equiv Fe_3O^{-0.5} + Na^+ + Cl^- = \equiv Fe_3ONaCl^{-0.5}$ | 8.5[a] | 1[a] | -1[a] |
| (9) $\equiv FeOH^{-0.5} + 2H^+ + PO_4^{-3} = \equiv FeOPO_2OH^{-1.5} + H_2O$ | *27.25, (27.97[b],27.65[c],19.64[d],26.36[e]) | *0.32, (0.40[b],0.28[c,e],0.22[d]) | *-1.32, (-1.40[b], -1.28[c,e], -2.22[d]) |
| (10) $2\equiv FeOH^{-0.5} + 2H^+ + PO_4^{-3} = (\equiv FeO)_2PO_2^{-2} + 2H_2O$ | *28.45, (29.69[b],29.77[c],27.73[d],28.31[e]) | *0.46[c,d,e], (0.48[b]) | *-1.46[c,d,e], (-1.48[b]) |
| (11) $2\equiv FeOH^{-0.5} + 2H^+ + PO_4^{-3} + H^+ = (\equiv FeO)_2POOH^- + 2H_2O$ | *33.52[e], (34.4[b],32.06[d]) | *0.65[e], (0.82[b],0.58[c],0.63[d]) | *-0.65[e], (-0.82[b], 0.58[c], -0.63[d]) |
| (12) $2\equiv FeOH^{-0.5} + H_4SiO_4 = (\equiv FeO)_2Si(OH)_2^{-1} + 2H_2O$ | *5.75, (5.85[f]) | *0.40, (0.29[f]) | *-0.30, (-0.29[f]) |
| (13) $2\equiv FeOH^{-0.5} + 4H_4SiO_4 = (\equiv FeO)_2SiOHOSi_3O_2(OH)_7^{-1} + 5H_2O$ | *13.98[f] | *0.29[f] | *-0.29[f] |
| (14) $2\equiv FeOH^{-0.5} + 4H_4SiO_4 = (\equiv FeO)_2SiOHOSi_3O_3(OH)_6^{-2} + 4H_2O + 3H+$ | *7.47[f], (6.15[g]) | *0.29[f] | *-0.29[f] |

**NOTE:** With multiple values, those with an asterisk (*) on the left were used in this study.

*This study: $H_2NaPO_4$ (50 µM), $Na_2SiO_3.9H_2O$ (50 to 1000 µM), goethite (0.5 g/L, 15.0 m²/g, PZC=10), NaCl (0.01 M), 6 hours at RT, ICP-OES

[a]Rahnemaie et al., (2006): NaCl and LiCl (0.01 to 0.1 M), goethite (16.5 g/L, 98.6 m²/g, PZC = 8.5 and 9.0 in LiCl and NaCl solution, respectively), at 20.0±0.1 °C

[b]Rahnemaie et al., (2007b): NaHPO4 (0.01-10 mM) in NaNO3 (0.05 to 0.5 M), goethite (2.5 to 10 g/L, 100 m²/g, PZC=9.2), 24 hours at 20 °C, Mo-blue method

[c]Stachowicz et al., (2008): NaNO3 (0.01 to 0.1 M), phosphate (0.25 to 0.75 mM), goethite (5 g/L, 100 m²/g, PZC =9.2), 24 hours at 22 °C, ICP-AES

[d]Antelo et al., (2010): NaNO3 (0.01 to 0.5 M), 24 hours at 25°C , ferrihydrite (1.0 g/L, 350 m²/g, PZC= 8.7), Mo-blue method

[e]Hiemstra, (2018): NaHPO4 (0.039 mM), Na2SiO3.9H2O (0.1 to 1.0 mM), NaNO3 (0.01 to 2.0 M), ferrihydrite (0.12 to 0.40 g/L, PZC = 8.1, 610 m²/g), Mo-blue method

[f]Hiemstra et al., (2007): Na2SiO3·9H2O (0.1 to 1 mM), NaNO3 (0.1 M), 1 to 3 g/L goethite (100 m²/g), Mo-blue method

[g]Kersten and Vlasova, (2009): Na2SiO3.9H2O (10 to 100 µM), goethite (1 g/L, 20 m²/g, PZC=9.1), NaNO3 (10 to 100 mM), 24 hours at 10 to 25ºC, Mo-blue method

## 2.4 Results and discussion

### 2.4.1 Adsorption kinetics

Kinetic parameters for the adsorption of phosphate and silicate at variable aqueous phase Si:P ratio were extracted by fitting the experimental data using Equation (2.2) according to Luengo et al., (2007).

$$\theta(t) = \theta_1 + \theta_2(1 - e^{-k.t}) \cdots\cdots\cdots (2.2)$$

where, $\theta(t)$ is the amount of phosphate or silicate covering the goethite surface ($\mu mol/m^2$) at a given time t, and $\theta_1$ and $\theta_2(1 - e^{-k.t})$ are the amounts of sorbed phosphate or silicate on the goethite surface as a result of fast and slow adsorption processes, respectively. Fast phosphate adsorption generally takes place within 5 min and the slow adsorption starts after that (Luengo et al., 2007). The time required to complete these processes depends on factors such as the nature of the sorbent and adsorbing species, their concentrations, and temperature (Luengo et al., 2007). Adsorption is assumed to be completed when the slow process becomes negligible (Luengo et al., 2007; Torrent et al., 1992), which depends on the rate constant k. The adsorption rate at time t during the slow process ($R_{slow,0}$) can be calculated using the following equation:

$$R_{slow} = k\theta_2 e^{-k\cdot t} \cdots\cdots\cdots (2.3)$$

At t = 0, the initial rate $R_{slow,0}$ is given by:

$$R_{slow,0} = k\theta_2 \cdots\cdots\cdots (2.4)$$

The kinetic data for the individual adsorption of phosphate and silicate fitted to equation (2.2) are shown in Figure 2.2. The extracted kinetic parameters for the adsorption of phosphate and silicate are presented in Table 2.2. The comparisons between experimental data with the kinetic model (Equitation 2.1) are shown in terms of chi-square ($\chi^2$) values (Table 2.2). The equation for the calculation of $\chi^2$ and a table with critical chi-square ($\chi_c^2$) values are available in the supplementary material (section SM-2.2 and Table SM-2.2). According to Equation 2.2, the rate of the fast adsorption process is infinity. The amount of phosphate sorbed to goethite in the fast process (within 5 min) was about $1.4\pm0.1$ $\mu mol/m^2$, which was about 74% of the total amount sorbed to goethite at pH 7. The $\theta_1$ values show that the initial adsorption of phosphate (50 $\mu M$) was unaffected by the presence of silicate (Table 2.2). The adsorption of silicate (50 $\mu M$) at pH 7, on the other hand, was greatly influenced by the presence of phosphate. For example, the $\theta_1$ value for silicate adsorption was 0.39 $\mu mol/m^2$ in the absence of phosphate, which is about 38% of the total amount of silicate sorbed to goethite at pH 7.

However, the $\theta_1$ values for silicate adsorption in the presence of phosphate were nearly zero, indicating the strong competitive effect from aqueous phosphate for the adsorption sites on goethite.
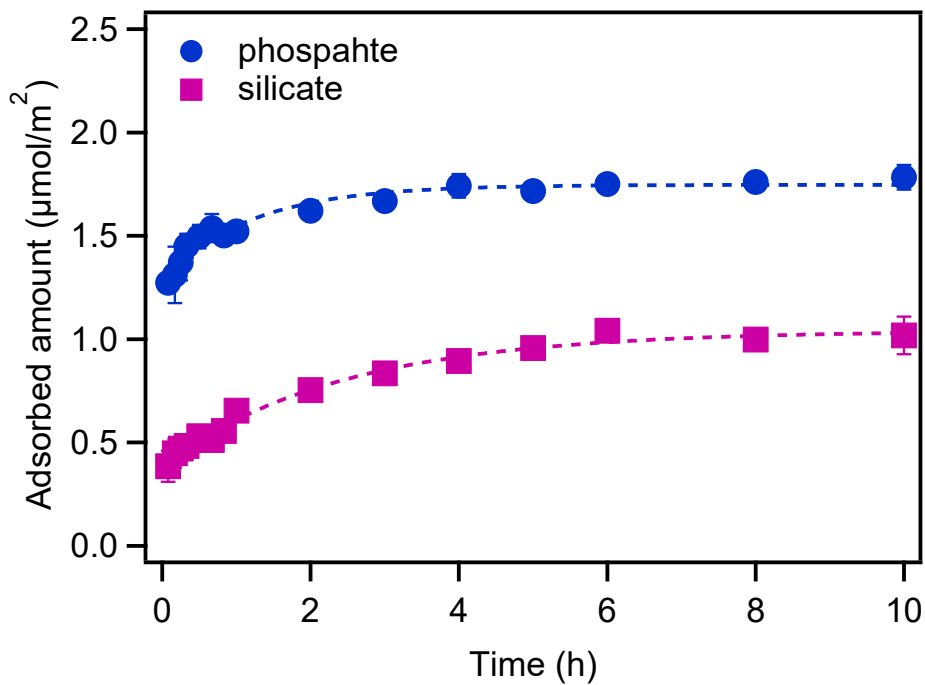


**Figure 2.2.** Kinetic data (symbols) for the individual adsorption of phosphate and silicate (50 µM each) on goethite (0.5 g/L). The adsorption experiments are conducted at pH 7 in 10 mM NaCl and 1.0 mM HEPES solution at 25°C. Kinetic parameters shown in Table 2.2 are extracted by fitting the experimental data to Equation 2.2 (dashed lines). The experimental data from concurrent phosphate and silicate adsorption are not included here for clarity, but the extracted kinetic parameters are included in Table 2.2. Error bars represent the range of values measured between duplicate experiments.

The adsorption of phosphate and silicate on metal (hydr)oxides is generally sensitive to the surface charge and hence, the pH. Therefore, the aqueous speciation of phosphate and silicate and the PZC of ferric (hydr)oxides are important in determining the anion adsorption at a given pH. The aqueous speciation diagrams for phosphoric acid ($H_3PO_4$) and silicic acid ($H_4SiO_4$) as a function of pH (see section 1.5.3.2, Figure 1.12) show that the dominant species of $H_3PO_4$ at pH 7 are the deprotonated forms ($H_2PO_4^-$ and $HPO_4^{2-}$, 1:1) whereas $H_4SiO_4$ exists in the unprotonated form. Therefore, a very weak influence of silicate on phosphate adsorption and a strong influence of phosphate on silicate adsorption is qualitatively in agreement with

the much higher proportion of deprotonated phosphate at pH 7 compared to very little deprotonated silicate.

**Table 2.2.** Kinetic parameters extracted for the adsorption of phosphate and silicate on goethite (0.5 g/L) at pH 7 and 25°C by fitting the experimental data to the equation 2.2 with 95% confidence limit and the goodness of fit is shown with chi-square ($\chi^2$) value. The critical chi-square ($\chi_c^2$) value based on the degree of freedom for each set of data is 7.26.

| Sorbate | Si:P ratio | $\theta_1$ ($\mu$mol/m$^2$) | $\theta_2$ ($\mu$mol/m$^2$) | $k$ (h$^{-1}$) | $R_{slow,0}$ ($\mu$mol/m$^2$) | $\chi^2$ |
|---|---|---|---|---|---|---|
| Phosphate (50 $\mu$M) | 0 | 1.29 | 0.46 | 0.83 | 0.38 | $1.8\times10^{-8}$ |
| | 1 | 1.46 | 0.49 | 0.86 | 0.42 | $1.3\times10^{-8}$ |
| | 2 | 1.32 | 0.35 | 0.45 | 0.16 | $2.9\times10^{-8}$ |
| Silicate (50 $\mu$M) | no phosphate | 0.39 | 0.65 | 0.41 | 0.27 | $9.3\times10^{-9}$ |

The adsorption of phosphate is assumed to be completed via the slow adsorption process, which accounts for about 25% of total phosphate sorbed to goethite by the end of the experiments. The adsorption kinetics of phosphate are slightly slower at a Si:P solution ratio 2 compared to the silicate free case, as shown by the $k$ and $R_{slow,0}$ values in Table 2.2. The adsorption of silicate, on the other hand, mostly occurs during the slow process in the absence of phosphate, accounting for about 62% of the total amount sorbed to goethite. However, no adsorption of silicate in the presence of phosphate was observed, even via the slow adsorption process. The kinetic parameters for silicate adsorption in the presence of phosphate were inconsistent and insignificant, likely due to the much stronger binding between phosphate and goethite at pH 7. The kinetic parameters extracted for the adsorption of silicate in the presence of phosphate are therefore not shown here.

### 2.4.2 pH effect

As observed by previous researchers, the adsorption of phosphate on goethite decreased with increasing solution pH (Figure 2.3a). Under acidic conditions, at pH values above the first pKa of $H_3PO_4$ acid (pH 2.15), the strong electrostatic attraction between deprotonated phosphate ($H_2PO_4^-$/$HPO_4^{2-}$) and the positively charged goethite surface results in maximum adsorption. With increasing pH, the electrostatic attractions become increasingly less favourable as the goethite surface becomes less positively charged, despite the transition to increasingly deprotonated phosphate species (Figure 2.3a). Surface complexes between fully protonated $H_4SiO_4$ and the positively charged goethite surface under acidic conditions are not likely,

although they are possible (Hiemstra et al., 2007; Swedlund and Webster, 1999). The maximum goethite surface coverage by silicate was observed at around the PZC of goethite (pH 10) shown in Figure 2.3b, above which the adsorption decreased again. Above pH 10, the concentration of the deprotonated form of silicic acid ($H_3SiO_4^-$) exceeds the unprotonated form. However, at a pH of greater than 10 the goethite surface also has a net negative charge. Therefore, above pH 10, electrostatic repulsion between an increasingly negatively charged surface and deprotonated silicate likely contributes to the decreased adsorption of silicate. A similar effect on phosphate adsorption was observed above near neutral pH.
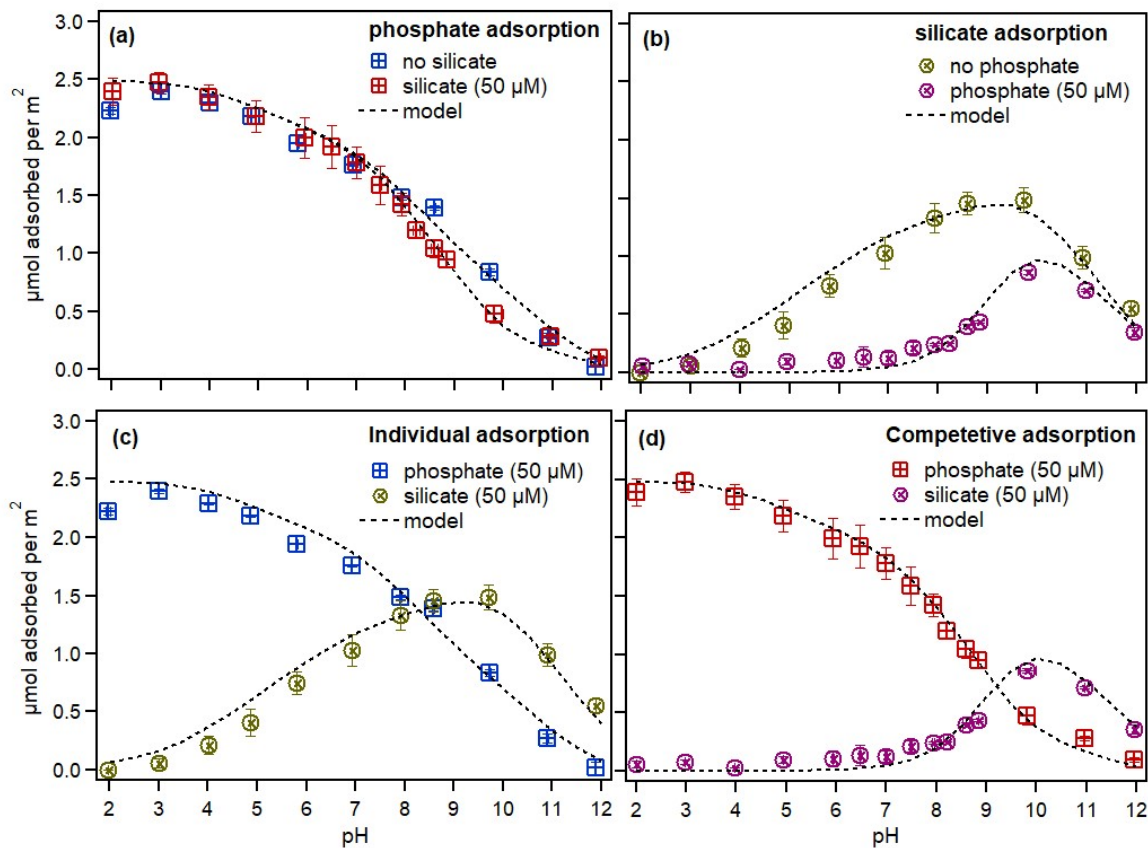


**Figure 2.3.** Individual and competitive adsorption of phosphate and silicate (50 μM each) on goethite (0.5 g/L) at 25°C and $I$=10 mM NaCl, between pH 2 and 12. Experimental results (markers) and predictions by CD-MUSIC model (dashed lines) are shown for (a) adsorption of phosphate (50 μM) in the absence and presence of silicate (50 μM); (b) adsorption of silicate (50 μM) in the absence and presence of phosphate (50 μM); (c) individual adsorption of phosphate and silicate (50 μM each), and (d) competitive adsorption of phosphate and silicate (50 μM each). Error bars represent the range of values measured between duplicate experiments.

In the experiments where both phosphate and silicate were present, the surface sites on goethite were available for both species. Therefore, the speciation of phosphate and silicate in solution plays a key role in determining their relative interactions with the active goethite sites. In this study, silicate present at equimolar concentration with phosphate slightly decreased phosphate adsorption under alkaline conditions, with no considerable effect below pH 7 (Figure 2.3a). This small but tangible competitive effect of silicate could not be statistically justified via a T-test from experimental data as only two replicates were conducted under each condition. The adsorption of silicate, on the other hand was strongly decreased by aqueous phosphate over a wide pH range (Figure 2.3b). For example, adsorption of silicate in the absence of phosphate was observed even at pH 3, but in the presence of phosphate, silicate adsorption only occurred above pH 5. However, both in isolation and in the presence of phosphate, adsorption of silicate reached a maximum around pH 10 (Figure 2.3b).

Further, the amount of sorbed silicate on goethite exceeded the amount of sorbed phosphate between pH 8 and 9, when phosphate and silicate were sorbed independently (Figure 2.3c). However, this only happened above pH 9 in the competitive adsorption experiments (Figure 2.3d). The results of the CD-MUSIC surface complexation modeling for the adsorption of phosphate and silicate are also presented in Figure 2.3. The results show that the model accurately reproduces the experimental data, confirmed by the RMSE and chi-square values (Table 2.3).

**Table 2.3.** The calculated RMSE and chi-square $(\chi^2)$ values between the experimental data and model estimated calculations for the adsorption of phosphate (50 µM) and silicate (50 µM) on goethite (0.5 g/L) at 25°C and $I=$10 mM NaCl. The critical chi-square $(\chi_c^2)$ values based on the degree of freedom are shown beside the observed $\chi^2$ values.

| Adsorption | adsorbate | RMSE | $\chi^2$ | $\chi_c^2$ |
|---|---|---|---|---|
| Individual | Phosphate | 0.12 | 0.17 | 3.94 |
| | Silicate | 0.11 | 0.33 | |
| Competitive | Phosphate | 0.06 | 0.16 | 6.57 |
| | Silicate | 0.08 | 0.60 | |

### 2.4.3 CD-MUSIC model: assessment

The surface complexation reaction parameters were optimized in this study against the experimental data obtained from the individual adsorption of phosphate and silicate plus the simultaneous adsorption data from the 1:1 aqueous phase Si:P molar ratio experiments.

However, in natural aquatic environments the concentrations of silicate and phosphate are highly variable (see Figure 1.7). Typically, silicate concentrations are much higher than those of aqueous phosphate. Therefore, the model was also compared to experimental results over a wider range of conditions. Specifically, the adsorption of phosphate (50 µM) was evaluated in the presence of higher silicate (250, 500 and 1000 µM) concentrations (Figure 2.4). The experiments were conducted under alkaline conditions where silicate can potentially influence the adsorption of phosphate. The results show that the model predictions are consistent with the experimental results for the adsorption of phosphate (Figure 2.4a) and silicate (Figure 2.4b).
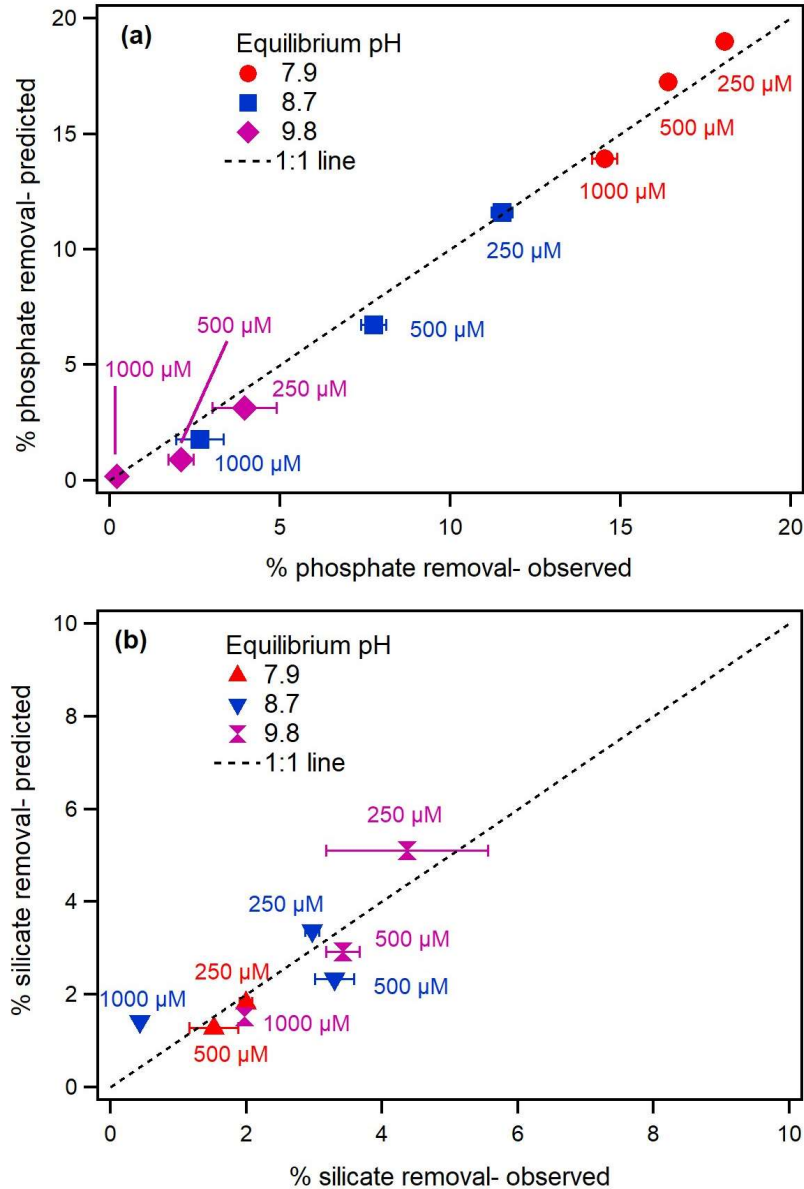
**Figure 2.4.** The experimental results (observed) and the predictions from CD-MUSIC model (estimated) for the simultaneous adsorption of (a) phosphate (50 µM) and (b) silicate (250, 500 and 1000 µM) on goethite (0.5 g/L) at 25°C and $I$=10 mM NaCl. Percentages of phosphate and silicate removal (points) were calculated by comparing their aqueous concentrations before and after the adsorption experiments. The numbers next to the points represent the initial concentrations of aqueous silicate present with 50 µM phosphate. The different solid markers identify the equilibrium pH. The black dashed lines indicate the 1:1 line where the experimental results and the model estimation are in complete agreement. The calculated RMSE values between the average experimental data and the model-estimation for the phosphate and silicate adsorption are 0.80 and 0.63, respectively.

## 2.4.4 CD-MUSIC model: effect of Si:P aqueous ratios

The CD-MUSIC model was applied to a wide range of Si:P solution ratios and a wide solution pH range. The ranges were determined based on the dissolved Si:P ratios in groundwater and surface water according to the NWIS data for 2010-2016 (Figure 2.5).
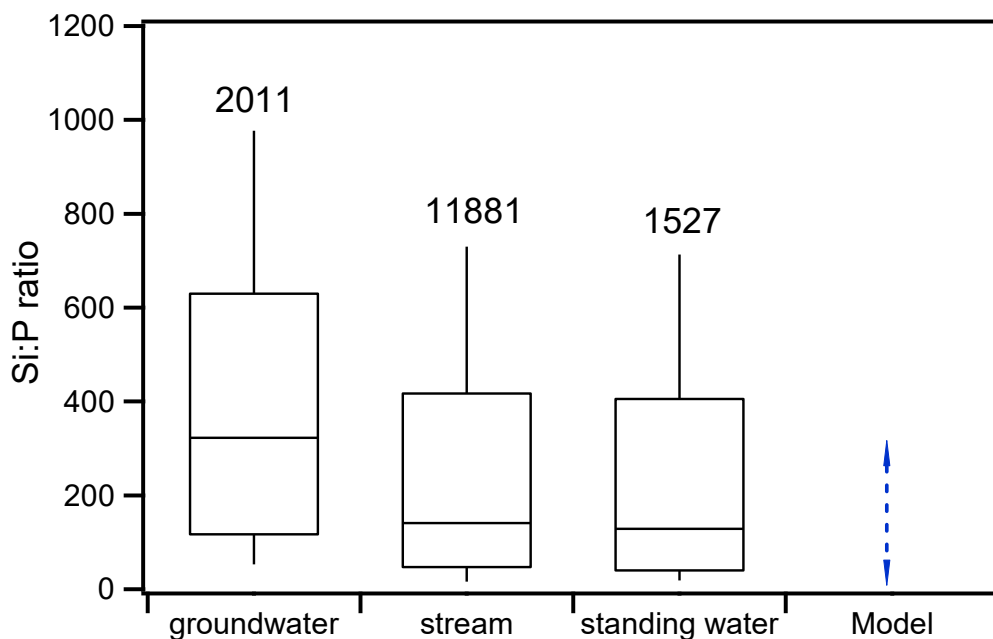


**Figure 2.5.** The Si:P molar ratios calculated from the concentrations of phosphate and silicate extracted from NWIS (2010-2016) data for groundwater, stream, standing water bodies, e.g., lakes and reservoirs. The number on each box represents the number of data points, which are extracted from all water depths available in the database. The lower and upper boundary of each box represents $25^{th}$ and $75^{th}$ percentile, respectively, and the line within the box shows the median value. The whiskers are drawn down to the $10^{th}$ percentile and up to the $90^{th}$. The blue double headed arrow represents the range of equilibrium aqueous phase Si:P ratio for adsorption on goethite covered by the CD-MUSIC model calculations.

The model was implemented using the parameters for the adsorption of phosphate and silicate on goethite presented in Table 2.1. The initial concentrations of phosphate and silicate used in the model ranged from 20 to 50 μM and 50 to 1000 μM, respectively. Goethite used in the model was a constant 0.5 g/L for consistency. The maximum Si:P solution ratio was 300 in equilibrium with goethite, for the lowest initial phosphate (20 μM) and highest initial silicate (1000 μM) concentrations used in the model. For example, the aqueous phase Si:P ratio for the 20 μM initial phosphate and 1000 μM initial silicate is 50. Under acidic conditions, e.g., at pH

4 the greater adsorption of phosphate (to goethite) over silicate results in the Si:P ratio of ~300 in solution.

The adsorption of phosphate and silicate on goethite at an initial aqueous Si:P ratio up to 10 (for 50 µM phosphate) is shown in Figure 2.6. The results show that a higher Si:P ratio decreases the adsorption of phosphate. However, silicate exerts only a relatively minor influence under slightly acidic conditions even at the highest aqueous Si:P ratio. Under alkaline conditions, as the pH increases, the adsorption of phosphate is decreased by the influence of dissolved silicate at higher concentrations. For example, the goethite surface coverage by phosphate at an initial Si:P solution ratio of 10, decreases by 9% at pH 7, but by 29%, 75% and 92% at pH 8, 9 and 10, respectively, compared to the conditions with no aqueous silicate. The competitive effect of silicate, which inhibits phosphate adsorption, is maximal at around pH 10, where the maximum silicate adsorption occurs and decreases above this pH (Figure 2.6).
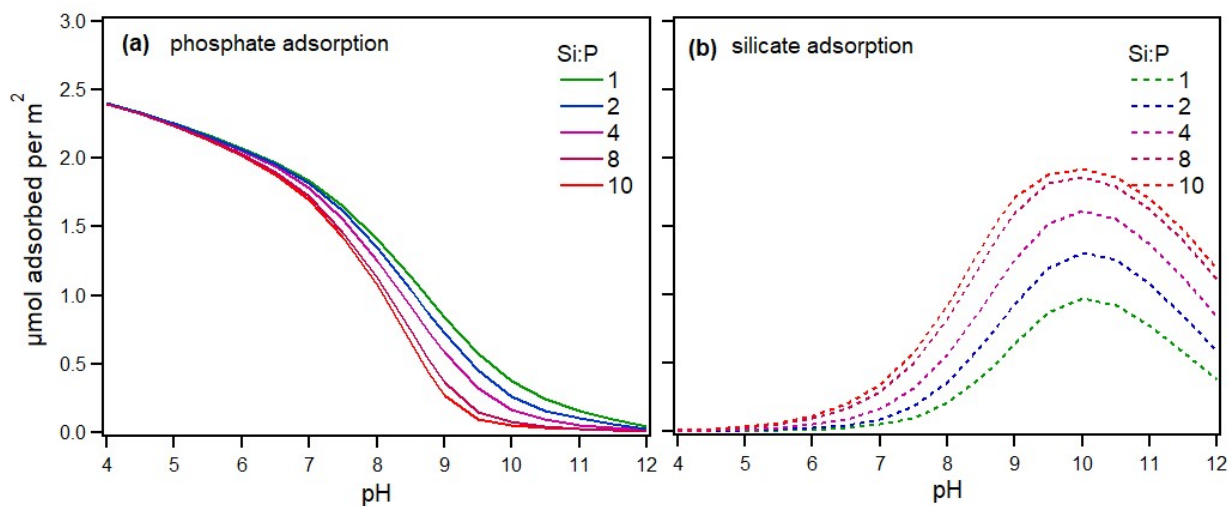


**Figure 2.6.** Simultaneous adsorption of (a) phosphate (50 µM) at various initial Si:P solution ratio, and (b) silicate on goethite (0.5 g/L) at 25°C and $I$=10 mM NaCl, as a function of pH. The adsorption of phosphate and silicate was calculated using the CD-MUSIC model with the parameters shown in Table 2.1.

The amount of sorbed silicate on goethite increases with increasing Si:P ratio in solution (Figure 2.6). Therefore, the decreased phosphate adsorption and increased silicate adsorption with increasing aqueous phase Si:P ratio illustrates their competition for the goethite binding sites. However, dissolved silicate, even at higher concentrations than phosphate, requires

favorable pH conditions to affect phosphate adsorption. In other words, though higher aqueous phase Si:P ratios decrease phosphate adsorption on goethite, solution pH plays a key regulatory role in determining the amount of phosphate that will sorb to goethite or remain in solution.

## 2.4.5 CD-MUSIC model: Effect of ionic strength

The solution ionic strength affects the formation of both inner- and outer-sphere surface complexes (Antelo et al., 2005; Goldberg, 2014; Hiemstra, 2018). The type of electrolyte in solution contributing to ionic strength is also important in the formation of surface complexes. The background electrolyte may compete with a sorbate for the surface binding sites, form strong aqueous complexes with the sorbate, and change the surface charge and electrical double layer thickness, and hence play an important role in the formation of surface complexes (Antelo et al., 2005; Goldberg, 2014; Hiemstra, 2018; Spiteri et al., 2008).

The CD-MUSIC model is applied to elucidate the effect of ionic strength (i.e., NaCl used herein) on the individual (P or Si) and simultaneous (P+Si) adsorption of phosphate and silicate. Results from the model show that higher concentrations of NaCl enhance the adsorption of phosphate (no Si) on goethite within the pH range of 4 and 12 (Figure 2.7a). For example, the amount of sorbed phosphate on goethite at pH 7 in the presence of 10 mM NaCl is 1.76 µmol/m$^2$, and 1.99 µmol/m$^2$ in the presence of 1 M NaCl. This effect of NaCl concentration is attributed to the increase of surface positive change via Na$^+$ adsorption, causing an increased electrostatic attraction between the goethite surface and aqueous phosphate, and hence increases phosphate adsorption.

The effect of NaCl concentration on increased phosphate adsorption increases as the pH in solution increases (i.e., from acidic to alkaline conditions). For example, phosphate adsorption (no Si) on goethite at pH 7 increases by 13% when the concentration of NaCl increases from 10 mM to 100 mM, and by 36% at pH 10. This pH dependent effect of background NaCl solution likely results due to higher Na$^+$ adsorption under alkaline conditions on the ferric (hydr)oxides (e.g., goethite) surface. The adsorbed Na$^+$ increases positive surface charge favoring the electrostatic attraction between the surface and the sorbate, phosphate. However, at pH below 3 (not shown in Figure 2.7), this effect of adsorbed Na$^+$ results in decreased phosphate adsorption. Under these strongly acidic conditions, the electrostatic

attraction between the fully protonated phosphoric acid ($H_3PO_4$), which exists at pH below 3, and the positively charged surface is not as favored as under the pH conditions above pH 3.
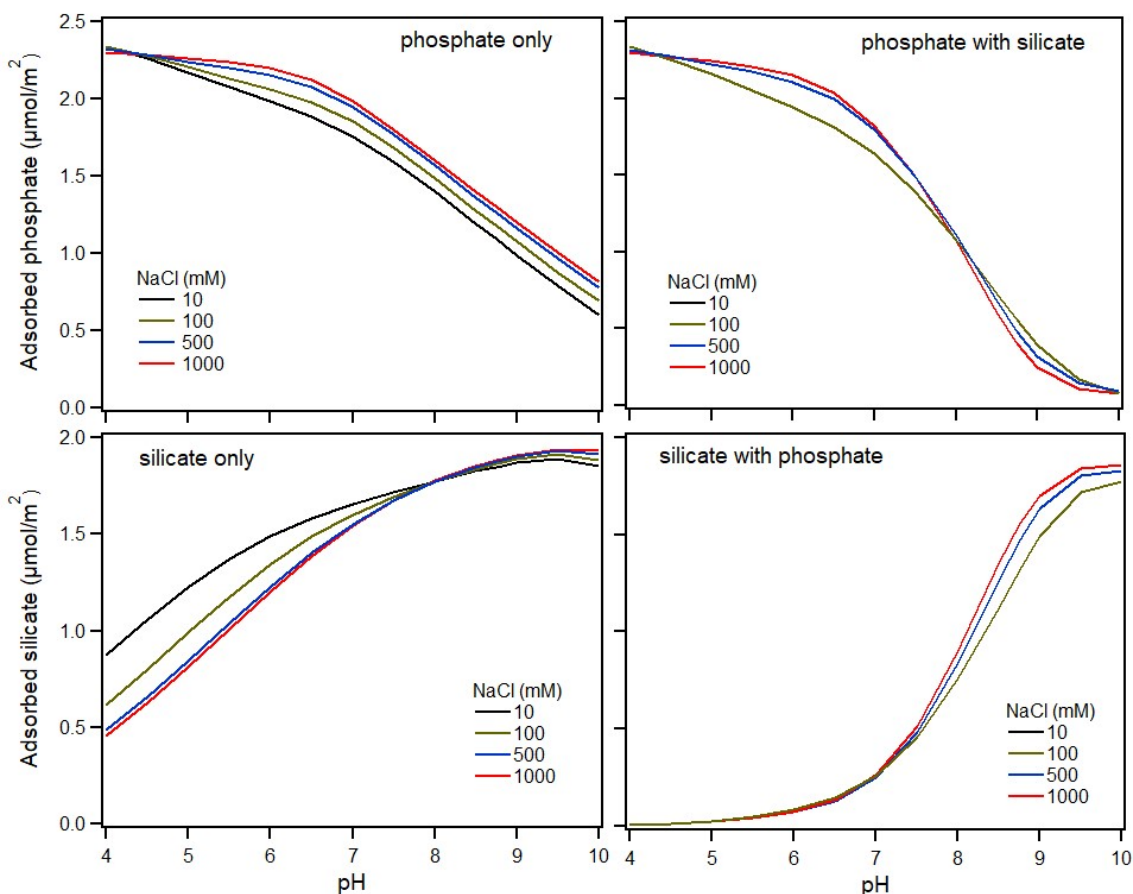


**Figure 2.7.** Adsorption of phosphate (25 µM) and silicate (250 µM) on goethite (0.25 g/L) at 25°C with varying NaCl concentrations (10 to 1000 µM). Phosphate and silicate adsorption were calculated using the CD-MUSIC model with the parameters presented in Table 2.1.

Ionic strength in solution also influences the adsorption of silicate and may increase or decrease silicate adsorption depending on the pH of the solution (Figure 2.7c). For example, higher concentrations of NaCl increase the adsorption of silicate under alkaline conditions, due to the neutralization of negative surface charge via $Na^+$ adsorption (Hiemstra, 2018), similar to the effect on phosphate adsorption. However, below pH ~8, higher concentrations of NaCl decrease the adsorption of silicate. This is because silicic acid under acidic conditions mostly exists in the fully protonated form (section 1.5.3.2, Figure 1.12b), where the adsorption of cations (e.g., $Na^+$) on goethite exerts an inhibitory effect on silicate adsorption (Hiemstra, 2018).

Under competitive conditions, the adsorption of silicate on goethite under acidic conditions is minor because of stronger adsorption of phosphate. Although higher concentration of NaCl decrease the individual adsorption of silicate (no P) at pH below 8 (Figure 2.7c), this effect of ionic strength on silicate adsorption in the presence of phosphate is not evident (Figure 2.7d). Therefore, the weak adsorption of silicate in the presence of phosphate does not display ionic strength dependency on phosphate adsorption under acidic conditions. However, the effect of higher NaCl concentrations on phosphate adsorption in the presence of silicate is evident under alkaline conditions. Under competitive conditions, the presence of aqueous silicate decreases the adsorption of phosphate on goethite under alkaline conditions (discussed in section 2.4.4, Figure 2.6a). This inhibitory effect of silicate on phosphate adsorption increases as the background concentration of NaCl in solution increase (Figure 2.7c).

## 2.4.6 Limitations of the implemented CD-MUSIC model

The effect of aqueous Si:P ratios on the adsorption of phosphate on goethite as a function of pH was investigated in simple solution-solid systems. For example, the phosphate and silicate adsorption experiments were conducted in a NaCl background solution. However, the chemical compositions of natural waters are generally much more complex, and typically contain a variety of inorganic anions (e.g., $HCO_3^-$, $SO_4^{2-}$) and cations (e.g., $Ca^{2+}$ and $Mg^{2+}$) as the major constituents. The concentrations of these dissolved anions (e.g., $HCO_3^-$ and $SO_4^{2-}$) in natural waters are also typically high relative to phosphate. These anions may decrease the adsorption of phosphate on ferric (hydr)oxides, but the effect could be minor (discussed in section 1.5.3.2) above neutral pH, where aqueous silicate affects the adsorption of phosphate. Therefore, the role of these anions (e.g., $HCO_3^-$ and $SO_4^{2-}$) in the silicate-mediated phosphate adsorption on ferric (hydr)oxides may be unimportant under alkaline conditions.

In contrast to the effect of anions, the presence of divalent cations (e.g., $Ca^{2+}$ and $Mg^{2+}$) are known to enhance phosphate adsorption on ferric (hydr)oxides via the formation of bridging complexes (e.g., $\equiv FeOCaHPO_4^-$, where " $\equiv$ " represents the mineral surface lattice) between adsorbed phosphate and the solid surface (Spiteri et al., 2008; Talebi et al., 2016). Further, $Ca^{2+}$ and $Mg^{2+}$ ions form strong aqueous complexes with phosphate in solution (Chughtai et al., 1968; Spiteri et al., 2008). The effect of aqueous complexation between

phosphate and $Ca^{2+}$ or $Mg^{2+}$ confines phosphate in solution, and thereby limits phosphate adsorption on the solid surface. Thus, the competition between these opposing roles played by $Ca^{2+}$ and $Mg^{2+}$ ions may determine the net adsorption of phosphate on ferric (hydr)oxides. The $Ca^{2+}$ and $Mg^{2+}$ ions can form aqueous complexes with silicate in solution, similar to phosphate (Santschi and Schindler, 1974). These cations may potentially also enhance the adsorption of silicate on ferric (hydr)oxides via the formation of bridging complexes with silicate. Therefore, accounting for these multiple processes in the surface complexation model may better describe the distribution of phosphate and silicate at the ferric (hydr)oxides-water interface.

## 2.5 Environmental significance

The potential influence of dissolved silicate on phosphate mobilization from goethite surfaces was assessed by comparing field level phosphate and silicate concentrations observed in various aquatic environments. The data were extracted from NWIS network (discussed in section 1.5.3.2.2). Based on the NWIS (2010-2016) data (shown in Table 1.3, Chapter 1), the average groundwater silicate concentration is higher (0.39±0.22 mM, N=2011) relative to stream (0.19±0.13 mM, N=11881) and standing water (0.15±0.12 mM, N=1527) (also discussed in the general introduction, Table 1.3). The higher concentration of silicate in groundwater generally occurs due to water-rock interactions (Davis, 1964) and decreases in standing water, due to its uptake by some primary producers (Maavara et al., 2015; Rocha et al., 2002; Struyf et al., 2009) as well as chemical precipitation and co-precipitation processes (Williams, 1985). The aqueous phase Si:P ratio is also higher in groundwater (Figure 2.5). The average phosphate concentrations are similar among groundwater ($3.11\times10^{-3}\pm8.85\times10^{-3}$ mM, N=2011), stream ($3.12\times10^{-3}\pm8.85\times10^{-3}$ mM, N=11881) and standing water ($3.16\times10^{-3}\pm8.5\times10^{-3}$ mM, N=1527). Therefore, based on the aqueous phase Si:P ratio, silicate would be expected to exert a tangible effect on phosphate mobilization in alkaline groundwater.
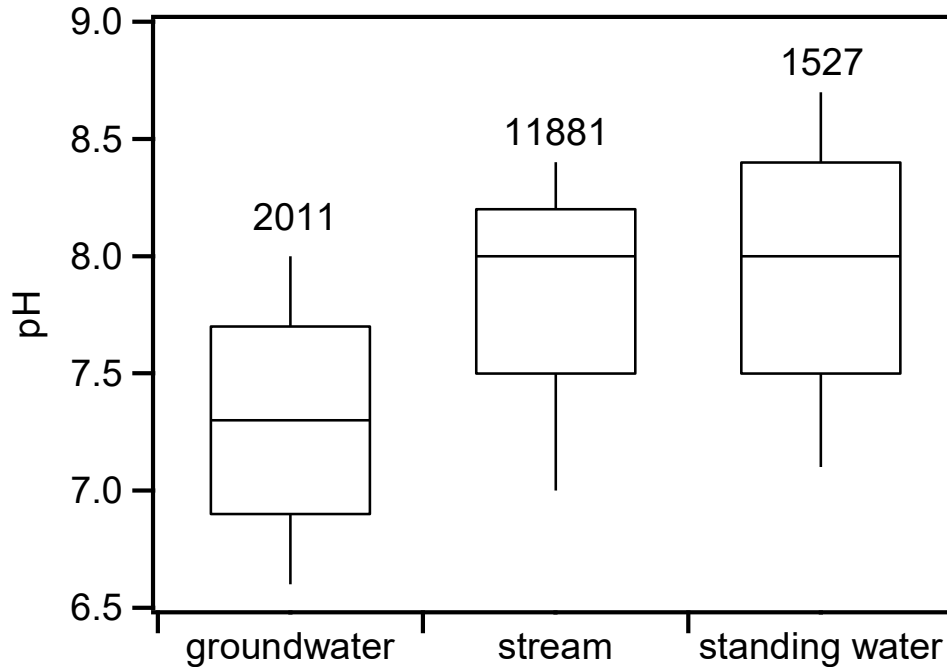
**Figure 2.8.** pH ranges in groundwater, streams, and standing waters bodies (lakes and reservoirs) according to the NWIS (2010-2016) database. The number on each box represents the number of data points, which are extracted from all water depths available in the database. The lower and upper boundary of each box represents 25th and 75th percentile, respectively, and the line within the box shows median value. The whiskers are drawn down to the 10th percentile and up to the 90th.

The aqueous phase pH is another important factor that largely controls the influence of silicate on the adsorption of phosphate on ferric (hydr)oxides. The NWIS data shows that the pH in groundwater is lower than the pH in stream and standing water (Figure 2.8). The average pH value in groundwater is 7.3±0.7 (N=2011) where the expected influence of dissolved silicate on the removal of aqueous phosphate via adsorption on ferric (hydr)oxides should be minor (see section 2.4.4). A similar effect of dissolved silicate can be expected for phosphate adsorption on other metal (hydr)oxides due to their comparable phosphate binding capacities with ferric (hydr)oxides (also discussed in general introduction, section 1.5.1.2). Furthermore, the relation between the concentration of phosphate and silicate in groundwater does not show any significant correlation ($r^2$ = <0.01, p value = 0.19) according to the NWIS data (Figure 2.9a). Therefore, even if, on average, the concentration of silicate and the aqueous phase Si:P ratio are much higher in groundwater, the influence of silicate on the mobilization of phosphate may be unimportant.
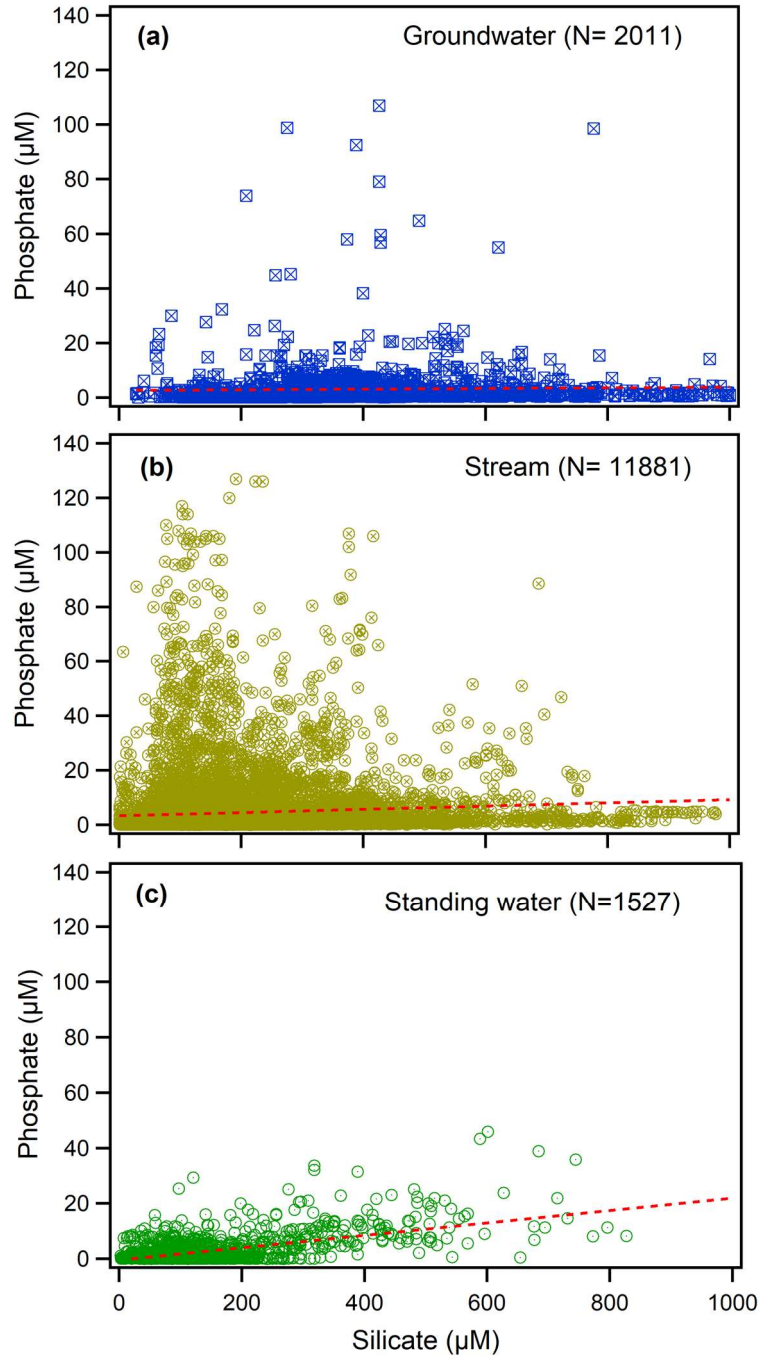
**Figure 2.9.** The relationship between phosphate and silicate concentrations in (a) groundwater, (b) stream water, and (c) in standing water bodies according to the NWIS data (2010-2016). [Note: The relationship between aqueous phosphate and silicate shown in Figure 2.9c for standing waters has already been presented in Figure 1.11 (section 1.5.3.2.2) and is repeated here for comparison with that of other water bodies]. The dashed lines represent the linear regression fits between the concentrations of phosphate and silicate, which are extracted from all water depths available in the database.

On average, stream water is slightly alkaline with a pH of 7.8±0.6 (N=11881) (Figure 2.8), and the Si:P ratio generally is high enough (Figure 2.5) to influence phosphate mobility based on the predictions by the CD-MUSIC model. However, the NWIS data do not show any strong relationship (Figure 2.9b) between aqueous phase phosphate and silicate ($r^2 = <0.01$, p value = <0.05), which may indicate that the effect of silicate on the mobilization of phosphate is of minor importance compared to other factors.

In standing water bodies, primarily lakes, impoundments and reservoirs, the concentrations of phosphate and silicate are positively correlated ($r^2 = 0.17$, p value = <0.05) (Figure 2.9c). In addition, the average pH in standing water bodies is alkaline (8.0±0.6, N=1530), which may arise from the combination of several factors. In some surface water systems which are buffered by carbonate minerals e.g., $CaCO_3$, the pH can be alkaline (Langmuir, 1997b). For example, the pH in some surface waters can be found above 8 where the water is in equilibrium with $CaCO_3$ and atmospheric $CO_2(g)$ (Langmuir, 1997b). Other important factors can increase pH in water such as (i) photosynthesis, which may increase pH up to about 9 when dissolved $CO_2$ and bicarbonate are used by plants and algae, and (ii) by biogeochemical reduction processes (Langmuir, 1997d; Verspagen et al., 2014). Further, the consumption of dissolved oxygen for the mineralization of biomass may increase pH in water, and by the reduction of nitrate, sulfate or ferric (hydr)oxides (Smolders et al., 2006). Therefore, higher aqueous phase Si:P ratio and the elevated pH levels in standing water bodies e.g., lakes and reservoirs may potentially decrease the adsorption of phosphate on metal (hydr)oxides in sediments. This effect of silicate may eventually promote the mobilization of phosphate in the aqueous phase, if surface sites are limited for the adsorption of phosphate and silicate.

## 2.6 Dissolution of goethite during phosphate and silicate adsorption

During the adsorption experiments, goethite dissolution was found to release small amounts of iron into solution (Figure 2.10). The dissolution of ferric (hydr)oxides is generally controlled by three basic mechanisms: reductive dissolution, proton promoted dissolution, and ligand promoted dissolution (Cornell and Schwertmann, 2003). The most common iron dissolution processes in soil/sediment are promoted by the biotic and abiotic reduction of ferric (hydr)oxides (Bonneville et al., 2004; Borch et al., 2010; Weber et al., 2006). The proton promoted dissolution of ferric (hydr)oxides can occur under acidic conditions below pH ~3

(Cornell and Schwertmann, 2003), which was also observed for goethite in this study (Figure 2.10).
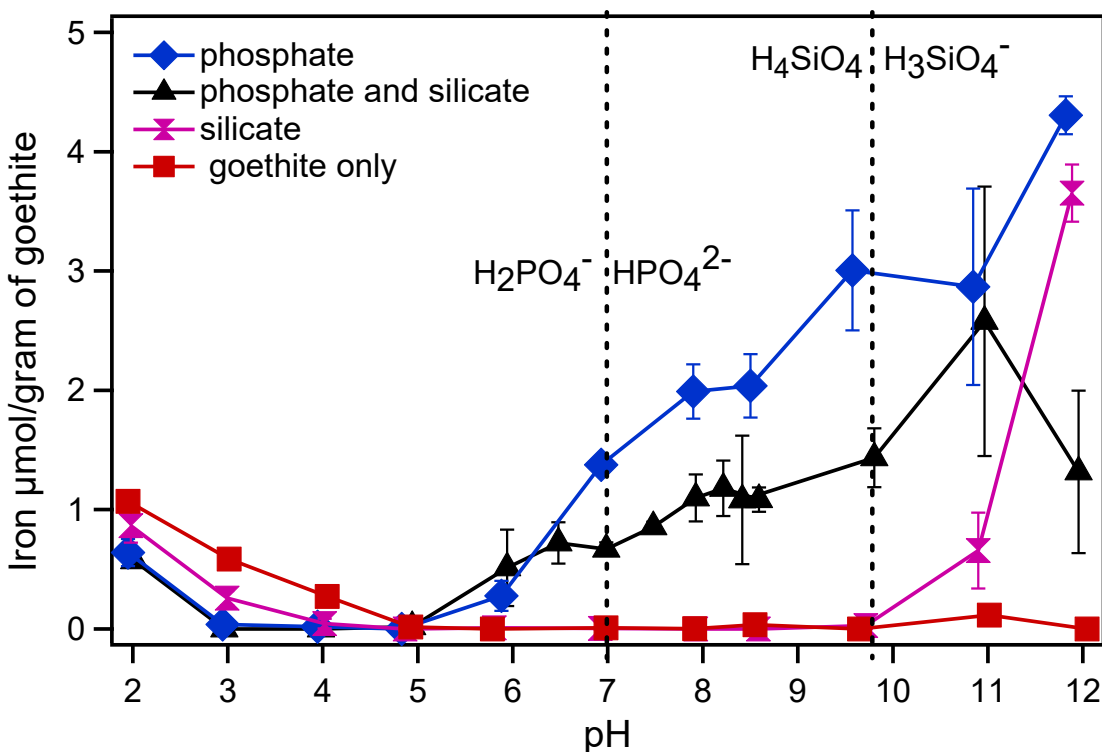


**Figure 2.10.** Dissolution of iron from goethite in the presence and absence of phosphate or/and silicate as a function of pH. The solutions of phosphate (50 µM) and silicate (50 µM) were equilibrated with goethite (0.5 g/L) at 25°C and $I$= 10 mM NaCl. In the control experiment, goethite was equilibrated for 6 hours in the absence of phosphate and silicate at 25°C and $I$=10 mM NaCl.

In this study, the proton promoted dissolution of iron from goethite was higher in the control system (with no phosphate and silicate) than in the presence of phosphate and silicate. This difference in the amount of dissolved iron indicates that the adsorption of phosphate and silicate may block the goethite surface sites, and hence restrict the release of iron. Furthermore, the equilibration of phosphate with goethite resulted in lower amounts of dissolved iron in solution relative to the silicate/goethite system. The formation of stronger surface complexes by phosphate (with goethite) relative to silicate under acidic conditions may potentially explain this difference in iron dissolution.

The presence of organic ligands and siderophores is known to cause the ligand promoted dissolution of iron from ferric (hydr)oxides (Cornell and Schwertmann, 2003; Kraemer, 2004;

Reichard et al., 2007). In this study, dissolution of goethite in the presence of phosphate was observed above pH 5 and increased with increasing solution pH (Figure 2.10). However, no iron was dissolved from goethite in the control solution (with no phosphate and silicate) above pH 5. This stability of goethite above pH 5 may indicate that 6 hours of equilibration time considered for the adsorption experiment was insufficient for the dissolution of iron. In phosphate/goethite systems, the concentrations of dissolved iron increased with increasing pH in the solutions (Figure 2.10). The adsorption of phosphate on goethite on the other hand decreases with increasing solution pH (Figure 2.3a and 2.6a).

The adsorption of phosphate on ferric (hydr)oxides generally takes place with concurrent desorption of adsorbed phosphate (Sabur and Al-Abadleh, 2015). Thus, net phosphate adsorption at a given pH is determined by the competition between the adsorption and desorption processes. Under alkaline conditions, the desorption of phosphate adsorbed becomes more important compared to acidic conditions. Therefore, it is likely that the desorption of phosphate (above pH 5) resulted in the dissolution of iron (attached to phosphate) from the goethite surface.

The presence of silicate (with no phosphate) had no effect on the dissolution of iron between pH 5 and 10, but enhanced iron dissolution above pH 10 (Figure 2.10). The pH adsorption envelope of silicate on goethite shows that the adsorption of silicate increases with increasing pH, with maximum adsorption at pH ~10 (Figure 2.3b and Figure 2.6b). Further increase in pH (above pH 10) results in a gradual decrease of silicate adsorption on goethite. Therefore, the silicate-mediated dissolution of iron above pH 10 may correspond to the concurrent adsorption-desorption process of silicate on/from goethite, similar to the phosphate/goethite system. Within the pH range of 5 to 10, no dissolution of iron in the silicate/goethite system (with no phosphate) may indicate that the adsorption of silicate occurs irreversibly (with little or no concurrent silicate desorption) on the goethite surface. Alternatively, dissolved silicate may undergo co-precipitation with aqueous iron and form a silicato-iron insoluble complex (e.g., $(Fe(OH)_3 \cdot SiO_2)$ below the pKa of $H_4SiO_4$ (pH 9.84) (Ewers, 1983; Gallup, 1989).

The dissolution of iron during the simultaneous adsorption of phosphate and silicate is moderate (Figure 2.10). For example, about 1.4 µmol iron was dissolved from each gram of goethite in the presence of phosphate (with no silicate) at pH 7, compared to 0.7 µmol Fe when

silicate co-existed with phosphate in solution. Note that no iron was dissolved from goethite in the control system (i.e., in the absence of phosphate and silicate) above pH 5. The pH envelopes for the competitive adsorption of phosphate and silicate on goethite show that the adsorption of phosphate gradually decreases (from pH 3) with increasing solution pH, while that of silicate increases up to pH 10. Under competitive adsorption conditions, increasing the initial aqueous phase Si:P ratios resulted in decreased phosphate adsorption under alkaline conditions (Figure 2.6a). The decreased adsorption of phosphate on goethite in the presence of silicate is also likely to decrease phosphate desorption, which occurs concurrently with the adsorption process. Therefore, the decreased phosphate desorption concurrent phosphate adsorption/desorption in the presence of silicate could have resulted in the decreased dissolution of iron from goethite. In addition, the presence of aqueous silicate in the phosphate/goethite system may decrease the solubility of dissolved iron (released via the ligand promoted mechanism by phosphate) via the formation of insoluble Fe-Si co-precipitates.

In sediments, if phosphate is associated with the surface of ferric (hydr)oxides, desorption of phosphate to the aqueous phase may result in the dissolution of host oxide minerals by the ligand promoted mechanism. However, if silicate co-exists with phosphate, silicate may indirectly decrease the dissolution of iron by decreasing the interactions between the aqueous phosphate and the solid goethite or by decreasing the solubility of dissolved iron via the formation of Fe-Si co-precipitates. Therefore, although dissolved silicate increases the mobility of phosphate in water by decreasing phosphate adsorption on ferric (hydr)oxides (see sections 2.4.2 and 2.4.4), it may slightly decrease the availability of dissolved iron in water under oxic conditions.

## 2.7 Conclusions

This study investigated the effect of aqueous phase Si:P ratio on the adsorption of phosphate on goethite through batch experiments and use of the CD-MUSIC model. The batch experiments were conducted to a) quantify the rate of phosphate and silicate adsorption on goethite at a pH of 7, and b) determine equilibrium adsorption envelopes for phosphate and silicate on goethite over a wide pH range, both as independent and competitive sorbates. The results of the kinetic study at pH 7 show that the rate of phosphate adsorption is largely

independent of aqueous silicate whereas that of silicate is strongly suppressed by aqueous phosphate. Results from pH adsorption envelope experiments together with the predictions from the CD-MUSIC model suggest that the effect of silicate on the adsorption of phosphate is highly pH dependent. It is very minor below neutral pH even at a high initial aqueous phase molar Si:P ratio (i.e., 10). However, under alkaline conditions, dissolved silicate exhibits an inhibitory effect on phosphate adsorption on ferric (hydr)oxides and this effect increases with increasing electrolyte concentration. The effect of aqueous phase Si:P ratio on the mobility of phosphate at the ferric (hydr)oxides-water interface is summarized in the following conceptual diagram (Figure 2.11).
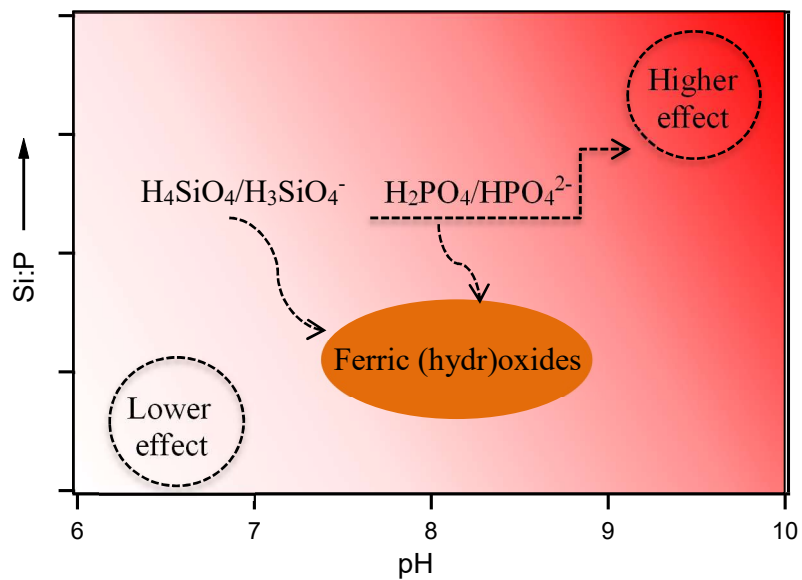


**Figure 2.11.** Conceptual diagram showing the effect of aqueous phase Si:P ratio on the mobilization of phosphate to water when both silicate and phosphate from aqueous solution interact with ferric (hydr)oxide surfaces. The mobility of phosphate increases from lighter to deeper color where the lower and higher effect of aqueous phase Si:P ratio are shown in dashed circles.

The water quality data extracted from the NWIS network together with experimental results and the CD-MUSIC model suggest that aqueous silicate can enhance the mobility of phosphate in high silicate standing water bodies (e.g., lakes) under alkaline conditions.

# Chapter 3

# Effect of silicate on phosphate adsorption and desorption under dynamic pH conditions

## 3.1 Summary

This study investigates the potential role of dissolved silicate in the interactions between phosphate and goethite under dynamic pH conditions. Desorption and adsorption experiments for phosphate were conducted in the absence and presence of silicate. Desorption of phosphate sorbed to goethite at pH 3 was induced by increasing the pH from 3 to 11, followed by the re-adsorption of phosphate by decreasing the pH from 11 to 3. Results show that increasing the pH in the phosphate/goethite system caused phosphate desorption, as expected. However, the amount of phosphate desorbed from goethite was lower than that estimated by a CD-MUSIC model previously calibrated based on phosphate adsorption data on goethite. Therefore, the fraction of sorbed phosphate that could not be desorbed by increasing the pH could correspond to phosphate immobilized on goethite via surface precipitation or via the formation of stronger bi-dentate surface complexes than represented in the CD-MUSIC model. In addition, the magnitude of this un-desorbed fraction was not affected by silicate, even under strong alkaline conditions where maximum silicate adsorption occurs. The silicate sorbed to goethite under alkaline conditions, however, reduced the amount of phosphate that could be re-adsorbed when the pH was brought down from 11 to 3. Thus, exposure to aqueous silicate reduces the number of adsorption sites on goethite that are accessible to phosphate.

## 3.2 Introduction

The effect of dissolved silicate on the adsorption of phosphate to ferric (hydr)oxides has been addressed in Chapter 2 where aqueous silicate at higher concentrations decreased phosphate adsorption under alkaline conditions. The work in Chapter 2 was conducted under static pH conditions and with pristine goethite. However, natural ferric (hydr)oxides surfaces generally carry various sorbates, including phosphate, which may undergo diffusion, precipitation, co-precipitation depending on the environmental conditions (e.g., pH). Initially adsorbed weaker phosphate surface complexes e.g., outer-sphere or mono-dentate complexes may convert into more stable forms, e.g., bi-dentate complexes (Zhong et al., 2007). The importance of such

time-dependent aging processes in controlling the mobility of phosphate, under dynamic pH variations, has not been addressed in the existing literature.

This study examines the effect of dissolved silicate in the desorption of phosphate caused by raising the pH of the aqueous medium from pH of 3 to 11 in a phosphate/goethite system, in the absence and presence of silicate. After reaching pH 11, the adsorption of phosphate was initiated in the same system by decreasing the pH stepwise from 11 to 3. The entire experiment is named a "time-series desorption and adsorption experiment". The experimental results better isolate the potential multiple roles dissolved silicate can play in controlling the interactions between phosphate and ferric (hydr)oxides via adsorption and desorption processes under dynamic pH conditions.

## 3.3 Experiments

### 3.3.1 Desorption kinetics

Goethite (0.5 g/L) (Bayferrox 910 MU) was equilibrated in 1995 mL of 10 mM NaCl solution, in a Teflon vessel, on a magnetic stir plate for 24 hours to maintain a homogeneous suspension at 22°C. The goethite suspension was degassed thoroughly by purging with nitrogen gas (99.998% pure) to remove residual carbon dioxide. The purging of nitrogen gas was continued throughout the experiment. Then 5 mL of 10 mM phosphate solution (prepared in 10 mM NaCl) was added to the goethite suspension. The expected phosphate concentration in the resulting solution was approximately 25 μM, assuming no adsorption. The goethite suspension with phosphate was equilibrated for 24 hours and then the pH was adjusted to 3 by the gradual addition of HCl. After further equilibration at pH 3 for 24 hours, an 11 mL sample from the goethite/phosphate suspension was collected. The pH in the goethite/phosphate suspension was then raised to 8 through the gradual addition of NaOH. The time taken to increase the pH from 3 to 8 was about an hour. Once a pH of 8 was achieved, the suspensions samples (11 mL each time) were collected as a function of time from 10 min to 24 hours. The pH was then raised from 8 to 9 and from 9 to 10 and desorption kinetic studies were conducted at each pH with a similar procedure as for pH 8. The time taken for altering the pH to 9 and 10 was about 10 min in each case. A total of 363 mL (11 mL×3pH's×11 time points) sample was removed for aqueous analysis throughout the entirety of the experiment, or roughly 18% of the initial solution volume. In every case, samples were centrifuged at 1690 RCF for 15 min (Thermo

Scientific, Sorvall ST 16R) and the supernatant was filtered using 0.45 µm pore size polypropylene (VWR Scientific Inc.) syringe filters, acidified to < pH 2 with ultra-pure nitric acid (EMD Millipore Corporation), and stored at 4°C until analysis by inductively coupled plasma atomic emission spectroscopy (ICP-OES). Unless otherwise mentioned, adjustments were done using a Metrohm 907 auto-titrator equipped with a Metrohm built pH glass electrode and 5 mL dosing unit (Dosino 800) with 10,000 pulse resolution.

### 3.3.2 Time-series desorption and adsorption experiment

The goethite suspension was prepared by equilibrating goethite (0.5 g/L) in 1197 mL of 10 mM NaCl solution for 24 hours in an Applikon bioreactor (1.2 L). Then 3 mL of 10 mM phosphate solution was injected into the system creating phosphate concentration of 25 µM. The goethite suspension with phosphate was equilibrated for 24 hours and the pH was lowered to 3 by the addition of HCl and further equilibrated for 6 hours. At that stage, an 11 mL sample was collected and the pH in the system was increased stepwise by one pH unit increments, using NaOH, to pH 11 to measure the release of phosphate from goethite. Next, the pH was decreased again stepwise from 11 to 3, using HCl, and the re-adsorption of the released phosphate back to goethite was monitored.

To investigate the effect of silicate on phosphate desorption, goethite was pre-equilibrated with phosphate at a pH of 3 as previously and a 11 mL sample was collected after 6 hours equilibration. Then 4.30 mL of 100 mM silicate was injected resulting in a total silicate concentration of 355 µM. Addition of silicate caused a pH increase to nearly 3.5 which was re-adjusted to 3 and equilibrated for 6 hours. The stepwise increase of pH from 3 to 11, the stepwise lowering back to pH 3, and the collection of samples were performed as per previous experiments. Throughout the experiment, the reaction medium (goethite suspension with and without phosphate and silicate) was degassed with nitrogen gas (99.998% pure) to remove residual carbon dioxide, as stated in section 3.3.1. The samples collected at each time were centrifuged, filtered and stored at 4ºC for ICP-OES as described in above.

### 3.3.3 Aqueous analyses

To avoid the interference from silicate in phosphate determination by colorimetry (Hartikainen et al., 1996), inductively coupled plasma atomic emission spectroscopy (ICP-OES) was used.

Total aqueous concentrations of iron, phosphate and silicate were measured (as elements; Fe, P and Si) by ICP-OES (Thermo Scientific iCAP 6300) after acidification with ultra-pure $HNO_3$ (EMD Millipore Corporation) to $<$ pH 2. ICP-OES has a precision of $<5\%$ RSD and an accuracy of $\pm 10\%$ with respect to NIST validated solutions for all analytes. Three wavelengths per analyte were selected and evaluated to ensure minimal interference from solution components. The method detection limit for Fe, P and Si were 0.89, 1.61, 1.78 µM, respectively. Matrix-matched standards were used for calibrations and all reagents were prepared with analytical grade salts from isoSPEC and 18.2 MΩcm-1 water (Millipore).

## 3.4 Results and discussion

### 3.4.1 Desorption kinetics

Kinetic data for the desorption of phosphate sorbed to goethite at pH 8, 9 and 10 are shown in Figure 3.1. Kinetic parameters were not extracted because of the very rapid desorption of phosphate during each pH transition. For example, goethite surface coverage by phosphate was decreased by 0.12 µmol/m$^2$ while the pH changed from 8 to 9, which corresponds to 50% of the total amount of phosphate desorbed at pH 9 plus the amounts desorbed during this pH transition. The results in Figure 3.1 were used to estimate the equilibration time for phosphate desorption in the time series desorption and adsorption studies. The kinetic data indicate that roughly 4 to 6 hours were required for the complete desorption of phosphate at each pH. Therefore, 6 hours equilibration time was selected for the time series desorption and adsorption experiments.
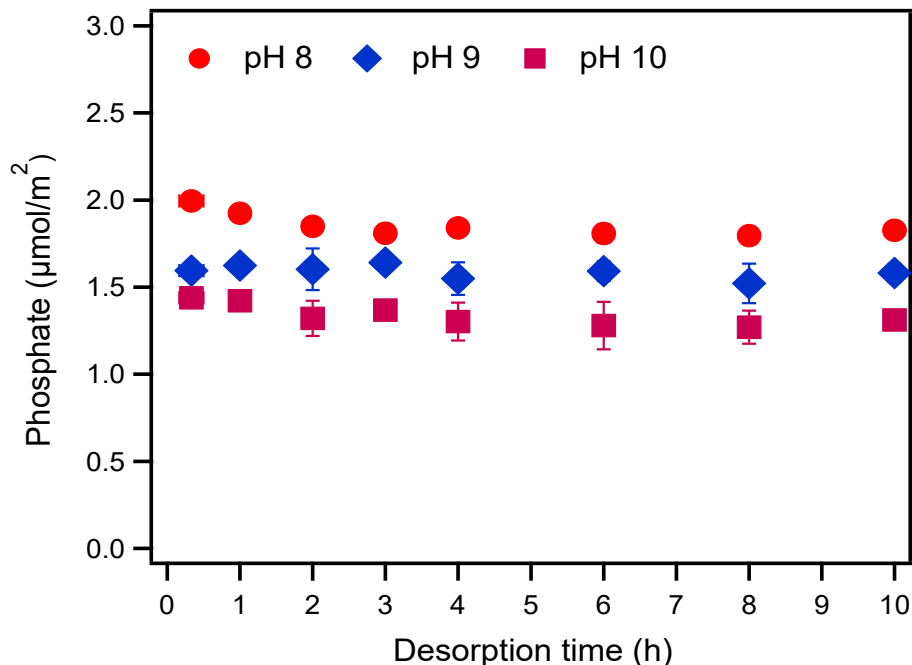
**Figure 3.1.** Kinetic data for the desorption of sorbed phosphate from goethite. Goethite (0.5 g/L) was previously exposed to phosphate (25 µM) at pH 3 and desorption of phosphate was conducted at pH 8, 9, and 10, respectively, at 22°C and $I$=10 mM NaCl. Error bars represent the range of values measured between duplicate experiments.

### 3.4.2 Time series desorption and adsorption experiment

### 3.4.2.1 Desorption of phosphate: effects of pH and silicate

Desorption of phosphate from goethite was calculated with respect to the amount sorbed at pH 3. The goethite in equilibrium with phosphate (25 µM) at pH 3, sorbed 61% of the initial solution phosphate. The stepwise increase of the pH from 3 to 11 resulted in the gradual release of sorbed phosphate. This phosphate release was expected based on the pH adsorption envelopes of phosphate on goethite, where the adsorption decreases with increasing pH (Chapter 2, sections 2.4.2 and 2.4.4). The amounts of desorbed phosphate at a given pH were compared with those estimated theoretically by the CD-MUSIC model. The model was previously calibrated with phosphate adsorption data in the absence and presence of silicate (Chapter 2). The results show that the percentages of desorbed phosphate measured experimentally in this study were lower than the amounts calculated by the model, and that this deviation increased during the transition from acidic to alkaline conditions (Figure 3.2). For example, 21% of the initially sorbed phosphate (at pH 3) was desorbed at pH 7 in the absence

of silicate while the model predicts 42% desorption, a 21% difference (Figure 3.2). This difference increased to 30% at pH 8. However, under strong alkaline conditions, e.g., above pH 8, the fractions of un-desorbed phosphate remained fairly constant (Figure 3.2), at about 0.5 $\mu mol/m^2$ (See supplementary material, Figure SM-3.1), similar to the amounts of phosphate sorbed with slow kinetics at pH 7 (Chapter 2, Table 2.2). Thus, the remaining un-desorbed phosphate with respect to the model prediction potentially indicates that a certain amount of phosphate sorbed at pH 3 remains strongly bound to the goethite surface.
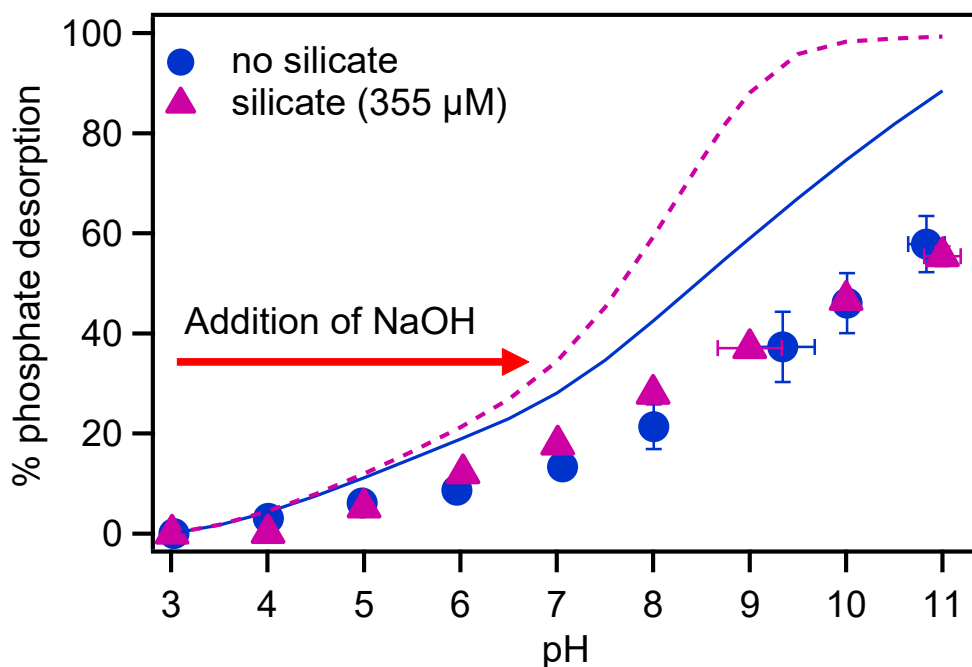


**Figure 3.2.** Percentage of phosphate desorption from goethite as a function of pH, in the absence (filled circles) and presence of 355 $\mu$M silicate (filled triangles), with respect to the amount sorbed at pH 3. The phosphate (25 $\mu$M) solution prepared in 10 mM NaCl was equilibrated with goethite (0.5 g/L) at pH 3 and at 22°C, which resulted in about 62% adsorption (~2.11 $\mu mol/m^2$) of the initial phosphate. The solid blue and dashed pink lines represent the amounts of phosphate desorption in the absence and presence of silicate, respectively, estimated by the CD-MUSIC model under the experimental conditions stated above. Error bars represent the range of values measured between duplicate experiments.

The irreversible immobilization of phosphate on goethite may occur through multiple possible mechanisms. For example, sorbed phosphate in long-term contact with goethite may undergo surface precipitation or form strong bridging complexes with iron dissolved from goethite (Ler and Stanforth, 2003), limiting its release back into solution. The transformation

of relatively weaker outer-sphere and/or mono-dentate phosphate-goethite surface complexes to the more stable bi-dentate form has also been suggested to take place with increasing solution pH (Zhong et al., 2007). Further, the detachment of bi-dentate phosphate complexes is thermodynamically less favorable compared to their formation on ferric (hydr)oxide surfaces (Farrell and Chaudhary, 2013), because a bi-dentate complex requires the cleavage of an $O_3PO$-Fe bond in the first step to form a mono-dentate complex before leaving the surface (Farrell and Chaudhary, 2013). The gradual diffusion of dissolved or sorbed phosphate into the lattice structure of the mineral is also possible (Fuller et al., 1993; Luengo et al., 2007), although this mechanism has been suggested to be unimportant for the phosphate/goethite system (Hongshao and Stanforth, 2001). Therefore, phosphate immobilization on goethite surface during the transition of pH from acidic to alkaline conditions could have resulted due to surface precipitation or the formation of strong bi-dentate surface complexes.

No effect of silicate on the desorption of sorbed phosphate from goethite was observed during the pH increase from 3 to 11 (Figure 3.2). Note that, the total concentration of silicate was ~15 times higher than that of phosphate. An effect of silicate on the desorption of phosphate could be expected from their competitive interactions with goethite, especially near the first $pK_a$ of $H_4SiO_4$ (pH 9.84) where maximum adsorption of silicate on goethite takes place (Chapter 2, sections 2.4.2 and 2.44). The adsorption of silicate, on the other hand, increased with increasing pH as shown by the decrease of silicate concentrations in solution (Figure 3.3). The lack of a silicate effect on phosphate desorption may indicate (i) either the desorption of phosphate is not likely by silicate, or (ii) the immobilization of phosphate occurred on goethite surface via surface precipitation or both.
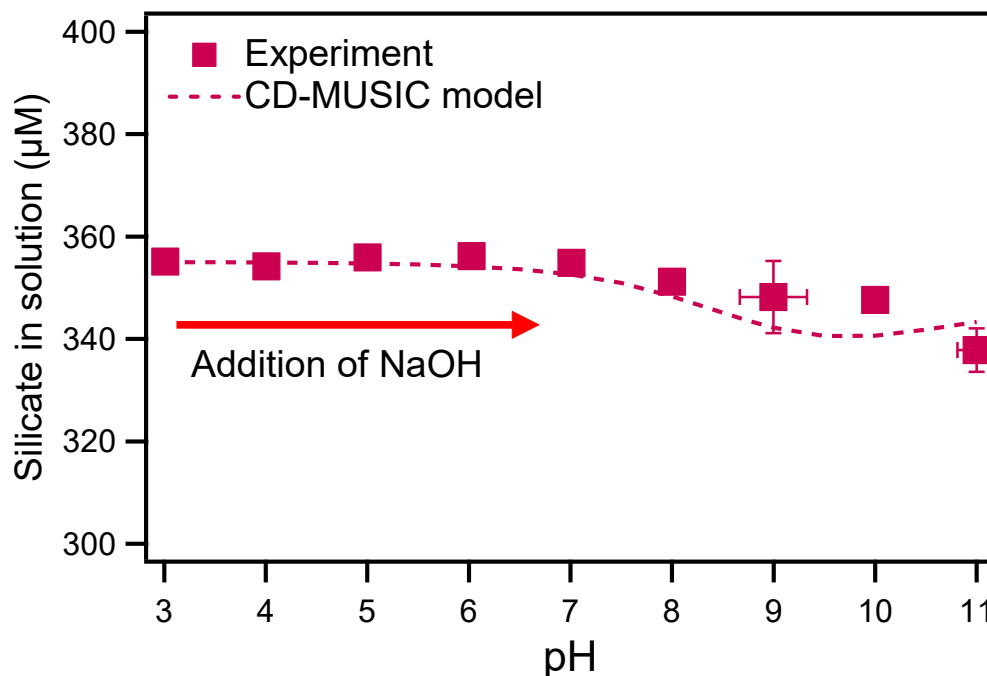
**Figure 3.3.** Concentrations of silicate (symbols) as a function of pH which was added into the system after equilibrating phosphate (25 µM) solution with goethite (0.5 g/L) at pH 3 and 22°C and $I$=10 mM NaCl. The dashed line represents the concentrations of aqueous silicate, estimated by the CD-MUSIC model under the experimental conditions stated above. Error bars represent the range of values measured between duplicates.

### 3.4.2.2 Adsorption of phosphate: effects of pH and silicate

The time-series re-adsorption experiments (pH 11 to 3) were conducted immediately after the desorption (pH 3 to 11) phase in the same system. During the stepwise transition of pH, adsorption of desorbed phosphate took place on goethite (Figure 3.4) which resulted in a near linear phosphate adsorption envelope between pH 10 and 3. In contrast, the phosphate adsorption envelope measured under static pH conditions presented in Chapter 2 (Figure 2.3a and Figure 2.6a) shows a different non-linear pH trend. The non-linear phosphate adsorption envelope under static pH conditions (Chapter 2, Figure 2.3a and 2.6a), with a distinctive change in the adsorption gradient around near neutral pH, can be explained by the change in the pronation state of $H_3PO_4$ around pH 7 (shown in Figure 1.12a, Chapter 1). In this study, the near linear pattern of phosphate adsorption envelope, instead of levelling off during the pH transition from alkaline to acidic conditions may imply that the goethite surfaces may have undergone significant changes during the imposed pH changes (3 to 11 followed by 11 to 3),

compared to the initial (pristine) surfaces. For example, dissolution of iron from goethite (see section 2.6, Chapter 1) and the possible reprecipitation of dissolved iron, could have altered the chemical structure of the goethite surfaces.
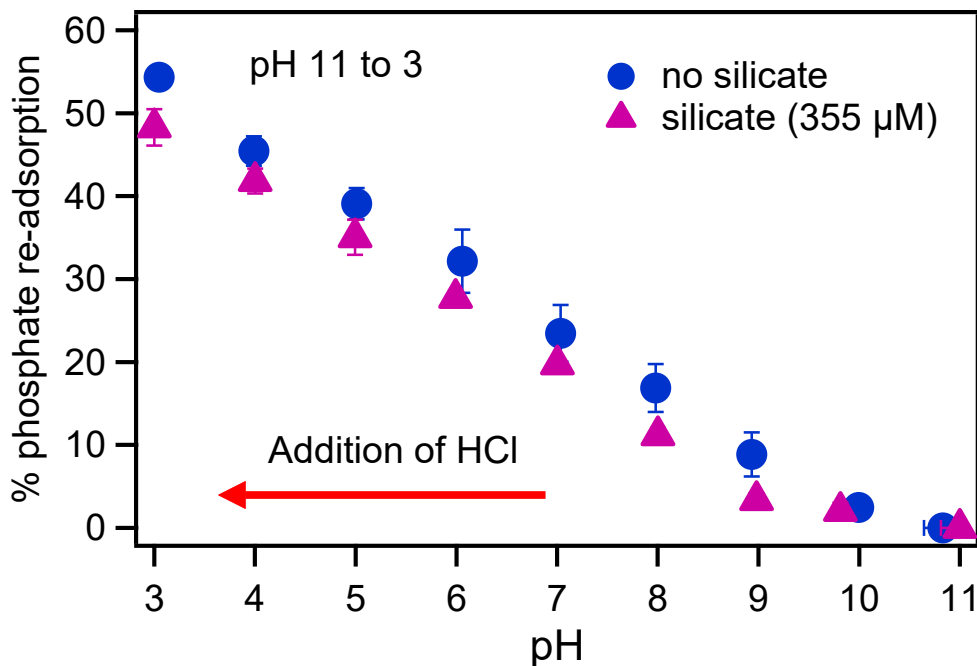


**Figure 3.4.** The percentage of adsorbed phosphate in the absence (filled circles) and presence (filled triangles) of silicate during the stepwise decrease of pH from 11 to 3 by the addition of HCl. The percentage of sorbed phosphate was calculated relative to the aqueous phosphate remaining in solution in equilibrium with goethite (0.5 g/L) at pH 11. Error bars represent the range of values measured between duplicates.

Adsorption of phosphate decreased in the presence of silicate, as compared to the system that contained no silicate (Figure 3.4). The decreased adsorption of phosphate in the presence of silicate was small (up to about 5%), but noticeable. In addition, no release of sorbed silicate was observed during the decrease of pH from 11 to 3, though expected from the adsorption pH envelopes of silicate on goethite by the CD-MUSIC model (Figure 3.5). The surface species formed by silicate on ferric (hydr)oxides can be monomeric, oligomeric or polymeric (Christl et al., 2012; Hiemstra et al., 2007; Swedlund and Webster, 1999). The monomeric or oligomeric surface complexes also form polymer complexes when in contact with ferric (hydr)oxides surface for an extended time (Christl et al., 2012). Thus, polymerization of silicate on the goethite surface and other mechanisms (e.g., co-precipitation) may protect the silicate

from desorbing during the transition of pH from alkaline to acidic conditions (Figure 3.5). The sorbed-silicate may further block surface sites on goethite (Wu et al., 2009), and hence explain the slight decrease in phosphate adsorption over a wide pH range (Figure 3.4).
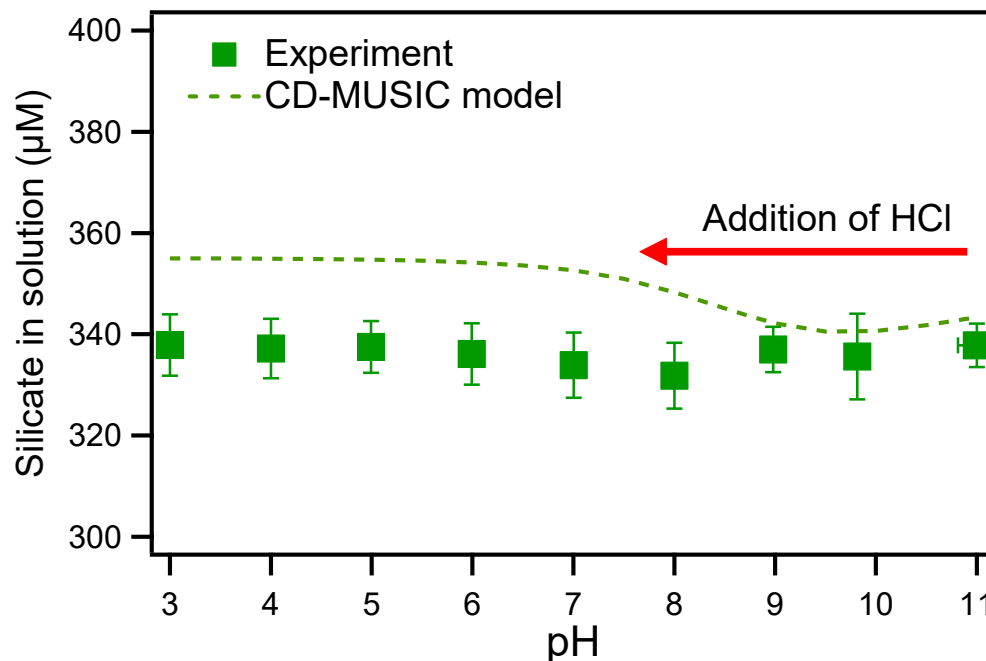


**Figure 3.5.** Concentration of silicate (filled squares) as a function of pH during the stepwise decrease of pH from 11 to 3 by the addition of HCl. The experimental conditions are stated in section 3.3.2. The dashed line represents the concentrations of aqueous silicate, estimated by the CD-MUSIC model under the similar experimental conditions. Error bars represent the range of values measured between duplicates.

## 3.5 Conclusions

This study investigates the effect of silicate in the desorption/adsorption of phosphate from/on goethite under dynamic pH conditions. Experimental results show that the stepwise transition of pH from acidic to alkaline conditions resulted in increased phosphate concentration in the aqueous phase, indicating that phosphate sorbed to goethite was released to solution. However, the amount of phosphate desorbed at a given pH was lower than the amount estimated by the CD-MUSIC model. This difference in the amount of desorbed phosphate at a given pH suggests that the sorbed phosphate could partially be irreversibly bound to the goethite surface. This immobilization of phosphate possibly occurs via the (co-)precipitation of phosphate on goethite, via the formation of strong bi-dentate surface complexes. This irreversibly bound

phosphate does not desorb, even in the presence of silicate under strong alkaline conditions. However, silicate presence on the surface of goethite and in solution decreased phosphate adsorption over a wide pH range (pH 11 to 3). This effect of silicate on phosphate adsorption is consistent with the results from their competitive adsorption on goethite presented in Chapter 2. In summary, silicate shows no influence on phosphate desorption; however, it limits phosphate adsorption by competitively interacting with the goethite surface. Hence, the presence of aqueous silicate may exert an important control over one of the key mechanisms determining phosphate mobility in sediments by limiting the adsorption of phosphate on metal oxide minerals.

# Chapter 4

## Iron-phosphate-silicate co-precipitates: Phosphate mobilization during reductive dissolution

### 4.1 Summary

Here, we investigate the dependence of the reductive dissolution of Fe-P-Si co-precipitates on the Si:Fe ratio and the associated mobilization of phosphate to solution. Ferric iron precipitates were synthesized in the presence of phosphate at various aqueous Si:Fe ratios via (i) the oxidation of $Fe^{2+}$, and (ii) direct precipitation of $Fe^{3+}$ by pH increase. Ferric precipitates were also prepared following both synthetic approaches in the absence of phosphate and silicate. The synthesized ferric precipitates and Fe-P-Si co-precipitates were characterized by a combination of chemical and spectroscopic techniques including ATR-FTIR and XRD. The chemical analyses of the co-precipitates show that higher initial aqueous Si:Fe ratios during co-precipitation resulted in higher solid phase Si:Fe ratios. However, variable aqueous Si:Fe ratios during synthesis did not influence the final P:Fe ratios in the solid phase. ATR-FTIR and XRD analyses indicated the absence of amorphous silica in any of the synthesized solids, suggesting the predominance of co-precipitation of iron, phosphate and silicate. Synthesized ferric (co-)precipitates were subsequently dissolved in buffered ascorbate-citrate solution at pH 7.5. The results show that the co-precipitates obtained from $Fe^{2+}$ oxidation were more reactive than those obtained via the pH increase method. However, regardless of synthesis method, slower iron and phosphate dissolution kinetics were obtained for solids with higher solid phase Si:Fe ratios. Furthermore, the reactivity of pure ferric precipitates was much lower than those of the co-precipitates, irrespective of synthesis method. The reductive dissolution of co-precipitates synthesized by $Fe^{2+}$ oxidation was also conducted in the presence of a facultative anaerobic iron reducing bacteria, *Shewanella putrefaciens*, but these experiments did not provide any clear trend in the reactivity of the co-precipitates. However, XRD analyses of residual co-precipitates subsequent to microbial reduction suggest that solids with a high Si:Fe ratio were more resistant to dissimilatory reduction, which agrees with the dissolution kinetics determined via abiotic ascorbate-citrate extraction.

## 4.2 Introduction

The potential effects of silicate on the mobility of phosphate through adsorption and desorption processes have been addressed in the previous chapters (Chapter 2 and Chapter 3). Experimental results have shown that silicate can decrease phosphate adsorption on goethite at alkaline pH (Chapter 2). However, dissolved silicate has no measurable effect on the desorption of phosphate already sorbed to goethite (Chapter 3). In aquatic environments, dissolved phosphate and silicate may undergo co-precipitation with iron and the resulting co-precipitates may also undergo dissolution during the redox cycling of iron. The removal of phosphate by co-precipitation with iron in the presence of dissolved silicate has also been suggested to affect the mobilization of phosphate in sediments (Mayer and Jarrell, 2000; Senn et al., 2015). However, the existing literature lacks clear characterization of the stability of ferric iron, phosphate, and silicate co-precipitates under dynamic bottom water redox regimes.

A limited number of published studies show that Fe-Si co-precipitates with variable Si:Fe ratios exhibit different physical and chemical properties (Cismasu et al., 2014; Karim, 1984; Saleh and Jones, 1984). For example, the specific surface area of Fe-Si co-precipitates has been shown to increase (Karim, 1984) or decrease (Zeng, 2003) with increasing solid phase silicate concentration. Further, silica-ferrihydrite ($Fe(OH)_3 \cdot SiO_2$) co-precipitates with Si:Fe ratios of 0.01 to 0.16 synthesized by oxidative $Fe^{2+}$ precipitation exhibit differing and complex reactivity in oxalic acid (Karim, 1984; Saleh and Jones, 1984). For example, the reactivity of $Fe(OH)_3 \cdot SiO_2$ has been shown to increase (Si:Fe 0 to 0.01), then decrease (Si:Fe 0.01 to 0.02), and increase again (Si:Fe 0.02 to 0.14) with increasing silicate concentration (Saleh and Jones, 1984). The rather unexpected decrease to reactivity at a solid phase Si:Fe ratio of (~0.02) was explained by the possible formation of a more ordered $Fe(OH)_3 \cdot SiO_2$ phase (Karim, 1984; Saleh and Jones, 1984).

One recent study has shown that iron in co-precipitates with high silicate concentrations could be incorporated inside polymeric silica, based on solid phase characterization by X-ray scattering and absorption spectroscopic techniques (Cismasu et al., 2014). The authors propose that iron structurally bound to polymeric silica could be less bioavailable as electron acceptor for microbial metabolism, and thus the release of iron from such solid co-precipitates to water would be limited. However, the role that co-precipitated silicate plays in the stabilization of ferric iron, that is, by inhibiting the reductive dissolution of Fe(III)-silicate co-precipitates, still

lacks experimental evidence. The Si:Fe ratio in Fe-Si co-precipitates may potentially be an important indicator of the reactivity of the co-precipitates in the reductive release of iron to water. However, phosphate is also likely to co-exist with silicate in ferric co-precipitates that form in natural environments. The chemical affinity of phosphate and silicate towards iron are different during co-precipitation (Kaegi et al., 2010; Voegelin et al., 2010), which may result in different reactivity of iron in Fe-P-Si and Fe-Si co-precipitates. Therefore, the effect of Si:Fe ratio on the reactivity of solid Fe-P-Si towards reductive dissolution requires further study.
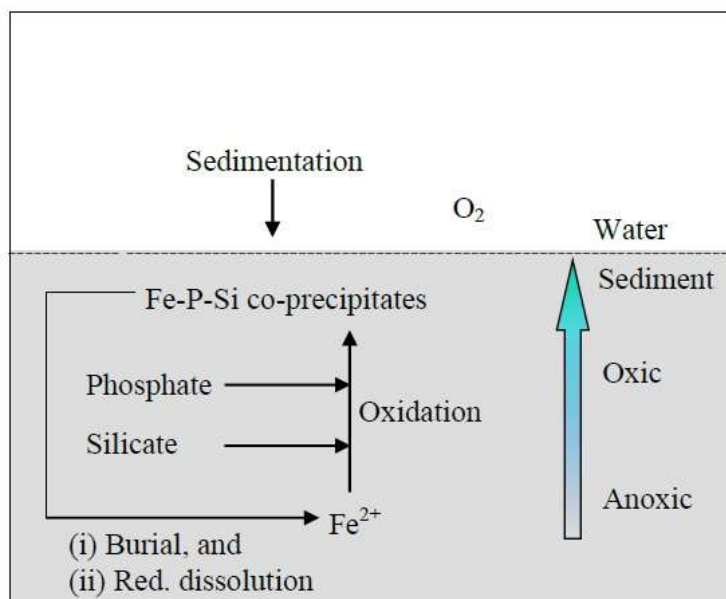


**Figure 4.1.** Schematic diagram showing the formation of ferric (hydr)oxides in the presence of phosphate and silicate during the upward diffusion of $Fe^{2+}$ from deeper sediments.

In this study, Fe-P-Si co-precipitates of variable Si:Fe ratios were synthesized by oxidizing ferrous ($Fe^{2+}$) iron in solution containing phosphate and variable concentrations of silicate. This simulates natural precipitation processes where the upward diffusion of reductively dissolved $Fe^{2+}$ from deeper sediments may be oxidized in the surface sediments (Figure 4.1) (Precht et al., 2004; Santschi et al., 1990) (also discussed in Chapter 1, section 1.5.2). The oxidation of $Fe^{2+}$ and resulting co-precipitates may also form at locations where groundwater interacts with surface waters (Figure 4.2) (Shiraishi et al., 2018; van der Grift et al., 2014). In aquatic environments, Fe-P-Si co-precipitates can also be deposited at the sediment-water interface due to sedimentation from the water column (Figure 4.1). Analogues of natural Fe-P-Si co-precipitates are often prepared in the laboratory to study geochemical

processes in freshwater sediments (Cismasu et al., 2014; Dyer et al., 2010; O'Melia and Stumm, 1967).

Although Fe-P-Si co-precipitates commonly form naturally by oxidative precipitation, synthesized analogues are frequently prepared by increasing the pH of an acidic solution containing aqueous ferric ($Fe^{3+}$) iron (Cismasu et al., 2014; Schwertmann and Cornell, 2000c). Therefore, we synthesized a second set of co-precipitates by precipitation of $Fe^{3+}$ induced by rapid pH increase, to compare their reactivity with those prepared by oxidative $Fe^{2+}$ precipitation. The removal of iron, phosphate, and silicate from aqueous solution during co-precipitation was determined by analyzing the aqueous species in the initial (pre-oxidation) and final (post-oxidation) solutions. In addition, following both the synthetic approaches, oxidative $Fe^{2+}$ precipitation and direct $Fe^{3+}$ precipitation, pure ferric precipitates were synthesized in the absence of phosphate and silicate to compare their reactivity to those of the Fe-P-Si co-precipitates.
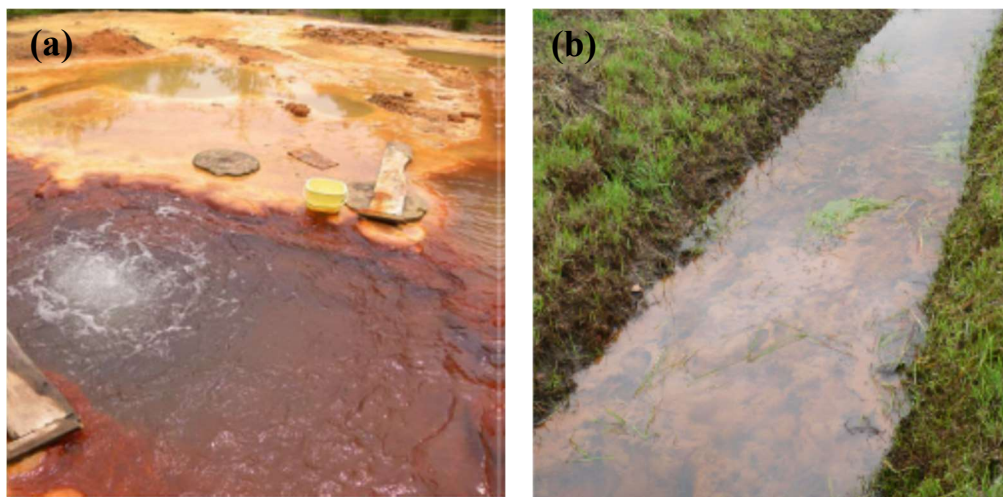


**Figure 4.2.** Ferric (hydr)oxide produced via $Fe^{2+}$ oxidation during the interaction of groundwater and surface water (a) at the Okuoku-hachikurou hot spring located in Japan, the figure has been reproduced from Shiraishi et al. (2018); and (b) in a ditch located in Hupsel Brook Catchment in The Netherlands, the figure has been reproduced from van der Grift et al. (2014).

The synthesized ferric iron precipitates and co-precipitates were subsequently reductively dissolved in buffered ascorbate-citrate solution at near neutral pH, a method used in past studies to compare the relative reactivity of ferric (hydr)oxides (Hyacinthe et al., 2006; Hyacinthe and Van Cappellen, 2004; Phillips et al., 1993; Raiswell et al., 2010; Suter et al.,

1991). Kinetic parameters describing the dissolution of iron, phosphate, and silicate were extracted by fitting the experimental data to the reactive continuum model (Hyacinthe et al., 2006; Hyacinthe and Van Cappellen, 2004; Raiswell et al., 2010). To estimate the bio-availability of iron (as an electron acceptor) and phosphate (as a nutrient) from co-precipitates obtained by $Fe^{2+}$ oxidation, an anaerobic dissolution experiment in the presence of the model facultative anaerobic iron reducing bacteria *Shewanella putrefaciens* was also conducted.

## 4.3 Materials and methods

### 4.3.1 Synthesis of co-precipitates by $Fe^{2+}$ oxidation

Co-precipitates of Fe-P-Si were synthesized by oxidizing $Fe^{2+}$ in the presence of phosphate and variable silicate concentrations similar to previously published synthesis approaches (Senn et al., 2015; Voegelin et al., 2010) with slight modifications. In the syntheses, ratios of phosphate and silicate with respect to iron (0.2 M) in solutions (P:Fe ratio 0.5, and Si:Fe ratio 0 to 0.5) were used based on ratios typically found in surface waters (Mayer and Jarrell, 2000). However, higher concentrations of each element were used in the initial solution to obtain sufficient precipitated material to conduct further experiments. For each co-precipitation experiment, an aqueous solution of phosphate (Sigma Aldrich, $H_2NaPO_4$, ≥99.0%) with or without silicate (Aldrich, $Na_2SiO_3.9H_2O$, ≥98.0%) prepared in 0.1 M $NaHCO_3$ (Sigma, 99.5-100.5%) solution, adjusted to pH 7.0, was added to solid crystals of $FeCl_2·4H_2O$ (Sigma-Aldrich, ≥99.0%). The solid ferrous salt ($FeCl_2·4H_2O$) was used instead of an $Fe^{2+}$ solution to avoid the oxidative precipitation of pure ferric precipitates before the complete mixing of the phosphate, silicate and iron solutions could occur. Aeration was started simultaneously with the addition of phosphate and silicate solution to the ferrous salt. The oxidation of $Fe^{2+}$ resulted in a pH drop, however; NaOH (1 M) solution was added to maintain pH at 7.0±0.5 during precipitation. The co-precipitation experiments were continued for 24 to 48 hours and were considered complete when a stable pH was reached. The co-precipitates were centrifuged at 1690 RCF for 15 min (Thermo Scientific, Sorvall ST 16R) and the supernatants were filtered (0.45 µm pore size, polypropylene) before analysis (see section 4.3.5.3 for analytical methods). The concentrated wet (co)-precipitates obtained from centrifugation were dialyzed (Spectra/Por 1 Dialysis Tubing) in 18.2 MΩ $cm^{-1}$ water (Millipore) until a stable conductivity was obtained. The solids collected from the dialysis bag were further centrifuged to remove

water as much as possible and freeze-dried. The dried samples were stored in a desiccator to minimize secondary surface reactions accelerated by atmospheric moisture.

## 4.3.2 Synthesis of co-precipitates by pH increase

For the synthesis of co-precipitates by direct $Fe^{3+}$ precipitation, a 500 mL of 0.4 M solution of $FeCl_3.6H_2O$ (EMD, 99.0-102.0%) was prepared in 18.2 MΩ $cm^{-1}$ water (Millipore). This solution was then used to dissolve sodium phosphate monobasic (Sigma Aldrich, $H_2NaPO_4$, ≥99.0%). Subsequently, silicate solution of variable concentrations (Aldrich, $Na_2SiO_3.9H_2O$, ≥98.0%) prepared in 1M NaOH, was added to the solution of $Fe^{3+}$ and phosphate. Further pH adjustment to 7.0 was achieved by adding 1M NaOH solution. The initial addition of NaOH solution was rapid but in 2 to 3 steps and then drop wise. The time taken for this pH adjustment was about 10 min. The initial aqueous phase P:Fe and Si:Fe ratios in this method were similar to the ratios used in the $Fe^{2+}$ oxidation method. Finally, the suspension was equilibrated for 24 hours with continuous stirring. The pH was measured and found to change ±0.2 unit after 24 hours. The samples were dialyzed and freeze-dried as per the method, above (section 4.3.1).

## 4.3.3 Synthesis of pure ferric precipitates

Ferric precipitates were synthesized in the absence of phosphate and silicate following the synthetic protocols described above i.e., $Fe^{2+}$ oxidation (section 4.3.1) and pH increase (section 4.3.2).

## 4.3.4 Reductive dissolution experiments
## 4.3.4.1 Reductive dissolution in buffered ascorbate-citrate solution

A solution (990 mL) of 0.17 M sodium citrate (Sodium citrate dehydrate, Sigma, ≥99%) and 0.59 M $NaHCO_3$ (Sigma, 99.5-100.5%) was prepared with 18.2 MΩ $cm^{-1}$ water (Millipore) in an Applikon bioreactor (1.2 L). Solid ascorbic acid (Sigma, ≥98%) was added slowly to the solution of sodium citrate and sodium bicarbonate with continuous stirring using a glass rod to avoid vigorous reaction between bicarbonate and ascorbic acid. The final concentration of ascorbic acid in the solution was 0.057 M. The solution was subsequently stirred at 200 rpm and purged continuously with nitrogen gas for an hour. The pH of this solution was measured as 7.60±0.05 which was then adjusted to 7.5 through the addition of approximately 0.5 mL of

6M HCl. Approximately 0.2 g (weighed to a precision of 4 decimal places) of co-precipitate was introduced into the reactor in the form of a suspension prepared in 10 mL of 18.2 MΩ cm$^{-1}$ water. Suspension samples were collected periodically via syringe through a sampling port in the head plate of the reactor. At each sampling time, 3 mL of filtered (0.45 μm, polypropylene) sample was quickly added to 6 mL of 0.5 M HCl to prevent $Fe^{2+}$ oxidation and possible secondary co-precipitation and then stored at 4°C before analysis (see section 4.3.5.3 for details of the analytical method). Dissolution experiments were conducted with (co)-precipitates produced via both synthesis methods. Control dissolution experiments were also conducted using a solution of 0.59 M NaHCO$_3$ and 0.17 M sodium citrate in the absence of ascorbic acid (the reductant). The resultant filtered (0.45 μm, polypropylene) samples were acidified and stored as discussed above before analysis.

### 4.3.4.2 Dissimilatory iron reduction by *Shewanella putrefaciens*

Dissolution kinetics experiments in the presence of *Shewanella putrefaciens* were conducted for the ferric precipitates and co-precipitates obtained via the $Fe^{2+}$ oxidation method. The ferric precipitate and co-precipitates were treated with UV light in an air-clean chamber (AirClean$^{600}$ workstation) for 2 hours to sterilize the solid surface. The sterilization via autoclaving was avoided to prevent undesirable structural changes in the ferric (co)-precipitates due to high temperature as well as the steam penetration into the solids (Berns et al., 2008; Emerson, 2009). Each precipitate/co-precipitate (2.5 mmol Fe per 100 mL) was added to a media bottle containing a solution of microbial growth media. The media solution contained KCl ($4×10^{-4}$ M), NaCl ($2.6×10^{-3}$ M), CaSO$_4$ ($4.8×10^{-3}$ M), MgSO$_4$ ($4×10^{-3}$ M), Na-lactate ($1×10^{-2}$ M) prepared in 0.02 M HEPES, adjusted to pH 7.5. The bottles containing the precipitate/co-precipitates with microbial growth media were introduced into an anaerobic chamber (Coy laboratory products, with a <1 ppmv O$_2$, 97% N$_2$ and 3% H$_2$) where the bottles were capped tightly using butyl rubber stoppers. Next, 1.55 mL of a concentrated suspension of *Shewanella putrefaciens* was injected through the stopper into each bottle giving final bacterial concentrations of $8.0×10^7±8.8×10^5$ cell/mL. After the addition of *Shewanella putrefaciens* (t=0), suspension samples were periodically collected using a needle and syringe for the determination of $Fe^{2+}$, dissolved phosphate, and ATP concentrations (see section 4.3.5.3 for analytical methods). The bottles were incubated outside of the anaerobic chamber at 25°C and

150 rpm in dark (Innova® 42). The bottles were introduced into the anaerobic chamber again at each sampling time. The dissolution experiment in *Shewanella* media for each precipitate/co-precipitate was conducted in triplicate (5×3=15 bottles). In addition, duplicate experiments (5×2=10 bottles) without bacteria were conducted as abiotic controls. Comprehensive sampling was continued up to 220 hours. The experiment was completed after 350 hours when ATP concentrations in the bottles were stable at minimal values. The remaining suspensions in each bottle were allowed to settle for 2 hours inside the anaerobic chamber. The residual wet precipitate/co-precipitates from each bottle were separated by decanting the top aqueous layer and stored in a freezer (-20 °C) before freeze-drying for further solid phase analysis.

### 4.3.5 Analytical methods

### 4.3.5.1 Solid phase characterization

**Specific surface area:** The specific surface area of the precipitates and co-precipitates were determined by absorbing nitrogen gas (with an eleven point isotherm) using the Brunauer-Emmett-Teller (BET) method (Brunauer et al., 1938) using a Gemini VII instrument.

**Scanning Electron Microscopy:** The surface morphology of the ferric co-precipitates were analyzed by Scanning Electron Microscopy (SEM). The granule samples were mounted on a carbon tape attached to an aluminum SEM stub and images for each sample were collected using an SEM microscope (TM3000, Hitachi) with 15 kV accelerating voltage. The relative elemental composition on precipitate or co-precipitate surfaces was measured using Energy Dispersive X-Ray Spectroscopy (EDS) and the QUANTAX 70 software.

**Powder XRD diffraction:** Powder XRD analyses were conducted on the precipitates and co-precipitates using a PANalytical Empyrean XRD with a Co-X-ray tube (operated at 40 kV 45 mA) and a PIXcel3D detector. The sieved (63 μm) samples were loaded into XRD sample holders using a back-loading technique. The XRD patterns for each sample were collected from 3 to 70° 2θ with a step size of 0.01° 2θ. The X-ray beam path was defined using a fixed 1/8° divergent slit, a 1/4° anti scatter receiving slit, and a 10 mm mask on the incident side, a large beta-filter (iron), and a 7.5 mm anti scatter slit on the diffraction side. Soller slits (0.04 rad) were fitted to both the incident and diffracted beams. Scans were accumulated for 24 hours to achieve each spectrum. The crystalline phases in the solid samples were identified using

HighScore Plus software and a combination of the free Crystallography Open Database and the PAN-ICSD Database. Once all crystalline phases were identified, a Rietveld refinement routine built into the HighScore Plus software was used to estimate the relative abundance of each crystalline phase.

**ATR-FTIR spectra:** For the collection of ATR-FTIR spectra (8700 FTIR spectrometer, Thermo Instruments), 20 mg of sample was mixed with 0.9 mL water and 0.4 mL ethanol and sonicated for an hour. The resultant slurry was deposited on an ATR flow cell and dried overnight on the laboratory bench. The ATR flow cell contains a 60° ZnSe crystal IRE (80×10×4 mm, 100 µL). Spectra were collected at 8 $cm^{-1}$ resolution with 100 averaged scans.

### 4.3.5.2 Chemical composition of precipitates and co-precipitates

Freeze-dried precipitate or co-precipitate sample (12.5 mg) was added to a polypropylene centrifuge tube (VWR, 50 mL) containing 20 mL of 2M HCl solution. The resulting suspension was agitated on a rotary shaker at 30 rpm (Glass-Col, 099A RD4512) at 22°C for 24 hours to dissolve the ferric precipitates and co-precipitates. Note that no remaining suspended particles of ferric (co)-precipitates were observed after 24 hours of dissolution. The aqueous samples were filtered through 0.45 µm pore size polypropylene syringe filters and stored at 4°C until analysis for iron, phosphorus and silicon contents (see section 4.3.5.3 for the analytical method).

### 4.3.5.3 Aqueous analyses

The aqueous samples collected to estimate (i) the removal of dissolved iron, phosphate and silicate via co-precipitation (discussed section 4.3.1), (ii) the dissolution of iron, phosphate and silicate from the precipitates and co-precipitates in buffered ascorbate-citrate solutions and in control solutions without ascorbic acid (discussed in section 4.3.4.1), and (iii) the chemical compositions of the synthesized precipitates and co-precipitates by dissolving the solids in 2M HCl solution (discussed section 4.3.5.2), were analyzed by inductively coupled plasma optical emission spectroscopy (ICP-OES) using a Thermo Scientific iCAP 6300 instrument. The analytical accuracy and the method detection limits for Fe, P and Si are discussed in Chapter 2 (section 2.3.2).

The suspension samples collected during the reductive dissolution experiments conducted in *Shewanella* media (discussed in 4.3.4.2) were filtered (polyethersulfone 0.2 μm pore size sterilized filter, VWR); 0.8 mL of the filtrates were acidified with equal volumes of 0.5 M HCl and stored at 4° until the concentrations of $Fe^{2+}$ and phosphate were analyzed. The concentration of $Fe^{2+}$ was determined by the ferrozine method (Viollier et al., 2000) and the dissolved phosphate was determined by the molybdate blue method (Ringuet et al., 2011) using an Ultra Violet Visible Spectrophotometer (FlexStation 3). For the quantification of $Fe^{2+}$ sorbed to the residual precipitate/co-precipitate surface or freshly precipitated during the experiment, 0.25 mL of the suspension samples was acidified with 0.5 mL of 0.5 M HCl and stored at 4 °C, the analysis was completed within 24 hours. Before analyzing the sorbed or precipitated $Fe^{2+}$, the acidified suspensions were equilibrated at room temperature for an hour and then agitated for 2 hours on a rotary shaker at 30 rpm (Glass-Col, 099A RD4512) and the filtered (0.2 μm pore size polypropylene) aqueous fractions were analyzed for the determination of $Fe^{2+}$ using the ferrozine method (Viollier et al., 2000). Adenosine triphosphate (ATP) concentrations were analyzed immediately in the suspension samples: 100 μL of the collected suspensions were mixed with 100 μL of ATP reagents (BacTiter-Glo$^{TM}$) and luminescence was measured (FlexStation 3) from which the concentration of ATP was calculated (Hammes et al., 2010).

## 4.4 Results and discussion

### 4.4.1 Chemical composition of precipitates and co-precipitates

The bulk chemical compositions obtained by dissolving the precipitates and co-precipitates in 2M HCl are presented in Table 4.1. All of the co-precipitates obtained by the $Fe^{2+}$ oxidation method contained similar solid phase P:Fe ratios (~0.49±0.01) which closely matched the initial solution P:Fe ratio (0.5). The P:Fe ratios in the co-precipitates synthesized via the pH increase method were 0.39±0.02, that is, lower than the P:Fe ratios in the co-precipitates obtained by $Fe^{2+}$ oxidation. In the $Fe^{2+}$ oxidation method, the co-precipitates were synthesized at pH 7.0±0.5 where aqueous phosphate exists mostly in deprotonated forms. For example, the ratio of deprotonated phosphate, $H_2PO_4^-$ to $HPO_4^{2-}$ at pH 7 in water is close to 1:1 (pKa$_2$=7.21, also discussed in Chapter 1, Figure 1.12a). In the pH increase method, the initial solution of $Fe^{3+}$ was strongly acidic with a pH near 2. Therefore, phosphate present with $Fe^{3+}$ during the

synthesis of co-precipitates (by the latter method) was mostly present in the singly deprotonated form, $H_2PO_4^-$ (~90%), while the remaining 10% existed in the fully protonated $H_3PO_4$ form. The singly deprotonated form of phosphate ($H_2PO_4^-$) is likely to show lower affinity towards aqueous $Fe^{3+}$ compared to the doubly deprotonated form ($HPO_4^{2-}$) during co-precipitation.

In the pH increase method, alkaline solution of silicate was added to an acidic solution of solution of $Fe^{3+}$ and phosphate (pH ~2). Further pH adjustment to 7.0 was achieved by adding 1M NaOH solution, initially rapidly but in 2 to 3 steps and then drop wise. During this pH increase, the formation of precipitate was still observed before reaching the final pH at 7.0, and even after the addition of alkaline silicate solution (before the addition of 1M NaOH). This implies that a significant portion of $Fe^{3+}$ in solution was likely co-precipitated with phosphate below pH 7.0 at which $H_2PO_4^-$ is dominate over $HPO_4^{2-}$ in solution. Adsorption of phosphate ($H_2PO_4^-$/ $HPO_4^{2-}$)to the freshly formed ferric (co)-precipitates is also possible, causing the removal of phosphate from solution. However, the concentrations of $HPO_4^{2-}$ and $H_2PO_4^-$ during the co-precipitation with $Fe^{3+}$ via the $Fe^{2+}$ oxidation method at pH 7.0 were nearly equal (1:1). Therefore, higher affinity of $HPO_4^{2-}$ towards $Fe^{3+}$ at pH 7.0 during $Fe^{2+}$ oxidation could have resulted in greater co-precipitation of phosphate with $Fe^{3+}$ compared to the co-precipitates obtained via pH increase method.

**Table 4.1.** Chemical compositions of the synthesized precipitates and co-precipitates obtained by dissolving the solids in 2M HCl. The "±" sign represents the range of values measured between duplicate analyses. The P:Fe and Si:Fe ratios were calculated with the average concentration of iron, phosphate (P) and silicate (Si) in the co-precipitates.

| Precipitate (ppt) or co-precipitate (co-ppt) | Solution composition | | Chemical compositions in the synthesized precipitates/co-precipitates | | |
|---|---|---|---|---|---|
| | P/Fe | Si/Fe | Fe (mmolg$^{-1}$) | P:Fe | Si:Fe |
| Synthesized via $Fe^{2+}$ oxidation | | | | | |
| Fe (ppt) | 0 | 0 | 10.00±0.09 | 0 | 0 |
| Fe-P (co-ppt) | 0.5 | 0 | 6.52±0.12 | 0.49 | 0 |
| F-P-Si (co-ppt) | 0.5 | 0.05 | 6.39±0.10 | 0.48 | 0.04 |
| Fe-P-Si (co-ppt) | 0.5 | 0.25 | 5.87±0.17 | 0.47 | 0.16 |
| Fe-P-Si (co-ppt) | 0.5 | 0.50 | 5.65±0.32 | 0.50 | 0.23 |
| Synthesized via pH increase | | | | | |
| Fe (ppt) | 0 | 0 | 10.18±0.92 | 0 | 0 |
| Fe-P (co-ppt) | 0.5 | 0 | 7.60±0.02 | 0.36 | 0 |
| F-P-Si (co-ppt) | 0.5 | 0.05 | 7.03±0.20 | 0.40 | 0.04 |
| Fe-P-Si (co-ppt) | 0.5 | 0.25 | 6.42±0.14 | 0.39 | 0.21 |
| Fe-P-Si (co-ppt) | 0.5 | 0.50 | 5.65±0.08 | 0.40 | 0.40 |

The silicate concentration in all co-precipitates was higher for solutions with higher initial aqueous silicate concentrations (Table 4.1). The Si:Fe ratios in the co-precipitates obtained with the pH increase method were higher than the co-precipitates obtained with the $Fe^{2+}$ oxidation method. For example, the Si:Fe aqueous ratio of 0.5 yielded a Si:Fe ratio of 0.23 in the co-precipitate obtained with the $Fe^{2+}$ oxidation method and 0.40 for the co-precipitate obtained with the pH increase method. Acidic conditions generally favor the polymerization and coagulation of silica in aqueous solution (Gorrepati et al., 2010; O'Melia and Stumm, 1967). This is because the point of zero charge (PZC) of amorphous silica falls between 1 and 3 (Langmuir, 1997a). The polymerization or self-coagulation of silica under acidic conditions could have resulted in the higher measured Si:Fe ratios in the co-precipitates obtained by the pH increase method compared to those obtained from the $Fe^{2+}$ oxidation method. However, the Si:Fe ratios in the co-precipitates were always lower than the initial Si:Fe ratios of the synthesis solutions.

### 4.4.2 Specific surface areas

The specific surface area of the ferric precipitate obtained via the $Fe^{2+}$ oxidation method (in the absence of phosphate and silicate) was 82 $m^2$/g. The presence of phosphate yielded a much higher specific surface area of 303 $m^2$/g which is comparable to that of the Fe-P-Si co-precipitate with a Si:Fe ratio of 0.04 (Figure 4.3a). Further incorporation of silicate in the Fe-P-Si co-precipitates, above Si:Fe ratios of 0.04, generally decreased the specific surface area of the solids produced (Figure 4.3a).

The specific surface area of the ferric precipitate obtained by the pH increase method was 304 $m^2$/g. The co-precipitation of phosphate with $Fe^{3+}$ resulted in a slightly higher specific surface area compared to the ferric precipitate with no phosphate. Increasing concentrations of silicate in the co-precipitates (i.e., increasing Si:Fe ratios) gradually decreased the specific surface area of the solids (Figure 4.3b). This effect is consistent with a previous study where increasing Si:Fe ratios in Fe-Si co-precipitates was associated with a decrease in the specific surface area of the solids (Zeng, 2003). Zeng (2003) suggested that incorporation of silica into ferric (hydr)oxides results in decreased specific surface area of Fe-Si co-precipitates because the specific surface area of amorphous silica is generally lower than that of ferric (hydr)oxides (Zeng, 2003).
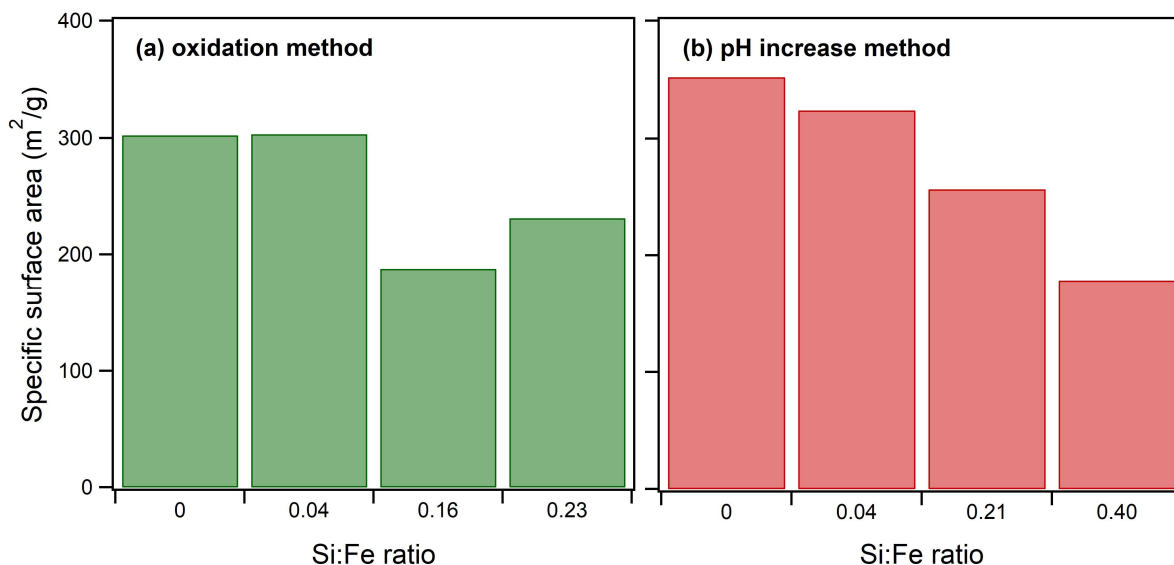
**Figure 4.3.** Specific surface areas of ferric co-precipitates obtained with the (a) $Fe^{2+}$ oxidation and (b) pH increase method. Within a set of co-precipitates based on the method of synthesis, the solid phase P:Fe ratios were similar but the Si:Fe ratios were different. The chemical compositions of these co-precipitates are presented in Table 4.1. The specific surface areas of ferric precipitates are not included in this figure but are provided in the text.

The ferric precipitate obtained by the $Fe^{2+}$ oxidation method had lower specific surface area (82 m$^2$/g) than the ferric precipitate obtained by the pH increase method (304 m$^2$/g). The presence of crystalline phases in the ferric precipitate obtained by $Fe^{2+}$ oxidation could explain the lower specific surface area while the ferric precipitates obtained by the pH increase method were amorphous to poorly crystalline phases (discussed in sections 4.4.3.1 and 4.4.4.1).

**4.4.3 XRD analyses of precipitates and co-precipitates**

**4.4.3.1 Ferric precipitates**

The ferric precipitate obtained from the $Fe^{2+}$ oxidation method showed characteristic diffraction patterns of crystalline phases (Figure 4.4, shown in red). The detected crystalline phases were goethite, lepidocrocite, and magnetite (76:20:4, weight% determined by Rietveld refinement). These findings are in agreement with previous studies where goethite and lepidocrocite were the detected crystalline phases in precipitates synthesized by $Fe^{2+}$ oxidation (Karim, 1984; Senn et al., 2015). The ferric precipitate obtained from the pH increase method showed a broad peak between 30 and 45° 2θ centered at around 40° 2θ which has been

characterized for ferrihydrite in previous studies (Rzepa et al., 2016; Wang et al., 2015; Zhou et al., 2018).
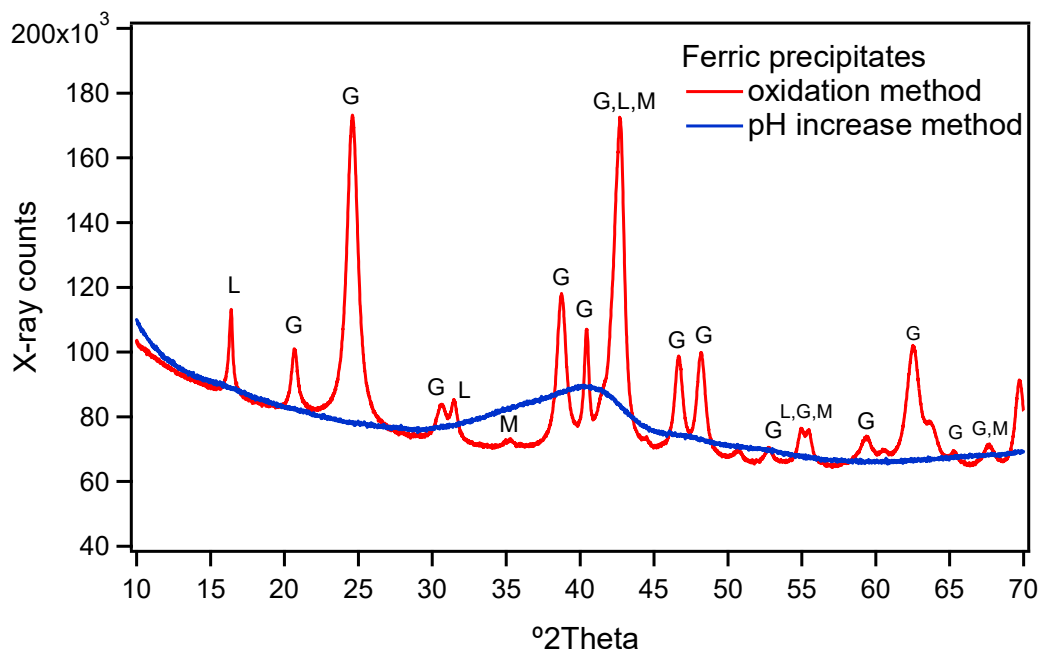


**Figure 4.4.** XRD patterns collected for the ferric precipitates synthesized by (a) $Fe^{2+}$ oxidation and (b) the pH increase method, in the absence of phosphate and silicate. The capital letters L, G and M represent the mineral phases lepidocrocite, goethite and magnetite, respectively.

### 4.4.3.2 Co-precipitates

Most of the co-precipitates synthesized by oxidative $Fe^{2+}$ precipitation showed no clearly defined diffraction patterns, indicating that the co-precipitates were amorphous or very poorly crystalline. The broad XRD peaks between 25 and 45° 2θ centered at ~35° 2θ for the co-precipitates containing variable phosphate and silicate concentrations were similar for all samples (Figure 4.5a). The reported XRD peak maxima for amorphous silica is centered at ~22-23° 2θ (Chan et al., 2016; Musić et al., 2011). This peak was absent in the diffraction patterns obtained from the co-precipitates (Chan et al., 2016). In another study, a broad peak at ~22-23° 2θ associated with amorphous silica was shifted towards lower 2θ° angles when co-precipitated with ferrihydrite (Cismasu et al., 2014; Rzepa et al., 2016). A broad peak centered at ~35° 2θ has previously been associated with ferric phosphate (Senn et al., 2015). A weak peak appeared at approximately this location in the Fe-P co-precipitates obtained by the $Fe^{2+}$ oxidation method (Figure 4.5a). Each of the co-precipitates synthesized in this study contained

similar P:Fe (0.49±0.01) ratios but the Si:Fe ratios were different (Table 4.1). The broad XRD peak centered at ~35° 2θ did not change in location, but the intensity of the peak decreased slightly with increasing solid phase Si:Fe ratios (Figure 4.5a). This was probably because, though the P:Fe ratios in the co-precipitates were similar, higher Si:Fe ratio in the co-precipitates resulted in decreased concentrations of iron and phosphate in the solids (Table 4.1).
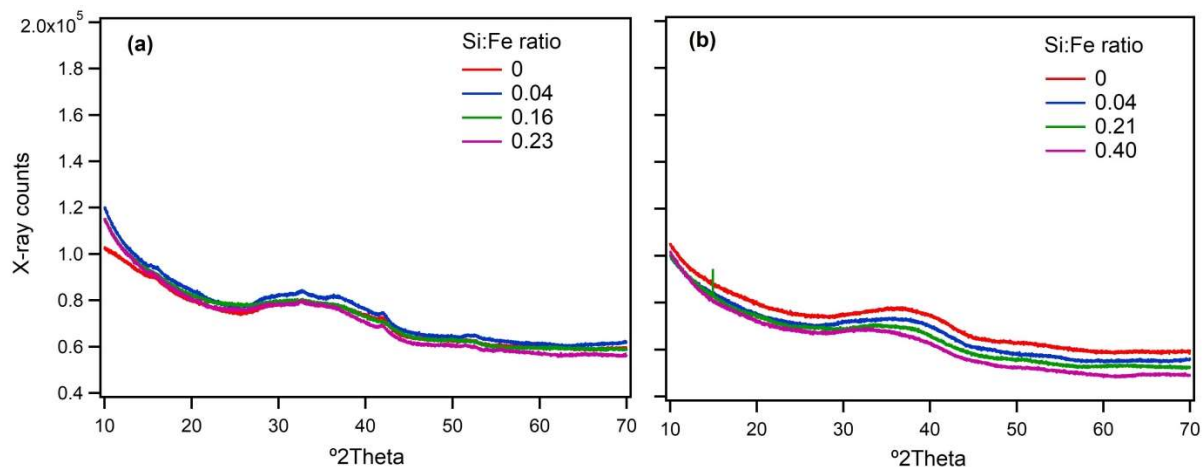


**Figure 4.5.** XRD patterns collected for the co-precipitates synthesized by (a) $Fe^{2+}$ oxidation and (b) the pH increase method. The P:Fe ratios within each set of co-precipitates were similar; 0.49±0.01 and 0.39±0.02 for the co-precipitates obtained from $Fe^{2+}$ oxidation and the pH increase method, respectively. The co-precipitates within each set based on the method of synthesis had different Si:Fe ratios as shown on the panels.

The Fe-P-Si co-precipitates obtained with the pH increase method showed no clearly defined diffraction patterns, indicating that the co-precipitates were amorphous or poorly crystalline (Figure 4.5b). The co-precipitates did exhibit a broad peak between 25 and 45° 2θ with maximum intensity at ~35° 2θ. The intensity of the peak at ~35° 2θ decreased slightly with increasing solid Si:Fe ratio in the co-precipitates, similar to the co-precipitates obtained from the $Fe^{2+}$ oxidation method. This may be due to the decrease of iron and phosphate concentration with increasing silicate concentration in the co-precipitates (Table 4.1). Further, the co-precipitates did not show the characteristic peak for amorphous-silica at ~22-23° 2θ, suggesting that silicate was removed from solution mostly by co-precipitation with iron rather than by precipitation of amorphous-silica.

## 4.4.4 ATR-FTIR analyses of precipitates and co-precipitates

### 4.4.4.1 Ferric precipitates

The ATR-FTIR spectra for the ferric precipitates obtained with the $Fe^{2+}$ oxidation and pH increase methods are shown in Figure 4.6. The spectral signatures at 887, 791 and 636 cm$^{-1}$ for the ferric precipitate obtained with the $Fe^{2+}$ oxidation method (Figure 4.6, blue line) are representative peaks for Fe-O bonds in goethite (Kugbe et al., 2009; Rahimi et al., 2015; Ruan et al., 2002). The peak at 1022 cm$^{-1}$ reveals the presence of lepidocrocite in the solid (Kinsela et al., 2016; Li et al., 2014; Rahimi et al., 2015). The characteristic IR absorption peaks for lepidocrocite at around 750 and 885 cm$^{-1}$ are generally weak in intensity compared to the goethite peaks within the same range (Rahimi et al., 2015). Therefore, the peaks at 750 and 885 cm$^{-1}$, characteristic of lepidocrocite, are not easily detected due to overlap with the more prominent goethite peaks. This is exacerbated by the small amount of lepidocrocite compared to goethite in the sample, in agreement with the Rietveld refinement of XRD data. The characteristic IR absorption band for magnetite is labeled at 636 cm$^{-1}$ (Figure 4.6, blue line).
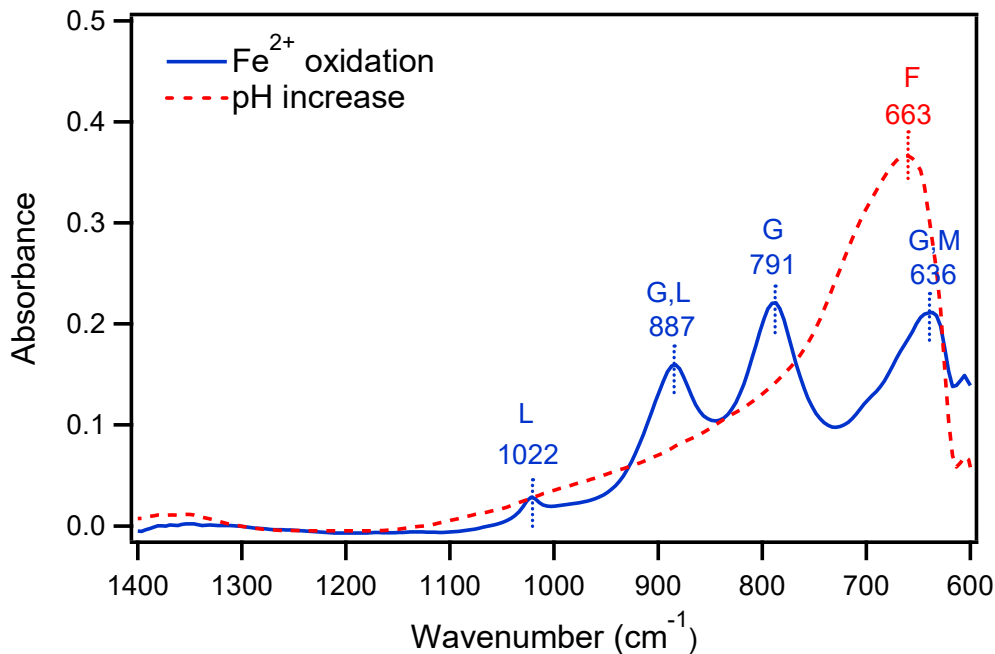


**Figure 4.6.** ATR-FTIR spectra collected for the ferric precipitates synthesized in the absence of phosphate and silicate by the $Fe^{2+}$ oxidation (blue line) and pH increase methods (red line). The capital letters F, G, L, and M represent the mineral phases; ferrihydrite, goethite, lepidocrocite, and magnetite, respectively.

The ferric precipitates obtained by the pH increase method showed an IR absorption band centered at 663 cm$^{-1}$ (Figure 4.6, red line) which has been attributed to the Fe-O bond at the tetrahedral and octahedral sites of ferrihydrite (Iyengar et al., 2014). Therefore, the peak observed at 663 cm$^{-1}$ indicates the presence of ferrihydrite in the ferric precipitate which was prepared in the absence of phosphate and silicate by the pH increase method (Xiao et al., 2017).

## 4.4.4.2 Co-precipitates

ATR-FTIR spectra collected for the co-precipitates obtained by the Fe$^{2+}$ oxidation method are shown in Figure 4.7a. A broad peak was observed at ~1065 cm$^{-1}$ for the co-precipitate with an Si:Fe ratio of 0 (Figure 4.7a, red). IR spectral features at 1036 and 1160 cm$^{-1}$ have been previously observed for dried ferrihydrite with surface sorbed phosphate (Wang et al., 2013; Willett et al., 1988). Individual peaks at 1102, 1028, and 1002 cm$^{-1}$ have also been identified for phosphate-ferrihydrite surface complexes analyzed in aqueous suspension in a previous study (Rzepa et al., 2016). Such differences in spectral pattern observed between these different studies could be the result of changes to the protonation state and symmetry of surface phosphate (Wang et al., 2017, 2013). Therefore, the peak present at ~1065 cm$^{-1}$ (Figure 4.7a) is tentatively attributed in this case to sorbed phosphate on the co-precipitate surface.
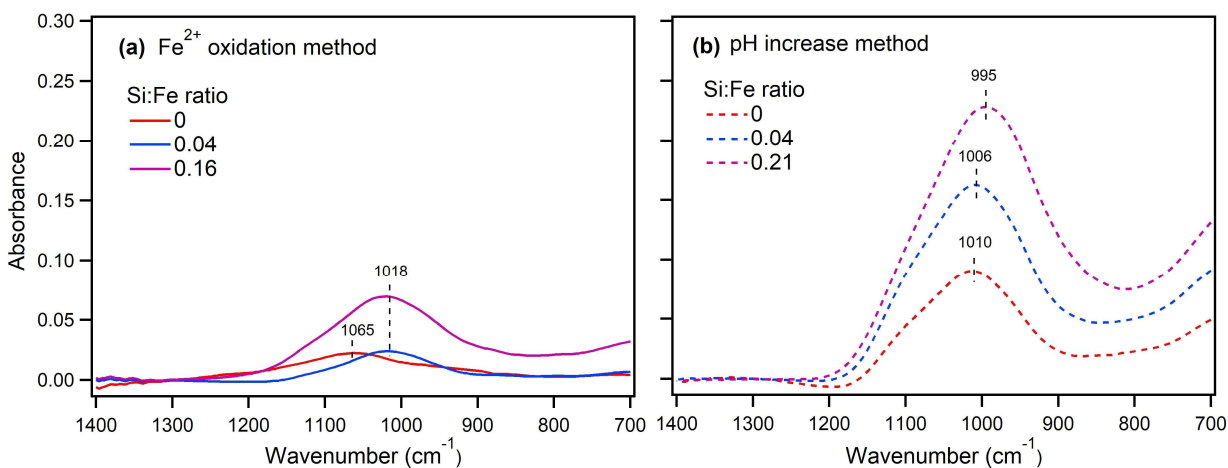


**Figure 4.7.** ATR-FTIR spectra collected for the co-precipitates synthesized from (a) Fe$^{2+}$ oxidation and (b) the pH increase method. The P:Fe ratios within each set of co-precipitates were similar; 0.49±0.01 and 0.39±0.02 for the co-precipitates obtained from Fe$^{2+}$ oxidation and the pH increase method, respectively. The co-precipitates obtained via the two synthesis methods had different Si:Fe ratios as shown on the panels.

IR absorbance at around ~1105 cm$^{-1}$ generally arises due to Si-O-Si asymmetric stretching vibrations in amorphous silica (Chan et al., 2016; Chen et al., 2014; Fabrizioli et al., 2002; Musić et al., 2011). This IR signal at ~1105 cm$^{-1}$ was not found in either set of co-precipitates synthesized by the two different methods (Figure 4.7). In previous studies, the position of the IR absorption band at ~1105 cm$^{-1}$ has been found to be unchanged for Fe-Si co-precipitates obtained by precipitation of Fe$^{3+}$ via pH increase (Chan et al., 2016; Fabrizioli et al., 2002). In those studies, acidic solutions of silicate and Fe$^{3+}$ were rapidly neutralized by the addition of NaOH and allowed to react for ~2 h before the precipitates were collected. The concentration of aqueous silicate in these previous studies was above the saturation limit of amorphous silica. Therefore, initial silica precipitation in those studies (Chan et al., 2016; Fabrizioli et al., 2002) might have resulted in incomplete incorporation of silicate in the co-precipitate with Fe$^{3+}$ within the experimental time-frame.

In our study, an under-saturated solution of silicate was prepared in NaOH, which was added to a solution of Fe$^{3+}$ that was rapidly neutralized to pH 7.0 and equilibrated for 24 hours. This method was selected to prevent the formation of amorphous silica. XRD patterns discussed in the previous section (section 4.4.3.2), indicate that amorphous or poorly crystalline silica was indeed absent in co-precipitates synthesized in this study. The Si-O stretching frequencies for sorbed silicate on ferric (hydr)oxides are generally within the range of ~930 to ~1080 cm$^{-1}$ for the Si-O···Fe bond (Swedlund et al., 2009). The exact location of the IR absorption band for the Si-O···Fe bond depends on the symmetry of surface sorbed silicate and also on whether silicate is in the monomeric, oligomeric or polymeric form on the ferric (hydr)oxides surface (Song et al., 2013; Swedlund et al., 2010b, 2009).

Generally, the IR absorption location for this bond shifts towards higher wavenumbers with an increasing degree of polymerization of silicate sorbed to ferric (hydr)oxide surfaces (Christl et al., 2012; Song et al., 2013; Swedlund et al., 2009). For example, spectral features at ~940 and ~1000 cm$^{-1}$ have been described for monomeric and oligomeric silicate sorbed to ferrihydrites (Song et al., 2013; Swedlund et al., 2009). However, an IR absorption band at a higher wave number (~1020 cm$^{-1}$) has been reported for oligomeric silicate sorbed to ferrihydrite (Swedlund et al., 2011). An IR spectral feature at ~1100 cm$^{-1}$ generally appears for polymeric silicate on ferrihydrite (Song et al., 2013; Swedlund et al., 2010a). The absence of an IR peak at ~1100 cm$^{-1}$ in our spectra therefore also indicates the absence of amorphous

silica in the co-precipitates synthesized during our study (Figure 4.7a). This is in agreement with the absence of a broad peak in the XRD patterns at ~22-23° 2θ as discussed in the previous section (discussed in section 4.4.3.2, Figure 4.5a).

For Fe-P-Si co-precipitates synthesized in this study by the $Fe^{2+}$ oxidation method, increasing silicate concentration resulted in an increase of the intensity of the IR peaks as well as a gradual shift to lower wavenumbers (Figure 4.7a). The change in the most intense spectral features (within the range 700-1400 $cm^{-1}$) for the co-precipitate with Si:Fe ratio of 0.16 could be due to the combination of phosphate and silicate on the co-precipitate's surfaces. For example, the IR peak centered at ~1065 $cm^{-1}$ obtained for the Fe-P co-precipitate (Figure 4.7a) can be attributed to phosphate sorbed or precipitated with $Fe^{3+}$ on the solid surface because the co-precipitate did not contain any silicate. Increasing the concentrations of silicate caused the location of the IR peak to shift towards a lower wavenumber (~1018 $cm^{-1}$) and the peak intensity to increase (Figure 4.7a). Therefore, IR spectral features at ~1018 $cm^{-1}$ may be assigned to surface sorbed phosphate, surface sorbed oligomeric silicate or a combination of the two.

The IR absorption band centered at 1010 $cm^{-1}$ for the dried Fe-P co-precipitate at a Si:Fe ratio of 0 obtained by the pH increase method could therefore also be assigned to sorbed phosphate or $Fe^{3+}PO_4$ precipitated on the ferrihydrite surface (Wang et al., 2017). This IR peak increased in intensity and shifted to lower wavenumbers with increasing Si:Fe ratio in the co-precipitates (Figure 4.7b). This may potentially indicate that the IR peak observed at 995 $cm^{-1}$ for the co-precipitate with a Si:Fe ratio of 0.21 obtained from the pH increase method could arise from a combination of phosphate and silicate associated with iron in the co-precipitates. The absence of characteristic IR bands at around 1105 $cm^{-1}$ in the co-precipitates likely indicates the absence of amorphous silicate in the solids.

## 4.4.5 Removal of aqueous iron, phosphate and silicate during co-precipitation

The supernatants separated from the wet co-precipitates obtained with the $Fe^{2+}$ oxidation method were analyzed for iron, phosphate, and silicate in solution. The percentages of removal of each element via co-precipitations were then calculated. The measured concentrations of iron in the supernatant from the co-precipitation experiments showed that 99.99% of $Fe^{2+}$ was removed from the aqueous phase via co-precipitation. This complete removal of dissolved iron

95

was not affected by the presence of phosphate and various silicate concentrations in solution. The removal of phosphate was slightly decreased by dissolved silicate during co-precipitation (Figure 4.8). For example, the highest concentration of silicate (0.1 M) during co-precipitation decreased the removal of phosphate only by 0.2%. Although the removal of aqueous phosphate in the presence of various silicate concentrations fall within the range of analytical variability with ICP-OES (discussed in section 2.3.2), the trend is noticeable. This minor effect of dissolved silicate was not reflected in P:Fe ratios in the co-precipitates, potentially due to analytical variability in the determination of chemical compositions in the solids.
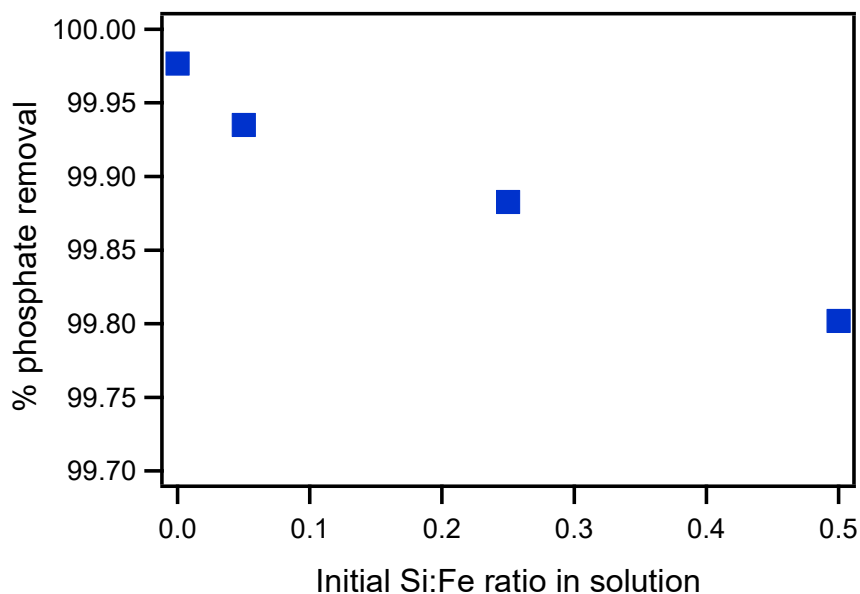


**Figure 4.8.** Percentages of phosphate removal from aqueous solution after the completion of $Fe^{2+}$ oxidation (0.2 M) at various silicate to iron solution ratios. The initial concentration of phosphate in solution before the start of $Fe^{2+}$ oxidation was 0.1 M. The co-precipitation experiment was conducted at room temperature.

The concentrations of silicate in the supernatants of the co-precipitation experiments conducted with the $Fe^{2+}$ oxidation method (experiment discussed in 4.3.1) show 96.4±1.2% removal of aqueous silicate. This ~96% removal of aqueous silicate should result in solid phase Si:Fe ratios close to the initial aqueous phase ratios (Table 4.1). However, the solid phase Si:Fe ratios in Fe-P-Si co-precipitates were lower than what was expected from aqueous silicate concentrations before and after co-precipitation experiments. The depleted Si:Fe ratios in the co-precipitates with respect to the expected Si:Fe ratios based on the aqueous phase analyses may have been due to loss of loosely bound silicate from the solids during dialysis. The

supernatants obtained from the co-precipitation experiments by the pH increase method were not analyzed because NaOH was added to $Fe^{3+}$ solutions rapidly and thus, the volume of added of NaOH could not be accounted for accurately.

## 4.4.6 Dissolution kinetics of the precipitates and co-precipitates
## 4.4.6.1 Dissolution kinetics in ascorbate-citrate solution

Reactivity of iron oxides is often described in terms of the dissolution kinetics under abiotic conditions (Kostka and Luther III, 1994; McKeague and Day, 1966; Poulton and Canfield, 2005; Raiswell et al., 2010; Suter et al., 1991) and in the presence of iron reducing bacteria (Bonneville et al., 2004; Hyacinthe et al., 2006; Roden and Zachara, 1996). Several types of chemical extractants are used for the dissolution of iron oxides, e.g., dilute and concentrated acids, ammonium oxalate solution, di-thionate solution, ascorbate-citrate solution. Among these chemical extractants, ascorbate-citrate solutions most effectively dissolve the amorphous and easily reducible fractions present in iron oxides whereas other extractants can extract amorphous fractions as well as more crystalline fractions (Kostka and Luther III, 1994).

Iron dissolution mechanisms differ based on the type of extractant, and thus different extractants target different pools of iron from solid iron oxides. For example, dilute HCl can extract iron from the amorphous fraction of poorly ordered iron oxides via the proton-promoted mechanism (Wallmann et al., 1993),  while ascorbate-citrate solution dissolves iron oxides via both proton-promoted and reductive dissolution mechanisms (Deng, 1997; Suter et al., 1991). Therefore, even for a single extractant such as ascorbate-citrate solution, the prevailing dissolution mechanisms may differ depending on the pH in the extraction medium.

Buffered ascorbate-citrate solution at pH 7.5, among other chemical extractants, has been used in many past studies to compare the reactivity of various pure iron oxides as well as sediment iron minerals (Ferdelman et al., 1991; Hyacinthe et al., 2006; Kostka and Luther III, 1994). Further, maximum amounts of dissolved iron from sediment iron minerals extracted by ascorbate-citrate solution at pH 7.5  and by iron reducing bacteria have been shown to correlate linearly (Hyacinthe et al., 2006).  This study, therefore, conducts dissolution kinetic studies for the ferric precipitates and co-precipitates in buffered ascorbate-citrate solution at pH 7.5.

In buffered ascorbate-citrate solution at pH 7.5, the reductive dissolution of solid phase $Fe^{3+}$ in the co-precipitate is primarily driven by the adsorption of ascorbate on the solid surface.

The subsequent transfer of an electron from adsorbed ascorbate to solid phase $Fe^{3+}$ iron results in the reductive dissolution of iron in the form of ($Fe^{2+}$) ferrous ion (Deng, 1997; Suter et al., 1991). This reductive dissolution of solid phase $Fe^{3+}$ depends on the adsorption pH envelope of ascorbate (Deng, 1997). The adsorption of ascorbate on ferric (hydr)oxides decreases with increasing solution pH and, hence, so does the reductive dissolution of iron (see supplementary material, Figure SM-4.1).

The citrate used stabilizes the dissolved $Fe^{2+}$ in solution by forming an aqueous complex, which prevents the adsorption of dissolved $Fe^{2+}$ on the solid surface. The adsorption of ascorbate on the ferric (hydr)oxide surface may also result in ligand promoted dissolution. The bicarbonate is used as a buffer against solution pH changes caused by the reductive iron dissolution of $Fe^{3+}$. Under strong acidic conditions, the dissolution of ferric precipitates or co-precipitates may occur by a combination of multiple mechanisms including reductive dissolution, proton-promoted dissolution and ligand-promoted dissolution. The dissolution of solid phase $Fe^{3+}$ therefore decreases from acidic to alkaline conditions. Under alkaline conditions (above pH 8-9), the dissolution of iron is also inhibited because of decreased adsorption of ascorbate on the solid surface. The dissolution experiments in this study were conducted at pH 7.5 to maximize the reductive iron dissolution with minimal effect of proton-promoted dissolution of solid phase $Fe^{3+}$.

The release of iron and phosphate from the precipitates or co-precipitates occurred during the reductive dissolution experiments conducted in buffered ascorbate citrate solution. The dissolution kinetic parameters were extracted by fitting the experimental data to the reactive continuum model (Hyacinthe et al., 2006; Hyacinthe and Van Cappellen, 2004; Raiswell et al., 2010). The mathematical form of the model is shown in Equation 4.1.

$$\frac{J}{M(0)} = \frac{v}{a} \left(\frac{M(t)}{M(0)}\right)^{1+\frac{1}{v}} \ldots\ldots\ldots\ldots (4.1)$$

where J is the apparent dissolution rate; $M(0)$ is the initial mass of an element in the solid phase and $M(t)$ is the corresponding un-dissolved mass at time t during the dissolution experiment. The coefficients $\frac{v}{a}$ and $1 + \frac{1}{v}$ in Equation 4.1 are the dissolution rate constant (mmol g$^{-1}$ h$^{-1}$) and apparent reaction order, respectively. The model (Equation 4.1) assumes that the initial reactivity distribution of the precipitates or co-precipitates follows a gamma function (Hyacinthe et al., 2006; Hyacinthe and Van Cappellen, 2004). According to the

reactive continuum model, the mass of un-dissolved co-precipitates $M(t)$ at time t is given by Equation 4.2.

$$M(t) = M(0)\left(\frac{a}{a+t}\right)^v \text{..............} (4.2)$$

The coefficients $v$ and $a$ were obtained by least square fitting of the experimental data to Equation 4.2. The $v$ and $a$ values were then used to calculate the apparent dissolution rate constants and the reaction order.

### 4.4.6.2 Dissolution kinetics of ferric precipitates in ascorbate-citrate solution

The reactivity of ferric precipitates was examined by dissolving the solids in buffered ascorbate-citrate solution at pH 7.5. Kinetic data for the dissolution of iron from ferric precipitates in buffered ascorbate-citrate solution were fitted to the reactive continuum model (Equation 4.2), shown in Figure 4.9. The extracted kinetic parameters are presented in Table 4.2.
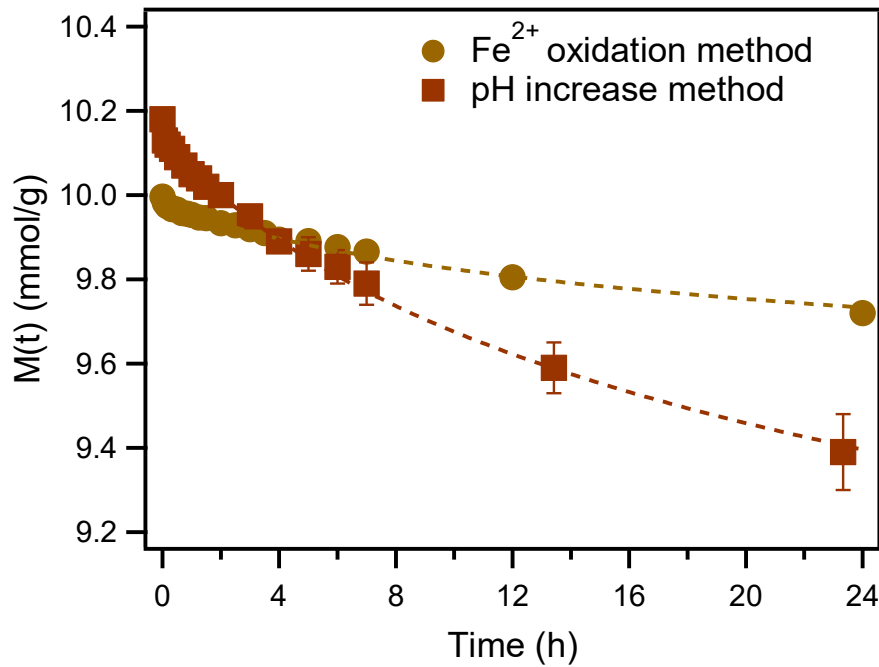


**Figure 4.9.** Experimental data (symbols) for the dissolution of iron from ferric precipitates, synthesized with the $Fe^{2+}$ oxidation (filled circle) and pH increase methods (filled square), in buffered ascorbate-citrate solution at pH 7.5 and 22°C. Kinetic parameters are extracted by fitting the experimental data to Equation 4.2 (dashed line). Error bars represent the range of values measured between duplicates.

**Table 4.2.** The rate constants $\left(\frac{v}{a}\right)$ and reaction orders for the dissolution of iron from ferric precipitates in buffered ascorbate-citrate solution at pH 7.5 and 22°C. The kinetic parameters were extracted by least square fitting the experimental data to the reactive continuum model (Equation 4.2) with a confidence limit of 95%. The goodness of fit is shown with the chi-squared ($\chi^2$) value. The critical chi-squared ($\chi_c^2$) value based on the degree of freedom for each set of data is also shown beside the $\chi^2$ values.

| Preparation method | $\frac{v}{a}$ (mmol g$^{-1}$ h$^{-1}$) | $1 + 1/v$ | $M(0)$ **(mmol/g)** | $\chi^2$ | $\chi_c^2$ |
|---|---|---|---|---|---|
| Fe$^{2+}$ oxidation | $3.05 \times 10^{-3}$ | 73.6 | $9.98 \pm 0.00$ | $9.23 \times 10^{-4}$ | 7.96 |
| pH increase | $8.19 \times 10^{-3}$ | 22.8 | $10.14 \pm 0.01$ | $3.59 \times 10^{-3}$ | 13.85 |

The $\frac{v}{a}$ value (Table 4.2) for the reductive dissolution of iron from ferric precipitate obtained with the Fe$^{2+}$ oxidation method was about 2.7 times slower than the value for the precipitate obtained by the pH increase method. The XRD (Figure 4.4) and ATR-FTIR spectra (Figure 4.6) show that the ferric precipitate obtained with the Fe$^{2+}$ oxidation method contained goethite, magnetite and lepidocrocite. Three crystalline phases present in this ferric precipitate (Fe$^{2+}$ oxidation method) are relatively stable with lower solubility and reactivity as compared to ferrihydrite (Bonneville et al., 2009). The differences in iron dissolution rate constants between the precipitates prepared by the two synthesis methods are present when normalized by the amount (g) or by the specific surface area (m$^2$) (Figure 4.10). Therefore, this difference is more likely related to the mineralogy of the precipitates rather than their surface area.
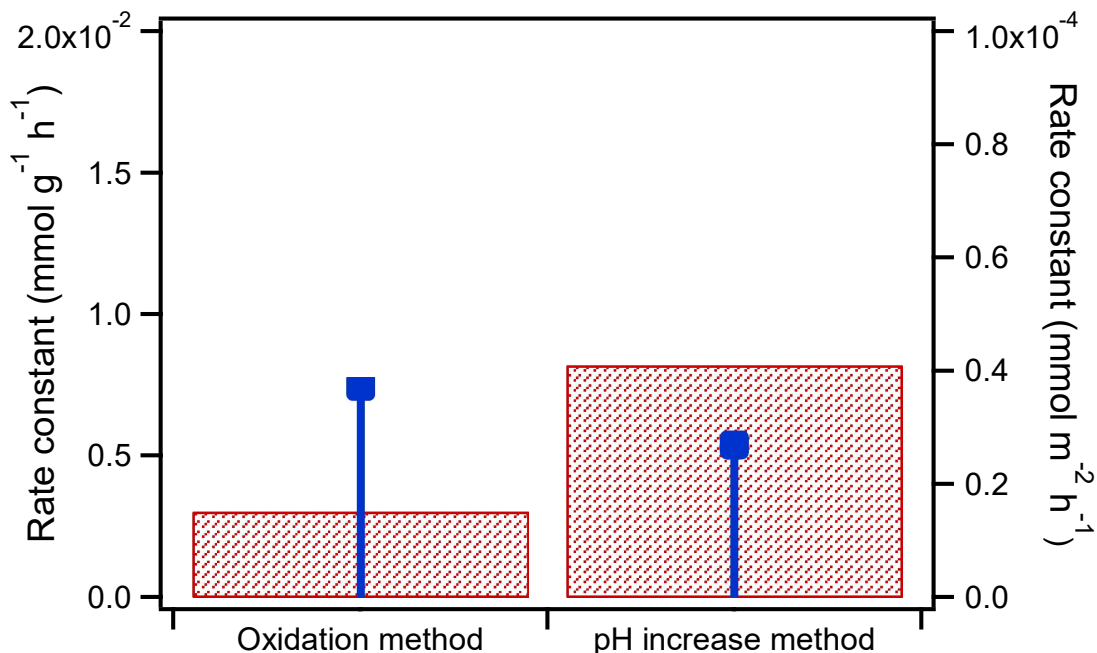
**Figure 4.10.** Apparent rate constants (shaded bar) and the rate constants normalized to the specific surface area (blue bar) for the dissolution of ferric precipitates obtained with the $Fe^{2+}$ oxidation and pH increase method. The dissolution experiments are conducted in buffered ascorbate-citrate solution at pH 7.5 and 22°C.

The observed dissolution orders $(1 + \frac{1}{v})$ for the ferric precipitates obtained by the $Fe^{2+}$ oxidation and pH increase method were 73.6 and 22.8, respectively, suggesting a complex dissolution mechanism for both the solids. During the 24 hours of the dissolution experiment, only 2.8% of the ferric precipitate obtained with the $Fe^{2+}$ oxidation method was dissolved, and 7.8% for the precipitate obtained from the pH increase method. Therefore, the very high $1 + \frac{1}{v}$ values clearly point to heterogeneous solid phase mixtures with large ranges in reactivity.

### 4.4.6.3 Dissolution kinetics of ferric co-precipitates in ascorbate-citrate solution

Kinetic data for the dissolution of iron and phosphate from the co-precipitates obtained from both the synthesis methods are compared in Figure 4.11. Kinetic parameters were extracted by fitting the dissolution data to Equation 4.2 are presented in Table 4.3.
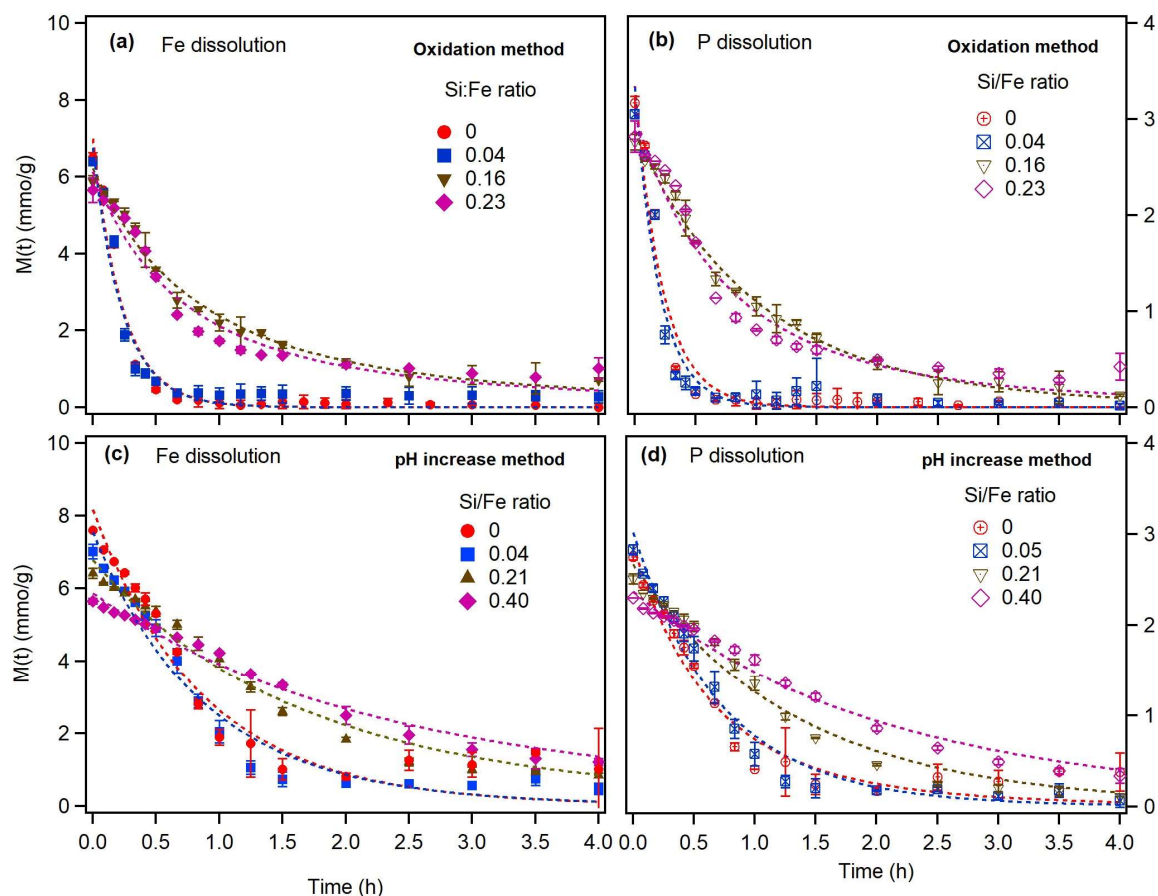
**Figure 4.11.** Kinetic data (symbols) for the dissolution of (a,c) iron and (b,d) phosphate from the co-precipitates obtained with the $Fe^{2+}$ oxidation (upper panels) and pH increase method (bottom panels). Kinetic parameters are extracted by fitting the experimental data to Equation 4.2 (dashed lines) and are shown in Table 4.3. Within a set of co-precipitates based on the method of synthesis, the solid phase P:Fe ratios were similar, but the Si:Fe ratios were different as indicated on the panels. The experiments were conducted at 22°C. Error bars represent the range of values measured between duplicates.

**Table 4.3.** Kinetic parameters and model predicted $M(0)$ values for the dissolution of iron and phosphate from the co-precipitates conducted in buffered ascorbate-citrate solution at pH 7.5 extracted by least square fitting of the experimental data to Equation 4.2 with 95% confidence limit. The goodness of fit is shown with the chi-square ($\chi^2$) value. The critical chi-square ($\chi_c^2$) value based on the degree of freedom for each set of data is also shown beside the $\chi^2$ values.

| Si:Fe ratio in the solids | | $\frac{v}{a}$ (mmol g$^{-1}$h$^{-1}$) | $1 + \frac{1}{v}$ | $M(0)$ (mmol/g) | $\chi^2$ | $\chi_c^2$ |
|---|---|---|---|---|---|---|
| *Synthesized via Fe$^{2+}$ oxidation* | | | | | | |
| 0 | Fe | 4.25 | 1.01 | 6.98±0.68 | 2.05 | 8.67 |
| | P | 4.36 | 1.01 | 3.34±0.38 | 0.60 | |
| 0.04 | Fe | 4.29 | 1.02 | 6.76±1.01 | 3.44 | 8.67 |
| | P | 4.91 | 1.01 | 3.33±0.46 | 0.84 | |
| 0.16 | Fe | 1.19 | 1.43 | 6.22±0.35 | 0.78 | 9.30 |
| | P | 1.00 | 1.09 | 2.86±0.11 | 0.14 | |
| 0.23 | Fe | 1.41 | 1.51 | 6.14±0.62 | 2.30 | 9.30 |
| | P | 1.34 | 1.32 | 3.05±0.31 | 0.60 | |
| *Synthesized via pH increase* | | | | | | |
| 0 | Fe | 1.15 | 1.04 | 8.17±0.74 | 2.85 | 7.96 |
| | P | 1.55 | 1.19 | 2.88±0.33 | 0.61 | |
| 0.04 | Fe | 1.14 | 1.05 | 7.56±0.78 | 5.69 | 9.39 |
| | P | 1.40 | 1.04 | 3.02±0.27 | 0.60 | |
| 0.21 | Fe | 0.61 | 1.15 | 6.79±0.45 | 2.09 | 10.12 |
| | P | 0.76 | 1.04 | 2.67±0.14 | 0.36 | |
| 0.40 | Fe | 0.43 | 1.20 | 5.88±0.23 | 1.02 | 10.85 |
| | P | 0.48 | 1.10 | 2.37±0.10 | 0.20 | |

The reactivity of the ferric co-precipitates (i.e., Fe-P and Fe-P-Si) is in general much higher than that of the pure ferric precipitates (no P and Si) obtained via both Fe$^{2+}$ oxidation and pH increase methods. For example, for the ferric precipitates and co-precipitates obtained with the Fe$^{2+}$ method, the iron dissolution rate constant ($\frac{v}{a}$) from the Fe-P co-precipitate is about 1400 times higher than that observed from the pure ferric precipitate. This $\frac{v}{a}$ value for iron dissolution from the Fe-P co-precipitates, obtained via the pH increase method, is about 150 times higher than that of the ferric precipitates.

The $\frac{v}{a}$ values for the dissolution of iron from the co-precipitates at the solid phase Si:Fe ratios of 0 and 0.04 obtained by the Fe$^{2+}$ oxidation method were comparable; 4.25 and 4.29 mmol g$^{-1}$ h$^{-1}$, respectively (Table 4.3 and Figure 4.12a). The $\frac{v}{a}$ values for iron dissolution decreased considerably when the Si:Fe ratios increased to 0.04 to 0.16, indicating that increased concentration of silicate in the co-precipitates decreases the reactivity of the iron towards reductive dissolution (Figure 4.12a). However, the $\frac{v}{a}$ value for iron dissolution

increased from 1.19 to 1.41 with increasing solid phase Si:Fe ratios from 0.16 to 0.23 (obtained by $Fe^{2+}$ oxidation). The reason for this slight increase in $\frac{v}{a}$ value is not clear but could be due to the relatively higher specific surface area of the co-precipitate with Si:Fe ratio 0.23 (Figure 4.3a). Alternatively, the difference in reactivity may be attributable to differences in the morphology of the co-precipitates. The co-precipitate with a Si:Fe ratio of 0.23 included acicular crystal that were not observed in the SEM images of other co-precipitates (see supplementary material, Figure SM-4.2). Those acicular particles could not be differentiated from the rest of solids by their elemental ratios (e.g., P:Fe or Si:Fe) determined by EDS.
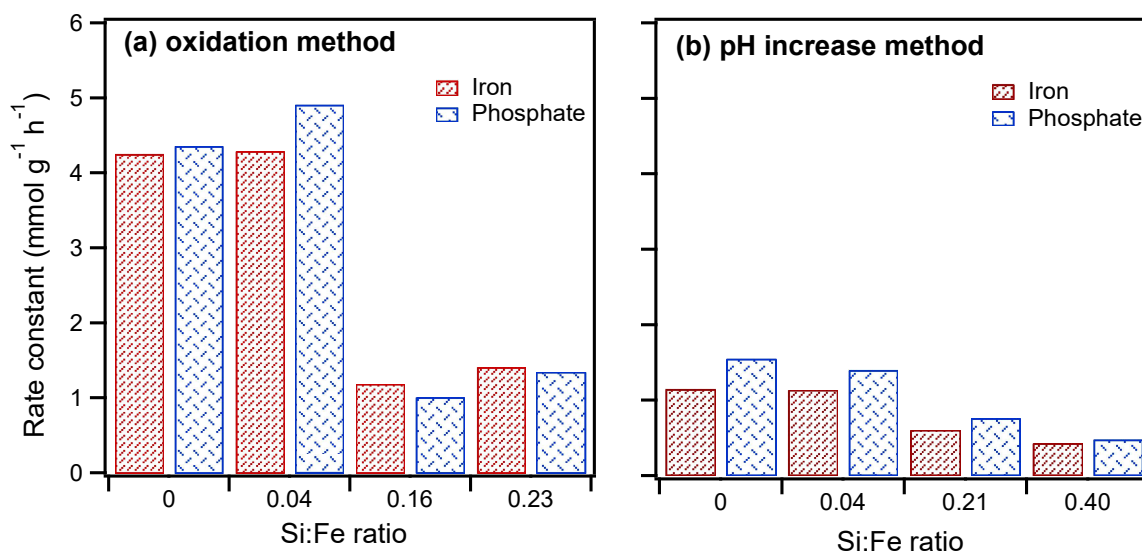


**Figure 4.12.** Apparent rate constants for the dissolution of iron and phosphate from the co-precipitates obtained by the (a) $Fe^{2+}$ oxidation and (b) pH increase methods. The dissolution experiments were conducted in buffered ascorbate-citrate solution at pH 7.5 and 22°C and the kinetics parameters were extracted by fitting the experimental data to the reactive continuum model (Equation 4.2).

A previous study by Senn et al., (2015) has shown that higher silicate concentration during $Fe^{2+}$ oxidation in the presence of phosphate delayed the transformation of initially formed Fe(III)-phosphate to Fe-P-Si co-precipitates. These authors, based on EXAFS results have suggested that surface coating of Fe(III)-phosphate phases by silica-ferrihydrite preserved the Fe(III)-phosphate phase (Senn et al., 2015). Therefore, the possible presence of Fe(III)-phosphate phases in the co-precipitates with higher solid phase Si:Fe ratios, e.g., 0.23 may explain the higher $\frac{v}{a}$ value for iron dissolution than that of the co-precipitate with Si:Fe ratio

0.16. The $\frac{v}{a}$ values for the dissolution of phosphate from the co-precipitates obtained via the $Fe^{2+}$ oxidation method follow a similar trend as observed for iron dissolution (Table 4.3 and Figure 4.12a).

The results from the dissolution kinetics of iron and phosphate from co-precipitates obtained by the pH increase method also show that higher Si:Fe ratios in the co-precipitates generally lower the dissolution rate constants for iron and phosphate (Figure 4.12). Slightly higher $\frac{v}{a}$ values were obtained for the dissolution of phosphate relative to iron (Figure 4.12), which was also observed in the dissolution experiments conducted in the absence of ascorbic acid (shown in Table 4.3, section 4.4.6.4). Therefore, the higher $\frac{v}{a}$ values for phosphate dissolution relative to iron dissolution could be due to excess phosphate release via desorption from the co-precipitate surface rather than release directly coupled to the reductive dissolution of iron.

The apparent reaction orders $(1 + \frac{1}{v})$ for the dissolution of iron and phosphate from both sets of co-precipitates with no or very low solid phase silicate concentration (e.g., Si:Fe of 0.04) were nearly 1.0 (Table 4.3), indicating the homogeneity of both iron and phosphate pools in the solids. However, increasing Si:Fe ratios in the solids resulted in higher $1 + \frac{1}{v}$ values for both iron and phosphate (Table 4.3) suggesting that silicate increased the heterogeneity of the co-precipitates.

**4.4.6.4 Dissolution kinetics in the absence of ascorbic acid**

Dissolution rate constants $(\frac{v}{a})$ attributable to ligand enhanced dissolution only were also determined for the co-precipitates, in duplicate, by dissolving them in a control solution in the absence of ascorbic acid. In this solution, ligand enhanced dissolution would be expected to be the main dissolution mechanism compared to a combination of reductive dissolution and ligand enhanced dissolution in the solution with both ascorbate and citrate. The $\frac{v}{a}$ values for the co-precipitates in the two solvents (with or without ascorbic acid) are shown in Table 4.4. The $\frac{v}{a}$ values for the dissolution of iron and phosphate were lower at higher solid phase Si:Fe ratios (Table 4.4), indicating that Si:P ratio influences the reactivity with respect to ligand enhanced dissolution as well as reductive dissolution, regardless of the synthesis method. Furthermore,

slightly different values of $\frac{v}{a}$ were observed between the co-precipitates prepared via the two different synthesis methods. For example, the $\frac{v}{a}$ values for the dissolution of iron for the co-precipitates with solid phase Si:Fe ratio of 0.04 obtained by the $Fe^{2+}$ oxidation and pH increase methods were 0.14 and 0.12, respectively.

Overall, the differences in $\frac{v}{a}$ values for the different solid phase Si:Fe ratios within two sets of co-precipitates are fairly small. Yet, the trend in $\frac{v}{a}$ values for iron and phosphate dissolution in the absence of ascorbic acid follows a similar trend to those obtained in the presence of the reductant. Dissolution in the control solutions without ascorbic acid can be attributed primarily to the complexation of iron with citrate. Ascorbic acid when present as a reducing agent, dissolved more than double the iron and phosphate (in 4 hours) than sodium bicarbonate and sodium citrate alone (Table 4.4).

**Table 4.4.** Dissolution rate constants $(\frac{v}{a})$ and the percentages of iron and phosphate dissolved from the co-precipitates in 4 hours in the buffered solution of $NaHCO_3$ and sodium citrate at pH 7.5, in the presence and absence of ascorbic acid. The $\frac{v}{a}$ values were extracted by least squares fitting of the experimental data to the reactive continuum model (Equation 4.2) with a confidence limit of 95%. The goodness of fit is shown by the chi-square $(\chi^2)$ value. The critical chi-square $(\chi_c^2)$ value based on the degree of freedom for each set of data is also shown beside the $\chi^2$ values.

| Si:Fe ratio in the solids | | Ascorbic acid **present** | | | Ascorbic acid **absent** | | | |
|---|---|---|---|---|---|---|---|---|
| | | $\frac{v}{a}$ (mmolg$^{-1}$h$^{-1}$) | % dissolved | $\chi^2$ | $\frac{v}{a}$ (mmolg$^{-1}$h$^{-1}$) | % dissolved | $\chi^2$ | $\chi_c^2$ |
| Synthesized via $Fe^{2+}$ oxidation | | | | | | | | |
| 0.04 | Fe | 4.29 | 95.7±2.5 | 6.07 | 0.14 | 38.9 | 0.04 | 3.33 |
| | P | 4.91 | 100±0.0 | 1.20 | 0.20 | 53.6 | 0.07 | |
| 0.16 | Fe | 1.19 | 87.8±0.5 | 1.04 | 0.10 | 35.0 | 0.12 | 2.17 |
| | P | 1.00 | 95.6±0.4 | 0.17 | 0.11 | 39.4 | 0.04 | |
| Synthesized via pH increase | | | | | | | | |
| 0.04 | Fe | 1.14 | 93.1±2.2 | 6.51 | 0.12 | 37.6 | 0.08 | 3.33 |
| | P | 1.40 | 96.3±0.5 | 0.68 | 0.24 | 66.7 | 0.10 | |
| 0.21 | Fe | 0.61 | 86.9±1.0 | 2.55 | 0.08 | 28.7 | 0.05 | 3.33 |
| | P | 0.76 | 96.0±0.3 | 0.36 | 0.14 | 47.5 | 0.10 | |

## 4.4.6.5 Dissolution of phosphate and silicate with iron

The release of phosphate and silicate with respect to iron during the reductive dissolution experiments are compared in Figure 4.13. The release of iron and phosphate from the co-

precipitates obtained with the $Fe^{2+}$ oxidation method show a linear relationship throughout the dissolution experiments, with slopes close to the P:Fe ratio (0.49±0.01) in the solids (Figure 4.13a), indicating stoichiometric dissolution of the co-precipitated phosphate. Similarly, the release of iron and associated phosphate from the co-precipitates obtained by the pH increase method also show a linear relationship with slopes close to the solid phase P:Fe ratio (0.39±02) (Figure 4.13b). The near constant P:Fe ratios released during the dissolution experiments implies a homogeneous distribution of phosphate in the co-precipitates. This is consistent with the similar reaction order $(1 + \frac{1}{v})$ obtained for iron and phosphate (Table 4.3).

Both sets of co-precipitates that contained silicate released silicate during the reductive dissolution of iron from both sets of co-precipitates (Figure 4.13c and 4.13d). The experimental data show that the release of silicate with respect to iron from the co-precipitates was initially lower than expected based on the solid phase Si:Fe ratios (compare data trends to the dashed lines, which correspond to the solid phase Si:Fe ratios in the co-precipitates). The lower Si:Fe in the dissolved fractions compared to the solid phase Si:Fe may indicate that silicate was not uniformly associated with iron in the co-precipitates. The increasing trend of released Si:Fe with increasing iron dissolution suggests that iron bound to silicate in the co-precipitates is less reactive towards reductive dissolution, which agrees with the trends in the rate constants with increasing solid phase Si:Fe (Figure 4.12).
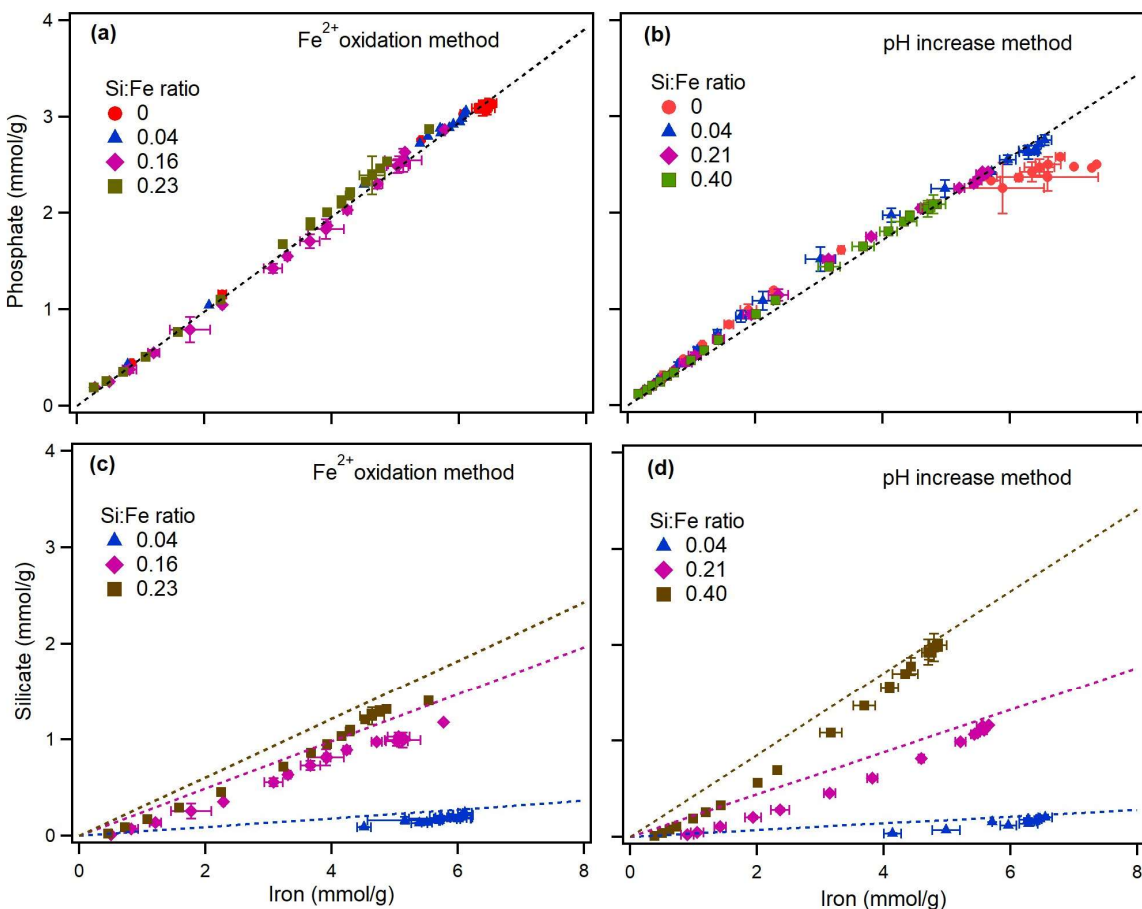
**Figure 4.13.** The dissolution of phosphate (upper panels; a,b) and silicate (lower panels; c,d) with respect to iron from the co-precipitates obtained with the $Fe^{2+}$ oxidation (left panels; a,c), and pH increase method (right panels; b,d). The dissolution kinetic experiments were conducted in buffered ascorbate-citrate solution at pH 7.5 and 22°C. The dashed lines represent the dissolved P:Fe (upper panels; a,b) or Si:Fe ratios (bottom panels; c,d) assuming that phosphate and silicate were uniformly associated with iron in the co-precipitates. Error bars represent the range of values measured between duplicates.

A previous study by Cismasu et al., (2014) has shown that higher concentrations of aqueous silicate during the co-precipitation with iron results in polymeric silica in addition to ferrihydrite in the resultant solid phase. Based on X-ray scattering and absorption spectroscopic studies, these authors suggested that a fraction of iron during co-precipitation was incorporated into polymeric silicate, and that this iron was more resistant towards reductive dissolution. Alternatively, phosphate and silicate in Fe-P-Si co-precipitates could be bound to iron through the formation of Fe-O-P and Fe-O-Si bonds. The oxygen atom in both of these bonds pulls electron density away from the $Fe^{3+}$. In an aqueous solution, phosphoric acid ($H_3PO_4$) is more

acidic than silicic acid ($H_3SiO_4$) (discussed in Chapter 1, Figure 1.12). The oxygen atom attached to a hydrogen atom in a phosphoric acid molecule (H-O-PO$_4$H$_2$) is thus more electronegative than the corresponding oxygen atom in silicic acid (H-O-SiO$_3$H$_3$). Therefore, the oxygen atom in a Fe-O-P bond may more strongly withdraw electron density form $Fe^{3+}$ than the oxygen atom in a Fe-O-Si bond. This effect would increase the reactivity of $Fe^{3+}$ towards reduction in a Fe-O-P bond than in a Fe-O-Si bond.

## 4.4.6.6 Relative reactivity of the co-precipitates obtained by the two synthesis methods

The co-precipitates obtained via the $Fe^{2+}$ oxidation method were more reactive towards dissolution of iron and phosphate than those obtained with the pH increase method. In the oxidation method, $Fe^{2+}$ was oxidized in a solution in the presence of phosphate and silicate by aerating the solution at pH ~7. Therefore, the gradual oxidation of $Fe^{2+}$ resulted in the gradual incorporation of phosphate, and silicate when present in the co-precipitates. In the pH increase method, the pH of an initially acidic solution of $Fe^{3+}$ with phosphate, and silicate (when present) was increased rapidly causing the formation of less homogeneous co-precipitate phases. The relative interactions between phosphate and $Fe^{3+}$ under different pH conditions (acidic and neutral) is likely responsible for the different solid phase P:Fe ratios between the two synthesis methods (Table 4.1). The co-precipitation of silicate appeared to be more favorable under acidic conditions, in part due to concurrent silicate polymerization or self-coagulation (discussed in section 4.4.1). In contrast to phosphate, similar solution Si:Fe ratios resulted in higher solid phase Si:Fe ratios in the co-precipitates obtained by the pH increase method than those obtained with the $Fe^{2+}$ oxidation method. The higher Si:Fe ratios in the Fe-P-Si co-precipitates obtained by the pH increase method were accompanied by lower reactivity of solid iron towards reduction than the iron in the co-precipitates synthesized by the $Fe^{2+}$ oxidation method.

The rate constants of the co-precipitates extracted from the dissolution kinetics conducted in buffered ascorbate-citrate solution were compared to their specific surface areas (see supplementary material, Figure SM-4.3). Although an increasing trend of $\frac{v}{a}$ values for the dissolution of iron and phosphate were observed for the ferric precipitates and co-precipitates with increasing specific surface area, this relation was not linear. The absence of a linear

relationship between $\frac{v}{a}$ and specific surface area suggests that other solid-phase properties including mineralogy, affect the reactivity of the co-precipitates. In addition, the $\frac{v}{a}$ values for the dissolution of iron and phosphate from the co-precipitates obtained by the $Fe^{2+}$ oxidation method were higher than those obtained by the pH increase method. For example, while the Fe-P co-precipitates obtained by the $Fe^{2+}$ oxidation method had lower specific surface areas than those obtained by the pH increase method (Figure 4.3), the $\frac{v}{a}$ values for the dissolution of iron and phosphate from Fe-P co-precipitates obtained by the former method were higher than by the pH increase method (Figure 4.12). These differences in $\frac{v}{a}$ values suggest that the synthesis method plays an important role in controlling the reactivity of the ferric co-precipitates, likely by producing variable structural arrangements of iron, phosphate and silicate in the solids. Furthermore, P:Fe ratios in the co-precipitates, obtained by the $Fe^{2+}$ oxidation method, were in general higher than in those obtained by the pH increase method (Table 4.1). The higher P:Fe ratios of the co-precipitates in turn increase their reactivity towards reductive dissolution, as discussed above.

### 4.4.6.7 Reductive dissolution by *Shewanella putrefaciens*

**Aqueous analysis**: Reductive dissolution experiments in the presence of the model $Fe^{3+}$ reducing bacteria *Shewanella putrefaciens* show the release of $Fe^{2+}$ to aqueous solution from the ferric precipitate and co-precipitates obtained by the $Fe^{2+}$ oxidation (Figure 4.14). Reduced $Fe^{2+}$ can be re-adsorbed on the un-dissolved surfaces (Géhin et al., 2007; Klein et al., 2010; Parsons et al., 2017) or may form fresh ferrous precipitates (Géhin et al., 2007; Jensen et al., 2002; Parsons et al., 2017). This fraction of $Fe^{2+}$ (reduced but associated with the solid phase) was estimated by extracting suspension samples with 0.5 M HCl (Figure 4.14a). The results show that the concentrations of both aqueous and HCl extractable $Fe^{2+}$ dissolved from the ferric precipitate and co-precipitates increased gradually during the course of the dissolution experiments. However, the concentration of aqueous $Fe^{2+}$ (Figure 4.14b) was always small compared to the HCl extractable $Fe^{2+}$ concentrations (Figure 4.14a). The production of extractable and aqueous $Fe^{2+}$ do not show any significant trends based on the solid phase silicate concentrations in the co-precipitates (Figure 4.14a).
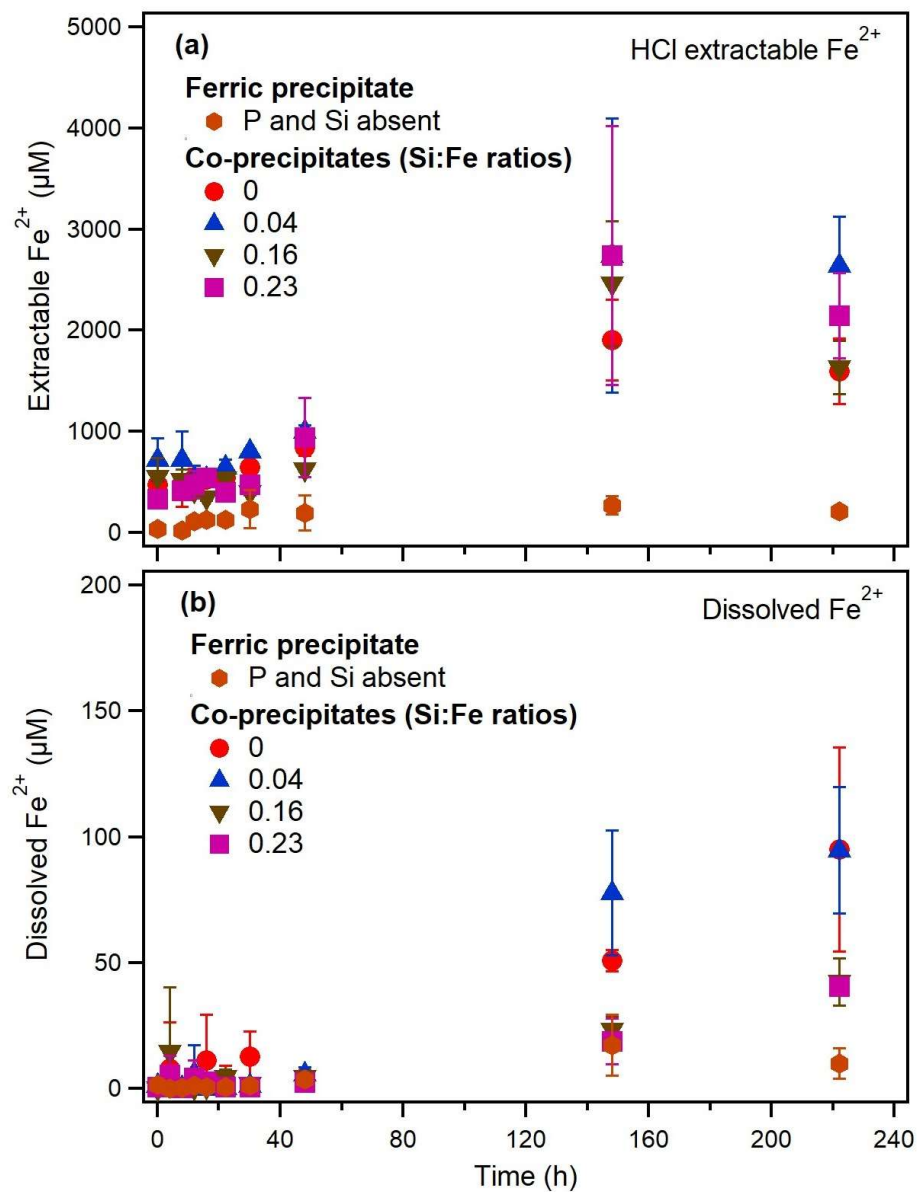
**Figure 4.14.** Concentrations of reduced $Fe^{2+}$ (a) extractable with 0.5 M HCl and (b) in the aqueous phase during the reductive dissolution of ferric precipitates and co-precipitates by *S. putrefaciens*. Among the co-precipitates, the solid phase P:Fe ratios were similar (0.49±0.01) but the Si:Fe ratios were different as indicated in the figure legend. Error bars represent the range of values measured between triplicates.

Over the course of the 220 hours of the dissolution experiments, about 1% of iron initially present in the ferric iron precipitate was reduced, as derived from the concentration of $Fe^{2+}$ measured in the HCl extract. The average concentration of aqueous $Fe^{2+}$ at 220 hours was about

10±6 μM for the ferric precipitates, accounting for about 5% of the total reduced iron. Similarly, the amounts of reduced and dissolved iron from the ferric co-precipitates were calculated. At 220 hours, about 8 to 10% of iron initially present in each of the solids was reduced based on the concentrations of HCl extrcatable $Fe^{2+}$. About 2 to 6% of the reduced $Fe^{2+}$ from the co-precipitates was found in solution, leaving the remaining reduced $Fe^{2+}$ re-adsorbed on the residual solids or incorporated in new precipitates (Géhin et al., 2007; Jensen et al., 2002; Klein et al., 2010; Parsons et al., 2017).

The time series release of phosphate from the co-precipitates to the aqueous phase (Figure 4.15) do not display a dependence on the Si:Fe ratio in the solids, similar to the trends for aqueous and extractable $Fe^{2+}$. The concentration of dissolved phosphate in solution in the abiotic controls reached a plateau within 50 hours (Figure 4.15b). This initial release of phosphate could be associated mostly with the co-precipitate surface, potentially via desorption. The release of dissolved phosphate from the co-precipitates by *S. putrefaciens* reached a plateau after 150 hours (Figure 4.15a). The total release of phosphate from the co-precipitates in the presence of bacteria during 220 hours of dissolution experiments was about double the phosphate released under abiotic conditions (Figure 4.15). However, the release of phosphate in the presence of bacteria does not show any trend based on the Si:Fe ratio in the co-precipitates.

In the co-precipitates, phosphate was homogeneously associated with iron as revealed from their stoichiometric dissolution in buffered ascorbate-citrate solution (also discussed in section 4.4.6.5). In the presence of *S. putrefaciens*, the aqueous phase P:Fe ratios (dissolved from the co-precipitates) were either comparable to or higher than the solid phase P:Fe ratio of 0.49±0.01. However, the concentrations of dissolved phosphate with respect to the concentrations reduced $Fe^{2+}$ (HCl extractable) at 220 hours were much lower than the initial solid phase P:Fe ratios. For example, about 0.02 to 0.07 moles of phosphate were dissolved against the reduction of one mole of iron (HCl extractable). This result indicates that the phosphate release to the aqueous phase during the reduction of iron (by *S. putrefaciens*) could be prevented via the re-adsorption of phosphate on the residual co-precipitates or via incorporation in new precipitates with reduced $Fe^{2+}$ (Parsons et al., 2017) or could be partially assimilated to sustain bacterial growth (Orihel et al., 2017).
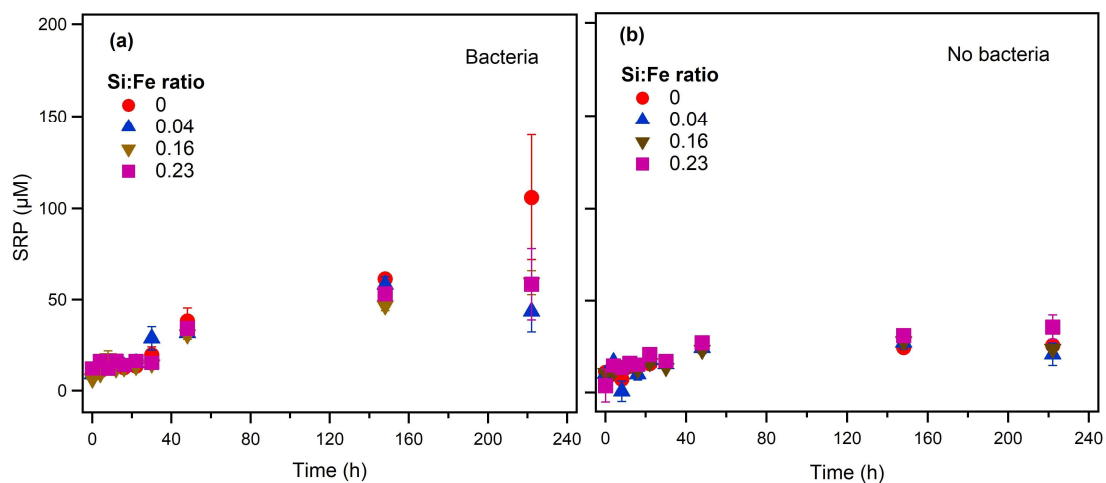
**Figure 4.15.** Concentrations of aqueous phosphate dissolved from the co-precipitates in the (a) presence and (b) absence of *S. putrefaciens*. Within the co-precipitates, the solid phase P:Fe ratios were similar (0.49±0.01) but the Si:Fe ratios were different as indicated on the panels. Error bars for the biotic experiments represent the range of values measured between triplicates and those for the abiotic experiments represent duplicates.

**Solid phase characterization of un-dissolved co-precipitate:** The ferric precipitate synthesized in the absence of phosphate and silicate by oxidative $Fe^{2+}$ precipitation contained goethite, lepidocrocite, and magnetite as revealed by XRD patterns (Figure 4.16, red line). However, the XRD pattern of the residual un-dissolved ferric precipitate (Figure 4.16, blue line) collected after the dissolution experiment with *S. Shewanella* did not show the characteristic lepidocrocite peak (labeled with a horizontal line). The quantification of mineral phases with XRD showed that the residual solid contained 94% goethite and 6% magnetite. The conversion of lepidocrocite to goethite via recrystallization in the presence of reductively dissolved $Fe^{2+}$ has been suggested in previous studies (Boland et al., 2014; Liu et al., 2016). Based on the XRD analysis of the ferric precipitates before dissolution, the concentrations of lepidocrocite, goethite and magnetite were 20, 76 and 4%, repetitively. Thus, the XRD results suggest that lepidocrocite was the main solid phase reduced by the bacteria.
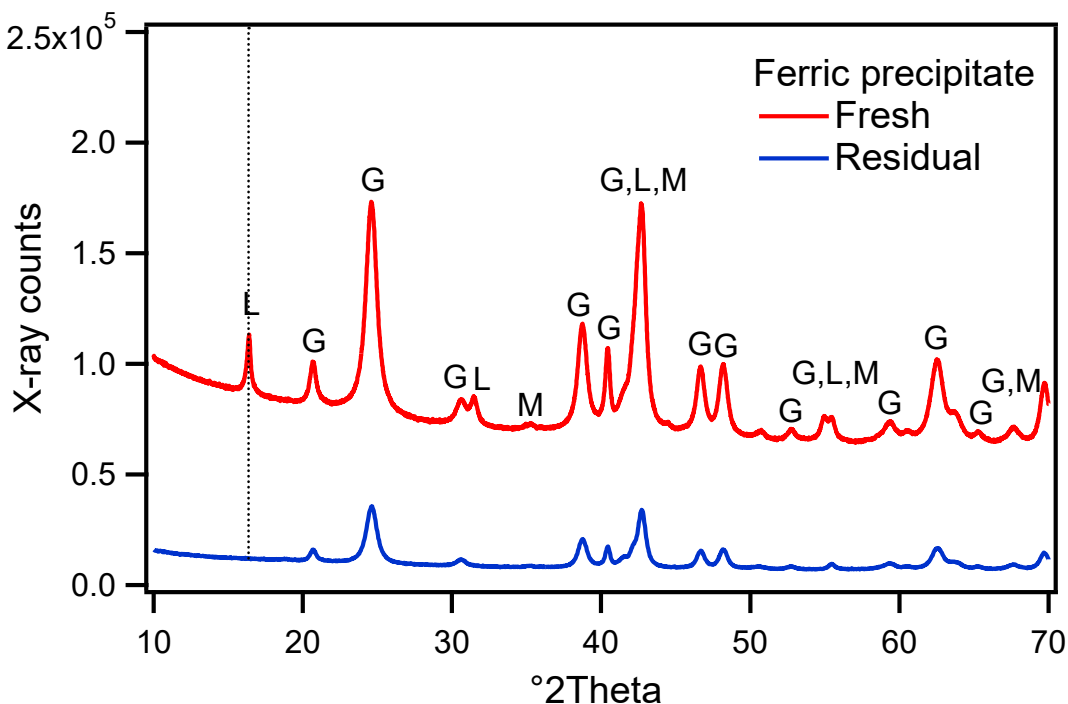
**Figure 4.16.** XRD patterns of ferric precipitates synthesized with the $Fe^{2+}$ oxidation method (red, diffraction mode) and the residual (un-dissolved) fraction (blue, transmission mode) collected after the completion of microbial reduction experiments (at 350 hours) in the presence of *S. putrefaciens*. Experimental details are described in section 4.3.4.2. The capital letters F, G, L, and M represent the mineral phases; ferrihydrite, goethite, lepidocrocite, and magnetite, respectively.

The residual co-precipitates from the reductive dissolution experiments by *S. putrefaciens* were also analyzed by XRD (Figure 4.17). The spectra showed the appearance of peaks at ~19 and ~51° 2θ for the residual co-precipitates with no and low silicate concentrations (Si:Fe ratios of 0 and 0.04). These peaks were absent from the XRD patterns of the initial co-precipitates (see section 4.4.3.2, Figure 4.5a). The diffraction peak at ~51° 2θ was also observed at very low intensity for the residual co-precipitates with high Si:Fe (0.16 and 0.23) ratios. The newly developed phases could not be assigned because of the absence of a sufficient number of characteristic peaks. However, the development of peaks at ~19 and ~51° 2θ for co-precipitates (Figure 4.17) with no and lowest silicate concentration (i.e., Si:Fe ratios of 0 and 0.04) could be an indication of the formation of new mineral products during reductive dissolution. The preferential emergence of these XRD peaks in residual co-precipitates with lower initial solid phase Si:Fe ratios (0 to 0.04) may suggest that a greater degree of iron

cycling occurred during the biotic dissolution experiments and that low silica co-precipitates were more reactive towards dissimilatory microbial iron reduction.
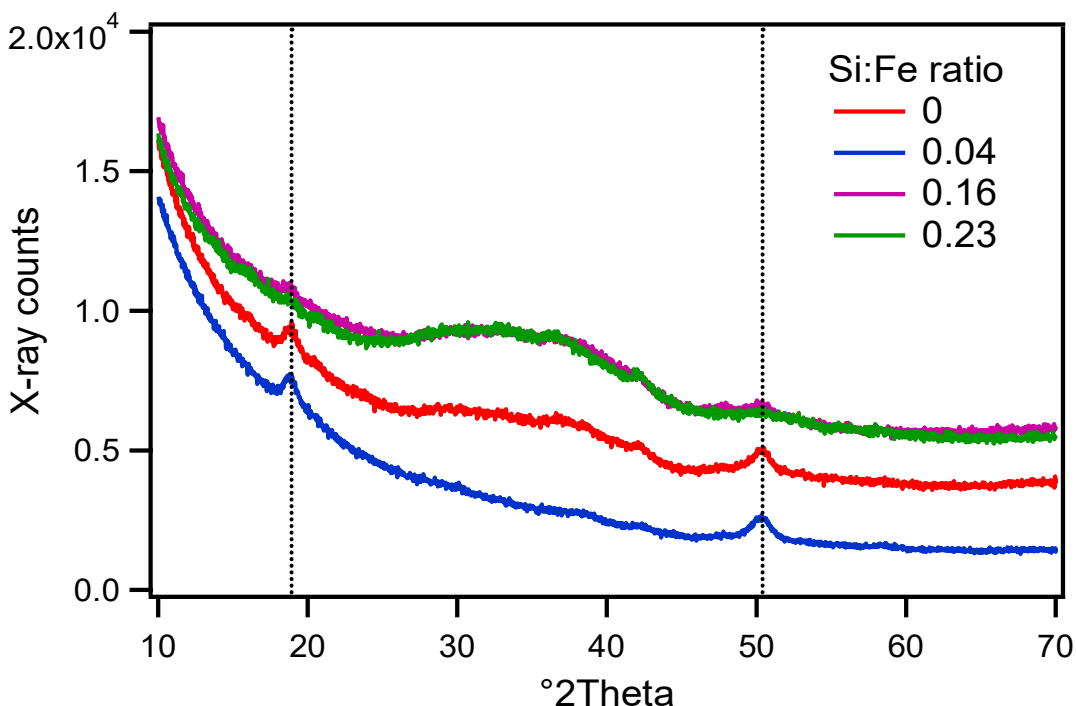


**Figure 4.17.** XRD spectra, collected in transmission mode, of the residual co-precipitates obtained after the completion of the dissolution experiments (350 hours) by *S. putrefaciens*. Experimental details are described in section 4.3.4.2.

## 4.5 Conclusions

This study investigates the reactivity of pure ferric iron precipitates and co-precipitates (i.e., Fe-P and Fe-P-Si) synthesized via two different methods; $Fe^{2+}$ oxidation and pH increase. The pure ferric precipitate obtained with the $Fe^{2+}$ oxidation synthesis method in the absence of phosphate and silicate is more reluctant towards reductive dissolution in buffered ascorbate-citrate solution than the corresponding precipitate obtained by the pH increase synthesis method. The opposite trend is observed for the ferric co-precipitates with silicate and phosphate. The lower reactivity of pure ferric precipitates obtained with the $Fe^{2+}$ oxidation method suggests the presence of more stable mineral phases compared to ferric precipitates obtained by the pH increase synthesis method.

The incorporation of phosphate into the ferric precipitates significantly increased the reactivity of the resulting co-precipitates, regardless of synthesis method. Between the two sets

of Fe-P co-precipitates, those derived from the $Fe^{2+}$ oxidation method exhibited higher solid phase P:Fe ratios and showed greater reactivity towards the reductive release of iron and associated phosphate.

Reactivity trends for Fe-P-Si co-precipitates obtained by the two different synthesis methods are consistent with those determined for Fe-P co-precipitates. The Fe-P-Si co-precipitates with a range of Si:Fe ratios were prepared by adding various concentrations of aqueous silicate with iron and phosphate during their synthesis. The incorporation of silicate into the co-precipitates (i.e., Si:Fe ratios) decreased the reactivity of the co-precipitates, without affecting the final solid phase P:Fe ratios. The dissolutions orders extracted from the kinetic data show that iron in the co-precipitates with higher solid phase Si:Fe ratios was heterogeneously distributed. Further, the initial release of silicate relative to iron (i.e., dissolved Si:Fe rations) from these co-precipitates in the buffered ascorbate-citrate solution were lower than the Si:Fe ratios initially present in the solids. These results potentially suggest that the fraction of iron mostly associated with silicate in the co-precipitates showed less reactivity towards reductive dissolution.

The reductive dissolution of the co-precipitates obtained with the $Fe^{2+}$ oxidation method was also conducted in the presence of an iron reducing bacteria *S. putrefaciens.* The XRD analysis on the residual (un-dissolved) co-precipitates suggests that the solids with higher Si:Fe ratios are more resistant to dissimilatory microbial iron reduction. This result agrees with the dissolution rate constants derived from the ascorbate-citrate extractions. Furthermore, the different reactivities shown by the two different sets of the (co)-precipitates suggest that the synthesis method plays an important role in controlling the chemical compositions as well as the structural arrangement of iron, phosphate and silicate in the solids. Therefore, the mobility of iron, phosphate, and silicate in aquatic environments may greatly depend on the aqueous phase chemical composition at the time of precipitation of ferric iron phases and the mechanism of precipitation.

# Chapter 5

## Internal phosphorus loading from marsh sediments: Effect of silicate under variable redox conditions

### 5.1 Summary

The potential influence of dissolved and co-precipitated silicate (Si) on the mobilization of phosphorus (P) from marsh sediment was investigated. Multiple sediment columns were constructed and the experiment was conducted in two phases. During phase-1, anoxic solutions of $Fe^{2+}$ with and without Si, prepared in Artificial Pore-Water (APW), were introduced to the columns horizontally from the bottom. The $Fe^{2+}$ reaching the surface sediments was oxidized by aerating the overlying waters to promote the formation of ferric (co)-precipitates. Phosphate for the co-precipitation with iron was not supplied with the APW but was released from the P rich sediments. The sediments also released Si to the aqueous phase, but the concentration of Si was higher during the period of $Fe^{2+}$ oxidation in the columns with added Si. During phase-2, two groups of columns with and without added Si from phase-1 were switched to anoxic water columns and the inflow solutions were replaced with APW without added $Fe^{2+}$ or Si. Meanwhile, the overlying water of the other flow through columns with no added Si from phase-1 remained aerated and the inflow solutions were replaced with (i) APW and (ii) APW with Si. The results show that the anoxic columns with added Si released a greater amount of Fe and P to the overlying waters. The release of Fe and P from the solid phase to the aqueous phase was also demonstrated via solid phase chemical analysis at the end of experiment. This result potentially indicates that ferric (co)-precipitates formed at higher aqueous Si:Fe ratios during oxic conditions show greater reactivity towards the reductive release of Fe and associated P under anoxic conditions. The aerated columns, which received Si enriched inflow solution during phase-2, released more P, indicating that dissolved Si increased the mobility of sediment P. However, the amounts of P release under anoxic conditions were substantially greater than the release under oxic conditions during phase-2. The results suggest that majority of P released by the anoxic sediments at the base of the flow through columns was immobilized in surface sediments under oxic conditions, potentially via P adsorption on mineral surfaces and via the incorporation of P in new precipitates.

## 5.2 Introduction

The analysis of the effects of dissolved and co-precipitated Si within simple model systems presented within the previous chapters (Chapter 2 to Chapter 4) elucidates the important underlying mechanisms of P release. The experiments in those studies were completed under highly controlled laboratory conditions. However, the chemical composition of natural sediments is complex where a plethora of processes may occur simultaneously. For example, the effect of dissolved silicate on the mobilization of P has been investigated by studying the adsorption and desorption of phosphate to goethite, a model ferric (hydr)oxides. However, naturally occurring sediments generally contain various minerals and organics with a range of point of zero charge (PZC) and have different binding affinities to dissolved P and Si (discussed in general introduction, section 1.5.3.2). Aqueous complexations of P and Si with other dissolved species, particularly metal ions e.g., $Ca^{2+}$ and $Mg^{2+}$, may also influence their interactions with minerals surfaces and hence, the mobilization of P.

Reactivity of iron-phosphate-silicate co-precipitates that were investigated in Chapter 4 are synthesized by chemical precipitation mechanisms; $Fe^{2+}$ oxidation and pH increase. These two synthesis methods have given rise to ferric (co)-precipitates with different reactivity. In addition, ferric iron precipitates resulting from $Fe^{2+}$ oxidation method may exhibit different physico-chemical proprieties depending on the dominant precipitation mechanisms; e.g., purely chemical or bacterially mediated. For example, Châtellier et al. (2004) has demonstrated that ferric oxides prepared via the oxidation of $Fe^{2+}$ mediated by iron oxidizing bacteria exhibit smaller particle size than that obtained via the oxidation under purely chemical condition. The presence of other co-precipitating dissolved constituents, e.g., silicate, may also influence the $Fe^{2+}$ oxidation mechanism as well as $Fe^{2+}$ oxidation rate differently under abiotic and biotic conditions (Gauger et al., 2016; Kinsela et al., 2016; Konhauser et al., 2007) (also discussed in section 1.6.3). Therefore, the dominant mechanism of $Fe^{2+}$ oxidation under various biogeochemical conditions may result in ferric (co)-precipitates with different reactivity towards reductive dissolution.

This study evaluates the potential multiple roles of Si on the mobilization of P through the interactions of Fe, P, and Si within the context of natural sediments. An experiment using lake sediments in a flow-through column system is presented, where experiments are designed to investigate the reactivity of ferric (co)-precipitates, form under variable concentrations of

dissolved Si, towards the reductive dissolution of Fe and the associated P. This study also evaluates the competitive effect of dissolved Si on the mobilization of P at the sediment-water interface. The relative importance of Si-mediated P mobilization under variable redox conditions is also discussed.

## 5.3 Materials and methods

### 5.3.1 Field sampling

Surficial sediment (top ~10 cm) was collected from West Pond (43°16'12.0" N 79°55'43.9" W) in Cootes Paradise Marsh (Figure 5.1a) on October 27, 2017. The mineralogical composition of surface sediments in this location is dominated by calcite and quartz, therefore the sediment pore-water is buffered by carbonate-bicarbonate equilibria (Parsons et al., 2017). The marsh has a history of high external P loading from a nearby wastewater treatment plant as well as from urban runoff. The sediments in this marsh contain high concentrations of P (57±4 μmol/g) (Parsons et al., 2017). The speciation of P in Cootes Paradise sediment, according to the data presented in Parsons et al. (2017), is shown in Figure 5.1b. The marsh experiences high internal P loading from sediments as well as extensive algal growth during summer (Kelton and Chow-Fraser, 2005).



(a)  (b)
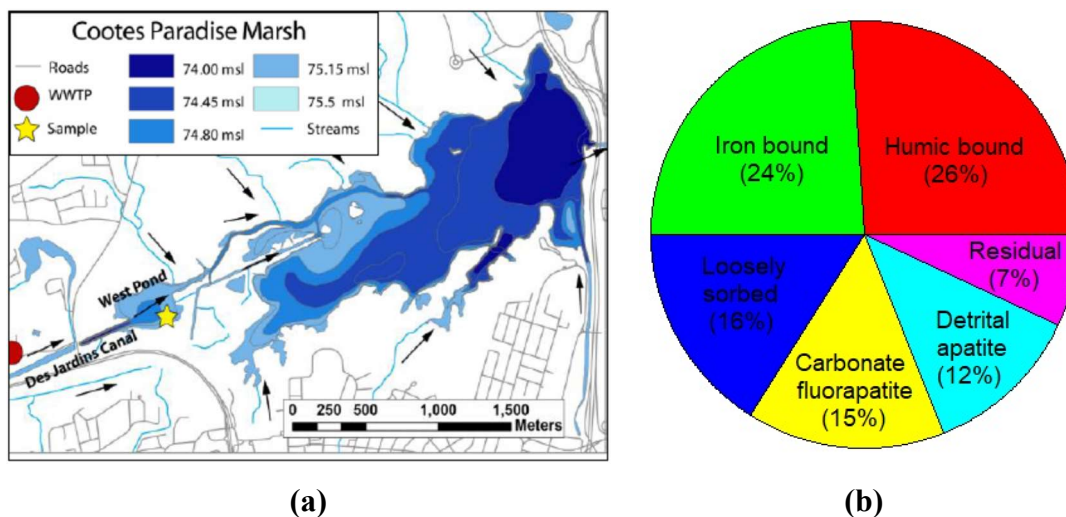
**Figure 5.1.** (a) Map of Cootes Paradise Marsh showing the location of sediment sampling. (b) Speciation of P in the Cootes Paradise sediment according to the data presented in Parsons et al. (2017).

### 5.3.2 Experimental setup

The experimental setup consisted of 14 sediment flow-through column systems (shown in Figure 5.2 for a single column), modified from Pallud et al. (2007). The cylindrical columns (Plexiglas, 12 cm height, 4.7 cm internal diameter) were filled with ~ 8.5 cm of sieved (500 µm) and homogenized sediments, which settled on top of two polypropylene filters (0.2 µm pore size), fitted to the bottom cap. The columns were fastened with a top cap with O-rings around the inside of the seal to prevent leakage. The inflow solution was introduced to each column through an opening in the bottom cap at a flow rate of 5 mL/h. The solutions were pumped vertically through the columns and were discharged through an opening at 10 cm height, which maintained an overlying water column of approximately 1.5 cm above the sediment surface. There were 2 cm of gas headspace above the top of the overlying water column. The experiment was conducted at 25°C. During the experiment, columns were subjected to different inflow solutions and overlying water column oxygenation conditions over two phases.
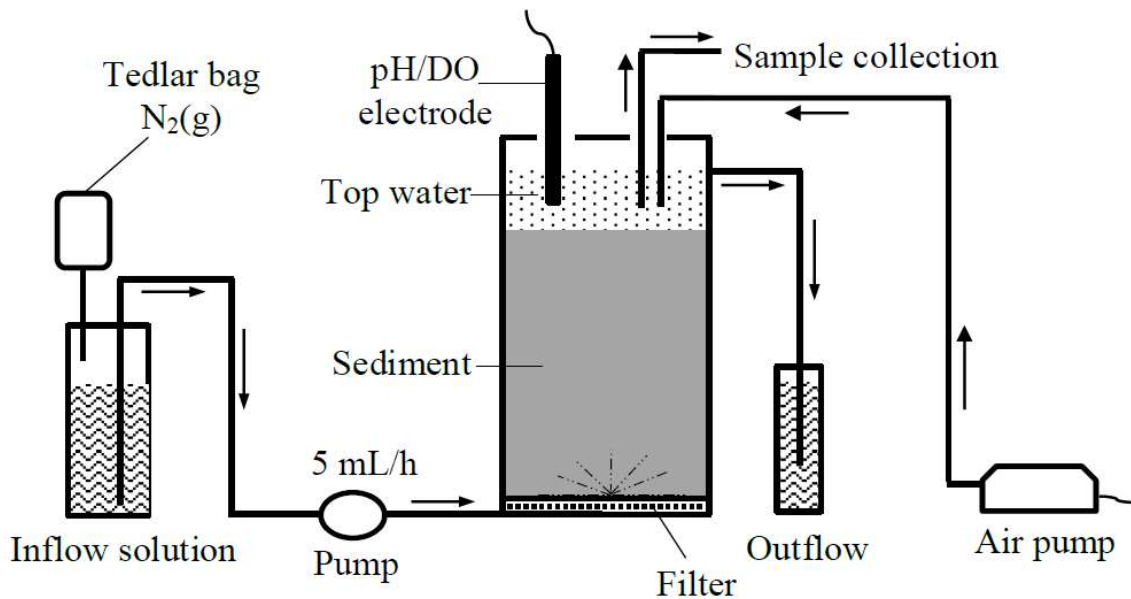


**Figure 5.2.** Schematic diagram of the experimental set-up of the flow-through column system during phase-1.

### 5.3.3 Solution preparation

For the preparation of anoxic inflow solutions, 18.2 MΩ cm$^{-1}$ water (Millipore) was boiled for 2 hours to enhance the removal of dissolved oxygen. The solutions were cooled to ~50-60°C

while being continuously purged with $N_2$ gas ($N_2$=99.998%, $O_2$=<3 ppm). Once cooled, the 18.2 $M\Omega$ $cm^{-1}$ deoxygenated water was introduced to an anaerobic chamber. The various inflow solutions were prepared within the anaerobic chamber according to Table 5.1. The pH of the solutions was adjusted to 7.00±0.02 using HCl and NaOH solutions. The inflow solutions used during phase-1 contained 125 µM bromide ($Br^-$) as an unreactive tracer to understand the solution transport properties of the sediments in the columns. Acetate was added to the inflow solution to avoid the depletion of natural organic matter in the sediment columns during the experiment. The solutions were stored inside the anaerobic chamber (98% $N_2$, 2% $H_2$ atmosphere, Coy Laboratory Products) for 2 to 3 days and capped before removal to the laboratory bench. A Tedlar bag filled with $N_2(g)$ (99.998% pure) was attached to each bottle of APW to maintain anoxic conditions and avoid formation of a vacuum inside the bottles due to solution pumping during the experiment.

**Table 5.1.** The chemical composition of the inflow Artificial Pore-Water (APW) solutions used for different columns during phase-1 and phase-2. The plus (+) and minus (-) signs indicate the presence and absence (respectively) of a chemical species in the inflow solutions of different columns, which are shown by the bold capital letters.

| Chemicals | Chemical Formula | Conc. (µM) | Phase-1 | | | Phase-2 | |
|---|---|---|---|---|---|---|---|
| | | | APW with $Fe^{2+}$ | APW with $Fe^{2+}$ and Si | APW | APW | APW with Si |
| | | | **A, B, C, D** | **E, F** | **G** | **D, F, G** | **B, C** |
| $Ca^{2+}$ | $CaCl_2 \cdot 2H_2O$ | 500 | + | + | + | + | + |
| $Mg^{2+}$ | $MgCl_2$ | 250 | + | + | + | + | + |
| $Fe^{2+}$ | $FeCl_2 \cdot 4H_2O$ | 1000 | + | + | - | - | - |
| Si | $Na_2O_3Si \cdot 9H_2O$ | 500 | - | + | - | - | + |
| Acetate | $CH_3COONa$ | 250 | + | + | + | + | + |
| $Br^-$ | KBr | 150 | + | + | + | - | - |
| HEPES | $C_8H_{18}N_2O_4S$ | 550 | + | + | + | + | + |

*NOTE: The concentration of $Ca^{2+}/Mg^{2+}$ in the inflow solutions was chosen according to the pore-water composition reported for the same field sampling site (Ridenour, 2017). HEPES (4-(2-hydroxyethyl)-1-piperazineethanesulfonic acid) was used an organic buffer to maintain the pH in the solutions as well as in the overlying waters.*

## 5.3.4 Experiments

Before beginning the experiment, the sediments in each column were equilibrated with an oxic solution of Artificial Pore-Water (APW) for 24 hours at 5.0 mL/h. Columns were divided into seven groups of duplicate columns: **A**, **B**, **C**, **D**, **E**, **F**, and **G** (Figure 5.3). All inflow solutions

during both phases were anoxic. Throughout the experiment, aqueous samples were collected from overlying water and aliquoted for the analyses of dissolved chemical constituents.

Phase-1 lasted from 0 to 240 hours. Three types of inflow solutions were used: (i) APW with $Fe^{2+}$ (groups **A**, **B**, **C,** and **D**), (ii) APW with $Fe^{2+}$ and Si (groups **E** and **F**), and (iii) APW only with no Fe or Si added (group **G**). The concentrations of $Fe^{2+}$ in the inflow solutions (filtered through 0.2 μm size polypropylene syringe filter) did not change throughout the experiment as analyzed by the ferrozine method (see section 5.3.5.1 for sample preparation and analysis). To promote oxidation of $Fe^{2+}$ in the surface sediments, the overlying water of all columns was sparged with air using an air pump (Figure 5.2). Holes in the top cap kept the overlying water column open to the atmosphere and enabled the collection of aqueous samples as well as pH and DO measurements using electrodes. Columns in groups **A** and **E** were sacrificed after phase-1 and frozen at -20°C for solid phase analyses.

Phase-2 lasted from 240 to 928 hours. Groups **B** and **C** were kept aerated but were switched to inflow solutions of (i) APW and (ii) APW and Si, respectively. Aqueous sample collections and the measurements of pH and DO were conducted as in phase-1. Groups **D**, **F**, and **G** were switched to an APW only inflow solution and to anoxic water column conditions. To create anoxic conditions, the holes in the top caps were closed with plastic bolts covered in silicon grease to create an airtight seal. The headspace of each column (**D**, **F**, and **G**) was connected to a Tedlar bag filled with $N_2(g)$ to avoid the formation of vacuum during sampling (not shown in Figure 5.2). Aqueous samples were collected periodically from the overlying waters through a luer-lock valve and a tygon tube, which passed through one of the plastic bolts in the top holes (not shown in Figure 5.2). After each sampling event, the headspace of all columns was purged with $N_2(g)$ to minimize potential air diffusion into the columns. Additionally, ~10 mL of aqueous sample was collected from each column on alternate days and moved to an anaerobic chamber for measurement of pH and DO. After phase 2, columns **D** and **F** were frozen at -20°C for solid phase analyses.
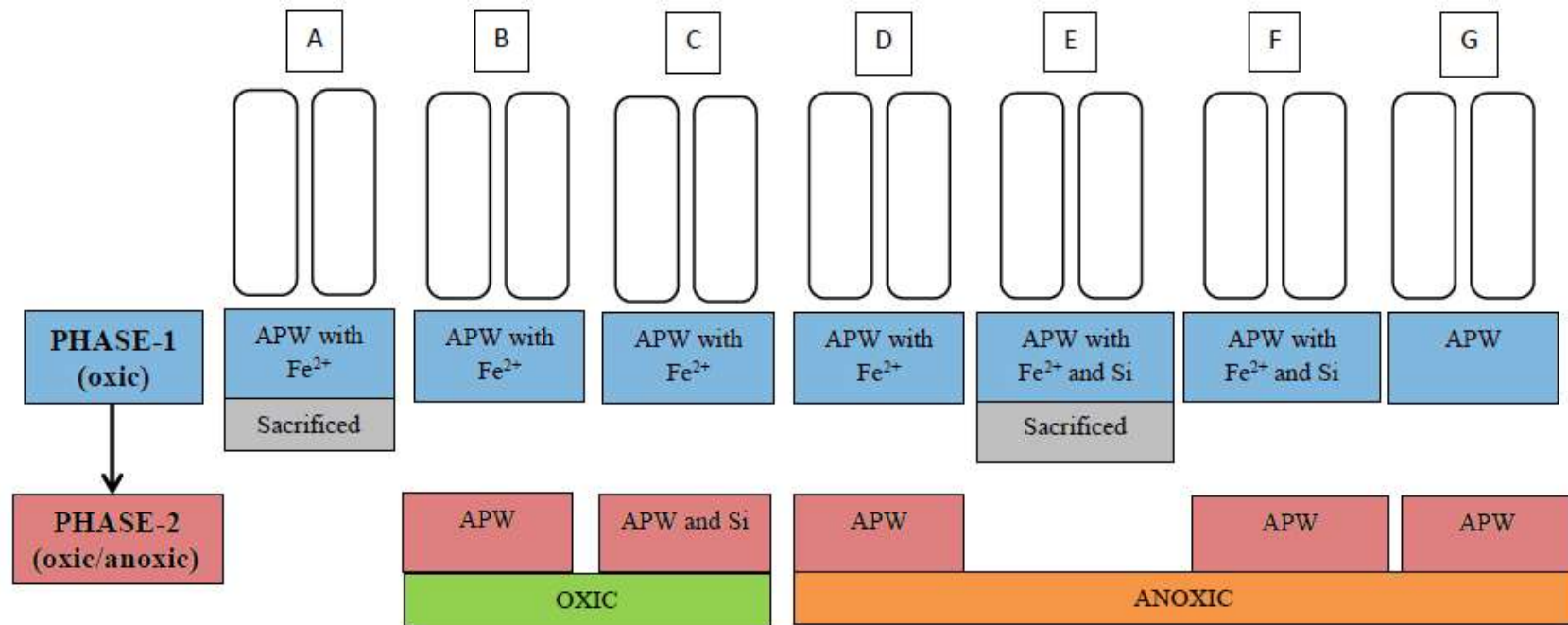
**Figure 5.3.** Schematic diagram of sediment columns and experimental conditions during phase-1 (0 to 240 hours) and phase-2 (240 to 940 hours). The capital letters (**A**, **B**, **C**, **D**, **E**, **F**, and **G**) indicate groups of duplicate columns. Inflow solutions of Artificial Pore-Water (APW) with or without amendments of $Fe^{2+}$ and/or Si for each column group are indicated in the blue (phase-1) and pink (phase-2) boxes. All inflow solutions during both phases were anoxic. The overlying water column of all columns was aerated and open to the atmosphere during the first phase. In the second phase, groups **B** and **C** continued to be aerated, while groups **D**, **F** and **G** were sealed from the atmosphere to create anoxic conditions (see text for details). Groups **A** and **E** were sacrificed after phase-1 for solid phase analyses.

### 5.3.5 Analytical methods

### 5.3.5.1 Analyses of overlying waters

Aqueous samples collected from the overlying waters were filtered through 0.2 μm (pore size) syringe filters (polypropylene except when indicated otherwise) and stored at 4°C until analysis. For the analysis of major elements, e.g., Fe, Mn, Si, P, Ca and Mg, 2 mL of filtered sample was added to 6 mL of 0.5 M HCl and analyzed by Inductively Coupled Plasma Optical Emission Spectroscopy (ICP-OES, Thermo Scientific iCAP 6300). The analytical details with ICP-OES are discussed in Chapter 2 (section 2.3.2). The samples for the determination of dissolved $Fe^{2+}$ were prepared by adding 0.8 mL of filtered aqueous sample to 0.8 mL of 0.5 M HCl and analyzed by the ferrozine method (Viollier et al., 2000). For the determination of dissolved organic carbon (DOC), 1 mL of filtered sample was diluted with 6 mL water and analyzed using an organic carbon analyzer (TOC-L, Shimadzu). The concentrations of anions ($Br^-$, $NO_3^-$, $SO_4^{2-}$) were analyzed by ion chromatography (Dionex ICS-5000) in the aqueous samples filtered through 0.2 μm pore size polyethersulfonate syringe filter.

### 5.3.5.2 Analyses of sediments

The frozen sediment columns were sliced with a saw at 0.5 cm intervals from 0 to 2 cm depth, then in 1 cm intervals between 2 and 5 cm depth of sediment (Figure 5.4). The sliced sediments were returned to -20°C and freeze-dried. Subsamples (except the subsamples 2 to 3 cm and 4 to 5 cm) of the freeze-dried sediments were extracted in two ways, 1) by a buffered ascorbate-citrate solution (BAC) at pH ~7.5 and 2) by 1.0 M HCl. The solutions were prepared in deoxygenated water and mixed with sediments inside an anaerobic chamber. Buffered ascorbate-citrate solution (pH ~7.5) was prepared with 10 g of ascorbic acid ($C_6H_8O_6$, Sigma, ≥98%), 50 g of sodium citrate ($HOC(CO_2Na)(CH_2CO_2Na)_2 \cdot 2H_2O$, Sigma, ≥99%) and 50 g of sodium bicarbonate ($NaHCO_3$, Sigma, 99.5-100.5%) to give final concentrations of approximately 0.057 M ascorbic acid, 0.17 M sodium citrate and 0.59 M $NaHCO_3$. The solution of HCl (1.0 mM) was prepared by diluting concentrated HCl (ACS 37%, Sigma Aldrich) in water, and the solution was purged with $N_2(g)$ before introducing it to the anaerobic chamber. Total extractions (24 hours) with BAC and HCl (separately) were conducted for sediments from columns **A**, **D**, **E** and **F** as well as initial sediments that were collected at the

time of sampling. The kinetic extractions (0 to 24 hours) were conducted only for surface sediments (0 to 0.5 cm) from columns **A** and **E** and the initial (pre-experimental) sediment.
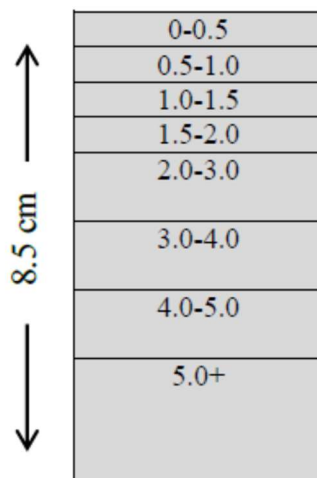


**Figure 5.4.** Schematic diagram showing the sliced fractions of each sediment column. The sliced subsamples (except the subsamples 2 to 3 cm and 4 to 5 cm) were used for the solid phase analyses.

### 5.3.5.2.1 Solid phase extractions

Within an anaerobic chamber, 10 mL of BAC or HCl was added to a polypropylene centrifuge tube (VWR, 50 mL size) containing 5 mg (weighed to the nearest 0.1 mg) of dried sediment. The tubes were capped, using Teflon tape for an airtight seal, and removed from the anaerobic chamber. The tubes were then transferred to an incubator (Glass-Col, 099A RD4512) where they were shaken at 30 rpm for 24 hours at 22°C. After 24 hours of equilibration, the suspensions were centrifuged at 1690 RCF for 15 min (Thermo Scientific, Sorvall ST 16R) and the supernatants were filtered through 0.2 μm pore size syringe filters. 3 mL of the filtered supernatants was added to 6 mL of 0.5 M HCl and the samples were stored at 4°C until they were analyzed for Fe, Mn, P, and Si by ICP-OES. The concentrations of $Fe^{2+}$ in the aqueous fractions, extracted with 1M HCl, were also quantified by the ferrozine method (Viollier et al., 2000).

### 5.3.5.2.2 Kinetic extractions

Freeze-dried sediment (450 mg, weighed up to 0.1 mg) was added to 150 mL of BAC solution inside an anaerobic chamber. The suspension was stirred at 400 rpm on a magnetic stir plate (Corning stirrer, multi-position) at 22°C for 24 hours. The suspensions were collected periodically and filtered through 0.2 μm pore size syringe filters. 2 mL of the filtered samples were added to 7 mL of 0.5 M HCl and stored at 4°C until analysis for Fe, Si, and P using ICP-OES.

## 5.4 Results and discussion
### 5.4.1 Solution transport properties of the sediment columns

The transport properties of the sediments in the columns are shown in terms of $Br^-$ break-through curves of $C_t/C_0$ versus pore-volume (Figures 5.5), where $C_t$ is the $Br^-$ concentration in the overlying water at time t, and $C_0$ is the $Br^-$ concentration in the inflow solution. Sediment pore-volume was calculated according to Equation 5.1 where $p_t$ is the number of sediment pore-volumes elapsed at time t (h), Q is the flow rate (5 $cm^3$/h), L is the length (height) of the sediment column in centimeters (cm), A is the cross-sectional area of the sediment column in $cm^2$, and $\emptyset$ is the porosity of the sediment. Porosity was calculated from sediment bulk density ($\rho_{bulk}$) and particle density ($\rho_{particle}$) using Equation 5.2. Bulk density ($\rho_{bulk}$) was measured as 1.21±0.05 $g/cm^3$ by weighing about 50 mL of wet sediment, and the particle density ($\rho_{particle}$) was assumed as 2.65 $g/cm^3$, which was taken from a previous study (Ridenour, 2017). Note that the sediments used in this study and in Ridenour's (2017) were collected from the same location in Cootes Paradise Marsh.

$$p_t = \frac{Q \cdot t}{\emptyset \cdot L \cdot A} \dotfill (5.1)$$

$$\emptyset = 1 - \frac{\rho_{bulk}}{\rho_{particle}} \dotfill (5.2)$$
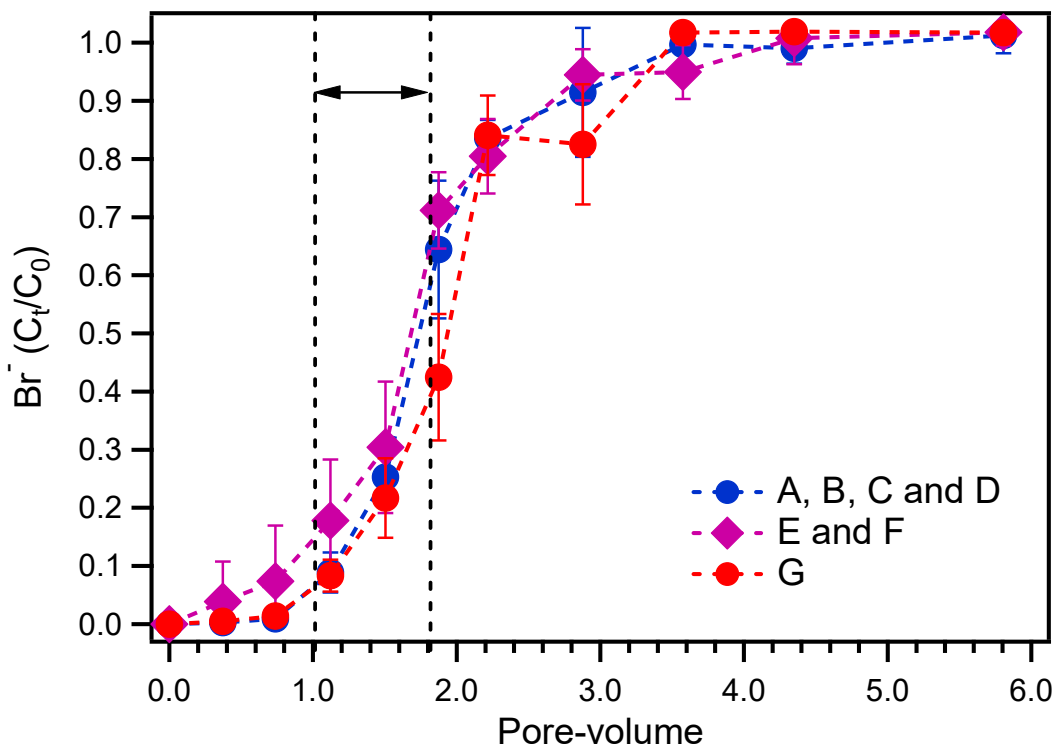
**Figure 5.5.** Break-through curves for Br⁻ for the columns during phase-1. The double-headed arrow shows the delayed response of break-through Br⁻ concentrations (discussed in this section). Error bars represent the range of values measured between the columns as shown on the figure by the capital letters.

Figure 5.5 shows that the columns achieved a break-through for Br⁻ at ~1.8 pore-volumes at about 29 hours, which corresponds to a $C_t/C_0$ ratio of ~0.65. The surface sediments in the columns should have achieved the break-through concentration of Br⁻ at one pore-volume, which corresponds to at $C_t/C_0$ ratio of ~0.10 (at ~16 hours, one pore-volume ≈ 0.08 L) according to Equation 5.1. Note that Equation 5.1 considers the length of the column which is filled with sediment. However, the columns had about 1.5 cm of water on the top of sediments. Therefore, the delayed break-through Br⁻ concentration (shown by the double-headed arrow in Figure 5.5) achieved at ~1.8 pore-volumes instead of the theoretically expected one pore-volume (~0.08 L), could have resulted due to dilution of Br⁻ in the overlying water. The attenuation of Br⁻ via the oxidative bromination of organic compounds in sediments may have also contributed to this delay (Leri and Ravel, 2015). However, the Br⁻ break-through curves show that all columns were similar in terms of their solution transport properties (Figure 5.5).

### 5.4.2 pH and DO in the overlying waters

The pH of the sediment pore-water was ~8.50 prior to the experiment. pH decreased to 7.60±0.10 after equilibrating the sediments with the APW solution and remained around this value throughout experimental phase-1. During phase-2, pH decreased to ~7.25±0.05 in the overlying waters of the sealed anoxic columns (**D**, **F,** and **G**). The drop of pH in these anoxic columns could be attributed to the build-up of dissolved $CO_2$ in the overlying water as a by-product of fermentation or organic matter oxidation coupled to the reduction of nitrate, sulfate or $Fe^{3+}/Mn^{4+}$-phases in sediments. This explanation is consistent with the observation that the pH of the overlying waters of columns **B** and **C**, which remained open to the atmosphere and aerated during phase-2, did not change from phase-1 to phase-2.

During phase-1, the concentrations of DO in the overlying waters of the $Fe^{2+}$ addition columns (**A**, **B**, **C**, **D**, **E,** and **F**) and of the control column (**G**) were ~3.5±0.5 and ~2.5±0.5 ppm, respectively. The slightly lower DO levels in the control column (**G**) could have been by the consumption of $O_2$ during the aerobic respiration of DOC, which was higher in the control column (**G**) (see section 5.4.3, Figure 5.6). During phase-2, the DO concentrations in the overlying waters of the anoxic columns (**D**, **F,** and **G**) were below the detection limit (0.1 mg/L), indicating that anoxic conditions at the sediment-water interface was achieved. The DO concentrations for oxic columns **B** and **C** during phase-2 did not change (~3.5±0.5 ppm) from phase-1.

### 5.4.3 DOC, nitrate, and sulfate in the overlying waters

At the beginning of phase-1, the average concentration of DOC in the overlying water of the columns was 64±8 mg/L. After passing one 1.8 pore-volume of APW (~29 hours), the concentration of DOC increased compared to the inflow solution DOC concentration (102 mg/L), presumably due to the added HEPES and acetate (Figure 5.6). Among all the columns, the DOC concentration was higher for the control column (**G**). The inflow solution supplied to the duplicate **G** columns did not contain $Fe^{2+}$ while the inflow solutions of the other columns (**A**, **B**, **C**, **D**, **E,** and **F**) contained $Fe^{2+}$.

The addition of $Fe^{2+}$ to the other columns (**A**, **B**, **C**, **D**, **E,** and **F**) could have decreased the concentration of DOC in the overlying waters by a few possible reasons. For example, DOC from the aqueous phase can be removed via the adsorption on or via the co-precipitation

with ferric (hydr)oxides during the oxidation of $Fe^{2+}$ at the sediment-water interface (Adhikari et al., 2017; Du et al., 2018; Grybos et al., 2009; Zhao et al., 2017). The removal of DOC, via these mechanisms (adsorption and co-precipitation) could be higher in the $Fe^{2+}$ addition columns (**A**, **B**, **C**, **D**, **E,** and **F**) where greater amounts of $Fe^{3+}$ precipitation was likely in the surface sediments in comparison to the column with no added $Fe^{2+}$ (**G**).
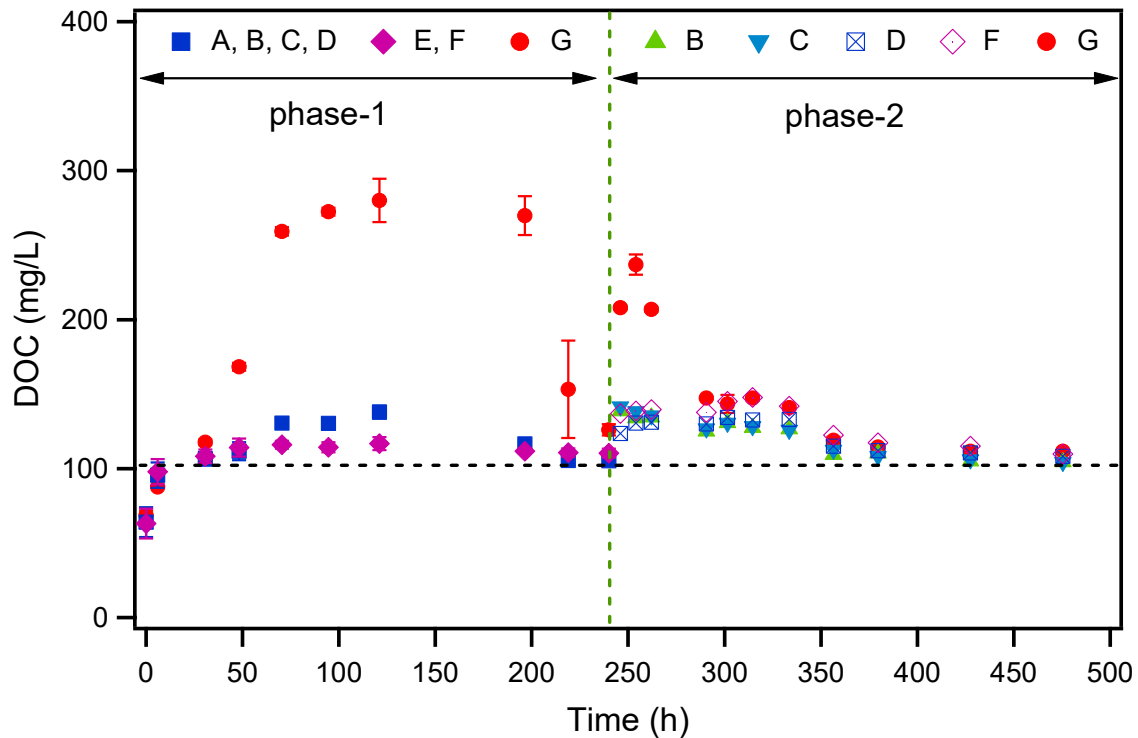


**Figure 5.6.** Concentrations of DOC in the overlying waters of the columns as a function of time. The inflow solutions during phase-1 for the columns were (i) APW with $Fe^{2+}$ (**A**, **B**, **C**, and **D**), (ii) APW with $Fe^{2+}$ and Si (**E** and **F**), and (iii) APW only (**G**). Before the start of phase-2, the inflow solutions for columns **B** and **C** were replaced with APW and APW with Si, respectively while that of **D**, **F** and **G** were replaced with APW only. Error bars represent the range of values measured between the columns shown on the figure by the capital letters.

Dissolved $Fe^{2+}$ can increase the activity of extracellular enzymes, such as phenoloxidase, which can enhance the decomposition of organic matter under anoxic conditions (Hall and Silver, 2013; Van Bodegom et al., 2005). In addition, $Fe^{2+}$ reacts with hydrogen peroxide ($H_2O_2$), and produces highly reactive ·OH radicals (via the Fenton reactions), which act as a non-selective oxidant for a wide variety of organic matter (Hall and Silver, 2013; Sekar and DiChristina, 2014). Thus, the generation of ·OH radicals could have decreased DOC

concentrations in the overlying water through the oxidation of organic matter. $H_2O_2$ can be produced under both oxic and anoxic conditions via abiotic and biotic processes (Hall and Silver, 2013; Sekar and DiChristina, 2014; Wood, 1994). The abiotic production of $\cdot OH$ via the Fenton reactions is shown by the following three reactions, which proceeds with the oxidation of $Fe^{2+}$ (Hall and Silver, 2013).

$$Fe^{2+} + O_2 + H^+ \rightarrow Fe^{3+} + \cdot O_2H \qquad (i)$$

$$Fe^{2+} + H^+ + \cdot O_2H \rightarrow H_2O_2 + Fe^{3+} \qquad (ii)$$

$$Fe^{2+} + H_2O_2 \rightarrow \cdot OH + Fe^{3+} + OH^- \qquad (iii)$$
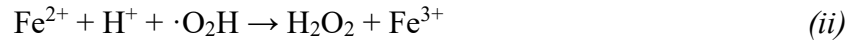
During phase-2, the DOC concentrations in the overlying waters of columns **D**, **F** and **G** increased immediately following the end of phase-1 and the onset of anoxic conditions. This increase of DOC concentrations may have been caused by the reductive dissolution of $Fe^{3+}$-OC co-precipitates (Adhikari et al., 2017; Zhao et al., 2017). Such co-precipitates could have formed under oxic conditions during phase-1 since DOC with multiple functional groups has been known to occupy the surface or structural part of metal (hydr)oxides (Adhikari et al., 2017; Du et al., 2018; Grybos et al., 2009; Zhao et al., 2017). This co-precipitated OC may be released to the aqueous phase during the reductive dissolution of iron co-precipitated with OC (Adhikari et al., 2017; Zhao et al., 2016). The results show that the release of DOC from the control column (**G**) was higher than the $Fe^{2+}$ addition columns (**D** and **F**) under anoxic conditions during phase-2. This higher release of DOC by the control column (**G**) potentially suggests that higher DOC concentrations in the overlying water of this group of columns resulted in a greater amount of DOC incorporation in $Fe^{3+}$-OC co-precipitates under oxic condition during phase-1.

The concentrations of $NO_3^-$ and $SO_4^{2-}$ in the overlying waters, before the start of Phase-1 but after equilibrating with an oxic APW inflow solution, were $30\pm20$ µM and $100\pm60$ µM. The concentrations of $NO_3^-$ and $SO_4^{2-}$ in the overlying waters decreased to below their detection limits ($NO_3^-$: 0.8 µM and $SO_4^{2-}$: 1.3 µM), within the first 1.8 pore-volume (~29 h), presumably due to the influence of anoxic inflow solutions. Flowing of anoxic solution (with no $NO_3^-$ and $SO_4^{2-}$) through the columns was likely to remove $NO_3^-$ or $SO_4^{2-}$ from the pore-water as well as from the overlying water with the outflow. The anoxia promoted

denitrification and sulfate reduction below the surface sediments may also cause the depleted $NO_3^-$ and $SO_4^{2-}$ conditions in the overlying waters.

## 5.4.4 Formation and dissolution of ferric (co)-precipitates: effect of silicate

During phase-1, $Fe^{2+}$ was oxidized in surface sediments of the columns (**A**, **B**, **C**, **D**, **E**, and **F**) under variable dissolved Si concentrations. This was achieved by introducing solutions of $Fe^{2+}$ prepared in APW to the base of the sediment columns, with and without added Si. For example, Si was absent in the inflow solution of columns **A**, **B**, **C**, and **D**, while it was present in the inflow solution of columns **E** and **F**. Although P was not added to the inflow solutions, it was expected to be released from the P rich sediments and form co-precipitate with Fe during the oxidation of $Fe^{2+}$. The inflow solution of the control column (**G**) did not contain either $Fe^{2+}$ or silicate.

Columns **A** (APW with $Fe^{2+}$) and **E** (APW with $Fe^{2+}$ and Si) were not continued to phase-2 as they were sacrificed for solid phase analyses after phase-1. Columns **D** and **F** were similar to columns **A** and **E** during phase-1. Columns **D**, **F**, and control column **G** were continued to phase-2 by creating anoxic water columns and by replacing the inflow solutions with anoxic APW solution. The objective of this part of the experiment was to understand the reactivity of ferric (co)-precipitates, formed in the absence and presence of added Si, towards reductive dissolution under anoxic conditions. Experimental results from columns **A**, **D**, **E**, **F**, and **G** are discussed separately based on the analysis of overlying waters and the chemical extractions of solid sediments.

The total amounts of Fe, Mn, Si, P, Ca and Al released from all the columns during the different experimental phases are shown in Table 5.2. The release of each element is shown in terms of cumulative release according to Equation 5.3:

$$m_{cum(t)} = m_{t_1} + m_{t_2} + m_{t_3} + \cdots\cdots + m_t \quad \cdots\cdots\cdots\cdots\cdots\cdots\cdots (5.3)$$

where $m_{cum(t)}$ is the cumulative release (in µmol) of an element from a sediment column to the overlying water at time t, and $m_{t_1}$, $m_{t_2}$, $m_{t_3}$ and $m_t$ are the amounts of that element (in µmol) released in the overlying water at time $t_1$, $t_2$, $t_3$, and $t$, respectively.

**Table 5.2.** Total amounts (μmol) of Fe, Mn, P, Si, Ca and Mg released from sediment columns during the experiment based on the analysis of overlying waters by ICP-OES. The "±" sign indicates the range of minimum and maximum values measured between the columns.

| Column | Oxic/ anoxic | Inflow solution | Fe | Mn | P | Si | Ca | Mg |
|---|---|---|---|---|---|---|---|---|
| | | | | | Phase-1 | | | |
| **A, B, C, D** | Oxic | APW+Fe$^{2+}$ | 13±11 | 20±3 | 73±9 | 293±26 | 2133±364 | 663±89 |
| **E, F** | Oxic | APW+Fe$^{2+}$+Si | 7±4 | 22±3 | 68±10 | 541±18 | 2069±57 | 675±48 |
| **G** | Oxic | APW | 27±1 | 50±12 | 74±2 | 359±22 | 2970±12 | 937±59 |
| | | | | | Phase-2 | | | |
| **D** | Anoxic | APW | 226±13 | 54±0 | 110±7 | 825±67 | 3847±126 | 841±1 |
| **F** | Anoxic | APW | 320±45 | 68±4 | 123±42 | 974±112 | 4135±70 | 803±14 |
| **G** | Anoxic | APW | 225±37 | 61±5 | 132±16 | 848±48 | 4473±86 | 812±19 |

## 5.4.4.1 Iron cycling

### 5.4.4.1.1 Iron in the overlying waters

During phase-1, all sediment columns released small amounts of iron (Fe) from sediments to the overlying waters (Table 5.2, Figure 5.7). For the columns where Fe was present in the inflow solution (**A**, **D**, **E**, and **F**), the total amount of Fe that reached the overlying water was less than 4% of the total input of 660 μmol Fe$^{2+}$ during Phase-1. Thus, the sediments attenuated more than 96% of the added Fe$^{2+}$. This is consistent with the effect of aeration in the water column and the subsequent oxidation of aqueous Fe$^{2+}$ to solid Fe$^{3+}$ under these conditions. The added Fe$^{2+}$ can also be attenuated via chemical precipitation with phosphate, sulfide, and carbonate under anoxic conditions below the top oxic layer of the surface sediments (Connell et al., 2015; Gächter and Müller, 2003; Orihel et al., 2017; Rothe et al., 2014). However, the removal of Fe$^{2+}$ via this chemical precipitation mechanism was not evident from the analyses of solid sediments. Because the concentrations of Fe$^{2+}$ in the solid sediments throughout columns **A** and **E** (analysed after phase-1) were comparable to the Fe$^{2+}$ concentration measured for the initial sediment (shown latter in this section, Figure 5.9d).

The release of Fe in the overlying waters of columns **A, D**, **E, F**, and **G** is shown in Figure 5.7. Columns **E** and **F** received Si with the Fe$^{2+}$ containing inflow solutions during phase-1, but columns **A** and **D** did not. The added Si to columns **E** and **F** did not make a significant difference in Fe release from the sediments in comparison to columns **A** and **D** (Figure 5.7 and Table 5.2).

The control column (**G**) that did not receive $Fe^{2+}$ with the inflow solution, released a greater amount of Fe (during phase-1) than the columns (**A**, **D**, **E** and **F**) with added $Fe^{2+}$ (Table 5.2, Figure 5.7). The release of Fe from the control column (**G**) indicates that the sediments were a source of Fe. While the overlying waters were aerated during this phase, sediments below the oxic top thin sediment layer were primarily anoxic due to the influence of anoxic inflow solutions. Thus, the release of Fe via the reductive dissolution of sediment $Fe^{3+}$-minerals was possible, even for the columns with added $Fe^{2+}$. The greater release of Fe from the control column (**G**) could have resulted from the low DO levels ($\sim$2.5$\pm$0.5 mg/L) in the overlying water, which perhaps was not sufficient for the complete oxidation of $Fe^{2+}$ released from the sediments.
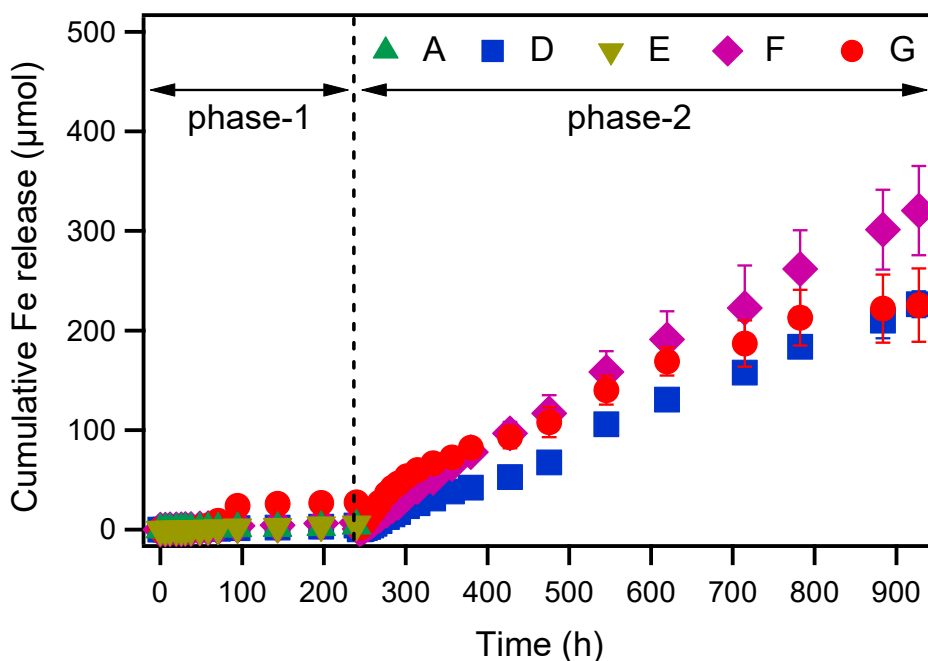


**Figure 5.7.** Cumulative release of Fe to the overlying waters during phase-1 and phase-2 as a function of time. The inflow solutions for the columns during phase-1 were (i) APW with $Fe^{2+}$ (**A** and **D**) and (ii) APW with $Fe^{2+}$ and Si (**E** and **F**), and (iii) APW only (**G**). Before the start of phase-2, columns **A** and **E** were sacrificed for solid phase analysis while columns **D**, **F** and **G** were continued in phase-2 and the inflow solutions were replaced with APW only. Error bars represent the range of values measured between duplicate columns.

During experimental phase-2, there was a greater release of Fe from all sediment columns compared to phase-1 (Table 5.2, Figure 5.7). About 90% of the released iron was in the form of $Fe^{2+}$, regardless of the type of the columns based on the inflow solution during phase-1 (see supplementary material, Figure SM-5.1). This ratio of $Fe^{2+}$ to total Fe ($\sim$0.9)

indicates that the release of Fe during this phase was primarily due to the reductive dissolution of solid phase $Fe^{3+}$ in sediments under anoxic conditions, although dissolution of solid phase $Fe^{2+}$ was also possible. The control column (**G**) initially released a greater amount of Fe even under anoxic conditions than columns **D** and **F** (Figure 5.7), although these latter columns contained greater amounts of Fe due to the accumulation of Fe (more than 96% of added iron) from the inflow solution during phase-1.

The concentrations of DOC in the overlying waters were similar for all columns at the end of phase-1 (Figure 5.6). However, the concentrations of DOC in column **G** increased above that of the other columns upon the onset of anoxic conditions during phase-2 (Figure 5.6). This increase in DOC concentrations during the initial time of phase-2 (Figure 5.6) was possibly due to the dissolution of co-precipitated organic carbon (OC) with $Fe^{3+}$ that likely formed during phase-1. As the concentrations of DOC was higher in the control column (**G**) during phase-1, it was possible that a greater amount of OC co-precipitated with solid $Fe^{3+}$ phases during phase-1, leading to a greater initial release under anoxic conditions during phase-2. The released DOC in the overlying water can further be used in the microbial reduction of ferric (co)-precipitates formed in surface sediments (Adhikari et al., 2017). Thus, the higher concentrations of DOC in the overlying water of the control column (**G**) may explain the higher initial release of Fe (during phase-2) by this column in comparison to columns **D** and **F**. However, the total mass (average) of Fe released from column **F** ($320\pm45$ µmol) was 1.4 times higher than the release by the control column (**G**) (Table 5.2 and Figure 5.7), with comparable amounts of Fe released by the columns **D** and **G**.

During phase-2, column **F** released 1.4 times more Fe than column **D** (Figure 5.7). Columns **D** and **F** were similar in terms of their set-up and the solution transport properties. The concentrations of DO, DOC, and pH in their (**D** and **F**) overlying waters were also comparable. The only difference between columns **D** and **F** was that, column **F** received Si with the inflow solution during phase-1 whereas column **D** did not. The higher release of Fe from column **F** during phase-2 appears to be the effect of added Si during phase-1. This result suggests that the dissolved Si added (with $Fe^{2+}$) to the inflow solution (during phase-1) of column **F** increased the reactivity of ferric (co)-precipitates towards microbial reduction (during phase-2) under anoxic conditions.

### 5.4.4.1.2 Iron in the sediments

The final chemical compositions of the sediments from columns **A**, **D**, **E** and **F** as well as the initial (pre-experimental) sediments were evaluated through chemical extractions with solutions of buffered ascorbate-citrate (BAC) and 1 M HCl. The BAC extractable iron, $Fe_{(BAC)}$, generally represents the labile and reducible fraction of Fe (Hyacinthe et al., 2006; Larsen et al., 2006; Raiswell et al., 2010). Dilute HCl (1.0 M) solution, mostly extracts the amorphous fraction of $Fe^{3+}$ minerals (e.g., ferrihydrite), or crystalline $Fe^{2+}$ minerals (e.g., vivianite or siderite) (Wallmann et al., 1993). Therefore, both of the solutions are capable of extracting some common pool of iron from sediments.

The results from the extraction of sediment by the BAC solution show that the concentrations of $Fe_{(BAC)}$ (µmol Fe per gram of dried sediment) in the post experimental surface sediments (0 to 0.5 cm) of columns **A** and **E** were comparable (117.08±5.7 and 118.8±5.6 µmol/g, respectively), which are about 1.7 times higher than that of the initial sediments (Figure 5.8a). Within columns **A** and **E**, the concentrations of $Fe_{(BAC)}$ were also higher in surface sediments (0 to 0.5 cm)  relative to the bottom sediments (Figure 5.8a). This result indicates that the accumulation of Fe primarily took place in the surface sediments (0 to 0.5 cm) where the greatest oxidation of $Fe^{2+}$ likely occurred. Furthermore, similar $Fe_{(BAC)}$ concentrations in the surface sediments of columns **A** and **E** suggest that the added Si to column **E** (during phase-1) did not influence the retention of iron, as ferric (co)-precipitate, via the oxidation of $Fe^{2+}$. This observation is consistent with the comparable concentrations of Fe in the overlying waters of columns **A** and **E** during phase-1 (Figure 5.7 and Table 5.2).

Column **A** (APW with $Fe^{2+}$) and **E** (APW with $Fe^{2+}$ and Si) were treated similarly to the columns **D** and **F** during phase-1. The sediments of columns **A** and **E** were analyzed after phase-1, but columns **D** and **F** were analyzed after phase-2. The concentrations of $Fe_{(BAC)}$ in the surface sediments (0-0.5 cm) of columns **A** and **E** were similar (Figure 5.8a), while that of columns **D** and **F** were lower, with **F** more depleted than **D** (Figure 5.8b and 5.8c). Assuming that the concentrations of $Fe_{(BAC)}$ in columns **A** and **E** were the initial $Fe_{(BAC)}$ concentrations in columns **D** and **F**, respectively at the start of phase-2, ~13% of $Fe_{(BAC)}$ from column **D** and ~26% of $Fe_{(BAC)}$ from column **F** were released from the surface sediments (0 to 0.5 cm) during phase-2. This observation is consistent with the overlying water chemistry of the columns (Table 5.2 and Figure 5.7) where column **F** released ~1.4 times greater amounts of Fe

compared to column **D**, suggesting that column **F** was more depleted in $Fe_{(BAC)}$ after phase-2. Therefore, a greater release of Fe from column **F** than column **D** under anoxic conditions (phase-2) can be attributed to the effect of added Si to column **F**, where $Fe^{2+}$ oxidation occurred in the presence of higher Si concentrations than in **D**.
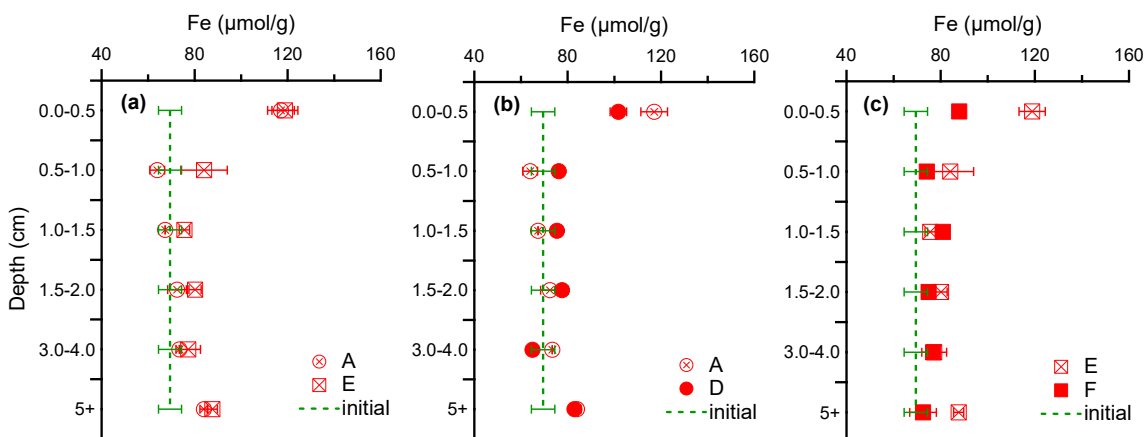


**Figure 5.8.** Concentrations of Fe in the sediments extracted with a buffered ascorbate-citrate solution. The inflow solutions for columns **A** and **D** during phase-1 was APW with $Fe^{2+}$ while that for **E** and **F** was APW with $Fe^{2+}$ and Si, respectively. Columns **A** and **E** were analyzed after the phase-1, but columns **D** and **F** were analyzed after the completion of phase-2. The dashed line represents the concentration of Fe in the initial sediment. Error bars represent the range of values measured between duplicate columns.

The concentrations of $Fe_{(HCl)}$ (µmol Fe per gram of dried sediment) in the initial sediments as well as in the sediments of the $Fe^{2+}$ addition columns (**A**, **D** and **E**, **F**) are shown in Figure 5.9. The results show that the concentrations of $Fe_{(HCl)}$ in the surface sediments (0 to 0.5 cm) of columns **A** ($APW+Fe^{2+}$) and **E** ($APW+Fe^{2+}+Si$) are comparable (278.7±2.9 and 283.9±1.6 µmol/g, respectively), and are higher than that of the initial sediments (251.8±3.1 µmol/g) (Figure 5.9a). This means that the accumulation of $Fe_{(HCl)}$ within the surface sediments (0 to 0.5 cm) of columns **A** and **E** was slightly higher for **E**, accounting for 11 and 13% enrichment of $Fe_{(HCl)}$ in **A** and **E**, respectively, relative to the initial sediments. The higher concentration of $Fe_{(HCl)}$ in the surface sediments of **E** potentially suggests that the ferric (co)-precipitates that formed in the surface sediments of column **F** during phase-1 were likely more amorphous than those formed in column **A**. The higher concentrations of $Fe_{(HCl)}$ in the surface sediments of columns **A** and **E** indicate that the accumulation of Fe occurred within the top 0.5 cm in the columns and are consistent with the $Fe_{(BAC)}$ concentrations in sediments.
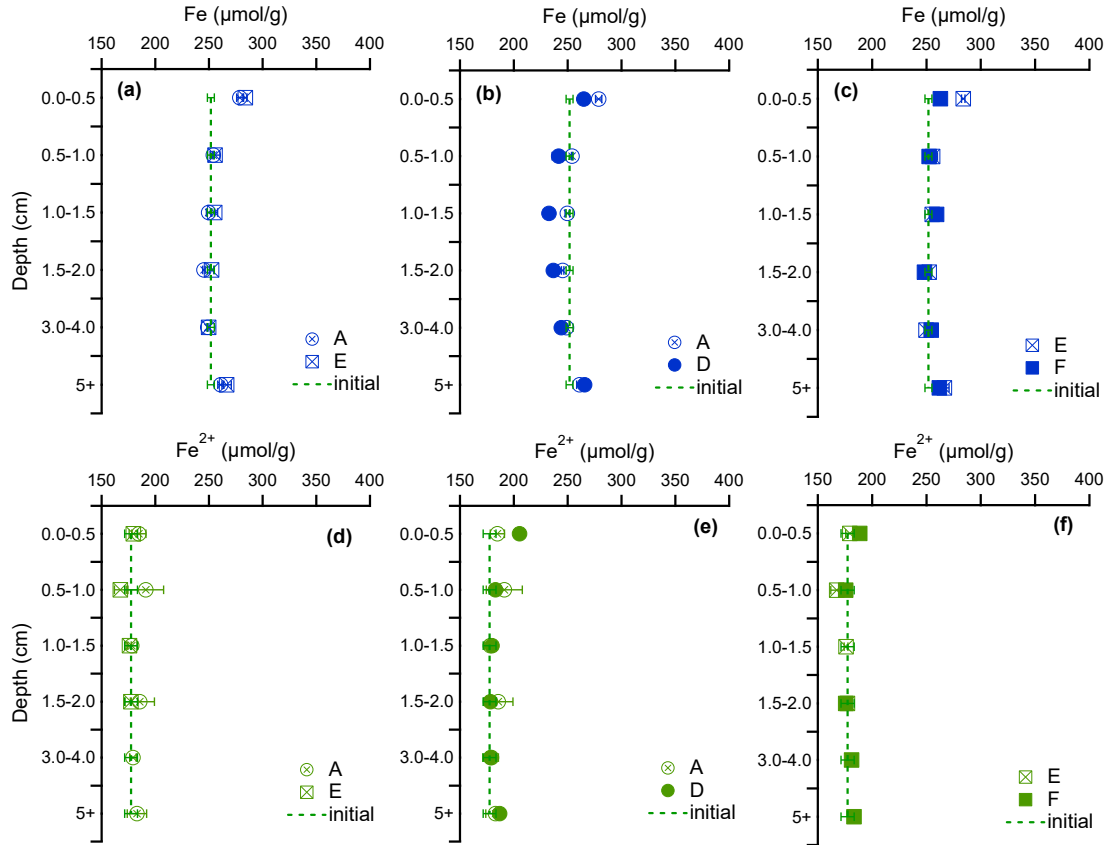
**Figure 5.9.** Concentrations of total Fe (a-c) and the $Fe^{2+}$ (d-f) in the sediments extracted with 1 M HCl solution. The inflow solutions for columns **A** and **D** during phase-1 was APW with $Fe^{2+}$ while that for **E** and **F** was APW with $Fe^{2+}$ and Si, respectively. Columns **A** and **E** were analyzed after the phase-1, but columns **D** and **F** were analyzed after the completion of phase-2. The dashed lines represent the concentration of iron ($Fe_{(HCl)}$ and $Fe^{2+}_{(HCl)}$) in the initial sediment. Error bars represent the range of values measured between duplicate columns.

During phase-1, although the concentrations of $Fe_{(HCl)}$ increased in the surface sediments (0 to 0.5 cm) of columns **A** and **E** with respect to the initial sediments (Figure 5.9a), the concentrations of ferrous iron, $Fe^{2+}_{(HCl)}$, remained similar (Figure 5.9d). This result indicates that the accumulation of Fe in the surface sediments of columns **A** and **E** occurred by the oxidative precipitation of $Fe^{2+}$. In the sediments below 5 cm depth, a slight increase of $Fe_{(HCl)}$ was observed (Figure 5.9), similar to $Fe_{(BAC)}$ (Figure 5.8), possibly due to the influence of added $Fe^{2+}$ in the inflow solutions.

The sediments from columns **D** and **F** were analyzed after phase-2 and these columns were similar to columns **A** and **E**, respectively during phase-1. The average concentrations of

Fe$_{(HCl)}$ in the surface sediments of columns **D** and **F** were lower compared to that of columns **A** and **E**, respectively (Figure 5.9b and Figure 5.9c). This result indicates that surface sediments (0 to 0.5 cm) of both anoxic columns **D** and **F** released Fe$_{(HCl)}$ during phase-2. Furthermore, the amounts of Fe$_{(HCl)}$ released from the surface sediments of column **F** was higher than that of column **D**. This difference is revealed by comparing the Fe$_{(HCl)}$ concentrations in the surface sediments of columns **F** and **D** with the respective background concentrations. For example, assuming that the concentrations of Fe$_{(HCl)}$ in the surface sediments of columns **A** and **D** were similar before the start of phase-2 (Figure 5.9a), the surface sediments of column **D** released 13.7 μmol Fe$_{(HCl)}$ from each gram of the sediments (Figure 5.9b). This release of Fe$_{(HCl)}$ was 21.0 μmol/g from the surface sediments of column **F** with respect to the concentrations measured in the surface sediments of **E** (Figure 5.9c).

The concentration of total Fe extracted by HCl, Fe$_{(HCl)}$, decreased in the surface sediments of **D** and **F** after phase-2 where the concentration of Fe$^{2+}$$_{(HCl)}$ slightly increased (Figure 5.9e and Figure 5.9f) in the surface sediments of columns **D** and **F**. The increased concentration of Fe$^{2+}$$_{(HCl)}$ in the surface sediments of columns **D** and **F** after phase-2 could have occurred by the accumulation of reductively dissolved Fe$^{2+}$ via adsorption on sediment mineral surfaces or by chemical precipitation (Connell et al., 2015; Gächter and Müller, 2003; Orihel et al., 2017; Rothe et al., 2014). Within columns **D** and **F**, the accumulation of Fe$^{2+}$$_{(HCl)}$ was higher in the surface sediments of **D** (Figure 5.9e and 5.9f). The total release of Fe (90% in the form of Fe$^{2+}$) to the overlying water of column **D** was lower in comparison to column **F** (Figure 5.7 and Table 5.2 and Figure SM-5.1). Thus, the greater accumulation of Fe$^{2+}$$_{(HCl)}$ via chemical precipitation in column **D** was not likely as the concentrations of other anions, e.g., phosphate, and possibly bicarbonate, were similar in the overlying water of columns **D** and **F**.

The accumulation of Fe$^{2+}$$_{(HCl)}$ in the surface sediments of columns **D** and **F** may also have occurred via the adsorption of reductively dissolved Fe$^{2+}$ to mineral surfaces. Between columns **D** and **F**, the depleted Fe$^{2+}$$_{(HCl)}$ concentrations in the surface sediments of **F** potentially indicate that ferric (co)-precipitates formed in column **F** (with added Si) had decreased affinity for the adsorption of Fe$^{2+}$ from the aqueous phase. This effect of co-precipitated Si is consistent with a previous study where the ferric (hydr)oxide co-precipitated with Si showed a weak affinity for the adsorption of Fe$^{2+}$ (Kinsela et al., 2016). Alternatively, the presence of dissolved silicate has been known to increase the rate of bacterially mediated Fe$^{2+}$ oxidation (Gauger et

al., 2016; Konhauser et al., 2007). On the contrary, the presence of dissolved Si decreases the rate of $Fe^{2+}$ oxidation under abiotic conditions (Kinsela et al., 2016). Therefore, if the oxidation of $Fe^{2+}$ during phase-1 was mostly driven by iron oxidizing bacteria, one may expect that the rate of $Fe^{2+}$ oxidation in the surface sediments of column **F** (with added Si) was higher than that of column **D** (with no added Si). Assuming this hypothesis, higher $Fe^{2+}$ oxidation rate could have resulted in the greater amounts of ferric iron (co)-precipitation in the surface sediments of column **F** compared to column **D**, although concentrations of total HCl extractable Fe are comparable for both columns. The results potentially indicate that a greater amount of $Fe^{2+}$ was accumulated in the ferric (co)-precipitates that formed in the surface sediments of column **D**, potentially via adsorption or via the formation of mixed $Fe^{2+}$ and $Fe^{3+}$ iron oxides, compared to column **F**.

### 5.4.4.2 Manganese cycling

### 5.4.4.2.1 Manganese in the overlying waters

All the columns released Mn during phase-1, although it was not added to the inflow solutions (Figure 5.10, Table 5.2). As the sediments below the top 0.5 cm were anoxic, the release of Mn likely occurred by the reductive dissolution of $Mn^{4+}$-phases present in the deeper sediments (Lovley, 2004; Parsons et al., 2017; Santschi et al., 1990). The total amount of Mn released by an individual group of columns during phase-1 was slightly higher than the total amount of Fe (total) released by the same column (Table 5.2). For example, columns **A** and **D** (APW with $Fe^{2+}$) released a total of $20\pm3$ µmol Mn during phase-1 relative to the total amount of Fe ($13\pm11$ µmol) released by those columns. The higher amounts of Mn release relative to the release of Fe could have occurred due to low DO concentrations in the overlying waters ($3.5\pm0.5$ mg/L) of the columns during phase-1. Although these DO levels ($3.5\pm0.5$ mg/L) effectively oxidized $Fe^{2+}$, it was most likely inadequate for the retention of Mn by oxidative precipitation, assuming that the release of $Mn^{2+}$ from the deeper sediments occurred by the reductive dissolution of $Mn^{4+}$-phases.
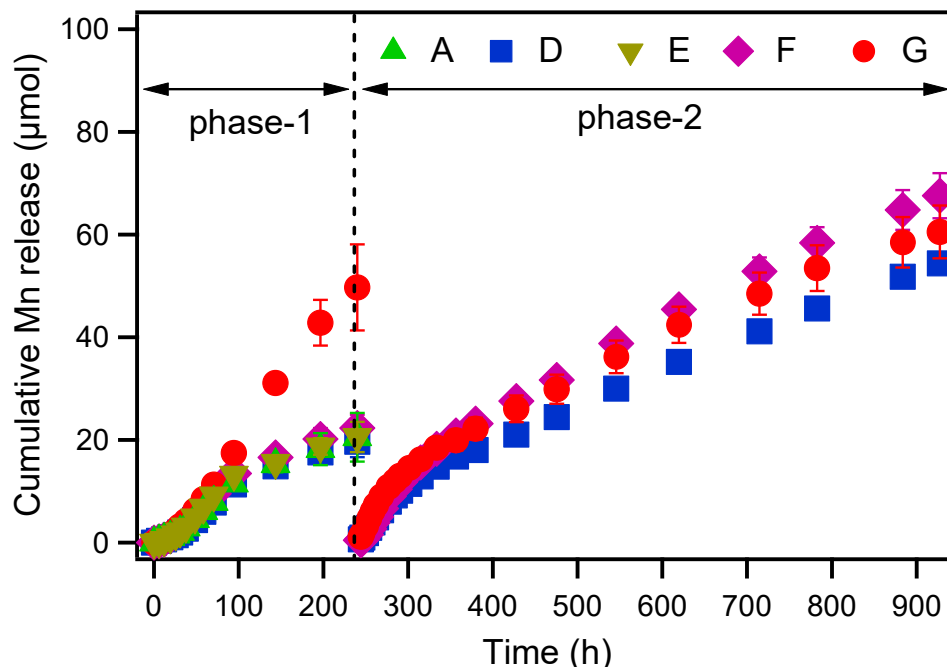
**Figure 5.10.** Cumulative release of Mn to the overlying waters during phase-1 and phase-2 as a function of time. The inflow solutions for columns during phase-1 were (i) APW with $Fe^{2+}$ (**A** and **D**) and (ii) APW with $Fe^{2+}$ and Si (**E** and **F**), and (iii) APW only (**G**). Before the start of phase-2, columns **A** and **E** were sacrificed for solid phase analysis while columns **D**, **F** and **G** were continued in phase-2 and the inflow solutions were replaced with APW only. Error bars represent the range of values measured between duplicate columns.

During phase-1, the control column (**G**) released a greater amount of Mn than the $Fe^{2+}$ addition columns (**A**, **D**, **E**, and **F**) and the release of Mn among these $Fe^{2+}$ addition columns were similar. During phase-2, the initial release of Mn was slightly higher by the control column (**G**) compared to columns **D** and **F** (Figure 5.10). Similar to Fe, the greater initial release of Mn by the control column (**G**) during phase-2 likely occurred due to the higher concentrations of DOC required for the microbial reduction of $Mn^{4+}$-phases in sediments. However, the total amount of Mn released from column **G** was lower than that released by column **F** (Table 5.2), and comparable to the amount of Fe release from the reactor **D**. Between columns **D** and **F**, column **F** with added Si during phase-1 released ~1.3 times greater amount of Mn. The trends of cumulative and total release of Mn are consistent with that of Fe. Therefore, Mn co-precipitates that potentially formed in the surface sediments of column **F** (with added Si) was likely more reactive under reducing conditions, resulting in a greater release of Mn during phase-2.

140

### 5.4.4.2.2 Manganese in the sediments

The results from extraction of sediments with BAC solution show that the concentrations of $Mn_{(BAC)}$ were higher in the surface sediments (0 to 0.5 cm) of columns **A** and **E** than the initial sediments (Figure 5.11a). Within columns **A** and **E**, the concentrations of $Mn_{(BAC)}$ in the surface sediments (0 to 0.5 cm) were higher than in the sediments below the top 0.5 cm (Figure 5.11a). This result indicates that Mn released by the bottom sediments was accumulated in surface sediments (0 to 0.5 cm), potentially via the oxidative precipitation of Mn under oxic conditions.
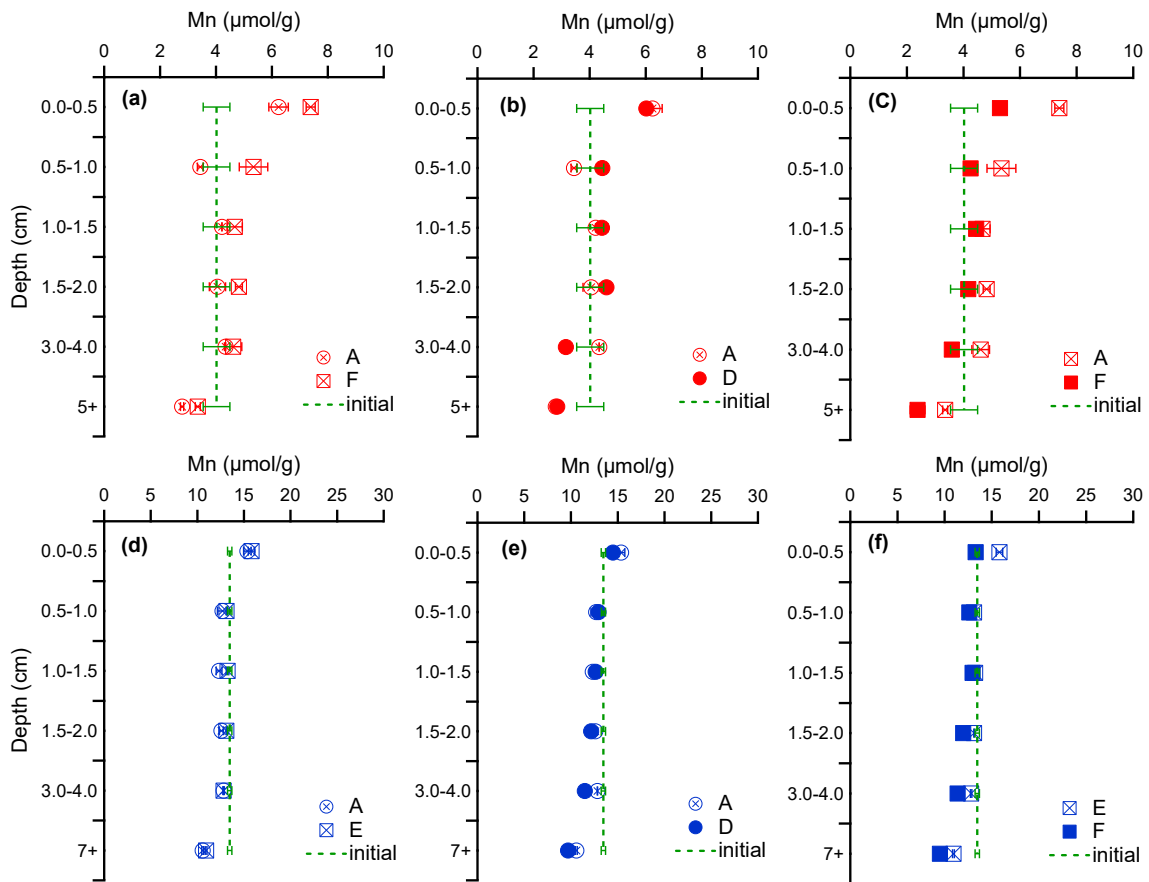


**Figure 5.11.** Concentrations of total Mn in the sediments extracted with buffered ascorbate-citrate (a-c) and 1 M HCl solution (d-f). The inflow solutions for columns **A** and **D** during phase-1 was APW with $Fe^{2+}$ while that for **E** and **F** was APW with $Fe^{2+}$ and Si, respectively. Columns **A** and **E** were analyzed after the phase-1, but columns **D** and **F** were analyzed after the completion of phase-2. The dashed lines represent the concentrations of Mn (($Mn_{BAC}$ and $Mn_{HCl}$)) in the initial sediment. Error bars represent the range of values measured between duplicate columns.

During phase-1, columns **A** and **E** were similar to columns **D** and **F**, respectively, where the sediments of columns **D** and **F** were analyzed after the completion of phase-2. Therefore, assuming that the concentrations of $Mn_{(BAC)}$ in the surface sediments (0 to 0.5 cm) of columns **A** and **D** were similar at the end of phase-1, the depleted concentration of $Mn_{(BAC)}$ from the surface sediments of column **D** during phase-2 was estimated. Similarly, the concentration of $Mn_{(BAC)}$ that depleted from the surface sediments of column **F** during phase-2 was estimated by comparing it with the $Mn_{(BAC)}$ concentration in the surface sediments of column **E**. Between columns **D** (APW with $Fe^{2+}$) and **F** (APW with $Fe^{2+}$ and Si), the surface sediments of column **F** was more depleted in $Mn_{(BAC)}$ concentration (Figure 5.11b and 5.11c), suggesting that more $Mn_{(BAC)}$ was released from the surface sediments of column **F** during phase-2.

The concentrations of HCl extractable Mn, $Mn_{(HCl)}$, were also higher in the surface sediments (0 to 0.5 cm) within columns **A** and **E** (Figure 5.11d). The analyses of columns **D** and **F** show that the surface sediments of these columns were depleted in $Mn_{(HCl)}$ compared to that of columns **A** and **E**, with **F** more depleted than **D**. This result suggest that the surface sediments of column **F** released more $Mn_{(HCl)}$ than the surface sediments of column **D**. A similar trend is observed for the concentrations of $Mn_{(BAC)}$ in the sediments of those columns. Thus, the addition of Si to columns **E** and **F** (during phase-1) likely resulted in the manganese (co)-precipitates with higher reactivity towards reductive dissolution (during phase-2) compared to that formed in columns **A** and **D** which did not receive added Si.

### 5.4.4.3 Silicon cycling
### 5.4.4.3.1 Silicon in the overlying waters

During phase-1, Si was added in the inflow solution of columns **E** and **F** only. Therefore, the release of Si from the columns (**A**, **D**, and **G**) with no added Si indicates that the sediments acted as a source of Si (Figure 5.12, Table 5.2). However, columns **E** and **F** (with added Si) released a greater amount of dissolved Si than columns **A, D**, and **G** (with no added Si) during phase-1. This result suggests that the concentrations of dissolved Si were higher during the oxidation of $Fe^{2+}$ in the surface sediments of columns **E** and **F**, compared to columns **A**, **D,** and **G**. For example, average concentrations of dissolved Si in the overlying waters of columns **E** and **F** were about 1.8 times higher than that of **A** and **D**, as calculated from the total amounts of released Si and the volume inflow solutions introduced to the columns.
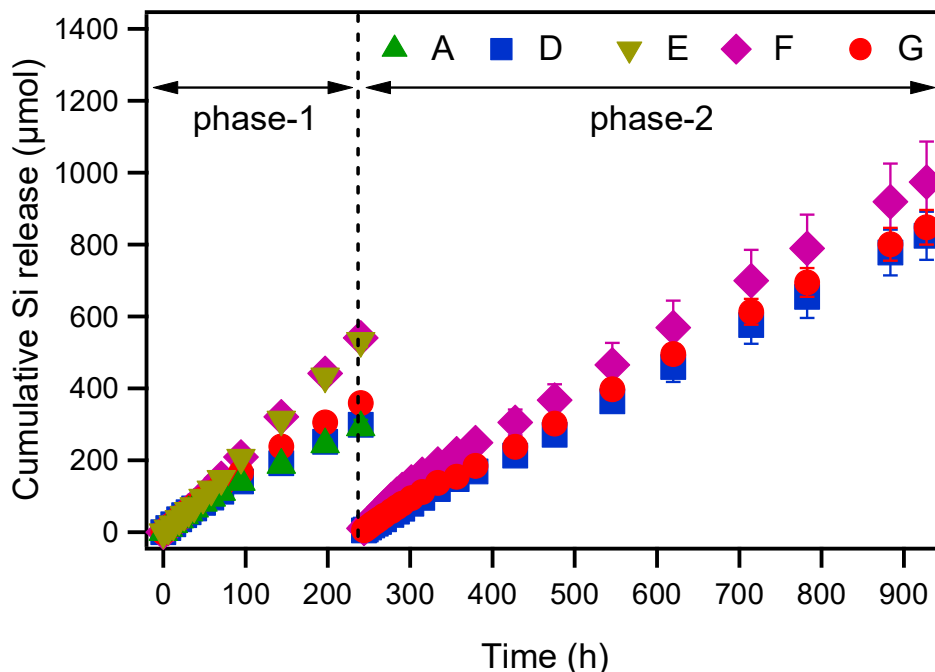
**Figure 5.12.** Cumulative release of Si to the overlying waters during phase-1 and phase-2 as a function of time. The inflow solutions for columns during phase-1 were (i) APW with $Fe^{2+}$ (**A** and **D**) and (ii) APW with $Fe^{2+}$ and Si (**E** and **F**), and (iii) APW only (**G**). Before the start of phase-2, columns **A** and **E** were sacrificed for solid phase analysis while columns **D**, **F** and **G** were continued in phase-2 and the inflow solutions were replaced with APW only. Error bars represent the range of values measured between duplicate columns.

During phase-2, the cumulative release of Si at each time point, including the endpoint, was higher from column **F** compared to columns **D** and **G**, with comparable release from the latter two columns (**D** and **G**) (Figure 5.12). For example, column **F** released about 149 μmol more Si than column **D** (calculated from the average values) in total. The inflow solution of **F** received Si with the inflow solution during phase-1 and therefore, the sediment pore-water, just before the start of phase-2, was pre-saturated with Si from phase-1. Therefore, the greater release of Si from column **F** during phase-2 compared to column **D** can be attributed to the dissolution of Si that could have co-precipitated with iron, or to the release of the excess Si (from phase-1) from column **F**. The amount of this excess Si inside column **F** from phase-1 is about 40 μmol, which was calculated from the concentration of Si in the overlying water before the start of phase-2 and the pore-volume of the sediment columns. If this amount of Si is considered, column **F** released 109 μmol (calculated using the average values from duplicate columns) more Si than column **D**. This result suggests that the release of this 109 μmol of Si

could have been associated with the reductive dissolution of iron, indicating the co-precipitation of Si with Fe during the oxidation of $Fe^{2+}$. However, the release of this Si associated with Fe seems insignificant compared to the variation in the amounts of Si released by the duplicate columns (shown with "±" sign in Table 5.2).

### 5.4.4.3.2 Silicon in the sediments

The concentrations of Si in the sediments based on the extractions with BAC as well as 1 M HCl solutions does not show any trend (see supplementary material, Figure SM-5.2). The BAC solution used to extract the reducible fraction of ferric (co)-precipitates from the sediments, can also dissolve amorphous silica (Ridenour, 2017). Similarly, the extraction with HCl solution may also result in the dissolution of clay minerals from the sediments (Cama and Ganor, 2015) along with Si bound to ferric iron. Thus, the greater dissolution of Si from other silica pools in sediments than the co-precipitated Si with iron (if formed) could have resulted in no meaningful trend in the concentrations of Si along the different depths of sediments in either of the columns.

The dissolution of Si during the extraction of sediments with BAC solution was further investigated with a kinetic approach (Figure 5.13). The results show that Si:Fe ratios in the extractants of the initial sediments deviates from linearity earlier than those from columns **A** and **E**. This result indicates that greater amounts of ferric bound-Si were present in the surface sediments of **A** and **E** than the initial sediments, suggesting that the co-precipitation of Si with Fe occurred during phase-1. Furthermore, the gradual increase of Si:Fe ratios (with increasing the concentrations of dissolved iron) in the BAC extractants of the surface sediments of **A** and **E** demonstrates that the released Si was not homogeneously associated with Fe, and that other sources were involved in Si release.

**Figure 5.13.** The release of Si and Fe into the aqueous phase during the extraction of surface sediments (0 to 0.5 cm) of columns **A** (APW+Fe$^{2+}$) and **E** (APW+Fe$^{2+}$+Si) plus the initial sediment in buffered ascorbate citrate solution. Columns **A** and **E** were analyzed after phase-1. Error bars for columns **A** and **E** represent the range of minimum and maximum values measured between duplicate columns while for the initial sediment, error bars represent the range of values measured between duplicate experiments.

### 5.4.4.4 Phosphorus cycling

### 5.4.4.4.1 Phosphorus in the overlying waters

All the columns released phosphorus (P) with no considerable differences between solution treatments during both experimental phases. The cumulative and the total releases of P are shown in Figure 5.14 and in Table 5.2. During phase-1, columns **A**, **D**, **E**, **F** and **G** released similar amounts of P which did not vary due to different chemical compositions of inflow solutions: (i) APW and Fe$^{2+}$ (**A** to **D**), (ii) APW with Fe$^{2+}$ and Si (**E** and **F**), and (iii) APW (**G**) (Figure 5.14). Dissolved Si, as a competitive ion to phosphate for the mineral binding sites, has previously been shown to increase the mobility of aqueous P in sediments (Koski-Vähälä et al., 2001; Koszelnik and Tomaszek, 2008; Tallberg et al., 2008; Tuominen et al., 1998). However, the addition of aqueous Si to columns **E** and **F** did not result in greater P release to the overlying waters during phase-1, indicating that the influence of dissolved Si on the release

of P was minor or not apparent. This effect of dissolved Si could be due to the fact that the pH in the overlying water of the columns was 7.60±0.10 at which dissolved Si is likely to exert a minor influence on the mobility of P (Chapter 2). In addition, the amounts of P dissolution from various organic and inorganic sources within the sediments may have been relatively large compared to the release of P mediated by dissolved Si. Therefore, if there was any effect of dissolved Si on P release, the effect was levelled off perhaps with the greater amounts of P release by the other sources.

During phase-2, no significant difference was observed in the release of P, at each experimental time point (Figure 5.14) including the endpoint, from columns **D**, **F** and **G** with different solution treatments (Table 5.2).
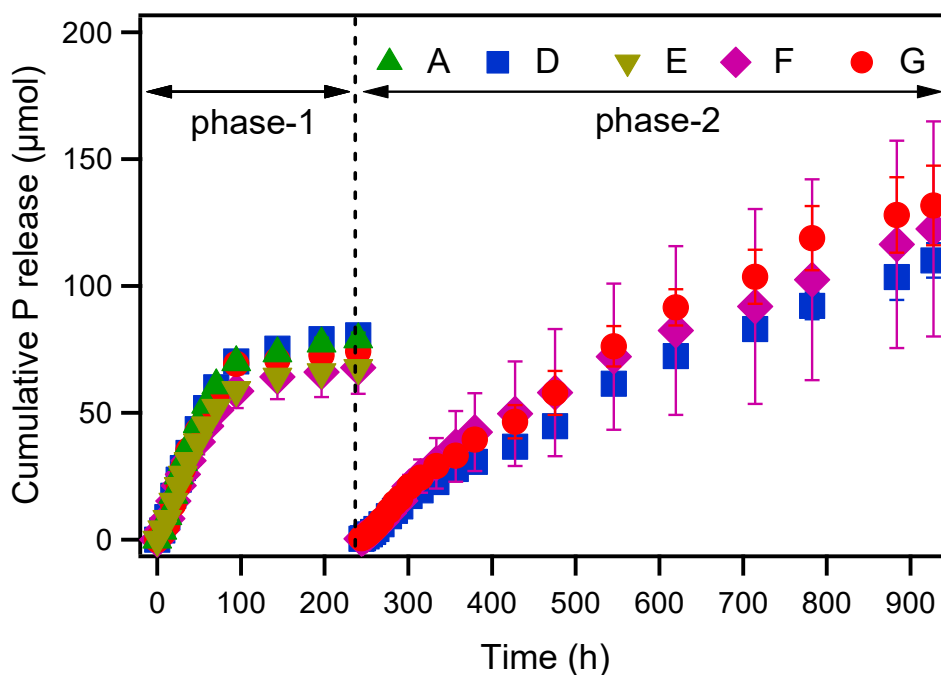


**Figure 5.14.** Cumulative release of P to the overlying waters during phase-1 and phase-2 as a function of time. The inflow solutions for the columns during phase-1 were (i) APW with $Fe^{2+}$ (**A** and **D**) and (ii) APW with $Fe^{2+}$ and Si (**E** and **F**), and (iii) APW only (**G**). Before the start of phase-2, columns **A** and **E** were sacrificed for solid phase analysis while columns **D**, **F** and **G** were continued in phase-2 and the inflow solutions were replaced with APW only. Error bars represent the range of values measured between duplicate columns.

### 5.4.4.4.2 Phosphors in the sediments

The results from the BAC extractions show that surface sediments (0 to 0.5 cm) of **A** and **E** were more enriched in $P_{(BAC)}$ (63.8±1.1 and 63.5±1.5 µmol P/g, respectively) compared to the

initial sediment (29.9±4.1 µmol P/g) (Figure 5.15a). Within columns **A** and **E**, the concentrations of P(BAC) was higher in the surface sediments (0 to 0.5 cm), while the sediments below the depth 1 cm were more depleted in P(BAC). Phosphate was not added to the inflow solutions of the columns during phase-1. Therefore, the higher concentrations of P(BAC) in the surface sediments of columns **A** and **E** indicate that P released from the bottom sediments was accumulated in the surface sediments during phase-1, potentially via adsorption or via the incorporation into new precipitates. The concentrations of P(BAC) in the surface sediments (0 to 0.5 cm) of **A** and **E** were similar which indicate that the added Si to column **E** did not influence the co-precipitation of P with $Fe^{3+}$ during phase-1.
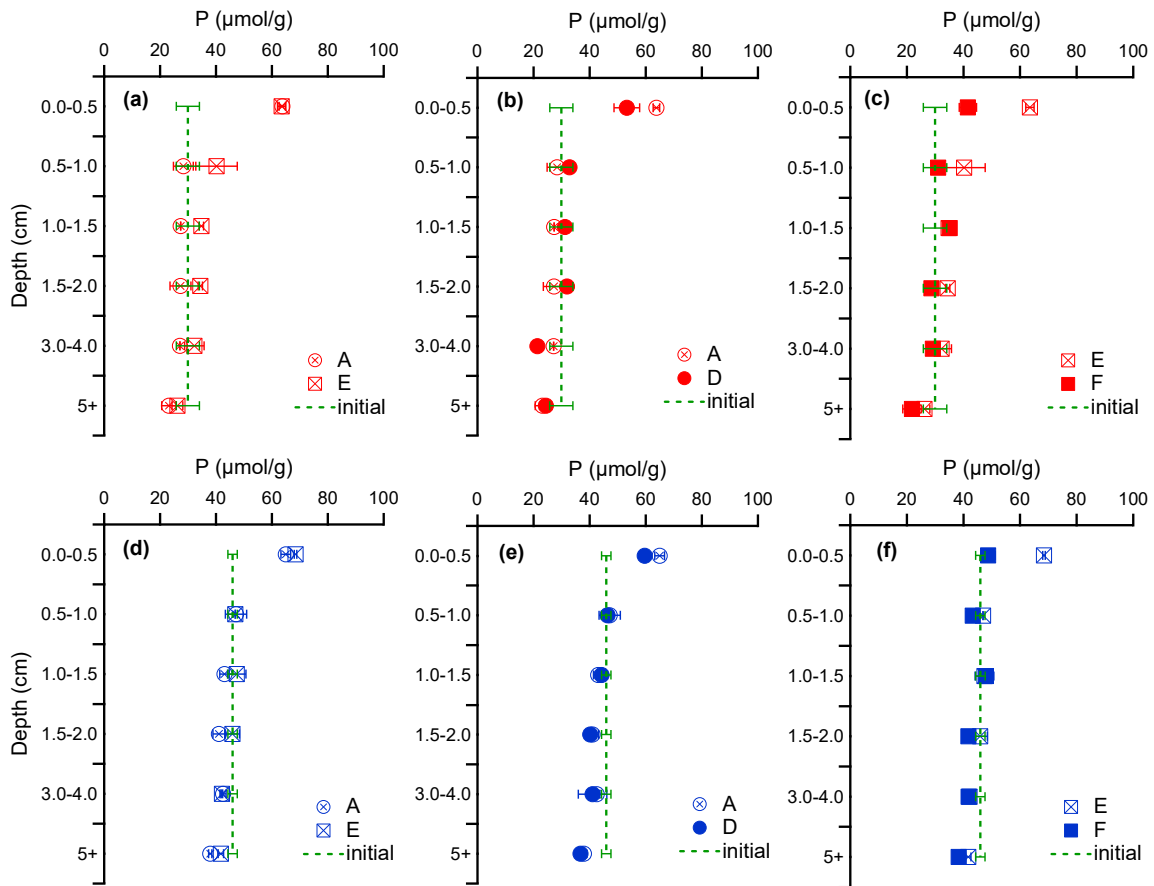


**Figure 5.15.** Concentrations of P in the sediments extracted with buffered ascorbate-citrate (a-c) and 1 M HCl solution (d-f). The inflow solutions for columns **A** and **D** consisted of APW with $Fe^{2+}$ while that for **E** and **F** was APW with $Fe^{2+}$ and Si, respectively. Columns **A** and **E** were analyzed after the phase-1, but columns **D** and **F** were analyzed after the completion of phase-2. The dashed lines represent the concentrations of P ($P_{BAC}$ and $P_{HCl}$) in the initial sediment. Error bars represent the range of values measured between duplicate columns.

Columns **A** and **E** were analyzed after phase-1, but their representative columns **D** and **F** during phase-1 were analyzed after phase-2. Therefore, the surface sediments (0 to 0.5 cm) of **D** and **F** can be assumed to contain similar concentrations $P_{(BAC)}$ before the start of phase-2, based on the analysis of columns **A** and **E**, respectively (Figure 5.15a). Between columns **D** (APW with $Fe^{2+}$) and **F** (APW with $Fe^{2+}$ and Si), the surface sediments of **F** were more depleted in $P_{(BAC)}$. This means that greater amounts of P were released from the surface sediments of **F** compared to **D** (during phase-2) under anoxic conditions. For example, about 21.9 µmol P (average from duplicate column) was released from each gram of surface sediment form column **F** during phase 2, which was 10.6 µmol/g from column **D**.

Similar to concentrations of $P_{(BAC)}$, the concentrations of HCl extractable $P_{(HCl)}$ in sediments suggest that the surface sediments of column **F** released more P under anoxic conditions compared to column **D** (Figure 5.15d-f). The greater P release from the surface sediments of column **F** (Figure 5.15) was not evident with the cumulative and total P released from columns **D** and **F** to the overlying waters during phase-2 (Table 5.2). This was probably because the cumulative and the total release of P were calculated from the amounts of P release to the overlying waters, which were contributed by the entire sediments present in the columns.

To further investigate the reactivity ferric (co)-precipitates, the surface sediments of columns **A** and **E**, as well as the initial sediments, were extracted with BAC solution, and the samples were collected periodically. The results demonstrate that the P:Fe ratios in the extractants were higher for columns **A** and **E** (0.55 and 0.56, respectively) than that observed for the initial sediments (0.48), as shown by the respective slopes (Figure 5.16). Furthermore, aqueous P:Fe ratios in extractants released from the surface sediments of **A** and **E** were similar (i.e., stoichiometric dissolution of P and Fe), suggesting that P was homogeneously distributed with Fe in the surface sediments of these columns (Figure 5.16). Similar P:Fe ratios in the extracted fractions for the surface sediments (0 to 0.5 cm) of columns **A** and **E** potentially indicate that the higher (~1.8x) concentrations of Si in column **E** during $Fe^{2+}$ oxidation did not influence the co-precipitation of P with Fe during phase-1. Therefore, although a higher concentration of dissolved Si did not affect the solid phase P:Fe ratios, it increased the reactivity ferric (co)-precipitates towards reductive dissolution of iron and the associated P under anoxic conditions.
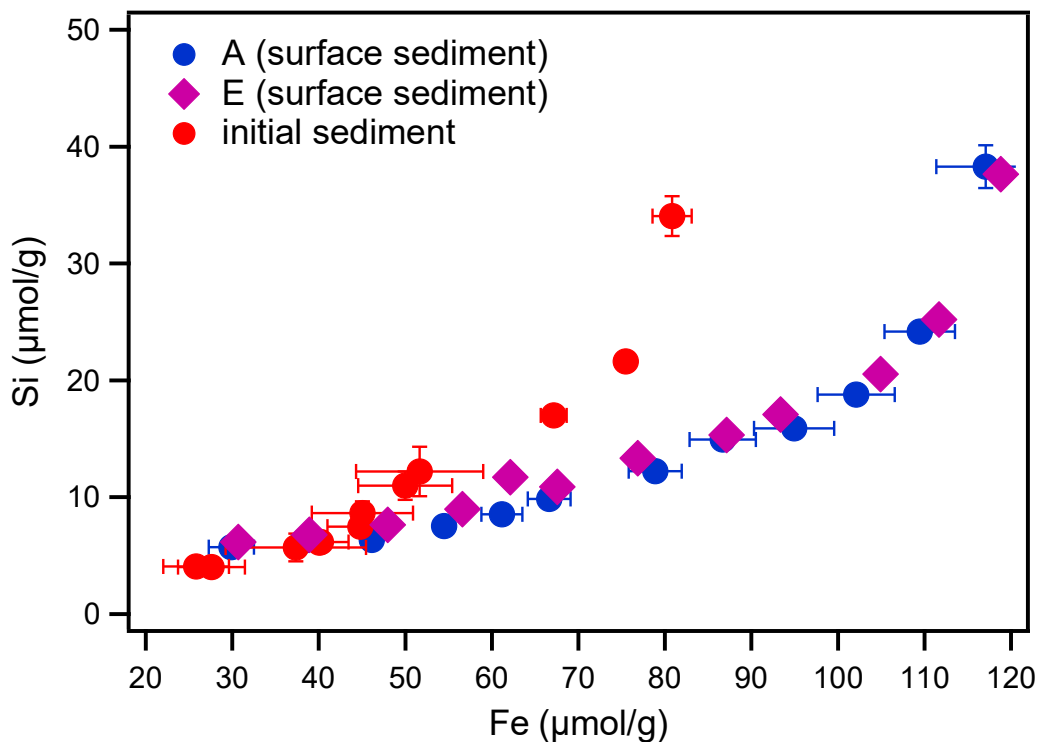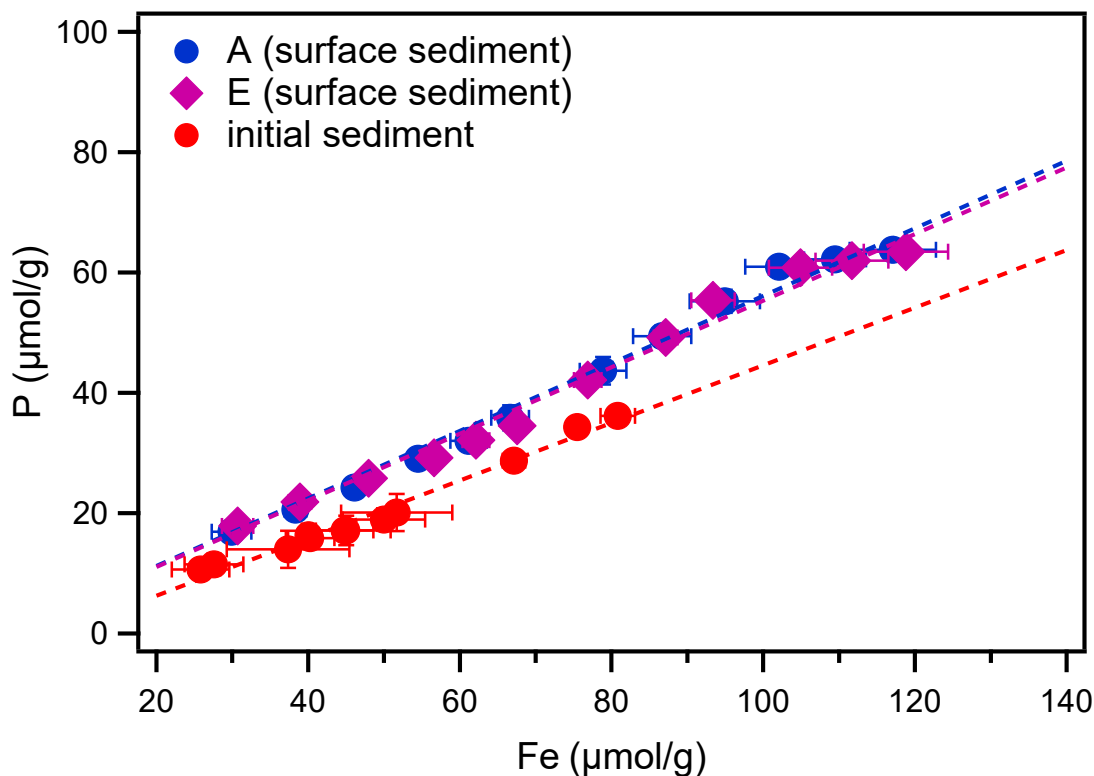
**Figure 5.16.** The release of P and Fe into the aqueous phase during the extraction of surface sediments (0 to 0.5 cm) of columns **A** (APW+Fe$^{2+}$) and **E** (APW+Fe$^{2+}$+Si) plus the initial sediments in buffered ascorbate citrate solution. Columns **A** and **E** were analyzed after phase-1. The dashed lines represent the linear regression fits between the concentrations of P and Fe. The slopes of these lines indicate the aqueous phase P to Fe ratios in the BAC extractant, which for the columns **A** and **E** are 0.55 ($r^2 = 0.99$) and 0.56 ($r^2 = 0.99$), respectively, and for initial sediment is 0.48 ($r^2 = 0.98$). Error bars for columns **A** and **E** represent the range of values measured between duplicate columns while for the initial sediment, error bars represent the range of values measured between duplicate experiments.

### 5.4.4.5 Ferric (co)-precipitates: chemical composition and reactivity

The concentrations of Fe, P and Si in the surface sediments of column **A** (APW+Fe$^{2+}$) and **E** (APW+Fe$^{2+}$+Si) as well as in the initial sediment, obtained from the 24 hours of extractions with BAC solution, are shown in Figure 5.17a. The results show that concentration of Fe and P in the surface sediments of **A** and **E** are comparable and noticeably higher than that of the initial sediment. Further, the concentrations of Fe in the surface of these two columns increased (after phase-1) by 36.3 and 38.0 μmol/g relative to initial sediment concentration, and by 27.6 and 27.3 μmol/g for P. The solid phase P:Fe ratios in the fresh ferric (co)-precipitates that

formed in the surface sediments under aerated conditions (during phase-1) of **A** and **E** are also comparable, 0.76 and 0.72, respectively. This result, along with stoichiometric dissolution of P with Fe in the BAC extractants shown in Figure 5.16, indicates the strong association of P with Fe is the result of co-precipitation during the oxidation of $Fe^{2+}$, and that this Fe-P is not significantly affected by the variations in dissolved Si concentrations.
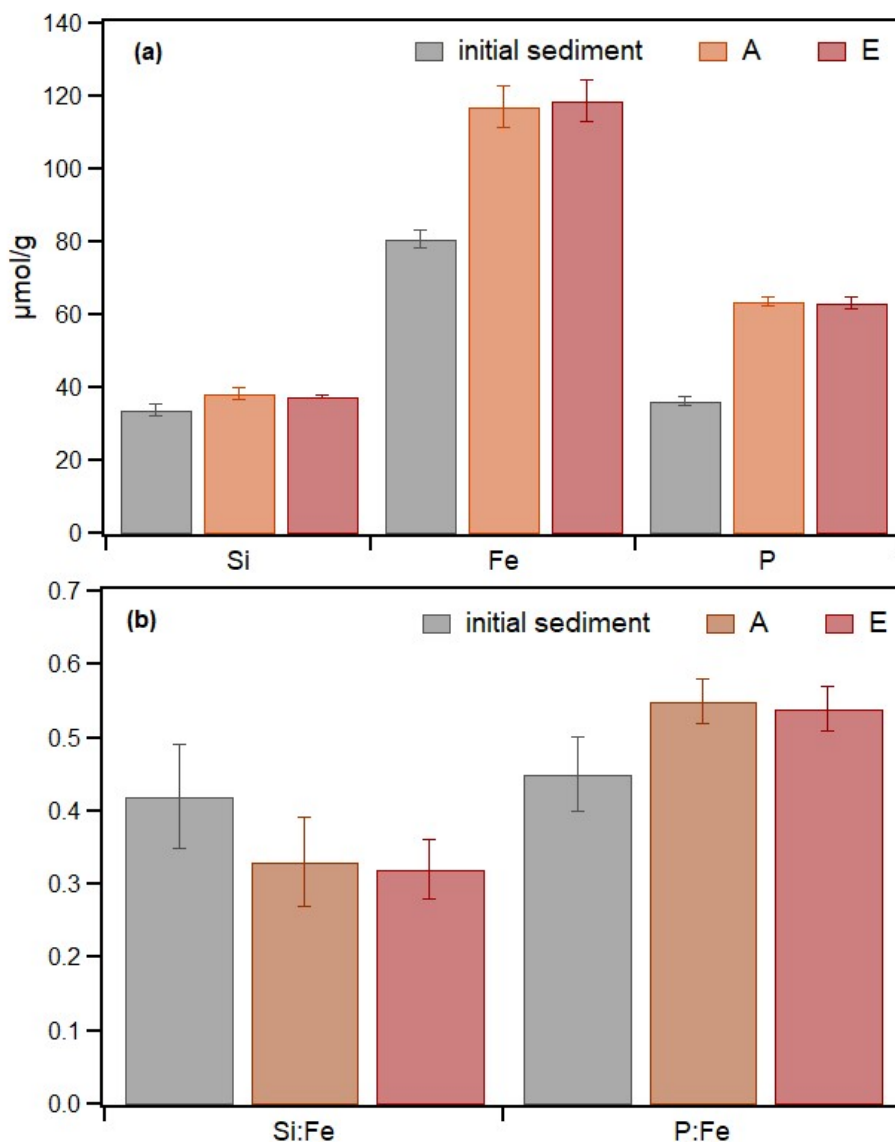


**Figure 5.17.** (a) Concentrations of Fe, P and Si in the surface sediments of columns **A** (APW+$Fe^{2+}$) and **E** (APW+$Fe^{2+}$+Si) as well as the initial sediment based on their concentrations in BAC extractants after 24 hours. (b) Solid phase P:Fe and Si:Fe ratios calculated from the concentrations presented in Figure 5.17a. Error bars represent the range of values measured between duplicate columns while for the initial sediment, error bars represent the range of values measured between duplicate experiments.

Concentrations of Si in the surface sediments of column **A** and **E** are also similar, but do not increase significantly from the initial sediment concentrations, as occurred for Fe and P. However, Si:Fe ratio in the initial sediment is still higher than that of the surface sediments of columns **A** and **E** (Figure 5.17b), indicating a greater accumulation of iron (via $Fe^{2+}$ oxidation) than of Si. Furthermore, the solid phase Si:Fe ratios within the surface sediments of columns **A** and **E** are similar. However, higher solid phase Si:Fe ratios for column **E** compared to column **A** may be expected, where a greater incorporation of Si into ferric (co)-precipitates is likely. This assumption is based on the presence of higher (~1.8 times) Si concentrations during $Fe^{2+}$ oxidation in this column (**E**), particularly if $Fe^{2+}$ is oxidized abiotically by molecular oxygen (Chapter 4). Further, Si:Fe ratios in the surface sediments (resulted from $Fe^{2+}$ oxidation) of columns **A** ($APW+Fe^{2+}$) and **E** ($APW+Fe^{2+}+Si$) are higher by 0.12 and 0.09, respectively, than that in the initial sediment.

Based on results from BAC extractions, the amount of Fe accumulated within the top 0.5 cm of sediments (~4.2 g as dried sediment) of columns **A** and **E** is about 152 and 159 µmol, respectively. This accumulated Fe represents about 23 and 24% of the supplied Fe with the inflow solution for columns **A** and **E**, respectively. If this 152 µmol Fe is assumed to be (co)-precipitated oxidatively at constant concentrations in the surface sediments of column **A**, the concentrations of $Fe^{2+}$ during its oxidation would be about 126 µM. This concentration of $Fe^{2+}$ is 133 µM for column **F**. Average concentrations of Si during the oxidation $Fe^{2+}$ are 244 and 451 µM in columns **A** (no added Si) and **E** (with added Si), respectively. This calculation gives aqueous phase Si:Fe ratios of 1.9 and 3.4 during the oxidation of $Fe^{2+}$ in the surface sediments of columns **A** and **E**, respectively. However, the Si:Fe ratios associated with the accumulated ferric iron (via $Fe^{2+}$ oxidation) are 0.12 and 0.09, respectively for columns **A** and **E**. These solid phase Si:Fe ratios in fresh ferric (co)-precipitates are less than half of the expected values, based on their aqueous phase ratios during abiotic $Fe^{2+}$ oxidation, as observed in Chapter 4 as well as in another study (Châtellier et al., 2004). For example, an aqueous phase Si:Fe ratio of 0.5 in Chapter 4 resulted in a solid phase Si:Fe ratio of 0.23.

Dissolved silicate is known to enhance the rate of $Fe^{2+}$ oxidation when the oxidation is mediated by iron oxidizing bacteria (Gauger et al., 2016; Konhauser et al., 2007). However, the iron minerals resulted from microbial $Fe^{2+}$ oxidation in the absence and presence of dissolved Si have been shown to be indifferent, as analyzed by SEM and TEM images as well

as Mossbauer spectroscopy in a previous study (Gauger et al., 2016). In another study, $Fe^{2+}$ was oxidized in the presence and absence of iron oxidizing bacteria, and in the absence and presence of Si (Châtellier et al., 2004). These authors show that microbial oxidation of $Fe^{2+}$ results in iron oxides of smaller particles compared to the iron oxides prepared via purely chemical oxidation by molecular oxygen. The study, by Châtellier et al. (2004), propose that a fraction of the oxidized iron ($Fe^{3+}$) under biotic conditions gets absorbed to bacterial cells, and does not contribute to mineral formations outside the cells. The amount of this adsorbed $Fe^{3+}$ (to bacterial cells) increase in the presence of dissolved Si during the oxidation of $Fe^{2+}$, as proposed by these authors. Yet, the role of dissolved Si in increasing the rate of $Fe^{2+}$ oxidation as well as in altering iron minerology is not fully understood.

## 5.4.4.6 Reactivity of ferric (co)-precipitates: effect of synthesis methods

Reactivity of ferric (co)-precipitates formed under variable concentrations of dissolved Si observed in this study is in apparent contradiction to reactivity observed for synthesized Fe-P-Si co-precipitates in Chapter 4. The ferric co-precipitates (i.e., Fe-P-Si) were synthesized in Chapter 4 from high concentrations of iron, phosphate and silicate under abiotic conditions, and by imposing either rapid aeration or pH increase (from acidic to neutral). The ferric co-precipitates in chapter 4 are therefore representative of the natural analogues that form in the aquatic environments where co-precipitation may occur rapidly and abiotically (e.g., groundwater springs), particularly when the concentrations of these dissolved constituents are fairly high (Phoenix et al., 2003). However, in many other aquatic environments, e.g., lake sediments, the diffusion-controlled transport of $Fe^{2+}$ from the deeper sediments results in the gradual oxidation of $Fe^{2+}$ at the sediment-water interface by molecular oxygen, or by nitrate or chlorate catalyzed by microorganisms (Weber et al., 2006). This gradual oxidation (at relatively low concentrations of $Fe^{2+}$) results in the slow formation of ferric (co)-precipitates, which may not be similar to the synthesized ferric co-precipitates discussed in Chapter 4. Ferric iron (co)-precipitates synthesized with the flow-through rector system in this study may therefore be better analogues of the natural ferric co-precipitates that are likely to form slowly in diffusion dominated or moderately advection influenced aquatic sediments.

## 5.4.5 Mobilization of P under oxic conditions: effect of dissolved silicate

To understand the effect of dissolved silicate (Si) on the mobilization of P, the release of P from columns **B** and **C** (during phase-2) were compared. This is because- these columns (**B** and **C**) were similar during phase-1 with APW and $Fe^{2+}$ inflow solution and released comparable amounts of P during phase-1 (Figure 5.18). However, at the start of phase-2, the inflow solutions of columns **B** and **C** were replaced by (i) APW and (ii) APW with Si, respectively but remained aerated similar to phase-1. The amounts of Fe, Mn, P, Si, Ca and Mg release from columns **B** and **C** during phase-2 are presented in Table 5.3.

**Table 5.3.** Total amounts (µmol) of Fe, Mn, P, Si, Ca and Mg released from the $Fe^{2+}$ addition columns (B and C) under oxic conditions during phase-2 based on the analysis of overlying waters by ICP-OES. The release of these elements from these columns during phase-1 are presented in Table 5.2. The "±" sign indicates the range of minimum and maximum values measured between the columns.

| Column | Inflow solution | Fe | Mn | P | Si | Ca | Mg |
|--------|-----------------|------|------|------|---------|---------|--------|
| **B** | APW | 9±0 | 8±1 | 17±0 | 839±24 | 4589±94 | 746±14 |
| **C** | APW+Si | 20±0 | 16±0 | 22±1 | 1755±23 | 4921±89 | 857±8 |

As the overlying waters of columns **B** and **C** were aerated during the entire experiment, the release of Fe by those columns was minor, less than 4% (during phase-1) with respect to the total $Fe^{2+}$ added into the columns (discussed in section 5.4.4.1.1). The total amounts of Fe released from the columns during the 928 hours of phase-2 were comparable to the release that occurred during the 10 days of phase-1 (Table 5.2).

During phase-1, columns **B** and **C** (APW+$Fe^{2+}$) released similar amounts of Si (293±26 µmol) to the overlying waters (Figure 5.18a and Table 5.3). During phase-2, although column **B** did not receive Si with the inflow solution, this column released about 839±24 µmol of Si, indicating that sediment acted as source of Si. Column **C** (with added Si), on the other hand, released 1755±23 µmol of Si during phase-2, slightly greater than the amounts (1709 µmol Si) added to the inflow solutions. This result suggests that concentrations of Si in the sediment pore-water of column **C** (with added Si) during phase-2 were about two times higher than the concentrations in column **B** (with no added Si).
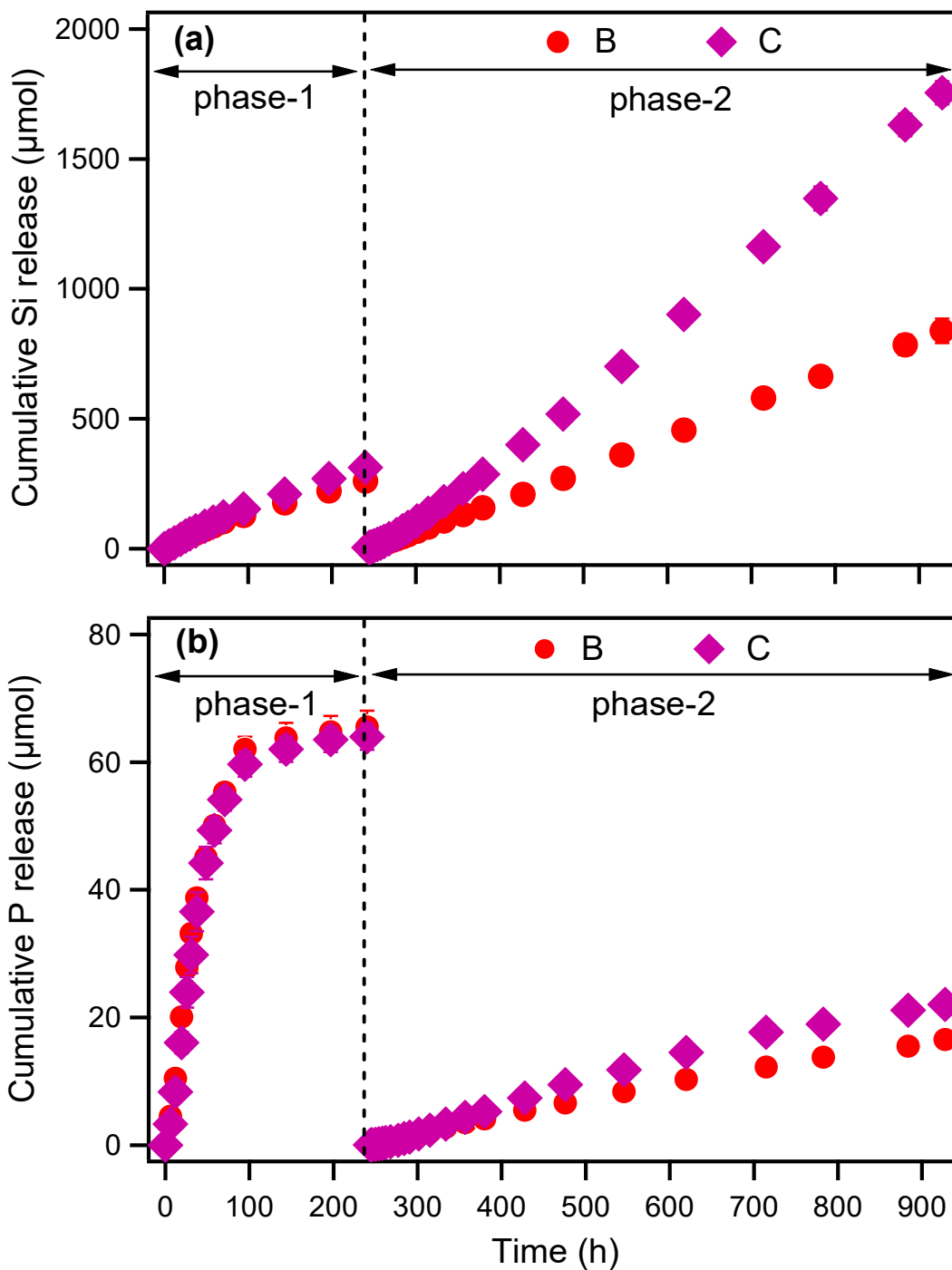
**Figure 5.18.** Cumulative release of Si (a) and P (b) to the overlying waters of columns **B** and **C** during phase-1 and phase-2 as a function of time. The inflow solutions for columns **B** and **C** contained APW and $Fe^{2+}$ (no added Si) during phase-1, and were replaced with APW, and APW with Si, respectively, during phase-2. Overlying waters of these columns were aerated during both experimental phases. Error bars represent the range of values measured between duplicate columns.

The total amounts of P released from columns **B** and **C** (APW+$Fe^{2+}$) during phase-1 were comparable (Table 5.3), which was expected due to similar experimental conditions for both. During phase-2, column **C** (with added Si) released slightly greater amounts of P than the release by column **B** (with no added Si), as revealed by comparing the cumulative release of P from both columns (Figure 5.18b). The total releases of P (during phase-2) from columns **B** and **C** were 17±0 and 22±1 µmol, respectively (Table 5.2). This means that column **C** released 30% more P than column **B** during phase-2, examplifying the effect of dissolved Si added (with inflow solution) to column **C**. However, the total amounts of P release from column **B** (17±0 µmol) and **C** (22±1 µmol) during the 30 days of phase-2 were less than half the amounts (73±9 µmol P) released from these colunms during the 10 days of phase-1. The lower release of P from columns **B** and **C** during phase-2 could have occurred due to the depletion of major fractions of labile organic and inorganic P pools in sediments during phase-1.

The release of P from columns **B** and **C** (during phase-2) cannot be described solely as desorbed P. This is because: major part of the sediments in those columns (below the top oxic layer) were anoxic, where the release of P from the dissolution of phosphorus containing minerals and organic-P compounds was possible. The overlying waters of columns **B** and **C** were aerated during phase-2 and thus were oxic. Therefore, the immobilization of dissolved P likely occurred in the surface sediments via the adsorption of P on mineral surfaces or via the incorporation in new precipitates. The only difference between columns **B** and **C** during phase-2 was that, the inflow solution of column **C** had added Si, but that of column **B** had not. Therefore, the additional release of P from column **C** in comparison to column **B** can be attributed to the effect of dissolved Si.

The major part of the sediments in column **C** below the top few millimeters were anoxic where the immobilization of P may also occur by the formation of vivianite ($Fe_3(PO_4)_2.8H_2O$) via chemical precipitation (Connell et al., 2015; Nriagu and Dell, 1974). Although the chemical precipitation of Si with $Fe^{2+}$ is theoretically possible, the formation of $Fe_2SiO_4$ generally requires nearly zero sulfide, and low $HCO_3^-$ and $CO_3^{2-}$ concentrations (Curtis and Spears, 1968). The Cootes Paradise sediment used in this study was buffered with carbonate minerals (e.g., calcite), which during the experiment released Ca (Table 5.2) and might have resulted in $HCO_3^-/CO_3^{2-}$ release (note that the amount of Ca added to each column during phase-1 was

600 µmol). Therefore, the influence of dissolved Si on the removal of P via the preferential formation of $Fe_2SiO_4$ over vivianite was not likely.

The effects of dissolved Si on the adsorption and desorption of phosphate to and from goethite were investigated in the previous chapters (Chapter 2 and Chapter 3). Although dissolved Si increased the mobility of phosphate in water by decreasing phosphate adsorption on goethite (Chapter 2), it showed no measurable influence on phosphate desorption (Chapter 3). Therefore, based on the understanding from the adsorption and desorption studies, dissolved Si added to column **C** during phase-2 promoted P release potentially by mobilizing sediment released P in the aqueous phase, at least by decreasing phosphate adsorption on sediment ferric (hydr)oxides.

### 5.4.6 Phosphorus release under oxic and anoxic conditions

To understand the relative importance of P release under oxic and anoxic conditions, the amount of P released during phase-2 by the oxic (**B** and **C**) and anoxic (**D**, **F,** and **G**) columns were compared. The results show that the amounts of P released from columns **B** and **C** under oxic conditions (during phase-2) was ~5 to 7 times lower than the release by the anoxic columns (**D**, **F,** and **G**) during phase-2. This is likely because the P released from the deeper sediments of columns **B** and **C** could have been further immobilized in the surface sediments via chemical precipitation or via the adsorption of P onto the mineral surfaces under oxic conditions (Connell et al., 2015; Gächter and Müller, 2003; Orihel et al., 2017; Rothe et al., 2014). This means that anoxic conditions are critically important for P release at the sediment-water interface and thus contribute to the internal P loading. In this study, none of the inflow solutions of anoxic columns **D**, **F** and **G** during phase-2 contained Si. However, if the inflow solutions of anoxic columns **D**, **E** and **G** would contain Si during phase-2, these columns would have likely released greater amounts of P compared to the release observed in the absence of added Si.

### 5.5 Conclusions

This study presents the effects of dissolved Si on the mobilization of P from calcareous marsh sediments through the interactions between Fe, P and Si under variable redox conditions. During the first phase of the experiment, ferric (co)-precipitates are formed via the oxidation

of $Fe^{2+}$ in the presence of variable concentrations of dissolved Si in the surface sediments of the columns under oxic conditions. The second phase investigates the reactivity of the ferric (co)-precipitates, formed in the presence of variable Si concentrations during phase-1, towards the reductive dissolution of Fe and the associated P under anoxic conditions. The effects of dissolved Si on the mobilization of P from sediments is also investigated under oxic conditions.

The results from anoxic columns (**D** and **F**, during phase-2) suggest that ferric (co)-precipitates that formed in the presence of higher concentrations of dissolved Si are more reactive towards reductive dissolution of Fe and the associated P. The results from the oxic columns (from phase-2) with and without added Si, to the inflow solutions of columns **C** and **B**, respectively, demonstrate that higher concentrations of dissolved Si increase the mobility of sediment-released P in the aqueous phase. However, the P release from the sediments under anoxic conditions is higher (5 to 7 times) than the release under oxic conditions. This result highlights the importance of oxygen levels at the sediment-water interface in regulating the benthic release of P to the overlying water.

The evidence of coupled cycling of Si and Mn under oxic and anoxic conditions reinforces the underlying mechanism presented for the coupled Si and Fe cycling in sediment. In lake sediments, ferric (co)-precipitates that form in the surface sediments under oxic conditions may be buried into the deeper sediments where the reductive dissolution of Fe and the associated P is possible. Reductive dissolution of these ferric (co)-precipitates is also possible when the redox conditions of the overlying water changes from oxic to anoxic, which could be regulated by diurnal cycles or by seasonal changes. Therefore, ferric (co)-precipitates that form in the presence of higher concentrations of Si may result in greater release of Fe and the associated P from sediments under reducing conditions. High concentrations of dissolved Si may further increase the mobility of this reductively dissolved P, by inhibiting the re-adsorption of P on sediment ferric (hydr)oxides, particularly under alkaline conditions.

# Chapter 6
## General conclusions

### 6.1 Summary of key findings

This thesis has demonstrated the potential roles of silicate on the mobilization of phosphate in aquatic environments. Silicate both in dissolved and co-precipitated forms may exert multiple controls on the mobilization of phosphate from sediment to the aqueous phase.

### 6.1.1 Competitive adsorption of silicate and phosphate on goethite

Phosphate is released to sediment pore-water from various organic and inorganic sources. Dissolved silicate may increase the mobility of phosphate by decreasing the re-adsorption of phosphate on ferric (hydr)oxides due to a competitive adsorption effect (Chapter 2). This effect of silicate is unimportant under acidic conditions but is of environmental relevance under alkaline conditions due to increased concentration of deprotonated silicate which is a stronger competitor with phosphate for adsorption sites compared to the protonated form which dominates at low to neutral pH. However, increased dissolved silicate concentrations over time are not likely to cause the release of phosphate which is already sorbed to ferric (hydr)oxides even under alkaline conditions. This is because of immobilization of phosphate on goethite's surface, potentially via surface precipitation or due to the formation of stronger surface complexes (Chapter 3). The experimental results shown in Chapter 4 indicate that the effect of dissolved silicate on phosphorus incorporation during precipitation of authigenic iron is likely minor.

### 6.1.2 Reactivity of ferric (co)-precipitates formed under variable silicate concentrations

Experimental results in Chapters 4 and 5 show that presence of variable silicate concentrations during $Fe^{2+}$ oxidation influence reactivity of resulting ferric (co)-precipitates towards reductive dissolution. However, these results also demonstrate that the effect of silicate on the stability of ferric (co)-precipitates is complex and may promote or decrease iron and phosphate mobility depending on the environmental conditions under which the co-precipitates are formed. For

example, ferric (co)-precipitates (i.e., Fe-P-Si) synthesized in the presence of higher silicate concentrations exhibited lower reactivity towards abiotic reductive dissolution in experiments presented in Chapter 4. However, in biotic experiments conducted with natural sediments (Chapter 5), the ferric (co)-precipitates formed at higher aqueous silicate concentrations were shown to release more iron and associated phosphate during anoxic conditions at the sediment-water interface. In the experiments presented in Chapter 4, the ferric (co)-precipitates were precipitated rapidly from a solution containing high concentrations of iron, phosphate, and silicate. This synthesis method is therefore likely representative of environments where groundwater interacts rapidly with surface waters and co-precipitation of iron, phosphate, and silicate occurs very quickly (e.g., springs). However, in other natural environments where aqueous concentrations of iron, phosphate, and silicate are more moderate and co-precipitation is more gradual, such as diffusion limited precipitation at the sediment-water interface in lake sediments, an increased concentration of co-precipitated silicate may increase the mobility of iron and phosphate under reducing conditions, as revealed from flow-through column experiments using natural sediments (Chapter 5).

### 6.1.3 Different precipitation processes, different reactivities

Ferric precipitates and co-precipitates synthesized via the $Fe^{2+}$ oxidation and pH increase methods showed different reactivity towards reductive dissolution (Chapter 4). Ferric (co)-precipitates synthesized by oxidative precipitation always exhibited higher reactivity than those formed by pH increase. Further, dramatic differences were present between pure iron precipitates and co-precipitates, irrespective of synthesis method and even when the concentration of phosphate and silicate in the co-precipitate was relatively low. As pure minerals rarely form in natural conditions, researchers preparing synthetic analogues of natural minerals should, therefore, consider the use of synthetic co-precipitates, rather than pure minerals, to minimize differences between natural and experimental conditions. These differences determined experimentally may also be applicable to similar minerals, which precipitate via different mechanisms in natural systems, e.g., rapid vs slow precipitation, and oxidative precipitation vs pH-induced changes to solubility. The stability of the precipitates formed under these different conditions likely has implications for the mobility of associated anions including phosphate and silicate as well as common contaminants such as arsenate.

## 6.2 Future work

The reactivity of ferric (co)-precipitates in this thesis is addressed based on the results of dissolution experiments. The information on the interactions between iron, phosphate, and silicate in the co-precipitates may provide additional information on their reactivity. The next steps to be undertaken subsequent to this thesis are to characterize the synthesized co-precipitates by $^{57}$Fe Mössbauer and X-ray absorption spectroscopic techniques. These spectroscopic studies along with the existing data are expected to provide better insights into the reasons for reactivity differences between the co-precipitates at a structural level.

The chemical composition of ferric co-precipitates formed via $Fe^{2+}$ oxidation under variable silicate concentrations demonstrate that the co-precipitates synthesized in the presence of higher silicate concentrations exhibit higher concentrations of solid phase silicate (i.e., Si:Fe ratio) (Chapter 4). However, this greater incorporation of silicate into ferric co-precipitates is not observed where $Fe^{2+}$ is oxidized in natural sediments (Chapter 5). The reactivity of the ferric (co)-precipitates synthesized abiotically under controlled laboratory conditions (Chapter 4) and in sediments (Chapter 5) show opposing trends based on the silicate concentrations during their synthesis. Dissolved silicate is known to decrease $Fe^{2+}$ oxidation rate under abiotic conditions but under biotic conditions (Kinsela et al., 2016), when $Fe^{2+}$ oxidation is mediated by iron reducing bacteria, silicate increases the rate (Gauger et al., 2016; Konhauser et al., 2007). Further, iron mineral products formed via the oxidation of $Fe^{2+}$ in presence of silicate exhibit smaller particle size and lower crystallinity than the minerals formed in the absence of silicate (Châtellier et al., 2004). However, the mechanisms by which dissolved silicate increases bacterially-mediated $Fe^{2+}$ oxidation, and alters the chemical properties (i.e., chemical composition and reactivity) of resulting ferric (co)-precipitates are not well understood. Therefore, studying the biotic and abiotic oxidation of $Fe^{2+}$ under variable concentrations of dissolved silicate as well as the chemical properties of the resulting iron minerals would provide further understanding in the coupled cycling of iron, phosphorus and silicon in natural environments.

Studies within this thesis show that dissolved silicate at higher concentrations can influence phosphate mobilization, with greater effect under alkaline conditions. In aquatic environments, sediments buffered with carbonate minerals (e.g., calcite and dolomite) experience alkaline pH (Langmuir, 1997b). In surface waters, photosynthesis may result in

alkaline pH when aquatic plants and algae consume dissolved carbon dioxide and bicarbonate from water, and also by biogeochemical reduction processes (Langmuir, 1997d; Verspagen et al., 2014). The sediments buffered with carbonate minerals are also likely to have higher calcium and magnesium concentrations. Dissolved calcium and magnesium have previously been shown to increase the adsorption of phosphate on ferric (hydr)oxides, particularly under alkaline conditions (Atouei et al., 2016; Millero et al., 2001; Rietra et al., 2001). Therefore, the combined effects of dissolved calcium and magnesium on silicate mediated phosphate mobilization require further investigation. For example, adsorption and desorption of phosphate in the presence of silicate and various calcium or magnesium concentrations should be investigated. The adsorption pH envelope for the concurrent adsorption of phosphate, silicate, and calcium/magnesium could be used, for example, to calibrate a CD-MUSIC model. Finally, the model could be applied to elucidate how calcium and magnesium can influence the effect of dissolved silicate on the adsorption of phosphate on ferric (hydr)oxides in natural systems.

The NWIS database holds a plethora of water quality information (e.g., physical, chemical and biological, geological etc.). Biogeochemical processes at the sediment-water interface are site-specific, which depends on local geology, biology, and climatic conditions including anthropogenic factors. Therefore, categorizing the eutrophic surface water systems based on local geology, climatic conditions and anthropogenic activities along with the NWIS data could be used to evaluate the importance of controls on phosphate mobilization in aquatic environments.

## 6.3 Environmental significance

Surface runoff, fluvial transport, and atmospheric deposition may increase phosphate concentrations in surface waters which can be deposited in sediment as particulate organic and inorganic phosphorus. Internal loading due to degradation of particulate organic and inorganic phosphorus from sediments along with the desorption of phosphate from the mineral surfaces may further increase the availability of phosphate in water. Dissolved silicate occurs ubiquitously in natural waters due to the dissolution of diatom frustules, plant phytoliths, and detrital silicate minerals. The sources of iron in surface waters are mostly from fluvial and atmospheric transport in particulate form, primarily in the $Fe^{3+}$ oxidation state. Particulate

ferric iron buried in the deeper sediment may also be a source of $Fe^{2+}$ release in sediment pore-water under reducing conditions. The upward diffusion of $Fe^{2+}$ may result in its immobilization via co-precipitation with phosphate, silicate and with other ions in oxic surface sediments. The ferric (co)-precipitates that form in surface sediments in the presence of higher silicate concentrations may result in a faster release of iron and phosphate under reducing conditions. The presence of an elevated concentration of dissolved silicate may increase the mobility of reductively dissolved phosphate in water by decreasing its re-adsorption on mineral surfaces. The upward diffusion of iron, phosphate, and silicate from sediment pore-water to the overlying waters may contribute to the internal nutrient loads, which may enhance the growth of phytoplankton. Conversely, ferric (co)-precipitates (i.e., Fe-P-Si) with higher solid phase Si:Fe ratios that may form in the presence of higher silicate during the mixing of groundwater and surface water could be more stable under reducing conditions causing the decreased mobility of iron and phosphate in the aqueous phase.

# Copyright permissions

## Figure 1.1 (Chapter 1)

**Title:** A brief history of phosphorus: From the philosopher's stone to nutrient recovery and reuse

**Author:** K. Ashley,D. Cordell,D. Mavinic

**Publication:** Chemosphere

**Publisher:** Elsevier

**Date:** August 2011

Copyright © 2011, Elsevier

**Order Completed**

Thank you for your order.

This Agreement between University of Waterloo ("You") and Elsevier ("Elsevier") consists of your license details and the terms and conditions provided by Elsevier and Copyright Clearance Center.

Your confirmation email will contain your order number for future reference.

printable details

| | |
|---|---|
| License Number | 4560880237954 |
| License date | Apr 02, 2019 |
| Licensed Content Publisher | Elsevier |
| Licensed Content Publication | Chemosphere |
| Licensed Content Title | A brief history of phosphorus: From the philosopher's stone to nutrient recovery and reuse |
| Licensed Content Author | K. Ashley,D. Cordell,D. Mavinic |
| Licensed Content Date | Aug 1, 2011 |
| Licensed Content Volume | 84 |
| Licensed Content Issue | 6 |
| Licensed Content Pages | 10 |

| | |
|---|---|
| Type of Use | reuse in a thesis/dissertation |
| Portion | figures/tables/illustrations |
| Number of figures/tables/illustrations | 1 |
| Format | both print and electronic |
| Are you the author of this Elsevier article? | No |
| Will you be translating? | No |
| Original figure numbers | Fig. 1 |
| Title of your thesis/dissertation | Interactions of Phosphate and Silicate with Iron oxides in Freshwater Environments |
| Expected completion date | Apr 2019 |
| Estimated size (number of pages) | 200 |
| Requestor Location | University of Waterloo 200 University Avenue West Waterloo, ON N2L 3G1 Canada Attn: University of Waterloo |
| Publisher Tax ID | GB 494 6272 12 |

**Figure 1.4 (Chapter 1)**

**Figure 1.5 (Chapter 1)**

Copyright Clearance Center — RightsLink®

| | |
|---|---|
| **Title:** | Environmental reviews |
| **Article ID:** | 1181-8700 |
| **Publication:** | Publication1 |
| **Publisher:** | CCC Republication |
| **Date:** | Jan 1, 1993 |

Copyright © 1993, CCC Republication

**Order Completed**

Thank you for your order.

This Agreement between Md Abdus Sabur ("You") and Canadian Science Publishing ("Canadian Science Publishing") consists of your order details and the terms and conditions provided by Canadian Science Publishing and Copyright Clearance Center.

| | |
|---|---|
| License number | Reference confirmation email for license number |
| License date | Apr, 14 2019 |
| Licensed content publisher | Canadian Science Publishing |
| Licensed content title | Environmental reviews |
| Licensed content date | Jan 1, 1993 |
| Type of use | Thesis/Dissertation |
| Requestor type | Academic institution |
| Format | Print, Electronic |
| Portion | image/photo |
| Number of images/photos requested | 1 |
| The requesting person/organization | Md Abdus Sabur |
| Title or numeric reference of the portion(s) | Fig. 1 |

| | |
|---|---|
| Title of the article or chapter the portion is from | Phosphate adsorption on metal oxides and metal hydroxides: A comparative review |
| Editor of portion(s) | N/A |
| Author of portion(s) | Qian, Guangren ; et al |
| Volume of serial or monograph | 24 |
| Issue, if republishing an article from a serial | 3 |
| Page range of portion | 319-332 |
| Publication date of portion | May 16, 2016 |
| Rights for | Main product and any product related to main product |
| Duration of use | Life of current edition |
| Creation of copies for the disabled | no |
| With minor editing privileges | yes |
| For distribution to | Canada |
| In the following language(s) | Original language of publication |
| With incidental promotional use | yes |
| Lifetime unit quantity of new product | More than 2,000,000 |
| Title | Interactions of Phosphate and Silicate with Iron oxides in Freshwater Environments |
| Institution name | n/a |
| Expected presentation date | Apr 2019 |
| Requestor Location | University of Waterloo 200 University Avenue West Waterloo, ON N2L 3G1 Canada Attn: University of Waterloo |
| Billing Type | Invoice |

| Billing address | University of Waterloo |
| | 200 University Avenue West |
| | Waterloo, ON N2L 3G1 |
| | Canada |
| | Attn: University of Waterloo |

**Figure 1.13 (Chapter 1)**

**Order Completed**

Thank you for your order.

This Agreement between University of Waterloo ("You") and Springer Nature ("Springer Nature") consists of your license details and the terms and conditions provided by Springer Nature and Copyright Clearance Center.

Your confirmation email will contain your order number for future reference.

printable details

| | |
|---|---|
| License Number | 4560890671664 |
| License date | Apr 02, 2019 |
| Licensed Content Publisher | Springer Nature |
| Licensed Content Publication | Nature Reviews Microbiology |
| Licensed Content Title | Microorganisms pumping iron: anaerobic microbial iron oxidation and reduction |
| Licensed Content Author | Karrie A. Weber, Laurie A. Achenbach, John D. Coates |
| Licensed Content Date | Oct 1, 2006 |
| Licensed Content Volume | 4 |
| Licensed Content Issue | 10 |

| | |
|---|---|
| Type of Use | Thesis/Dissertation |
| Requestor type | academic/university or research institute |
| Format | print and electronic |
| Portion | figures/tables/illustrations |
| Number of figures/tables/illustrations | 1 |
| High-res required | no |
| Will you be translating? | no |
| Circulation/distribution | >50,000 |
| Author of this Springer Nature content | no |
| Title | Interactions of Phosphate and Silicate with Iron oxides in Freshwater Environments |
| Institution name | n/a |
| Expected presentation date | Apr 2019 |
| Portions | Figure 1 |
| Requestor Location | University of Waterloo 200 University Avenue West  Waterloo, ON N2L 3G1 Canada Attn: University of Waterloo |
| Total | 0.00 USD |

**Figure 2.1 (Chapter 2)**

| | |
|---|---|
| Licensed Content Volume | 347 |
| Licensed Content Issue | 1 |
| Licensed Content Pages | 8 |
| Type of Use | reuse in a thesis/dissertation |
| Portion | figures/tables/illustrations |
| Number of figures/tables/illustrations | 1 |
| Format | both print and electronic |
| Are you the author of this Elsevier article? | No |
| Will you be translating? | No |
| Original figure numbers | Fig. 4 |
| Title of your thesis/dissertation | Interactions of Phosphate and Silicate with Iron oxides in Freshwater Environments |
| Expected completion date | Apr 2019 |
| Estimated size (number of pages) | 200 |
| Requestor Location | University of Waterloo 200 University Avenue West |
| | Waterloo, ON N2L 3G1 Canada Attn: University of Waterloo |
| Publisher Tax ID | GB 494 6272 12 |

## Figure 4.2(a) (Chapter 4)
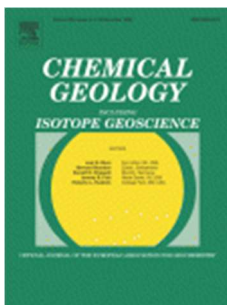
| | |
|---|---|
| **Title:** | Fe(II) oxidation processes at the surface of bacterially colonized iron deposits |
| **Author:** | Fumito Shiraishi,Kohei Nakao,Chizuru Takashima,Akihiro Kano,Takaaki Itai |
| **Publication:** | Chemical Geology |
| **Publisher:** | Elsevier |
| **Date:** | 5 January 2018 |

© 2017 Elsevier B.V. All rights reserved.

### Order Completed

Thank you for your order.

This Agreement between University of Waterloo ("You") and Elsevier ("Elsevier") consists of your license details and the terms and conditions provided by Elsevier and Copyright Clearance Center.

Your confirmation email will contain your order number for future reference.

printable details

| | |
|---|---|
| License Number | 4567960269358 |
| License date | Apr 14, 2019 |
| Licensed Content Publisher | Elsevier |
| Licensed Content Publication | Chemical Geology |
| Licensed Content Title | Fe(II) oxidation processes at the surface of bacterially colonized iron deposits |
| Licensed Content Author | Fumito Shiraishi,Kohei Nakao,Chizuru Takashima,Akihiro Kano,Takaaki Itai |
| Licensed Content Date | Jan 5, 2018 |

| | |
|---|---|
| Licensed Content Volume | 476 |
| Licensed Content Issue | n/a |
| Licensed Content Pages | 10 |
| Type of Use | reuse in a thesis/dissertation |
| Portion | figures/tables/illustrations |
| Number of figures/tables/illustrations | 1 |
| Format | both print and electronic |
| Are you the author of this Elsevier article? | No |
| Will you be translating? | No |
| Original figure numbers | Fig. 2 (D) |
| Title of your thesis/dissertation | Interactions of Phosphate and Silicate with Iron oxides in Freshwater Environments |
| Expected completion date | Apr 2019 |
| Estimated size (number of pages) | 200 |
| Requestor Location | University of Waterloo 200 University Avenue West |
| | Waterloo, ON N2L 3G1 Canada Attn: University of Waterloo |
| Publisher Tax ID | GB 494 6272 12 |

**Figure SM-4.1 (Supplementary material)**

# Bibliography

Adhikari, D., Zhao, Q., Das, K., Mejia, J., Huang, R., Wang, X., Poulson, S.R., Tang, Y., Roden, E.E., Yang, Y., 2017. Dynamics of ferrihydrite-bound organic carbon during microbial Fe reduction. Geochim. Cosmochim. Acta 212, 221–233. https://doi.org/10.1016/j.gca.2017.06.017

Antelo, J., Arce, F., Avena, M., Fiol, S., López, R., Macías, F., 2007. Adsorption of a soil humic acid at the surface of goethite and its competitive interaction with phosphate. Geoderma 138, 12–19. https://doi.org/10.1016/j.geoderma.2006.10.011

Antelo, J., Avena, M., Fiol, S., López, R., Arce, F., 2005. Effects of pH and ionic strength on the adsorption of phosphate and arsenate at the goethite-water interface. J. Colloid Interface Sci. 285, 476–486. https://doi.org/10.1016/j.jcis.2004.12.032

Antelo, J., Fiol, S., Pérez, C., Mariño, S., Arce, F., Gondar, D., López, R., 2010. Analysis of phosphate adsorption onto ferrihydrite using the CD-MUSIC model. J. Colloid Interface Sci. 347, 112–119. https://doi.org/10.1016/j.jcis.2010.03.020

Arakaki, T., Morse, J.W., 1993. Coprecipitation and adsorption of Mn(II) with mackinawite (FeS) under conditions similar to those found in anoxic sediments. Geochim. Cosmochim. Acta 57, 9–14. https://doi.org/10.1016/0016-7037(93)90463-7

Arts, D., Sabur, M.A., Al-Abadleh, H.A., 2013. Surface interactions of aromatic organoarsenical compounds with hematite nanoparticles using ATR-FTIR: kinetic studies. J. Phys. Chem. A 117, 2195–2204. https://doi.org/10.1021/jp311569m

Ashley, K., Cordell, D., Mavinic, D., 2011. A brief history of phosphorus: From the philosopher's stone to nutrient recovery and reuse. Chemosphere 84, 737–746. https://doi.org/10.1016/j.chemosphere.2011.03.001

Atouei, M.T., Rahnemaie, R., Kalanpa, E.G., Davoodi, M.H., 2016. Competitive adsorption of magnesium and calcium with phosphate at the goethite water interface: Kinetics, equilibrium and CD-MUSIC modeling. Chem. Geol. 437, 19–29. https://doi.org/10.1016/j.chemgeo.2016.05.004

Avnimelech, Y., 1983. Phosphorus and calcium carbonate solubilities in Lake Kinneret. Limnol. Oceanogr. 28, 640–645. https://doi.org/10.4319/lo.1983.28.4.0640

Baines, S.B., Twining, B.S., Vogt, S., Balch, W.M., Fisher, N.S., Nelson, D.M., 2011. Elemental composition of equatorial Pacific diatoms exposed to additions of silicic acid and iron. Deep. Res. Part II Top. Stud. Oceanogr. 58, 512–523. https://doi.org/10.1016/j.dsr2.2010.08.003

Baken, S., Moens, C., Grift, B. Van Der, Smolders, E., 2016a. Phosphate binding by natural iron-rich colloids in streams. Water Res. 98, 326–333. https://doi.org/10.1016/j.watres.2016.04.032

Baken, S., Regelink, I.C., Comans, R.N.J., Smolders, E., Koopmans, G.F., 2016b. Iron-rich colloids as carriers of phosphorus in streams: a field- flow fractionation study. Water Res. 99, 83–90. https://doi.org/10.1016/j.watres.2016.04.060

Baldwin, D.S., 2013. Organic phosphorus in the aquatic environment. Environ. Chem. 10,

439–454. https://doi.org/10.1071/EN13151

Berns, A.E., Philipp, H., Narres, H.-D., Burauel, P., Vereecken, H., Tappe, W., 2008. Effect of gamma-sterilization and autoclaving on soil organic matter structure as studied by solid state NMR, UV and fluorescence spectroscopy. Eur. J. Soil Sci. 59, 540–550. https://doi.org/10.1111/j.1365-2389.2008.01016.x

Boland, D.D., Collins, R.N., Miller, C.J., Glover, C.J., Waite, T.D., 2014. Effect of solution and solid-phase conditions on the Fe(II)-accelerated transformation of ferrihydrite to lepidocrocite and goethite. Environ. Sci. Technol. 48, 5477–5485. https://doi.org/10.1021/es4043275

Bondietti, G., Sinniger, J., Stumm, S., 1993. The reactivity of Fe (III) (hydr) oxides: in inhibiting the dissolution effects of ligands. Colloids Surfaces A Physicochem. Eng. Asp. 79, 157–167. https://doi.org/10.1021/es801352k

Bonneville, S., Behrends, T., Van Cappellen, P., 2009. Solubility and dissimilatory reduction kinetics of iron(III) oxyhydroxides: a linear free energy relationship. Geochim. Cosmochim. Acta 73, 5273–5282. https://doi.org/10.1016/j.gca.2009.06.006

Bonneville, S., Cappellen, P. Van, Behrends, T., 2004. Microbial reduction of iron (III) oxyhydroxides: effects of mineral solubility and availability. Chem. Geol. 212, 255–268. https://doi.org/10.1016/j.chemgeo.2004.08.015

Borch, T., Kretzschmar, R., Skappler, A., Van Cappellen, P., Ginder-Vogel, M., Voegelin, A., Campbell, K., 2010. Biogeochemical redox processes and their impact on contaminant dynamics. Environ. Sci. Technol. 44, 15–23. https://doi.org/10.1021/es9026248

Borggaard, O.K., Gimsing, A.L., Strobel, B.W., 2005. Influence of humic substances on phosphate adsorption by aluminium and iron oxides. Geoderma 127, 270–279. https://doi.org/10.1016/j.geoderma.2004.12.011

Böttcher, B.E., 1998. Manganese(II) partitioning during experimental precipitation of rhodochrosite–calcite solid solutions from aqueous solutions. Mar. Chem. 62, 287–297. https://doi.org/10.1016/S0304-4203(98)00039-5

Brown, D., Altermatt, D., 1985. Bond-valence parameters obtained from a systematic analysis of the inorganic crystal structure satabase. Acta Crystallogr. B41, 244–247.

Brunauer, S., Emmett, P.H., Teller, E., 1938. Adsorption of gases in multimolecular layers. J. Am. Chem. Soc. 60, 309–319. https://doi.org/10.1021/ja01269a023

Cama, J., Ganor, J., 2015. Dissolution kinetics of clay minerals, in: Developments in Clay Science. Elsevier, pp. 101–153. https://doi.org/10.1016/B978-0-08-100027-4.00004-8

Caraco, N.F., Cole, J.J., Likens, G.E., 1989. Evidence for sulphate controlled phosphorus release from sediments of aquatic systems. Nature 341, 316–318.

Carolina, N., 2002. Harmful algal blooms and eutrophication nutrient sources, composition, and consequences. Estuaries and Coasts 25, 704–726.

Carpenter, S.R., 2008. Phosphorus control is critical to mitigating eutrophication. Proc. Natl. Acad. Sci. U. S. A. 105, 11039–11040. https://doi.org/10.1073/pnas.0806112105

Chan, Y., Kuan, W., Tzou, Y., Chen, T., Liu, Y., Wang, M., Teah, H., 2016. Molecular structures of Al/Si and Fe/Si coprecipitates and the implication for selenite removal. Sci. Rep. 6, 24716. https://doi.org/doi: 10.1038/srep24716

Châtellier, X., Marcia West, M., Rose, J., Fortin, D., Leppard, G.G., Ferris, F.G., 2004. Characterization of iron-oxides formed by oxidation of ferrous ions in the presence of various bacterial species and inorganic ligands. Geomicrobiol. J. 21, 99–112. https://doi.org/10.1080/01490450490266343

Chen, X., Jiang, J., Yan, F., Tian, S., Li, K., 2014. A novel low temperature vapor phase hydrolysis method for the production of nano-structured silica materials using silicon tetrachloride. RSC Adv. 4, 8703–8710. https://doi.org/10.1039/C3RA47018K

Chislock, M.F., Doster, E., Zitomer, R.A., Wilson, A.E., 2013. Eutrophication: causes, consequences, and controls in aquatic ecosystems. Nat. Educ. Knowl. 4, 10.

Chitrakar, R., Tezuka, S., Sonoda, A., Sakane, K., Ooi, K., Hirotsu, T., 2006. Phosphate adsorption on synthetic goethite and akaganeite. J. Colloid Interface Sci. 298, 602–608. https://doi.org/10.1016/j.jcis.2005.12.054

Christl, I., Brechbühl, Y., Graf, M., Kretzschmar, R., 2012. Polymerization of silicate on hematite surfaces and its influence on arsenic sorption. Environ. Sci. Technol. 46, 13235–13243. https://doi.org/10.1021/es303297m

Christophoridis, C., Fytianos, K., 2006. Conditions affecting the release of phosphorus from surface lake sediments. J. Environ. Qual. 35, 1181–1192. https://doi.org/10.2134/jeq2005.0213

Chughtai, A., Marshall, R., Nancollas, G.H., 1968. Complexes in calcium phosphate solutions. J. Phys. Chem. 72, 208–211. https://doi.org/10.1021/j100847a039

Cismasu, A.C., Michel, F.M., Tcaciuc, A.P., Brown, G.E., 2014. Properties of impurity-bearing ferrihydrite III . Effects of Si on the structure of 2-line ferrihydrite. Geochim. Cosmochim. Acta 133, 168–185. https://doi.org/10.1016/j.gca.2014.02.018

Connell, D.W.O., Mark, M., Jakobsen, R., Thamdrup, B., Joest, T., Kovacs, A., Christian, H., Hansen, B., 2015. Vivianite formation and its role in phosphorus retention in Lake Ørn , Denmark. Chem. Geol. 409, 42–53. https://doi.org/10.1016/j.chemgeo.2015.05.002

Cornell, R.M., Schwertmann, U., 2003. Dissolution, in: The Iron Oxides: Structure, Properties, Reactions, Occurences and Uses, Second Edition. Wiley-VCH Verlag GmbH & Co., Weinheim, Germany, pp. 297–344.

Correll, D.L., 1998. The role of phosphorus in the eutrophication of receiving waters: a review. J. Environ. Qual. 27, 261. https://doi.org/10.2134/jeq1998.00472425002700020004x

Curtis, C.D., Spears, D.A., 1968. The formation of sedimentary iron minerals. Econ. Geol. 63, 257–270. https://doi.org/10.2113/gsecongeo.63.3.257

Danen-louwerse, H., Lijklema, L., Coenraats, M., 1993. Iron content of sediment and phosphate adsorption properties. Hydrobiologia 253, 311–317.

Davis, C.C., Chen, H., Edwards, M., 2002. Modeling silica sorption to iron hydroxide.

Environ. Sci. Technol. 36, 582–587. https://doi.org/10.1021/es010996t

Davis, S.N., 1964. Silica in streams and ground water. Am. J. Sci. 262, 870–891. https://doi.org/10.2475/ajs.262.7.870

Deng, Y., 1997. Effect of pH on the reductive dissolution rates of iron (III) hydroxide by ascorbate. Langmuir 13, 1835–1839. https://doi.org/10.1021/la9607013

Domagalski, J.L., Johnson, H., 2012. Phosphorus and groundwater: establishing links between agricultural use and transport to streams, Fact Sheet 2012–3004 (USGS).

Dorozhkin, V.S., 2016. Calcium orthophosphates ($CaPO_4$): occurrence and properties. Prog Biomater 5, 9–70. https://doi.org/10.1007/s40204-015-0045-z

Du, Y., Ramirez, C.E., Jaffé, R., 2018. Fractionation of Dissolved Organic Matter by Co-Precipitation with Iron : Effects of Composition. Environ. Process. 5, 5–21. https://doi.org/10.1007%2Fs40710-017-0281-4

Dyer, L., Fawell, P.D., Newman, O.M.G., Richmond, W.R., 2010. Synthesis and characterisation of ferrihydrite/silica co-precipitates. J. Colloid Interface Sci. 348, 65–70. https://doi.org/10.1016/j.jcis.2010.03.056

Eitzmann, J.L., Pilger, T.J., Pitts, K.L., Riley, A.J., Schloesser, J.T., Thornbrugh, D.J., 2009. Eutrophication of U.S. freshwaters: analysis of potential economic damages. Environ. Sci. Technol. 43, 12–19. https://doi.org/10.1021/es801217q

Emerson, D., 2009. Potential for iron-reduction and iron-cycling in iron oxyhydroxide-rich microbial mats at Loihi Seamount. Geomicrobiol. J. 26, 639–647. https://doi.org/org/10.1080/01490450903269985

Ewers, W.E., 1983. Chemical factors in the deposition and diagenesis of banded iron-formation, in: Trendall, A.F., Morris, R.. (Eds.), Developments in Precambrian Geology. Elsevier, Amsterdam, The Netherlands, pp. 491–512. https://doi.org/10.1016/S0166-2635(08)70054-9

Fabrizioli, P., Bürgi, T., Burgener, M., Doorslaer, S. van, Baiker, A., 2002. Synthesis, structural and chemical properties of iron oxide–silica aerogels. J. Mater. Chem. 12, 619–630. https://doi.org/10.1039/B108120A

Farrell, J., Chaudhary, B.K., 2013. Understanding arsenate reaction kinetics with ferric hydroxides. Environ. Sci. Technol. 47, 8342–8347.

Ferdelman, T.G., Church, T.M., Luther III, G.W., 1991. Sulfur enrichment of humic substances in a Delaware salt marsh sediment core. Geochim. Cosmochim. Acta 55, 979–988. https://doi.org/org/10.1016/0016-7037(91)90156-Y

Filippelli, G.M., 2008. The global phosphorus cycle: past, present, and future. Elements 4, 89–95. https://doi.org/10.2113/GSELEMENTS.4.2.89

Filippelli, G.M., Street, W.M., 2002. The global phosphorus cycle. Rev. Mineral. Geochemistry 48, 391–425. https://doi.org/10.2138/rmg.2002.48.10

Fitzsimmons, E.G., 2003. Tap Water Ban for Toledo Residents. New York Times.

Freeman, J.S., Rowell, D.L., 1981. The adsorption and precipitation of phosphate onto calcite. J. Soil Sci. 32, 75–84.

Fuller, C.C., Davis, J.A.M.A., Waychunas, G.A., 1993. Surface chemistry of ferrihydrite: Part 2 . Kinetics of arsenate adsorption and coprecipitation. Geochim. Cosmochim. Acta 57, 2271–2282. https://doi.org/10.1016/0016-7037(93)90568-H

Gächter, R., Müller, B., 2003. Why the phosphorus retention of lakes does not necessarily depend on the oxygen supply to their sediment surface. Limnol. Oceanogr. 48, 929–933. https://doi.org/10.4319/lo.2003.48.2.0929

Gallup, D.L., 1989. Iron silicate scale formation and inhibition at the salton sea geothermal field. Geothermics 18, 97–103. https://doi.org/10.1017/CBO9781107415324.004

Gao, Y., Mucci, A., 2003. Individual and competitive adsorption of phosphate and arsenate on goethite in artificial seawater. Chem. Geol. 199, 91–109. https://doi.org/10.1016/S0009-2541(03)00119-0

Gao, Y., Mucci, A., 2001. Acid base reactions, phosphate and arsenate complexation, and their competitive adsorption at the surface of goethite in 0.7 M NaCl solution. Geochim. Cosmochim. Acta 65, 2361–2378. https://doi.org/org/10.1016/S0016-7037(01)00589-0

Gauger, T., Byrne, J.M., Konhauser, K.O., Obst, M., Crowe, S., Kappler, A., 2016. Influence of organics and silica on Fe(II) oxidation rates and cell–mineral aggregate formation by the green-sulfur Fe(II)-oxidizing bacterium Chlorobium ferrooxidansKoFox – Implications for Fe(II) oxidation in ancient oceans. Earth Planet. Sci. Lett. 443, 81–89. https://doi.org/org/10.1016/j.epsl.2016.03.022

Geelhoed, J.S., Hiemstra, T., Van Riemsdijk, W.H., 1997. Phosphate and sulfate adsorption on goethite: single anion and competitive adsorption. Geochim. Cosmochim. Acta 61, 2389–2396. https://doi.org/10.1016/S0016-7037(97)00096-3

Géhin, A., Grenèche, J.-M., Tournassat, C., Brendlé, J., Rancourt, D.G., Charlet, L., 2007. Reversible surface-sorption-induced electron-transfer oxidation of Fe(II) at reactive sites on a synthetic clay mineral. Geochim. Cosmochim. Acta 71, 863–876. https://doi.org/10.1016/j.gca.2006.10.019

Gérard, F., 2016. Clay minerals, iron/aluminum oxides, and their contribution to phosphate sorption in soils — A myth revisited. Geoderma 262, 213–226. https://doi.org/10.1016/j.geoderma.2015.08.036

Giles, C.D., Lee, L.G., Cade-Menun, B.J., Hill, J.E., Isles, P.D.F., Schroth, A.W., Druschel, G.K., 2015. Characterization of organic phosphorus form and bioavailability in lake sediments using 31PNuclear magnetic resonance and enzymatic hydrolysis. J. Environ. Qual. 44, 882. https://doi.org/10.2134/jeq2014.06.0273

Goldberg, S., 2014. Application of surface complexation models to anion adsorption by natural materials. Environ. Toxicol. Chem. 33, 2172–2180. https://doi.org/10.1002/etc.2566

Gorrepati, E. a., Wongthahan, P., Raha, S., Fogler, H.S., 2010. Silica precipitation in acidic solutions: Mechanism, pH effect, and salt effect. Langmuir 26, 10467–10474. https://doi.org/10.1021/la904685x

Grybos, M., Davranche, M., Gruau, G., Petitjean, P., Pédrot, M., 2009. Increasing pH drives organic matter solubilization from wetland soils under reducing conditions. Geoderma

154, 13–19. https://doi.org/org/10.1016/j.geoderma.2009.09.001

Hall, S.J., Silver, W.L., 2013. Iron oxidation stimulates organic matter decomposition in humid tropical forest soils. Glob. Chang. Biol. 19, 2804–2813. https://doi.org/10.1111/gcb.12229

Hamad, M.E., Rimmer, D.L., Syers, J.., 1992. Effect of iron oxide on phosphate sorption by calcite and calcareous soils. J. Soil Sci. 43, 273–281. https://doi.org/10.1111/j.1365-2389.1992.tb00135.x

Hammes, F., Goldschmidt, F., Vital, M., Wang, Y., Egli, T., 2010. Measurement and interpretation of microbial adenosine tri-phosphate (ATP) in aquatic environments. Water Res. 44, 3915–3923. https://doi.org/10.1016/j.watres.2010.04.015

Hartikainen, H., Pitkänen, M., Kairesalo, T., Tuominen, L., 1996. Co-occurrence and potential chemical competition of phosphorus and silicon in lake sediment. Water Res. 30, 2472–2478. https://doi.org/10.1016/0043-1354(96)00139-X

Hartland, A., Larsen, J.R., Andersen, M.S., Baalousha, M., Carroll, D.O., 2015. Association of arsenic and phosphorus with iron nanoparticles between streams and aquifers: implications for arsenic mobility. Environ. Sci. Technol. 49, 14101–14109. https://doi.org/10.1021/acs.est.5b03506

He, Z., Fortuna, A.-M., Senwo, Z.N., Irenus, T.A., Honeycutt, C.W., Griffin, T.S., 2006. Hydrochloric fractions in Hedley fractionation may contain inorganic and organic phosphates. Soil Sci. Soc. Am. J. 70, 893. https://doi.org/10.2136/sssaj2005.0152

He, Z., Honeycutt, C.W., 2005. A modified molybdenum blue method for orthophosphate determination suitable for investigating enzymatic hydrolysis of organic phosphates. Commun. Soil Sci. Plant Anal. 36, 1373–1383. https://doi.org/10.1081/CSS-200056954

Heisler, J., Glibert, P.M., Burkholder, J.M., Anderson, D.M., Cochlan, W., Dennison, W.C., Dortch, Q., Gobler, C.J., Heil, C.A., Humphries, E., Lewitus, A., Magnien, R., Marshall, H.G., Sellner, K., Stockwell, D.A., Stoecker, D.K., Suddleson, M., 2008. Eutrophication and harmful algal blooms: a scientific consensus. Harmful Algae 8, 3–13. https://doi.org/10.1016/j.hal.2008.08.006

Hiemstra, T., 2018. Ferrihydrite interaction with silicate and competing oxyanions: geometry and hydrogen bonding of surface species. Geochim. Cosmochim. Acta 238, 453–476. https://doi.org/10.1016/j.gca.2018.07.017

Hiemstra, T., Barnett, M.O., van Riemsdijk, W.H., 2007. Interaction of silicic acid with goethite. J. Colloid Interface Sci. 310, 8–17. https://doi.org/10.1016/j.jcis.2007.01.065

Hiemstra, T., Riemsdijk, W.H. Van, 2006. On the relationship between charge distribution, surface hydration, and the structure of the interface of metal hydroxides 301, 1–18. https://doi.org/10.1016/j.jcis.2006.05.008

Hiemstra, T., van Riemsdijk, W.H., 1996. A surface structural approach to ion adsorption: the charge distribution (CD) model. J. Colloid Interface Sci. 179, 488–508. https://doi.org/10.1006/jcis.1996.0242

Hiemstra, T., Van Riemsdijk, W.H., 1999. Surface structural ion adsorption modeling of competitive binding of oxyanions by metal (hydr)oxides. J. Colloid Interface Sci. 210,

182–193. https://doi.org/10.1006/jcis.1998.5904

Hinkle, M.A.G., Wang, Z., Giammar, D.E., Catalano, J.G., 2015. Interaction of Fe(II) with phosphate and sulfate on iron oxide surfaces. Geochim. Cosmochim. Acta 158, 130–146. https://doi.org/10.1016/j.gca.2015.02.030

Holmer, M., Storkholm, P., 2001. Sulphate reduction and sulphur cycling in lake sediments: a review. Freshw. Biol. 46, 431–451. https://doi.org/10.1046/j.1365-2427.2001.00687.x

Hongshao, Z., Stanforth, R., 2001. Competitive adsorption of phosphate and arsenate on goethite. Environ. Sci. Technol. 35, 4753–4757. https://doi.org/10.1021/es010890y

Huang, Q., Wang, Z., Wang, C., Wang, S., Jin, X., 2005. Phosphorus release in response to pH variation in the lake sediments with different ratios of iron-bound P to calcium-bound P. Chem. Speciat. Bioavailab. 17, 55–61. https://doi.org/10.3184/095422905782774937

Hudnell, H.K., 2010. The state of U.S. freshwater harmful algal blooms assessments, policy and legislation. Toxicon 55, 1024–1034. https://doi.org/10.1016/j.toxicon.2009.07.021

Hyacinthe, C., Bonneville, S., Van Cappellen, P., 2006. Reactive iron (III) in sediments: chemical versus microbial extractions. Geochim. Cosmochim. Acta 70, 4166–4180. https://doi.org/10.1016/j.gca.2006.05.018

Hyacinthe, C., Van Cappellen, P., 2004. An authigenic iron phosphate phase in estuarine sediments: composition , formation and chemical reactivity 91, 227–251. https://doi.org/10.1016/j.marchem.2004.04.006

IISD, 2017. Costs of Pollution in Canada: Measuring the impacts on families, businesses and governments. Winnipeg, Manitoba.

Iler, R.K., 1979. The chemistry of silica: solubility, polymerization, colloid and surface properties, and biochemistry. John Wiley & Sons Inc, Canada. https://doi.org/10.1002/ange.19800920433

Ivanoff, D.B., Reddy, K.R., Robinson, S., 1998. Chemical fractionation of organic phosphorus in selected histosolts. Soil Sci. 163, 36–45. https://doi.org/10.1097/00010694-199801000-00006

Iyengar, S.J., Joy, M., Ghosh, C.K., Dey, S., Kotnala, R.K., Ghosh, S., 2014. Magnetic, X-ray and Mössbauer studies on magnetite/maghemite core–shell nanostructures fabricated through an aqueous route. RSC Adv. 4, 64919–64929. https://doi.org/10.1039/C4RA11283K

Jambor, J.L., Dutrizac, J.E., 1998. Occurrence and constitution of natural and synthetic ferrihydrite, a widespread iron oxyhydroxide. Chem. Rev. 98, 2549–2586. https://doi.org/10.1021/cr970105t

James, R.E., Ferris, F.G., 2004. Evidence for microbial-mediated iron oxidation at a neutrophilic groundwater spring. Chem. Geol. 212, 301–311. https://doi.org/10.1016/j.chemgeo.2004.08.020

Jensen, D.L., Boddum, J.K., Tjell, J.C., Christensen, T.H., 2002. The solubility of rhodochrosite ($MnCO_3$) and siderite ($FeCO_3$) in anaerobic aquatic environments. Appl.

Geochemistry 17, 503–511. https://doi.org/10.1016/S0883-2927(01)00118-4

Jin, X., Wang, S., Pang, Y., Chang, F., 2006. Phosphorus fractions and the effect of pH on the phosphorus release of the sediments from different trophic areas. Environ. Pollut. 139, 288–295. https://doi.org/10.1016/j.envpol.2005.05.010

Jordan, N., Marmier, N., Lomenech, C., Giffaut, E., Ehrhardt, J.J., 2009. Competition between selenium (IV) and silicic acid on the hematite surface. Chemosphere 75, 129–134. https://doi.org/10.1016/j.chemosphere.2008.11.018

Jordan, N., Marmier, N., Lomenech, C., Giffaut, E., Ehrhardt, J.J., 2007. Sorption of silicates on goethite, hematite, and magnetite: experiments and modelling. J. Colloid Interface Sci. 312, 224–229. https://doi.org/10.1016/j.jcis.2007.03.053

Joshi, S.R., Kukkadapu, R.K., Burdige, D.J., Bowden, M.E., Sparks, D.L., Jaisi, D.P., 2015. Organic matter remineralization predominates phosphorus cycling in the mid-bay sediments in the Chesapeake Bay. Environ. Sci. Technol. 49, 5887–5896. https://doi.org/10.1021/es5059617

Kaegi, R., Voegelin, A., Folini, D., Hug, S.J., 2010. Effect of phosphate, silicate, and Ca on the morphology, structure and elemental composition of Fe(III)-precipitates formed in aerated Fe(II) and As(III) containing water. Geochim. Cosmochim. Acta 74, 5798–5816. https://doi.org/10.1016/j.gca.2010.07.017

Kanematsu, M., Waychunas, G.A., 2018. Silicate binding and precipitation on iron oxyhydroxides. Environ. Sci. Technol 52, 1827–1833. https://doi.org/10.1021/acs.est.7b04098

Kanematsu, M., Young, T.M., Fukushi, K., Sverjensky, D.A., Green, P.G., Darby, J.L., 2011. Quantification of the effects of organic and carbonate buffers on arsenate and phosphate adsorption on a goethite-based granular porous adsorbent. Environ. Sci. Technol. 45, 561–568. https://doi.org/10.1021/es1026745

Karim, Z., 1984. Characteristics of ferrihydrites formed by oxidation of $FeCl_2$ solutions containing different amounts of silica. Clays Clay Miner. 32, 181–184. https://doi.org/10.1346/CCMN.1984.0320304

Katsev, S., Tsandev, I., L'Heureux, I., Rancourt, D.G., 2006. Factors controlling long-term phosphorus efflux from lake sediments: exploratory reactive-transport modeling. Chem. Geol. 234, 127–147. https://doi.org/10.1016/j.chemgeo.2006.05.001

Kelton, N., Chow-Fraser, P., 2005. A simplified assessment of factors controlling phosphorus loading from oxygenated sediments in a very shallow eutrophic lake. Lake Reserv. Manag. 21, 223–230. https://doi.org/10.1080/07438140509354432

Kendall, B., Anbar, A.D., Kappler, A., Konhauser, K.O., 2012. The global iron cycle, 1st Editio. ed, Fundamentals of Geobiology. Wiley Online Library. https://doi.org/10.1002/9781118280874

Kersten, M., Vlasova, N., 2009. Silicate adsorption by goethite at elevated temperatures. Chem. Geol. 262, 372–379. https://doi.org/10.1016/j.chemgeo.2009.02.002

Kim, J., Li, W., Philips, B.L., Grey, C.P., 2011. Phosphate adsorption on the iron oxyhydroxides goethite ($\alpha$-FeOOH), akaganeite ($\beta$-FeOOH), and lepidocrocite ($\gamma$-

FeOOH): a 31P NMR Study. Energy Environ. Sci. 4, 4298.
https://doi.org/10.1039/c1ee02093e

Kinsela, A.S., Jones, A.M., Bligh, M.W., Pham, A.N., Collins, R.N., Harrison, J.J., Wilsher, K.L., Payne, T.E., Waite, T.D., 2016. Influence of dissolved silicate on rates of Fe(II) oxidation. Environ. Sci. Technol 50, 11663–11671. https://doi.org/10.1021/acs.est.6b03015

Klein, A.R., Baldwin, D.S., Singh, B., Silvester, E., 2010. Salinity-induced acidification in a wetland sediment through the displacement of clay-bound iron(II). Environ. Chem. 7, 413–421. https://doi.org/10.1021/es025955r

Konhauser, K.O., Amskold, L., Lalonde, S. V., Posth, N.R., Kappler, A., Anbar, A., 2007. Decoupling photochemical Fe(II) oxidation from shallow-water BIF deposition. Earth Planet. Sci. Lett. 258, 87–100. https://doi.org/10.1016/j.epsl.2007.03.026

Koski-Vähälä, J., Hartikainen, H., Tallberg, P., 2001. Phosphorus mobilization from various sediment pools in response to increased pH and silicate concentration. J. Environ. Qual. 30, 546–552. https://doi.org/10.2134/jeq2001.302546x

Kosmulski, M., 2006. pH-dependent surface charging and points of zero charge III. Update. J. Colloid Interface Sci. 298, 730–741. https://doi.org/10.1016/j.cis.2017.10.005

Kostka, J.E., Luther III, G.W., 1994. Partitioning and speciation of solid phase iron in saltmarsh sediments. Geochim. Cosmochim. Acta 58, 1701–1710. https://doi.org/org/10.1016/0016-7037(94)90531-2

Koszelnik, P., Tomaszek, J. a., 2008. Dissolved silica retention and its impact on eutrophication in a complex of mountain reservoirs. Water. Air. Soil Pollut. 189, 189–198. https://doi.org/10.1007/s11270-007-9567-x

Kraemer, S.M., 2004. Iron oxide dissolution and solubility in the presence of siderophores. Aquat. Sci. 66, 3–18. https://doi.org/10.1007/s00027-003-0690-5

Kugbe, J., Matsue, N., Henmi, T., 2009. Synthesis of Linde type A zeolite–goethite nanocomposite as an adsorbent for cationic and anionic pollutants. J. Hazard. Mater. 164, 929–935. https://doi.org/10.1016/j.jhazmat.2008.08.080

Landsberg, J.H., 2002. The effects of harmful algal blooms on aquatic organisms. Rev. Fish. Sci. 10, 113–390. https://doi.org/10.1080/20026491051695

Langley, S., Gault, A., Ibrahim, A.., Renaud, R., Fortin, D., Clark, I.D., Grant Ferris, F., 2009. A comparison of the rates of Fe(III) reduction in synthetic and bacteriogenic iron oxides by Shewanella putrefaciens CN32. Geomicrobiol. J. 26, 57–70. https://doi.org/10.1080/01490450802674905

Langmuir, D., 1997a. Adsorption-desorption reactions, in: McConnin, R. (Ed.), Aqueous Environmental Geochemistry. Prentice-Hall. Inc., New Jersey, pp. 343–402.

Langmuir, D., 1997b. Carbonate chemistry, in: McConnin, R. (Ed.), Aqueous Environmental Geochemistry. Prentice-Hall. Inc., pp. 193–230.

Langmuir, D., 1997c. Iron and sulfur geochemistry, in: McConnin, R. (Ed.), Aqueous Environmental Geochemistry. Prentice-Hall. Inc., pp. 431–485.

Langmuir, D., 1997d. Chemical kinetics, in: McConnin, R. (Ed.), Aqueous Environmental Geochemistry. Prentice-Hall. Inc., pp. 50–81.

Larsen, O., Postma, D., Jakobsen, R., 2006. The reactivity of iron oxides towards reductive dissolution with ascorbic acid in a shallow sandy aquifer (Rømø , Denmark). Geochim. Cosmochim. Acta 70, 4827–4835. https://doi.org/10.1016/j.gca.2006.03.027

Ler, A., Stanforth, R., 2003. Evidence for surface precipitation of phosphate on goethite. Environ. Sci. Technol. 37, 2694–2700. https://doi.org/10.1021/es020773i

Leri, A.C., Ravel, B., 2015. Abiotic bromination of soil organic matter. Environ. Sci. Technol. 49, 13350–13359. https://doi.org/10.1021/acs.est.5b03937

Li, M., Liu, J., Xu, Y., Qian, G., 2016. Phosphate adsorption on metal oxides and metal hydroxides: A comparative review. Environ. Rev. 24, 319–332. https://doi.org/org/10.1139/er-2015-0080

Li, Y., Ma, Y., Zhang, B., Lei, B., Li, Y., 2014. Enhancement the adhesion between epoxy coating and rusted structural steel by tannic acid treatment. Acta Metall. Sin. (English Lett. 27, 1105–1113. https://doi.org/10.1007/s40195-014-0132-5

Liu, C., Zhu, Z., Li, F., Liu, T., Liao, C., Lee, J.-J., Shih, K., Tao, L., YundangWu, 2016. Fe(II)-induced phase transformation of ferrihydrite: the inhibition effects and stabilization of divalent metal cations. Chem. Geol. 444, 110–119. https://doi.org/10.1016/j.chemgeo.2016.10.002

Liu, G., Tang, Q., Zhou, Y., Cao, X., Zhao, J., Zhu, D., 2017. Photo-induced phosphate released from organic phosphorus degradation in deionized and natural water. Photochem. Photobiol. Sci. 16, 467–475. https://doi.org/10.1039/C6PP00313C

Liu, H., Chen, T., Frost, R.L., 2014. An overview of the role of goethite surfaces in the environment. Chemosphere 103, 1–11. https://doi.org/10.1016/j.chemosphere.2013.11.065

Lovley, D.R., 2004. Dissimilatory Fe(III) and Mn(IV) reduction. Adv. Microb. Physiol. 49, 219–286. https://doi.org/10.1016/S0065-2911(04)49005-5

Lü, C., Yan, D., He, J., Zhou, B., Li, L., Zheng, Q., 2017. Environmental geochemistry significance of organic phosphorus: an insight from its adsorption on iron oxides. Appl. Geochemistry 84, 52–60. https://doi.org/10.1016/j.apgeochem.2017.05.026

Luengo, C., Brigante, M., Avena, M., 2007. Adsorption kinetics of phosphate and arsenate on goethite. A comparative study. J. Colloid Interface Sci. 311, 354–360. https://doi.org/10.1016/j.jcis.2007.03.027

Maavara, T., Hood, J.L.A., North, R.L., Doig, L.E., Parsons, C.P., Johansson, J., Liber, K., Hudson, J.J., Lucas, B.T., Vandergucht, D.M., Van Cappellen, P., 2015. Reactive silicon dynamics in a large prairie reservoir (Lake Diefenbaker, Saskatchewan). J. Great Lakes Res. 2, 100–109. https://doi.org/10.1016/j.jglr.2015.04.003

Mason, C.F., Nedwell, D.B., Hine, R.E., Leaf, S., Dils, R., 2003. Environmental costs of freshwater eutrophication in England and Wales. Environ. Sci. Technol. 37, 201–208. https://doi.org/10.1021/es020793k

Matisoff, G., Kaltenberg, E.M., Steely, R.L., Hummel, S.K., Seo, J., Gibbons, K.J., Bridgeman, T.B., Seo, Y., Behbahani, M., James, W.F., Johnson, L.T., Doan, P., Dittrich, M., Anne, M., Chaf, J.D., 2016. Internal loading of phosphorus in western Lake Erie. J. Great Lakes Res. 42, 775–788. https://doi.org/10.1016/j.jglr.2016.04.004

Matisoff, G., Watson, S.B., Guo, J., Duewiger, A., Steely, R., 2017. Sediment and nutrient distribution and resuspension in Lake Winnipeg. Sci. Total Environ. 575, 173–186. https://doi.org/10.1016/j.scitotenv.2016.09.227

Mayer, T.D., Jarrell, W.M., 2000. Phosphorus sorption during iron(II) oxidation in the presence of dissolved silica. Water Res. 34, 3949–3956. https://doi.org/10.1016/S0043-1354(00)00158-5

McKeague, J.A., Day, J.H., 1966. Dithionite- and oxalate- extractable Fe and Al as aids in differentiating various classes of soils. Can. J. Soil Sci. 46, 13–22. https://doi.org/org/10.4141/cjss66-003

Melton, E.D., Swanner, E.D., Behrens, S., Schmidt, C., 2014. The interplay of microbially in the biogeochemical Fe cycle. Nat. Publ. Gr. 12, 797–809. https://doi.org/10.1038/nrmicro3347

Millero, F., Huang, F., Zhu, X., Liu, X., Zhang, J.-Z., 2001. Adsorption and Desorption of Phosphate on Calcite and Aragonite in Seawater. Aquat. Geochemistry 7, 33–56.

Mortimer, R.J.G., Galsworthy, A.M.J., Bottrell, S.H., Wilmot, L.E., Newton, R.J., 2011. Experimental evidence for rapid biotic and abiotic reduction of Fe (III) at low temperatures in salt marsh sediments: a possible mechanism for formation of modern sedimentary siderite concretions. Sedimentology 58, 1514–1529. https://doi.org/10.1111/j.1365-3091.2011.01224.x

Musić, S., Filipović-Vinceković, N., Sekovanić, L., 2011. Preparation of amorphous $SiO_2$ particles and their properties. Brazilian J. Chem. Eng. 28, 89–94. https://doi.org/10.1590/S0104-66322011000100011

Neupane, G., Donahoe, R.J., Arai, Y., 2014. Kinetics of competitive adsorption/desorption of arsenate and phosphate at the ferrihydrite – water interface. Chem. Geol. 368, 31–38. https://doi.org/10.1016/j.chemgeo.2013.12.020

Norton, S.A., Amirbahman, A., 2005. Aluminum control of phosphorus sorption by lake sediments. Environ. Sci. Technol 39, 8784–8789. https://doi.org/10.1021/es050916b

Nowack, B., Lützenkirchen, J., Behra, P., Sigg, L., 1996. Modeling the adsorption of metal-EDTA complexes onto oxides. Environ. Sci. Technol. 30, 2397–2405. https://doi.org/10.1021/es9508939

Nowack, B., Sigg, L., 1996. Adsorption of EDTA and metal-EDTA complexes onto goethite. J. Colloid Interface Sci. 177, 106–121. https://doi.org/10.1006/jcis.1996.0011

Nowack, B., Stone, A.T., 1999. Adsorption of phosphonates onto the goethite–water interface. J. Colloid Interface Sci. 214, 20–30. https://doi.org/10.1006/jcis.1999.6111

Nriagu, J.O., Dell, C.I., 1974. Diagenetic formation of iron phosphates in recent lake sediments. Am. Mineral. 59, 934–946.

Nürnberg, G.K., Lazerte, B.D., 2016. More than 20 years of estimated internal phosphorus loading in polymictic, eutrophic Lake Winnipeg, Manitoba. J. Great Lakes Res. 42, 18–27. https://doi.org/10.1016/j.jglr.2015.11.003

NWIS, 2017. National Water Information System [WWW Document]. Natl. Water Qual. Monit. Counc. USA. URL https://www.waterqualitydata.us/

O'Melia, C.R., Stumm, W., 1967. Aggregation of silica dispersions by iron(III). J. Colloid Interface Sci. 23, 437–447. https://doi.org/10.1016/0021-9797(67)90186-5

Orihel, D.M., Baulch, H.M., Casson, N.J., North, R.L., Parsons, C.T., Seckar, D.C.M., Venkiteswaran, J.J., 2017. Internal phosphorus loading in Canadian fresh waters: a critical review and data analysis. Can. J. Fish. Aquat. Sci. 74, 2005–2029. https://doi.org/10.1139/cjfas-2016-0500

Oxmann, J.F., Schwendenmann, L., 2015. Authigenic apatite and octacalcium phosphate formation due to adsorption – precipitation switching across estuarine salinity. Biogeosciences 12, 723–738. https://doi.org/10.5194/bg-12-723-2015

Pallud, C., Meile, C., Laverman, A.M., Abell, J., Van Cappellen, P., 2007. The use of flow-through sediment reactors in biogeochemical kinetics: methodology and examples of applications. Mar. Chem. 106, 256–271. https://doi.org/org/10.1016/j.marchem.2006.12.011

Parkhurst, D.L., Appelo, C.A.J., 2013. Description of input and examples for PHREEQC version 3--a Computer program for speciation, batch-reaction, one-dimensional transport, and inverse geochemical calculations: U.S. Geological Survey techniques and methods.

Parsons, C.T., Rezanezhad, F., O'Connell, D.W., Van Cappellen, P., 2017. Sediment phosphorus speciation and mobility under dynamic redox conditions. Biogeosciences 14, 3585–3602. https://doi.org/10.5194/bg-14-3585-2017

Pasek, M.A., 2008. Rethinking early earth phosphorus geochemistry. PANAS 105, 853–858. https://doi.org/10.1073/pnas.0708205105

Paytan, A., Mclaughlin, K., 2007. The oceanic phosphorus cycle. Chem. Rev. 107, 563–576. https://doi.org/10.1021/cr0503613

Paytan, A., Roberts, K., Watson, S., Peek, S., Chuang, P., Defforey, D., Kendall, C., 2017. Internal loading of phosphate in Lake Erie Central Basin. Sci. Total Environ. 579, 1356–1365. https://doi.org/10.1016/j.scitotenv.2016.11.133

Peak, D., Ford, R.G., Sparks, D.L., 1999. An in situ ATR-FTIR investigation of sulfate bonding mechanisms on goethite. J. Colloid Interface Sci. 218, 289–299. https://doi.org/10.1006/jcis.1999.6405

Phillips, E.J.P., Lovley, D.R., Roden, E.E., 1993. Composition of non-microbially reducible Fe(III ) in aquatic sediments. Appl. Environ. Microbiol. 59, 2727–2729.

Phoenix, V.R., Konhauser, K.O., Ferris, F.G., 2003. Experimental study of iron and silica immobilization by bacteria in mixed Fe–Si systems: implications for microbial silicification in hot springs. Can. J. Earth Sci. 40, 1669–1678. https://doi.org/10.1139/E03-044

Pissarides, A., Stewart, J.W.B., Rennie, D.A., 1968. Influence of cation saturation on phosphorus adsorption by selected clay minerals. Can. J. Soil Sci. 48, 151–157. https://doi.org/10.4141/cjss68-018

Pokrovsky, O.S., Schott, J., Thomas, F., Mielczarski, J., 1998. Surface speciation of Ca and Mg carbonate minerals in aqueous solutions: a combined potentiometric, electrokinetic, and DRIFT surface spectroscopy approach. Mineral. Mag. 62A, 1196–1197. https://doi.org/10.1180/minmag.1998.62A.2.291

Poulton, S.W., Canfield, D.E., 2005. Development of a sequential extraction procedure for iron: implications for iron partitioning in continentally derived particulates. Chem. Geol. 214, 209–221. https://doi.org/10.1016/j.chemgeo.2004.09.003

Precht, E., Franke, U., Polerecky, L., Huettel, M., 2004. Oxygen dynamics in permeable sediments with wave-driven pore water exchange. Limnol. Oceanogr. 49, 693–705. https://doi.org/10.4319/lo.2004.49.3.0693

Puccia, V., Luengo, C., Avena, M., 2009. Physicochemical and engineering aspects phosphate desorption kinetics from goethite as induced by arsenate. Colloids Surfaces A Physicochem. Eng. Asp. 348, 221–227. https://doi.org/10.1016/j.colsurfa.2009.07.026

Rahimi, S., Moattari, R.M., Rajabi, L., Derakhshan, A.A., Keyhani, M., 2015. Iron oxide/hydroxide ($\alpha,\gamma$-FeOOH) nanoparticles as high potential adsorbents for lead removal from polluted aquatic media. J. Ind. Eng. Chem. 23, 33–43. https://doi.org/10.1016/j.jiec.2014.07.039

Rahnemaie, R., Hiemstra, T., van Riemsdijk, W.H., 2007a. Carbonate adsorption on goethite in competition with phosphate. J. Colloid Interface Sci. 315, 415–425. https://doi.org/10.1016/j.jcis.2007.07.017

Rahnemaie, R., Hiemstra, T., van Riemsdijk, W.H., 2006. A new surface structural approach to ion adsorption: tracing the location of electrolyte ions. J. Colloid Interface Sci. 293, 312–321. https://doi.org/10.1016/j.jcis.2005.06.089

Rahnemaie, R., Hiemstra, T., Van Riemsdijk, W.H., 2007b. Geometry, charge distribution, and surface speciation of phosphate on goethite. Langmuir 23, 3680–3689. https://doi.org/10.1021/la062965n

Raiswell, R., Vu, H.P., Brinza, L., Benning, L.G., 2010. The determination of labile Fe in ferrihydrite by ascorbic acid extraction: methodology , dissolution kinetics and loss of solubility with age and de-watering. Chem. Geol. 278, 70–79. https://doi.org/10.1016/j.chemgeo.2010.09.002

Reichard, P.U., Kretzschmar, R., Kraemer, S.M., 2007. Dissolution mechanisms of goethite in the presence of siderophores and organic acids. Geochim. Cosmochim. Acta 71, 5635–5650. https://doi.org/10.1016/j.gca.2006.12.022

Reitzel, K., Ahlgren, J., DeBrabandere, H., Waldeback, M., Gogoll, A., Tranvik, L., Rydin, E., 2007. Degradation rates of organic phosphorus in lake sediment. Biogeochemistry 82, 15–28. https://doi.org/10.1007/s10533-006-9049-z

Ridenour, C., 2017. Biogeochemical cycling of nutrient silicon in a human-impacted large lake nearshore environment (Hamilton Harbour Area of Concern, Lake Ontario,

Canada). University of Waterloo. https://doi.org/10.1021/es503454a

Rietra, R.P.J.J., Hiemstra, T., Van Riemsdijk, W.H., 2001. Interaction between calcium and phosphate adsorption on goethite. Environ. Sci. Technol. 35, 3369–3374. https://doi.org/10.1021/es000210b

Ringuet, S., Sassanoa, L., Johnson, J.., 2011. A suite of microplate reader-based colorimetric methods to quantify ammonium, nitrate, orthophosphate and silicate concentrations for aquatic nutrient monitoring. J. Environ. Monit. 13, 370–576. https://doi.org/10.1039/c0em00290a

Rocha, C., Galvão, H., Barbosa, A., 2002. Role of transient silicon limitation in the development of cyanobacteria blooms in the Guadiana estuary , south-western Iberia. Mar. Ecol. Prog. Ser. 228, 35–45. https://doi.org/10.3354/meps228035

Roden, E.E., Zachara, J.M., 1996. Microbial reduction of crystalline iron(III) oxides: influence of oxide surface area and potential for cell growth. Environ. Sci. Technol. 30, 1618–1628. https://doi.org/10.1021/es9506216

Rothe, M., Frederichs, T., Eder, M., Kleeberg, A., Hupfer, M., 2014. Evidence for vivianite formation and its contribution to long-term phosphorus retention in a recent lake sediment: a novel analytical approach. Biogeosciences 11, 5169–5180. https://doi.org/10.5194/bg-11-5169-2014

Ruan, H.D., Frost, R.L., Kloprogge, J.T., Duong, L., 2002. Infrared spectroscopy of goethite dehydroxylation: III. FT-IR microscopy of in situ study of the thermal transformation of goethite to hematite. Spectrochim. Acta Part A 58, 967–981. https://doi.org/10.1016/S1386-1425(01)00574-1

Ruttenberg, K.C., 2003. The global phosphorus cycle, in: Turekian, K.K., Holland, H.D. (Eds.), Treatise on Geochemistry. pp. 585–643.

Ruttenberg, K.C., Dyhrman, S.T., 2012. Dissolved organic phosphorus production during simulated phytoplankton blooms in a coastal upwelling system. Front. Microbiol. 3:274, 1–12. https://doi.org/10.3389/fmicb.2012.00274

Ruttenberg, K.C., Sulak, D.J., 2011. Sorption and desorption of dissolved organic phosphorus onto iron (oxyhydr)oxides in seawater. Geochim. Cosmochim. Acta 75, 4095–4112. https://doi.org/10.1016/j.gca.2010.10.033

Rzepa, G., Pieczara, G., Gaweł, A., Tomczyk, A., Zalecki, R., 2016. The influence of silicate on transformation pathways of synthetic 2-line ferrihydrite. J. Therm. Anal. Calorim. 125, 407–421. https://doi.org/10.1007/s10973-016-5345-6

Sabur, M.A., Al-Abadleh, H.A., 2015. Surface interactions of monomethylarsonic acid with hematite nanoparticles studied using ATR-FTIR: adsorption and desorption kinetics. Can. J. Chem. 93, 1297–1304. https://doi.org/org/10.1139/cjc-2015-0350

Saleh, A.M., Jones, A.A., 1984. The crystallinity and surface characteristics of synthetic ferrihydrite and its relationship kaolinite surfaces to kaolinite surfaces. Clay Miner. 19, 745–755. https://doi.org/10.1180/claymin.1984.019.5.05

Santschi, P., Höhener, P., Benoit, G., Brink, M.B., 1990. Chemical processes at the sediment-water interface. Mar. Chem. 30, 269–315. https://doi.org/10.1016/0304-4203(90)90076-

O

Santschi, P.H., Schindler, P.W., 1974. Complex formation in the ternary systems CaII–$H_4SiO_4$–$H_2O$ and MgII–$H_4SiO_4$–$H_2O$. J. Chem. Soc., Dalt. Trans., 2, 181–184.

Scavia, D., David Allan, J., Arend, K.K., Bartell, S., Beletsky, D., Bosch, N.S., Brandt, S.B., Briland, R.D., Daloğlu, I., DePinto, J. V., Dolan, D.M., Evans, M.A., Farmer, T.M., Goto, D., Han, H., Höök, T.O., Knight, R., Ludsin, S. a., Mason, D., Michalak, A.M., Peter Richards, R., Roberts, J.J., Rucinski, D.K., Rutherford, E., Schwab, D.J., Sesterhenn, T.M., Zhang, H., Zhou, Y., 2014. Assessing and addressing the re-eutrophication of Lake Erie: central basin hypoxia. J. Great Lakes Res. 40, 226–246. https://doi.org/10.1016/j.jglr.2014.02.004

Schaller, J., Faucherre, S., Joss, H., Obst, M., Goeckede, M., Planer-Friedrich, B., Peiffer, S., Gilfedder, B., Elberling, B., 2019. Silicon increases the phosphorus availability of Arctic soils. Sci. Rep. 9, 1–11. https://doi.org/10.1038/s41598-018-37104-6

Schauser, I., Chorus, I., Lewandowski, J., 2006. Effects of nitrate on phosphorus release: comparison of two Berlin lakes. Acta Hydrochim. hydrobiol. 34, 325–332. https://doi.org/10.1002/aheh.200500632

Schindler, D.W., 1977. Evolution of phosphorus limitation in lakes. Science (80-. ). 195, 260–262. https://doi.org/10.1126/science.195.4275.260

Schindler, D.W., Hecky, R.E., Findlay, D.L., Stainton, M.P., Parker, B.R., Paterson, M.J., Beaty, K.G., Lyng, M., Kasian, S.E.M., 2008. Eutrophication of lakes cannot be controlled by reducing nitrogen input: results of a 37-year whole-ecosystem experiment. Proc. Natl. Acad. Sci. U. S. A. 105, 11254–11258. https://doi.org/10.1073/pnas.0805108105

Schwertmann, U., Cornell, R.M., 2000a. The iron oxides, in: Iron Oxides in the Laboratory: Preparation and Characterization. WILEY-VCH, Weinheim, Germany, pp. 5–18.

Schwertmann, U., Cornell, R.M., 2000b. General preperative techniques, in: Iron Oxides in the Laboratory: Preparation and Characterization. WILEY-VCH Verlag GmbH, Weinheim, Germany, pp. 19–26.

Schwertmann, U., Cornell, R.M., 2000c. Synthesis pathways, in: Iron Oxides in the Laboratory: Preparation and Characterization. WILEY-VCH Verlag GmbH, Weinheim, Germany, pp. 55–66.

Sekar, R., DiChristina, T.J., 2014. Microbially driven fenton reaction for degradation of the widespread environmental contaminant 1,4-Dioxane. Environ. Sci. Technol. 48, 12858−12867. https://doi.org/10.1021/es503454a

Senn, A.-C., Kaegi, R., Hug, S.J., Hering, J.G., Mangold, S., Voegelin, A., 2015. Composition and structure of Fe(III)-precipitates formed by Fe(II) oxidation in water at near-neutral pH: interdependent effects of phosphate, silicate and Ca. Geochim. Cosmochim. Acta 162, 220–246. https://doi.org/10.1016/j.gca.2015.04.032

Series, N., Mar, N., 2007. Why nature chose phosphates. Science (80-. ). 235, 1173–1178. https://doi.org/10.1126/science.2434996

Shinohara, R., Hiroki, M., Kohzu, A., Imai, A., Inoue, T., Furusato, E., Komatsu, K., Satou,

T., Tomioka, N., Shimotori, K., Miura, S., 2017. Role of organic phosphorus in sediment in a shallow eutrophic lake. Water Resour. Res. 53, 7175–7189. https://doi.org/10.1002/2017WR020486

Shiraishi, F., Nakao, K., Takashima, C., Kano, A., Itai, T., 2018. Fe(II) oxidation processes at the surface of bacterially colonized iron deposits. Chem. Geol. 476, 161–170. https://doi.org/10.1016/j.chemgeo.2017.11.014

Silburn, B., Kröger, S., Parker, E.R., Sivyer, D.B., Hicks, N., Powell, C.F., Johnson, M., Greenwood, N., 2017. Benthic pH gradients across a range of shelf sea sediment types linked to sediment characteristics and seasonal variability. Biogeochemistry 135, 69–88. https://doi.org/10.1007/s10533-017-0323-z

Smith, V.H., Schindler, D.W., 2009. Eutrophication science: where do we go from here? Trends Ecol. Evol. 24, 201–207. https://doi.org/10.1016/j.tree.2008.11.009

Smith, V.H., Tilman, G.D., Nekola, J.C., 1998. Eutrophication: impacts of excess nutrient inputs on freshwater, marine, and terrestrial ecosystems. Environ. Pollut. 100, 179–196. https://doi.org/10.1016/S0269-7491(99)00091-3

Smolders, A.J.P., Lamers, L.P.M., Lucassen, E.C.H.E.T., Velde, G.V.A.N.D.E.R., Roelofs, J.G.M., 2006. Internal eutrophication: how it works and what to do about it – a review. Chem. Ecol. 22, 93–111. https://doi.org/10.1080/02757540600579730

Søndergaard, M., Jensen, J.P., Jeppesen, E., 2003. Role of sediment and internal loading of phosphorus in shallow lakes. Hydrobiologia 506–509, 135–145. https://doi.org/10.1023/B:HYDR.0000008611.12704.dd

Song, Y., Swedlund, P.J., Zou, C., Hamid, R.D., 2013. The influence of surface structure on $H_4SiO_4$ sorption and oligomerization on goethite surfaces: an XPS study using goethites differing in morphology. Chem. Geol. 347, 114–122. https://doi.org/10.1016/j.chemgeo.2013.03.014

Spiteri, C., Cappellen, P. Van, Regnier, P., 2008. Surface complexation effects on phosphate adsorption to ferric iron oxyhydroxides along pH and salinity gradients in estuaries and coastal aquifers. Geochim. Cosmochim. Acta 72, 3431–3445. https://doi.org/10.1016/j.gca.2008.05.003

Stachowicz, M., Hiemstra, T., van Riemsdijk, W.H., 2008. Multi-competitive interaction of As(III) and As(V) oxyanions with $Ca^{2+}$, $Mg^{2+}$, $PO_4^{3-}$, and $CO_3^{2-}$ ions on goethite. J. Colloid Interface Sci. 320, 400–414. https://doi.org/10.1016/j.jcis.2008.01.007

Struyf, E., Smis, A., Damme, S. Van, Meire, P., Conley, D.J., 2009. The global biogeochemical silicon cycle. Silicon 1, 207–213. https://doi.org/10.1007/s12633-010-9035-x

Suter, D., Banwart, S., Stumm, W., 1991. Dissolution of hydrous iron (III) oxides by reductive rechanisms. Langmuir 7, 809–813. https://doi.org/10.1021/la00052a033

Swedlund, P.J., Hamid, R.D., Miskelly, G.M., 2010a. Insights into $H_4SiO_4$ surface chemistry on ferrihydrite suspensions from ATR-IR, Diffuse Layer Modeling and the adsorption enhancing effects of carbonate. J. Colloid Interface Sci. 352, 149–157. https://doi.org/10.1016/j.jcis.2010.08.011

Swedlund, P.J., Miskelly, G.M., McQuillan, A.J., 2010b. Silicic acid adsorption and oligomerization at the ferrihydrite-water interface: interpretation of ATR-IR spectra based on a model surface structure. Langmuir 26, 3394–3401. https://doi.org/10.1021/la903160q

Swedlund, P.J., Miskelly, G.M., McQuillan, A.J., 2009. An attenuated total reflectance IR study of silicic acid adsorbed onto a ferric oxyhydroxide surface. Geochim. Cosmochim. Acta 73, 4199–4214. https://doi.org/10.1016/j.gca.2009.04.007

Swedlund, P.J., Sivaloganathan, S., Miskelly, G.M., Waterhouse, G.I.N., 2011. Assessing the role of silicate polymerization on metal oxyhydroxide surfaces using X-ray photoelectron spectroscopy. Chem. Geol. 285, 62–69. https://doi.org/10.1016/j.chemgeo.2011.02.022

Swedlund, P.J., Webster, J.G., 1999. Adsorption and polymerisation of silicic acid on ferrihydrite, and its effect on arsenic adsorption. Water Res. 33, 3413–3422. https://doi.org/10.1021/la903160q

Talebi, M., Rahnemaie, R., Goli, E., Hossein, M., 2016. Competitive adsorption of magnesium and calcium with phosphate at the goethite water interface: kinetics, equilibrium and CD-MUSIC modeling. Chem. Geol. 437, 19–29. https://doi.org/10.1016/j.chemgeo.2016.05.004

Tallberg, P., Tréguer, P., Beucher, C., Corvaisier, R., 2008. Potentially mobile pools of phosphorus and silicon in sediment from the Bay of Brest: interactions and implications for phosphorus dynamics. Estuar. Coast. Shelf Sci. 76, 85–94. https://doi.org/10.1016/j.ecss.2007.06.003

Tilman, D., Fargione, J., Wolff, B., Antonio, C.D., Dobson, A., Howarth, R., Schindler, D., Schlesinger, W.H., Simberloff, D., Swackhamer, D., 2001. Forecasting agriculturally driven global environmental change. Science (80-. ). 292, 281–284. https://doi.org/10.1126/science.1057544

Tofan-Lazar, J., Al-Abadleh, H.A., 2012. Kinetic ATR-FTIR studies on phosphate adsorption on iron (oxyhydr)oxides in the absence and presence of surface arsenic: molecular-level insights into the ligand exchange mechanism. J. Phys. Chem. A 116, 10143–10149. https://doi.org/10.1021/jp308913j

Torrent, J., Schwertmann, U., Barron, V., 1992. Fast and slow phosphate sorption by goethite-rich natural materials. Clay Clay Miner. 40, 14–21. https://doi.org/10.1346/CCMN.1992.0400103

Tuominen, L., Hartikainen, H., Kairesalo, T., Tallberg, P., 1998. Increases bioavaliability of sediment phosphorus due to silicate enrichment. Water Res. 32, 2001–2008. https://doi.org/10.1016/S0043-1354(97)00455-7

Turner, B.L., Cade-Menun, B.J., Condron, L.M., Newman, S., 2005. Extraction of soil organic phosphorus. Talanta 66, 294–306. https://doi.org/10.1016/j.talanta.2004.11.012

Vakros, J., Kordulis, C., Lycourghiotis, A., 2002. Potentiometric mass titrations: a quick scan for determining the point of zero charge. Chem. Commun. 1980–1981. https://doi.org/10.1039/B205398E

Van Bodegom, P.M., Broekman, R., Van Dijk, J., Bakker, C., Aerts, R., 2005. Ferrous iron stimulates phenol oxidase activity and organic matter decomposition in waterlogged wetlands. Biogeochemistry 76, 69–83. https://doi.org/10.1007/s10533-005-2053-x

Van Cappellen, P., Charlet, L., Stumm, W., Wersin, P., 1993. A surface complexation model of the carbonate mineral-aqueous solution interface. Geochim. Cosmochim. Acta 57, 3505–3518. https://doi.org/10.1016/0016-7037(93)90135-J

van der Grift, B., Rozemeijer, J.C., Griffioen, J., van der Velde, Y., 2014. Iron oxidation kinetics and phosphate immobilization along the flow-path from groundwater into surface water. Hydrol. Earth Syst. Sci. 18, 4687–4702. https://doi.org/10.5194/hess-18-4687-2014

Verspagen, J.M.H., Van de Waal, D.B., Finke, J.F., Visser, P.M., Van Donk, E., Huisman, J., 2014. Rising $CO_2$ levels will intensify phytoplankton blooms in eutrophic and hypertrophiclakes. PLoS One 9, e104325. https://doi.org/10.1371/journal.pone.0104325

Vieira, A.R., 2006. Surface complexation modeling of Pb(II), Cd(II) and Se(IV) onto iron hydroxides in single and bisolute systems (PhD thesis). The University of Texas at Austin.

Viollier, E., Inglett, P.W., Hunter, K., Roychoudhury, A.N., Van Cappellen, P., 2000. The ferrozine method revisited: Fe(II)/Fe(III) determination in natural waters. Appl. Geochemistry 15, 785–790. https://doi.org/10.1016/s0883-2927(99)00097-9

Voegelin, A., Kaegi, R., Frommer, J., Vantelon, D., Hug, S.J., 2010. Effect of phosphate, silicate, and Ca on Fe(III)-precipitates formed in aerated Fe(II)- and As(III)-containing water studied by X-ray absorption spectroscopy. Geochim. Cosmochim. Acta 74, 164–186. https://doi.org/10.1016/j.gca.2009.09.020

Wallmann, K., Hennies, K., König, I., Petersen, W., Knauth, H.-D., 1993. New procedure for determining reactive Fe(III) and Fe(II) minerals in sediments. Limnol. Oceanogr. 38, 1803–1812.

Wang, L., Qin, L., Putnis, C.V., Ruiz-Agudo, E., King, H.E., Putnis, A., 2016. Visualizing organophosphate precipitation at the calcit−water interface by in situ Atomic-Force Microscopy. Environ. Sci. Technol. 50, 259−268. https://doi.org/10.1021/acs.est.5b05214

Wang, M.K., Tzou, Y.M., 1995. Phosphate sorption by calcite, and iron-rich calcareous soils. Geoderma 65, 249–261. https://doi.org/10.1016/0016-7061(95)94049-A

Wang, X., Hu, Y., Tang, Y., Yang, P., Feng, X., Xu, W., Zhu, M., 2017. Phosphate and phytate adsorption and precipitation on ferrihydrite surfaces. Environ. Sci. Nano 4, 2193–2204. https://doi.org/10.1039/C7EN00705A

Wang, X., Li, W., Harrington, R., Liu, F., Parise, J.B., Feng, X., Sparks, D.L., 2013. Effect of ferrihydrite crystallite size on phosphate adsorption reactivity. Environ. Sci. Technol. 47, 10322−10331. https://doi.org/10.1021/es401301z

Wang, X., Zhu, M., Lan, S., Ginder-Vogel, M., Liu, F., Feng, X., 2015. Formation and secondary mineralization of ferrihydrite in the presence of silicate and Mn(II). Chem. Geol. 415, 37–46. https://doi.org/10.1016/j.chemgeo.2015.09.009

Weber, K.A., Achenbach, L.A., Coates, J.D., 2006. Microorganisms pumping iron: anaerobic microbial iron oxidation and reduction. Nat. Rev. Microbiol. 4, 752–764. https://doi.org/10.1038/nrmicro1490

Willett, I.R., Chartress, C.J., Nguyen, T.T., 1988. Migration of phosphate into aggregated particles of ferrihydrite. J. Soil Sci. 39, 275–282. https://doi.org/10.1111/j.1365-2389.1988.tb01214.x

Williams, L.A., 1985. Silica diagenesis, II. General mechanisms. J. Sedimentory Petrol. 55, 312–321. https://doi.org/10.1306/212F86B1-2B24-11D7-8648000102C1865D

Wood, P.M., 1994. Pathways for production of Fenton's reagent by wood-rotting fungi. FEMS Microbiol. Rev. 13, 313–320. https://doi.org/10.1111/j.1574-6976.1994.tb00051.x

Wu, L., Beard, B.L., Roden, E.E., Johnson, C.M., 2009. Influence of pH and dissolved Si on Fe isotope fractionation during dissimilatory microbial reduction of hematite. Geochim. Cosmochim. Acta 73, 5584–5599. https://doi.org/10.1016/j.gca.2009.06.026

Xiao, W., Jones, A.M., Collins, R.N., Bligh, M.W., Waite, T.D., 2017. Use of fourier transform infrared spectroscopy to examine the Fe(II)-Catalyzed transformation of ferrihydrite. Talanta 175, 30–37. https://doi.org/10.1016/j.bbabio.2014.08.002

Zeng, L., 2003. A method for preparing silica-containing iron(III) oxide adsorbents for arsenic removal. Water Res. 37, 4351–4358. https://doi.org/10.1016/S0043-1354(03)00402-0

Zhang, H., Boegman, L., Scavia, D., Culver, D.A., 2016. Spatial distributions of external and internal phosphorus loads in Lake Erie and their impacts on phytoplankton and water quality. J. Great Lakes Res. 42, 1212–1227. https://doi.org/10.1016/j.jglr.2016.09.005

Zhao, Q., Adhikari, D., Huang, R., Patel, A., Wang, X., Tang, Y., Obrist, D., Roden, E.E., Yang, Y., 2017. Coupled dynamics of iron and iron-bound organic carbon in forest soils during anaerobic reduction. Chem. Geol. 464, 118–126. https://doi.org/10.1016/j.chemgeo.2016.12.014

Zhao, Q., Poulson, S.R., Obrist, D., Sumaila, S., Dynes, J.J., McBeth, J.M., Yang, Y., 2016. Iron-bound organic carbon in forest soils: quantification and characterization. Biogeosciences 13, 4777–4788. https://doi.org/10.5194/bg-13-4777-2016

Zhong, B., Stanforth, R., Wu, S., Chen, J.P., 2007. Proton interaction in phosphate adsorption onto goethite 308, 40–48. https://doi.org/10.1016/j.jcis.2006.12.055

Zhou, S., Sato, T., Otake, T., 2018. Dissolved silica effects on adsorption and co-precipitation of Sb(III) and Sb(V) with ferrihydrite. Minerals 8, 101. https://doi.org/10.3390/min8030101

Zhu, Y., Wu, F., He, Z., Guo, J., Qu, X., Xie, F., 2013. Characterization of organic phosphorus in lake sediments by sequential fractionation and enzymatic hydrolysis. Environ. Sci. Technol. 47, 7679–7687. https://doi.org/10.1021/es305277g

# Appendix

## Supplementary Material: Chapter 2

**Section SM-2.1: Optimization of CD-MUSIC model parameters**

The surface complexation reaction parameters reported in past studies for the individual sorption of phosphate and silicate on ferric (hydr)oxides by the CD-MUSIC model were used to compare the model-estimated phosphate and silicate sorption with the experimental data. The previously reported surface site densities and the Stern layer capacitance for synthetic goethite were used in the model (Hiemstra et al., 2007). The specific surface area and the point of zero charge (PZC) for goethite were determined in this study were used in the model. The model was implemented with the reported charge distribution coefficients ($\Delta z$) and the formation constants ($logK$) from each set of model parameters. The $\Delta z$ and logK values were optimized to achieve a better fit to our experimental dataset. This was done by trial and error, e.g. by manually changing the $\Delta z$ and $logK$ values. The comparison between the model-estimation and the experimental data for phosphate and silicate sorption are shown in Figure SM-2.1 and Figure SM-2.2 respectively. The different sets of CD-MUSIC model parameters including the optimized parameters obtained in this study were compared with the experimental data with the root mean square error (RMSE). The comparison shows that the $\Delta z$ and logK values optimized in this study provide the lowest RMSE values for phosphate and silicate sorption, both individually (P) and simultaneously (P+Si). RMSE values were calculated using the following equation SI-1. The calculated RMSE values between the experimental data and the model estimation are presented in Table SM-2.1.

$$RMSE = \frac{\sum_{pH}^{n}(O_{pH} - E_{pH})^2}{n} \ldots\ldots\ldots\ldots\ldots (SM-1)$$

where, O and E represents the experimentally determined and the model-estimated amount of phosphate and silicate sorbed on goethite at a given pH and n is the number of data points.
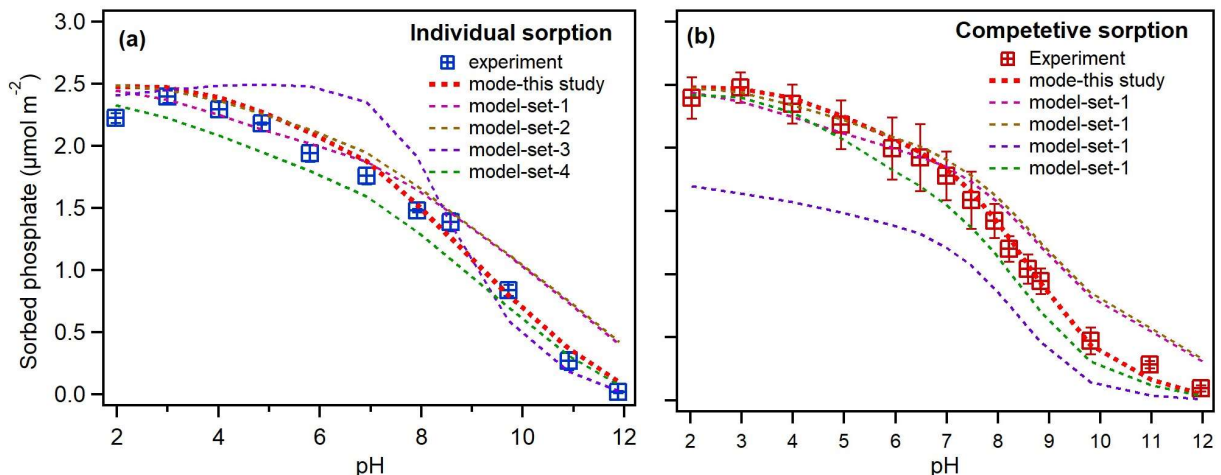
**Figure SM-2.1.** Sorption of 50 µM phosphate (a) in the absence and (b) presence of 50 µM silicate on goethite (0.5 g/L) at 25°C and $I$= 10 mM NaCl. The symbols represent the experimental data and dashed lines represent the model-estimated sorption of phosphate by the CD-MUSIC model using the $\Delta z$ and logK values presented in the main thesis (section 2.3.3.3, Table 2.1).
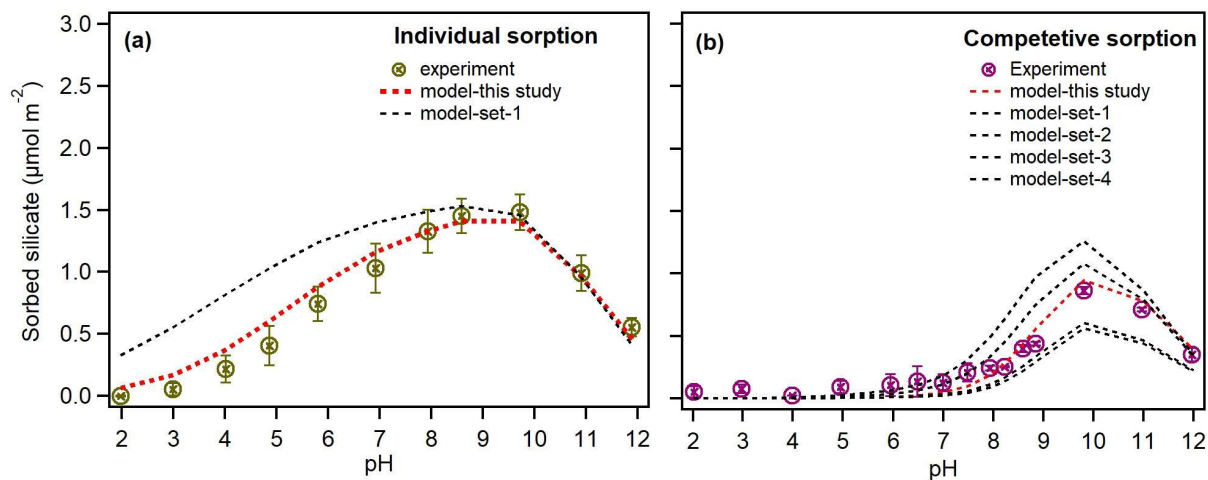


**Figure SM-2.2.** Sorption of 50 µM silicate (a) in the absence and (b) presence of 50 µM phosphate on goethite (0.5 g/L) at 25°C and $I$= 10 mM NaCl. The symbols represent the experimental data and dashed lines represent the estimated sorption predicted by the CD-MUSIC model using the $\Delta z$ and logK values in the main thesis (section 2.3.3.3, Table 2.1).

**Table SM-2.1.** RMSE calculated from the model-estimated sorption and the average experiments data points. The CD-MUSIC model implemented with the previously reported set of $\Delta z$ and logK value reported in previous studies (see Table 2.1, Chapter 2).

| Dataset | Phosphate | Silicate | RMSE |
|---|---|---|---|
| Phosphate sorption: individual (Figure SM-2.1a) | | | |
| This study | Start (*) marked values in Table 2.1 | Not used | 0.12 |
| Set-1 | Rahnemaie et al., (2007b) | Not used | 0.22 |
| Set-2 | Stachowicz et al., (2008) | Not used | 0.25 |
| Set-3 | Antelo et al., (2010) | Not used | 0.31 |
| Set-4 | Hiemstra, (2018) | Not used | 0.17 |
| Phosphate sorption: simultaneous (Figure SM-2.1b) | | | |
| This study | Start (*) marked values in Table 2.1 | Start (*) marked values in Table 2.1 | 0.06 |
| Set-1 | Rahnemaie et al., (2007b) | | 0.19 |
| Set-2 | Stachowicz et al., (2008) | Hiemstra et al., (2007) | 0.22 |
| Set-3 | Antelo et al., (2010) | | 0.56 |
| Set-4 | Hiemstra, (2018) | | 0.18 |
| Silicate sorption: individual (Figure SM-2.2a) | | | |
| This study | Not used | Start (*) marked values in Table 2.1 | 0.11 |
| Set-1 | Not used | Hiemstra et al., (2007) | 0.38 |
| Silicate sorption: simultaneous (Figure SM-2.2b) | | | |
| This study | Start (*) marked values in Table 2.1 | Start (*) marked values in Table 2.1 | 0.08 |
| Set-1 | Rahnemaie et al., (2007b) | | 0.14 |
| Set-2 | Stachowicz et al., (2008) | Hiemstra et al., (2007) | 0.15 |
| Set-3 | Antelo et al., (2010) | | 0.24 |
| Set-4 | Hiemstra, (2018) | | 0.14 |

## Section SM-2.2. Calculation of chi-square values

The goodness of fit between the experimental data and the model-estimation for the kinetic studies conducted in Chapter 2 and Chapter 4 are presented with chi-square values. The chi-square $(x^2)$ values were calculated using the following Equation SI-2.

$$\chi^2 = \sum_{pH} \frac{(O_{pH} - E_{pH})^2}{E_{pH}} \quad \ldots\ldots\ldots\ldots\ldots\ldots (SM-2)$$

where O and E represent the experimentally determined and the model predicted amount of phosphate and silicate sorbed on goethite at a given pH. The calculated $\chi^2$ value for a particular set of data with N degree of freedom can be compared with the critical chi-square $(\chi_c^2)$ values presented in Table SM-2.2. A calculated $\chi^2$ value lower than the $\chi_c^2$ value means that there is no significant difference between the experimental and model-estimated data. The greater different between $\chi^2$ and $\chi_c^2$ values (where, $\chi^2 < \chi_c^2$) means the better goodness of fit. The critical chi-squared values are presented in Table SM-2.2.

**Table SM-2.2.** Critical values of chi-square ($\chi_c^2$) distribution (Keller, 2015)

| Degree of freedom (N) | $\chi_{0.99}^2$ | $\chi_{0.95}^2$ | $\chi_{0.95}^2$ | $\chi_{0.75}^2$ | $\chi_{0.50}^2$ | $\chi_{0.25}^2$ |
|---|---|---|---|---|---|---|
| 1 | 0.00 | 0.00 | 0.02 | 0.10 | 0.45 | 1.32 |
| 2 | 0.02 | 0.10 | 0.21 | 0.58 | 1.39 | 2.77 |
| 3 | 0.11 | 0.35 | 0.58 | 1.21 | 2.37 | 4.11 |
| 4 | 0.30 | 0.71 | 1.06 | 1.92 | 3.36 | 5.39 |
| 5 | 0.55 | 1.15 | 1.61 | 2.67 | 4.35 | 6.63 |
| 6 | 0.87 | 1.64 | 2.20 | 3.45 | 5.35 | 7.84 |
| 7 | 1.24 | 2.17 | 2.83 | 4.25 | 6.35 | 9.04 |
| 8 | 1.65 | 2.73 | 3.49 | 5.07 | 7.34 | 10.22 |
| 9 | 2.09 | 3.33 | 4.17 | 5.90 | 8.34 | 11.39 |
| 10 | 2.56 | 3.94 | 4.87 | 6.74 | 9.34 | 12.55 |
| 11 | 3.05 | 4.57 | 5.58 | 7.58 | 10.34 | 13.70 |
| 12 | 3.57 | 5.23 | 6.30 | 8.44 | 11.34 | 14.85 |
| 13 | 4.11 | 5.89 | 7.04 | 9.30 | 12.34 | 15.98 |
| 14 | 4.66 | 6.57 | 7.79 | 10.17 | 13.34 | 17.12 |
| 15 | 5.23 | 7.26 | 8.55 | 11.04 | 14.34 | 18.25 |
| 16 | 5.81 | 7.96 | 9.31 | 11.91 | 15.34 | 19.37 |
| 17 | 6.41 | 8.67 | 10.09 | 12.79 | 16.34 | 20.49 |
| 18 | 7.01 | 9.39 | 10.86 | 13.68 | 17.34 | 21.60 |
| 19 | 7.63 | 10.12 | 11.65 | 14.56 | 18.34 | 22.72 |
| 20 | 8.26 | 10.85 | 12.44 | 15.45 | 19.34 | 23.83 |
| 21 | 8.90 | 11.59 | 13.24 | 16.34 | 20.34 | 24.93 |
| 22 | 9.54 | 12.34 | 14.04 | 17.24 | 21.34 | 26.04 |
| 23 | 10.20 | 13.09 | 14.85 | 18.14 | 22.34 | 27.14 |
| 24 | 10.86 | 13.85 | 15.66 | 19.04 | 23.34 | 28.24 |
| 25 | 11.52 | 14.61 | 16.47 | 19.94 | 24.34 | 29.34 |
| 26 | 12.20 | 15.38 | 17.29 | 20.84 | 25.34 | 30.43 |
| 27 | 12.88 | 16.15 | 18.11 | 21.75 | 26.34 | 31.53 |
| 28 | 13.56 | 16.93 | 18.94 | 22.66 | 27.34 | 32.62 |
| 29 | 14.26 | 17.71 | 19.77 | 23.57 | 28.34 | 33.71 |
| 30 | 14.95 | 18.49 | 20.60 | 24.48 | 29.34 | 34.80 |

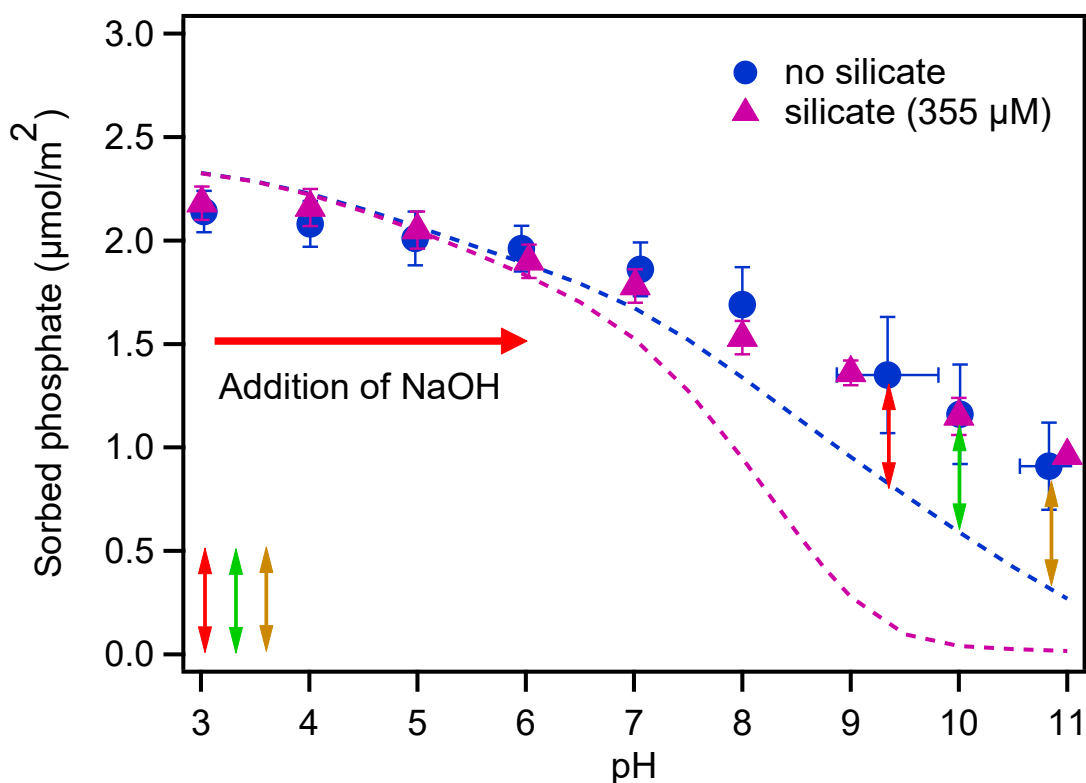**Source:** Keller, G., 2015. Statistics for Management and Economics, Cengage Learning

**Figure SM-3.1.** Amounts of phosphate sorbed to goethite as a function of pH, in the absence (filled circles) and presence of 355 µM silicate (filled triangles). The phosphate (25 µM) solution prepared in 10 mM NaCl was sorbed to goethite (0.5 g/L) at pH 3 and at 22°C, and the sorbed phosphate gradually released back to solution with increasing pH. The blue and pink dotted lines represent the amounts of phosphate bound to goethite in the absence and presence of silicate, respectively, estimated by the CD-MUSIC model under the experimental conditions stated above. Error bars represent the range of values measured between duplicate experiments.
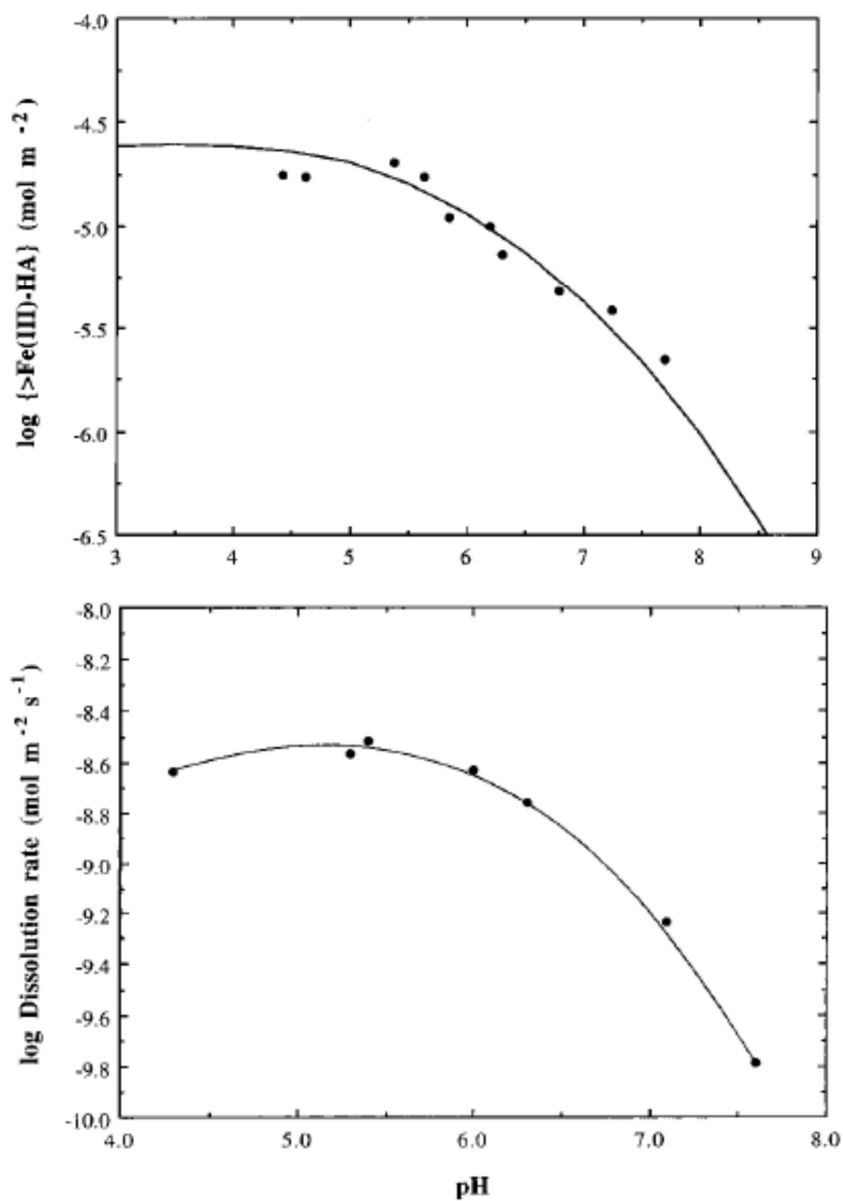
**Figure SM-4.1.** (a) The surface concentration of ascorbate ($4.8 \times 10^{-2}$ M) on a ferric (hydr)oxide ($1.0 \times 10^{-2}$ g/L, 680 $m^2$/g) as a function of pH at 20°C. (b) The rate of reductive iron dissolution from the ferric (hydr)oxide as a function of pH. Reproduced from Yiwei Deng (1997).

**Section SM-4.1: SEM analyses of ferric co-precipitates**

The co-precipitate surfaces observed by SEM (Figure SM-4.2) obtained with both synthesis methods have an amorphous appearance, with more compact surface morphology for the solids synthesized by the pH increase method. The co-precipitate with a Si:Fe ratio of 0.23 obtained with the $Fe^{2+}$ oxidation method contained acicular particles that were different from the rest of bulk material (Figure SM-4.2e, inside circles). The maximum length to width ratios of the needles were about ~5. The acicular particles could not be differentiated from the rest of the bulk material by P:Fe and Si:Fe ratios measured with EDS. These acicular particles were absent in the co-precipitates obtained with the pH increase method.
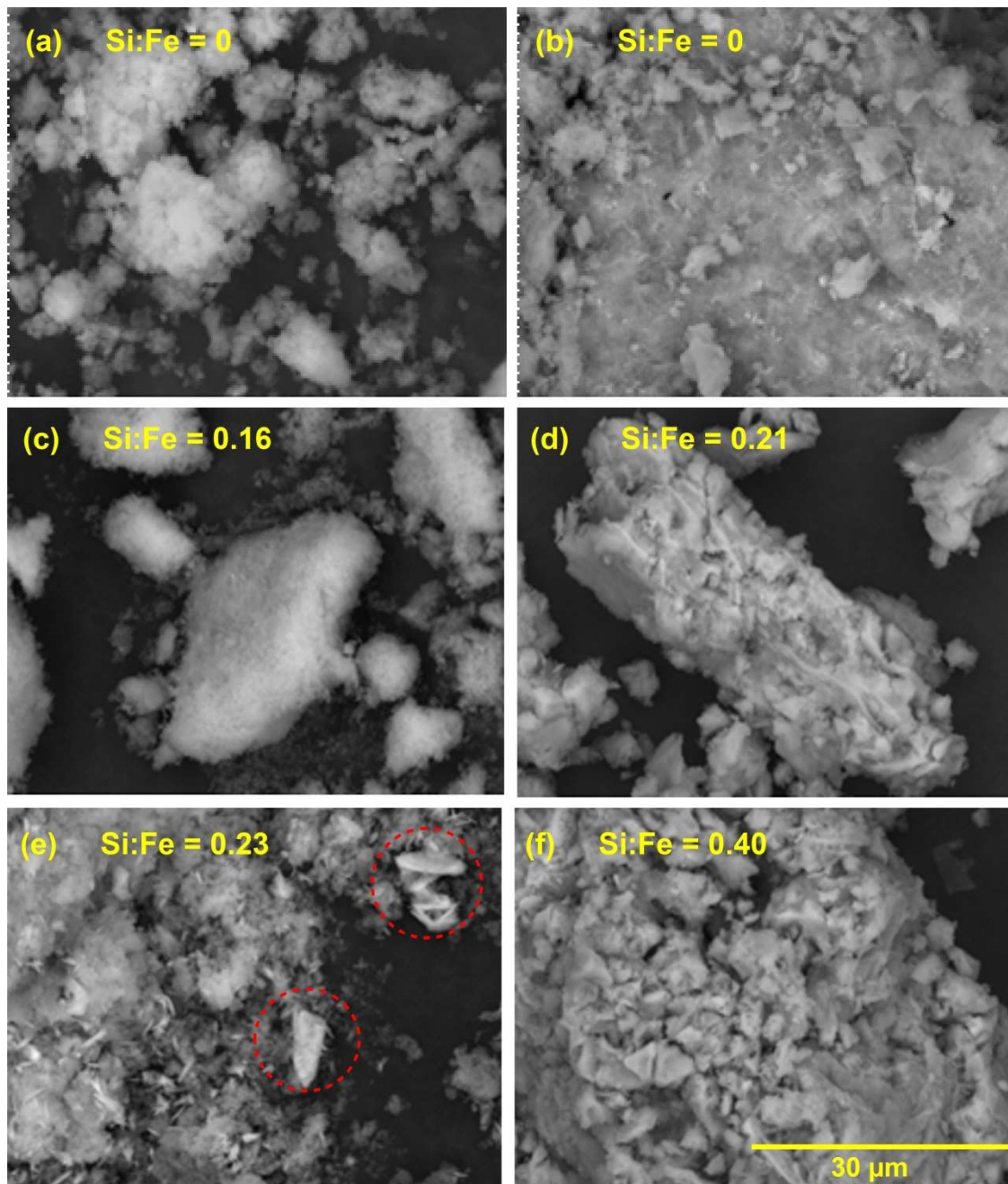
**Figure SM-4.2** SEM images collected on the co-precipitates obtained by the $Fe^{2+}$ oxidation method (left panel; a,c,e) and pH increase method (right panel; b,d,f). The P:Fe ratios within each set of co-precipitates were similar; $0.49\pm0.01$ and $0.39\pm0.02$ for the co-precipitates obtained from $Fe^{2+}$ oxidation and pH increase method, respectively. The co-precipitates within each set based on the method of synthesis had different Si:Fe ratio which are shown on the panels.
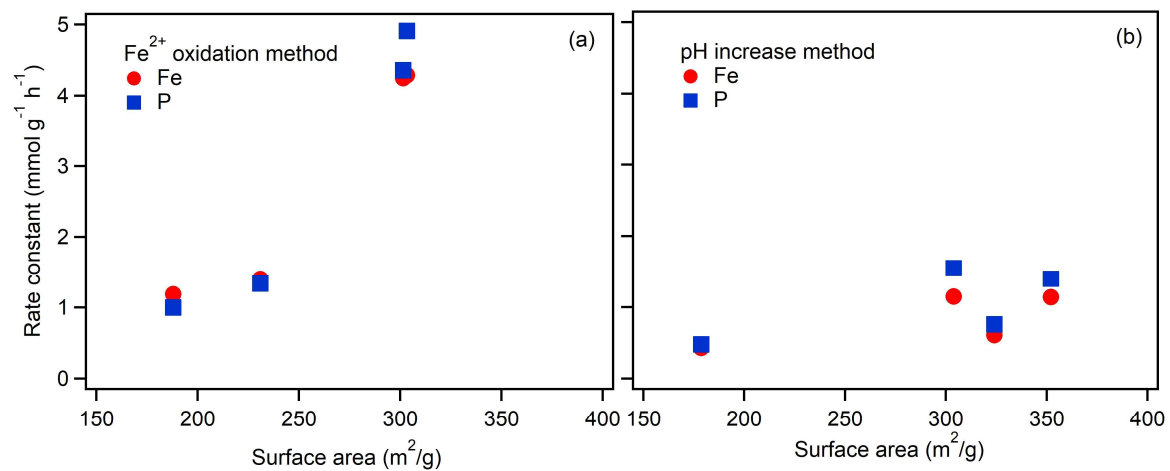
**Figure SM-4.3.** The relation between dissolution rate constant of iron (red) and phosphate (blue), from the ferric precipitates and co-precipitates obtained by $Fe^{2+}$ oxidation (a) and pH increase (b) method, with the specific surface area of the solids.
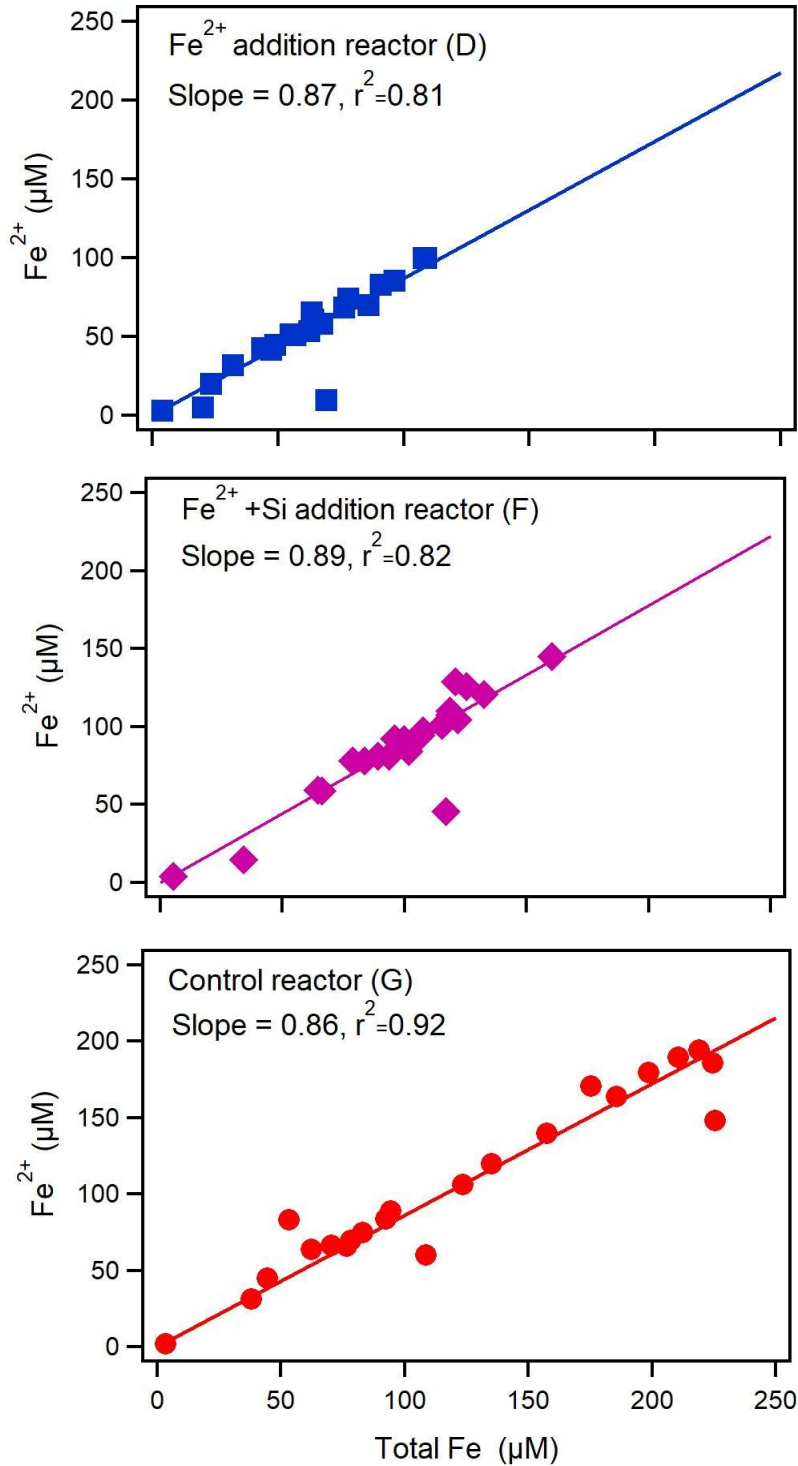
**Figure SM-5.1.** Average concentrations of $Fe^{2+}$ iron with respect to the average concentration of total Fe in the overlaying of the columns during phase-2. The inflow solutions for columns **D**, **F,** and **G** during phase-1 were APW with $Fe^{2+}$, APW with $Fe^{2+}$ and Si, and APW, respectively which were switched to APW for these columns in phase-2.
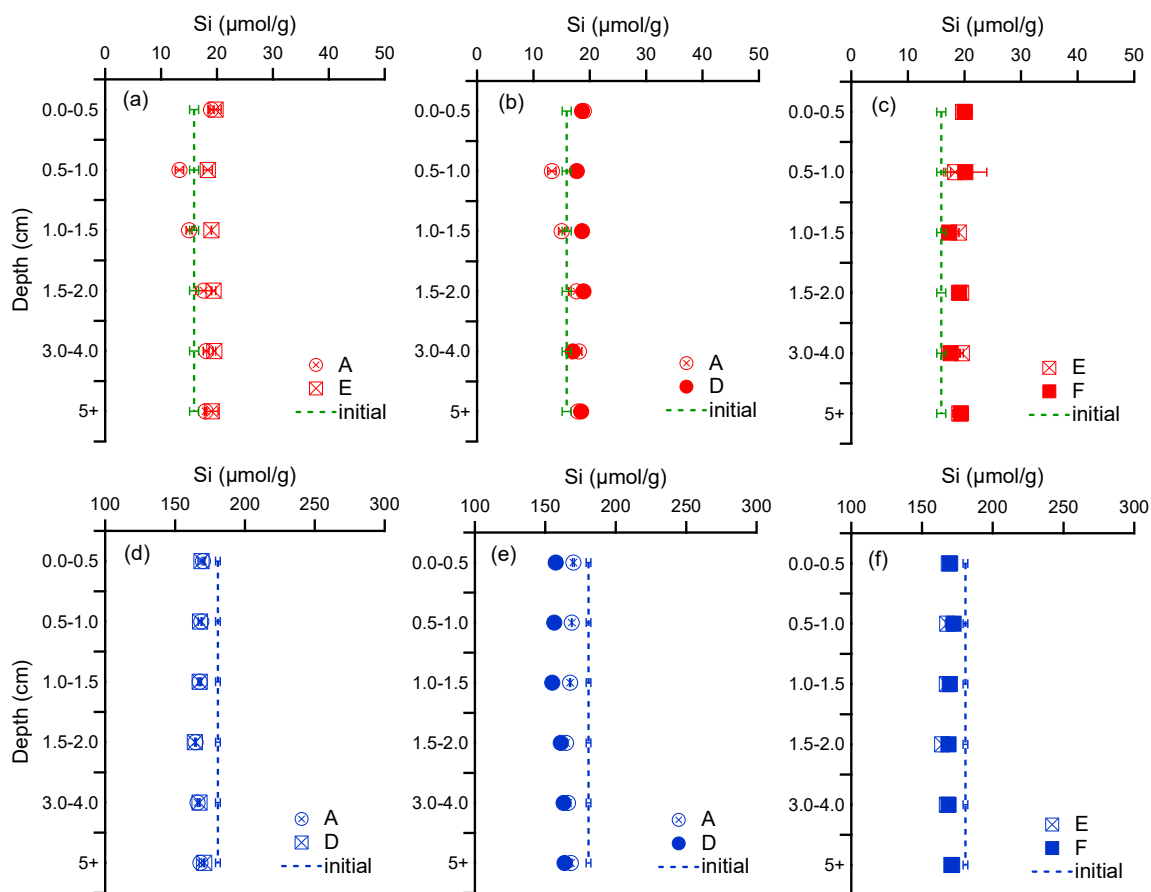
**Figure SM-5.2.** The concentrations of total Si in the sediments extracted with buffered ascorbate-citrate (a-c) and HCl (d-f) solution. The inflow solutions for columns **A** and **D** during phase-1 was APW with $Fe^{2+}$ while that for **E** and **F** was APW with $Fe^{2+}$ and Si, respectively. Columns **A** and **E** were analyzed after the phase-1, but columns **D** and **F** were analyzed after the completion of phase-2. Error bars represent the range of minimum and maximum values measured between duplicate columns.